UC Berkeley
UC Berkeley Electronic Theses and Dissertations

Title
Fiber-optic Seismology in Theory and Practice

Permalink
https://escholarship.org/uc/item/1fs925tc

Author
Lindsey, Nathaniel J

Publication Date
2019

Peer reviewed|Thesis/dissertation

Fiber-optic Seismology in Theory and Practice

by

Nathaniel J Lindsey

A dissertation submitted in partial satisfaction of the

requirements for the degree of

Doctor of Philosophy

in

Earth and Planetary Sciences

in the

Graduate Division

of the

University of California, Berkeley

Committee in charge:

Professor Michael Manga, Chair
Professor Douglas S. Dreger
Professor Richard Allen
Professor Kenichi Soga
Professor Jonathan Ajo-Franklin

Fall 2019

Fiber-optic Seismology in Theory and Practice

Abstract

Fiber-optic Seismology in Theory and Practice

by

Nathaniel J Lindsey

Doctor of Philosophy in Earth and Planetary Sciences

University of California, Berkeley

Professor Michael Manga, Chair

Distributed Acoustic Sensing (DAS) is an emerging tool in array seismology, which uses high frequency interferometry of pulsed laser backscattering inside optical fiber to analyze the axial strain induced on the fiber cable commonly buried in horizontal trenches and vertical wells at the surface of the Earth. This technology was developed over the last decade for hydrocarbon and carbon sequestration reservoir imaging and monitoring, but the focus in this thesis is to explore its application to problems in earth science, broadly defined. Combining DAS with telecommunications optical fiber networks offers meter-scale, long-term observations of ground motion over watershed apertures in sectors of the planet where traditional geophysics has been hindered by cost and field logistics, such as offshore and in urban areas. The thesis is organized as follows. I introduce the motivation for using fiber-optic seismology in Chapter 1. In Chapter 2, I define principles of the methodology and describe how the instrument works. In Chapter 3, I use continuous DAS recordings of ambient vehicular seismic noise generated on a local road to study degrading permafrost over a two-month period of artificial warming. In Chapter 4, I focus on earthquake ground motions recorded on horizontal DAS arrays. Unlike classic inertial seismometers, there is presently a limited amount of information about DAS instrument response, thus in Chapter 5 the aim is to use natural signals to quantify the broadband frequency range of DAS instruments and deduce the related amplitude and phase response functions. Lastly, in Chapter 6, I use fiber-optics on the seafloor of Monterey Bay, CA inside of an unused science cable to investigate the production of nearcoast primary and secondary microseisms, identify unmapped seafloor faults, and observe quasi-geodetic hydrodynamic phenomena in the milli-Hertz frequency range. In Chapter 7, I summarize my findings and speculate about future directions.

Contents

List of Figures

List of Tables

Acknowledgments

At Berkeley I benefited from extraordinary access to opportunities and resources as a result of the acts of many individuals. I would like to thank

- Jonathan Ajo-Franklin for ever-expanding opportunities, the freedom to explore each one, and the excitement to last a lifetime;

- Doug Dreger for an education in seismology and the practice of being a scientist;

- Michael Manga for calm, plumb-line guidance any time, every time;

- Larry Hutchings for introducing me to Berkeley, for giving me my first seismology research project, for clarifying the role we play in one anothers' lives, and for all of the free and partially-subsidized lunch;

- Horst for inspiring me to focus on seismic instrumentation;

- Verónica Rodríguez Tribaldos, Aleksei Titov, Julia Correa, Feng Cheng, Craig Ulrich, Ian Ekblaw, Michelle Robertson, Shan Dou, Brian Bonner, Ernie Majer, Kurt Nihei, Tom Daley, Bill Foxall, Greg Newman and all my colleagues at Lawrence Berkeley National Laboratory for an education in team-based, data-driven science;

- Bryan Taylor, Susan James, Sara Hefty, Margie Winn, Jill Fujisaki for your technical support with the financial, computational, and technological systems that enabled my daily research;

- Chris Tracy and Inder Monga for collaboration with the ESNet fiber in Sacramento and testing in Berkeley;

- Craig Dawe, Doug Neuhauser and the scientists and engineers at MBARI for collaboration with the MARS cable experiment;

- Anna Wagner and the CRREL team for constructing and carrying out the Fairbanks experiment, and also for bailing me out of jail;

- Eileen Martin for partnership in photonic seismology;

- Seth Saltiel, Tushar Mittal, Alex Robson, Avinash Nayak, Sierra Boyd, Noah Randolph-Flagg, Steve Breen, Lei-wei Chen, Carolina Muñoz-Saez, students of the Berkeley Seismological Laboratory and Earth and Planetary Science Department for your friendship, mentoring, ideas, and kindness;

- My parents, brother and family for your unconditional eagerness to share, support me and learn;

- Elizabeth for your daily perspective, your grounding humor, and your patience.

Chapter 1

Introduction

1.1 Motivation for new seismic instrumentation

Physical fields like displacement, strain, or temperature are continuous in space and time. Modern instruments sample these fields digitally using a sampling rate designed to capture sufficient evidence in order to support a specified hypothesis based on assumptions of the underlying process.

For over a century, seismic instruments have recorded ground vibrations with increasing sophistication. For example, globally recorded seismic waves produced by M>6 earthquakes have been used to infer Earth's structure first in a 1-D sense, and more recently in 3-D (Lehmann 1936; Dziewonski and D. L. Anderson 1981; French and Barbara Romanowicz 2015). The required costs of engineering, calibrating, deploying and maintaining a high-quality force-feedback broadband seismometer or seismometer network is non-trivial (Romanowic and Giardini 2001). As a result, for decades institutions maintaining an instrument contributed data to an international seismic campaign called the World-Wide Standardized Seismograph Network to study geodynamic and tectonic questions related to the planetary interior, but individual scientific experiments targeting processes operating at the continent scale down to the field scale were limited to seismic arrays of tens to a few hundred instruments at a time (e.g., EarthScope).

Less expensive open-loop geophones have been available for many decades for use in field-scale seismic imaging experiments. This type of instrument was designed to record short period or high frequency vibrations (frequency > 1 Hz) mostly for the purposes of hydrocarbon reservoir exploration and management and also geotechnical surveying. Advancements in semiconductor and battery manufacturing have led to relatively inexpensive all-in-one short-period seismic "nodes" (e.g., FairfieldNodal ZLand 3C 5 Hz). Today, node-based scientific experiments can use hundreds to thousands of instruments, spanning multi-kilometer apertures with 100 m separations, with deployments lasting up to ~45 days before batteries need to be replaced. As a result, an entirely new class of smaller-scale processes can be studied that answer environmental and near surface science questions, for example.

In the Long Beach Nodal Array experiment, one of the first node-based surveys, a total of 7800 nodes were deployed for 9 months in two different phases with a nominal intersensor separation of 120 m. This style of "Large-N(umber)" experiment infilled the incomplete record of minor earthquakes to address questions of seismogenic depth in the hazardous Los Angeles Basin (Brandon Schmandt and Clayton 2013; Inbal, Cristea-Platon, et al. 2018), led to new observations of coherent seismic phases from small magnitude earthquakes. It was also an opportunity to apply recently-developed ambient noise interferometry methods to treat anthropogenic noise, such as highways, passenger vehicles and commercial trucks, as non-traditional seismic sources (Inbal, Clayton, and Ampuero 2015; Meng and Yehuda Ben-Zion 2018; Brenguier et al. 2019), and integrate these sources into noise-based imaging methods (F.-C. Lin, D. Li, et al. 2013; Nori Nakata et al. 2015).

1.2 What are DAS data?

Distributed Acoustic Sensing (DAS) is an emerging form of Large-N seismology that utilizes the backscattered phase of laser pulses injected into single-mode optical fiber in an optical interferometry measurement to make continuous seismic array-type recordings at the meter-scale up to tens of kilometers in aperture (Figure 1.1). The laser pulses travel at predictable speed out and back to manufactured inhomogeneities in the fiber core where a portion of the light undergoes Rayleigh scattering and returns to the instrument, while the remainder of the pulse continues down the fiber. The backscattered light is recombined with a reference phase split from the outgoing pulse to measure the change in phase relative to the previous pulse. This photonic technique is also referred to as phase-sensitive optical time-domain reflectometry (ϕ-OTDR). DAS records the strain of ground motion at virtual locations based on the time-of-flight of laser pulses, called channels. The strain recorded at a channel is the change in length over a reference length, called the gauge length. As a result, DAS recordings are inherently array measurements. The linear distance between any two virtual Rayleigh scattering points in the fiber core used to make one DAS measurement is one the order of 100 microns based on current telecommunication-grade optical fiber standards. In practice, many scattering points are averaged to deliver 1 ground motion observation per meter subject to the gauge length and channel spacing. Regardless of whether one thinks of the DAS spatial resolution as the gauge length ($\sim$1-30 m), channel spacing ($\sim$0.1 - 10 m), or virtual scattering point interval ($\sim$1e-4 m), DAS captures elastic wavefields propagating through the Earth's crust up to 50 hz without losing information. It is this unaliased spatial recording capability that leads to the name 'Distributed' Acoustic Sensing.

1.3 Advantages and disadvantages

One key advantage of DAS is its combination of meter-scale spatial resolution and multi-kilometer aperture. Figure 1.2 demonstrates this with an example DAS dataset from Sacra-
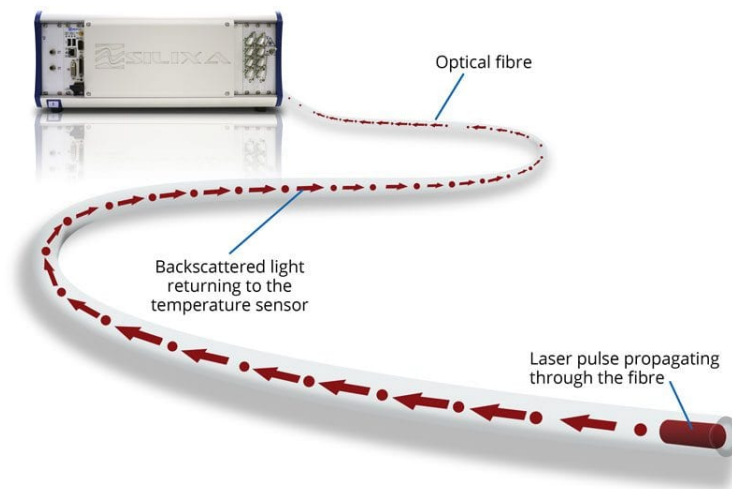
Figure 1.1: A DAS instrument connected to a single-mode fiber is used to record DAS data along the fiber [Source: Silixa].

mento, CA. This image represents a 5-minute recording by a DAS instrument connected to a buried fiber-optic cable, which has been transformed into an array of 10,000 horizontal DAS channels separated by 2 meters. This experiment used a 10 m gauge length and a sampling rate of 500 samples per second. In this type of experiment, unused ('dark fiber') telecommunications cables are leveraged as the sensing element of the DAS experiment, effectively enabling larger aperture experiments per field effort.

A continuous signal can be perfectly reconstructed if it is sampled over twice as fast as the highest frequency component (Nyquist theorem). Vehicle/train surface waves with frequency components around 1 - 50 Hz are adequately sampled by DAS. Seismometers installed in an urban area could also do this. But, along the space axis, where the vehicle-generated surface waves fall to zero in 100-200 m, the DAS sampling of 1-10 meter (depending on whether you treat the channel separation or the gauge length as the minimum spatial unit) is a significant innovation. In Chapters 5 and 6 we will see that this difference in spatial sampling enables transformation of DAS time-distance data into the frequency-wavenumber domain, and subsequent filtering and analysis of higher wavenumber wavefield components, which has traditionally not been possible with standard seismometer arrays (outside the oil and gas industry).

A second advantage of DAS is access and availability, including over long time periods. Large N urban surveys commonly require environmental permitting, a significant operations team to swap data cards and batteries at least every 4 weeks, and are likely to face security issues if nodes are not buried. In Chapter 4, we show that DAS can also be used with an existing optical fiber from a telecommunications company. DAS with telecommunications cables have not required permits, and operate continuously with from a secure facility. In principle, DAS surveys could be run over Large T(ime) also, to measure near surface property
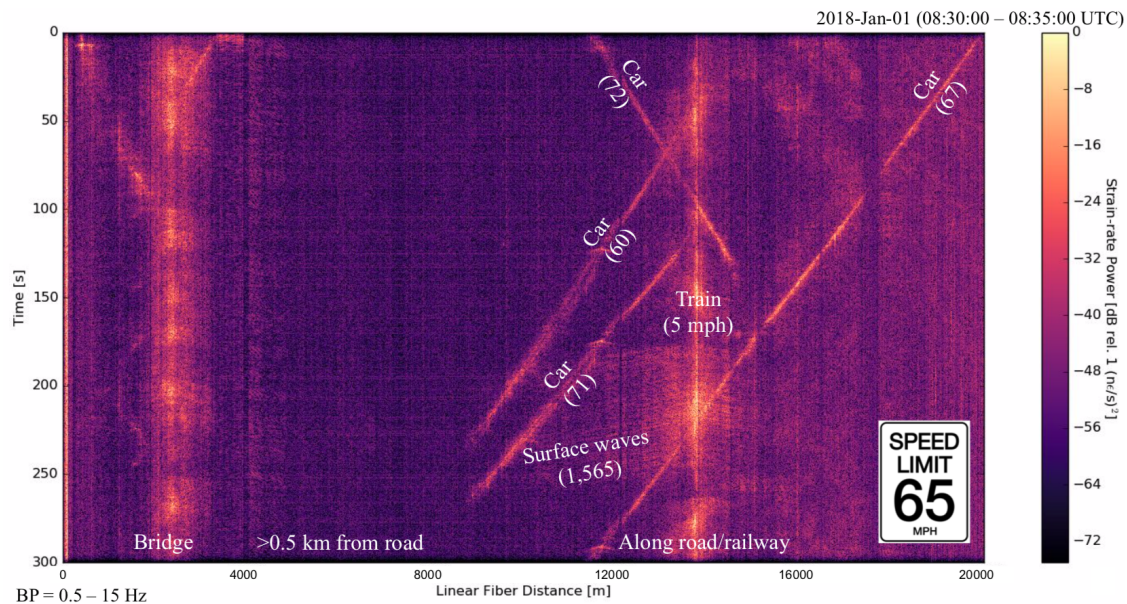
Figure 1.2: Example 5-minute dark fiber DAS recording (normalized strain-rate) from Sacramento, CA showing surface waves (BP 0.5 - 15 Hz) propagating away from moving vehicles (speeds in miles/hour), a train, and a bridge located along River Road in West Sacramento [Source: N.L.]. The local time is 1:30 am. The DAS instrument is located at 0 m.

changes over seasons to decades, because the same optical fiber can be re-occupied without significant variation in experimental setup. Optical fiber materials do age at the timescale of decades.

A third advantage is lower cost. Optical fiber is relatively inexpensive ($1-100/meter, https://www.occfiber.com/products/indooroutdoor-cables/). The cost of the instrument is not publicly available, but the value of information studies have concluded comparing the cost to deploy and maintain a pool of 10,000 seismometers with DAS is favorable (J Lopez et al. 2017). DAS is a realistic option onshore, but becomes even more attractive offshore, where there is a very high cost to house, deploy, and maintain scientific equipment in an underwater, saline, high pressure environment. Figure 1.3 illustrates the existing and planned distributions of optical fibers offshore. Utilizing a small fraction of this telecommunications network for sensing would present major opportunities for oceanography and the solid earth sciences.

While DAS is advantageous in many ways, it also has a few notable disadvantages. One drawback is that DAS only records the axial strain of the fiber-optic and is thus a single-component sensor. Helically-wrapping optical fiber around a central cable core could provide a means to obtain axis-orthogonal strain sensitivity (Kuvshinov 2016), however this is not available in existing telecommunications cables, and hence is less available for problems in earth sciences. A second disadvantage is the complicated pattern of fiber-ground coupling.
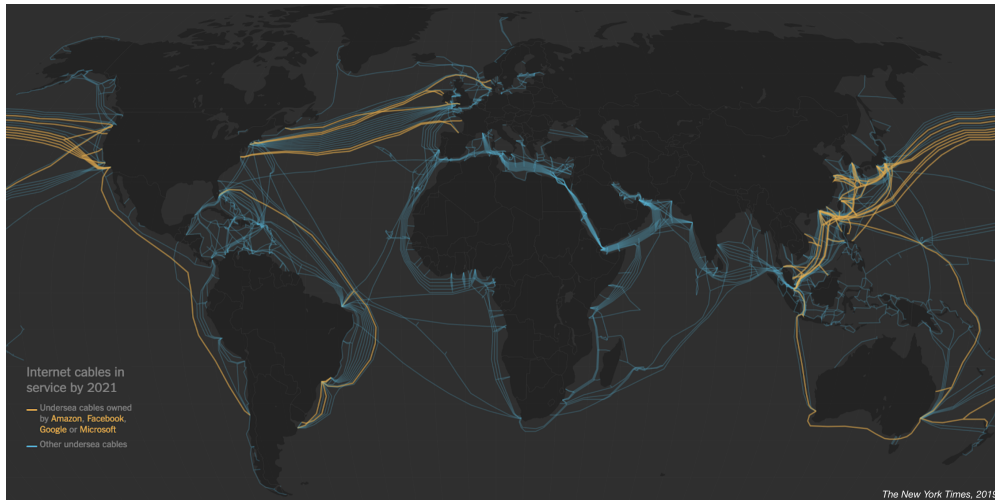
Figure 1.3: Global distribution of seafloor optical fiber [Source: New York Times, Mar 2019].

An additional reported disadvantage of DAS is that it is a lower fidelity measurement (T. M. Daley et al. 2013), although this has only been described in signal-to-noise ratios relative to downhole vertical seismic profile experiments an has not been quantified in absolute units, with description of the contributions due to photonics and fiber coupling. Advances in engineered fiber likely dramatically enhance the per sensor fidelity (Richter et al. 2019).

1.4 Development of DAS (1970-2019)

In the early 1990's, the concept of distributed optical fiber vibration sensing through analysis of the optical phase of coherent Rayleigh backscatter was first proposed in patent form (Dakin and Lamb 1991) and demonstrated with laboratory measurements (Juškaitis et al. 1992; S. V. Shatalin, Treschikov, and Rogers 1998). In 2000, the US Naval Research Laboratory demonstrated an alternative method based on differentiated phase measurement estimation (Posey, G. Johnson, and Vohra 2000). Both techniques yield a multiplexed ϕ-OTDR measurement that is a proxy for dynamic fiber strain. During this era the major application was water column acoustic ranging using fibers attached to submarines, which is why the method became known as Distributed 'Acoustic' Sensing. Since the early 2000's, several companies and institutions have continued to refine the photonic measurement, data processing methodology, and range of seismological applications. The curious reader is recommended to AH Hartog 2017 and Masoudi and Newson 2016, which describe more details of this early development period.

In the early 2010's, DAS began being used as a replacement for downhole VSP receivers (T. M. Daley et al. 2013; T. Parker, S. Shatalin, and Farhadiroushan 2014; Albena Mateeva et al. 2014). Additional applications in petroleum engineering included pipeline monitoring, hydraulic fracture monitoring, flow monitoring, and microearthquake analysis. Beyond the
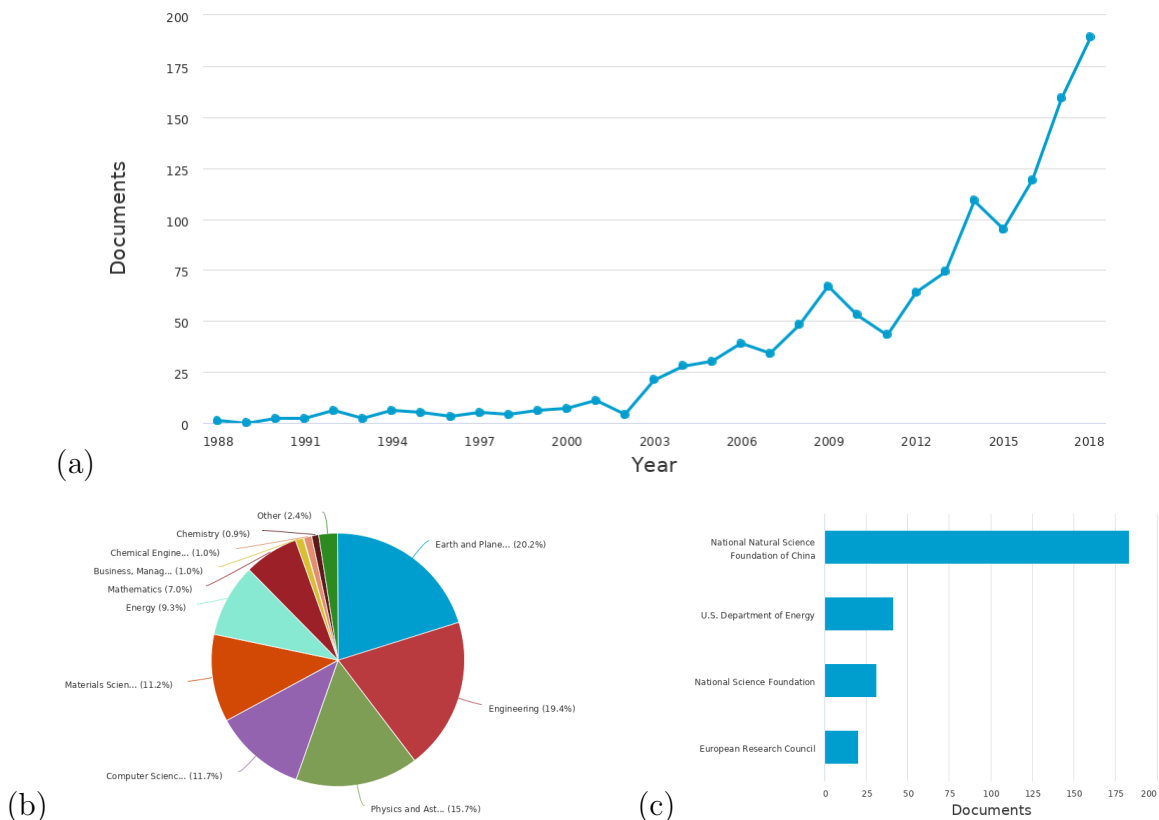
Figure 1.4: (a) Number of publications by year in Scopus database for 1988 - 2018 based on DAS keywords in article, title and abstract (704 journal articles; excludes conference proceedings and patents). (b) Sorted by research category. (c) Sorted by funding agency. [Source: Scopus].

oilfield, DAS begin being applied for critical infrastructure monitoring, border surveillance, and transportation monitoring. Around 2015, DAS began being used by academic and government research groups to study earth systems. As indicated in Figure 1.4, there was a large increase in the number of publications on DAS beginning around this time. In 2013-2014, our LBNL research group started using DAS with directly-buried optical fibers to record 8 - 25 Hz surface waves produced by nearby vehicles, and use these recordings for near surface structural imaging akin to multi-channel analysis of surface waves (MASW) for modeling shear velocity of the upper 30 m (Vs30). Several of the Lawrence Berkeley National Laboratory (LBNL) experiments which began around this time are the basis for this thesis. In September 2019, the global DAS market was valued at \$330M and forecasted to grow to \$770M during 2019 - 2025, with the largest market shares being represented by oil and gas, defense, and transportation (`https://www.alliedmarketresearch.com/distributed-acoustic-sensing-market`).

1.5   Thesis organization

This thesis is an exploration of the nuances of an emerging technology, and the application of some of its capabilities in three areas of geoscience. It is organized according to the logic with which component parts were embarked upon (but some things take longer than others). Below we synopsize the chapters that follow.

1. Principles of Distributed Acoustic Sensing

   We begin in Chapter 1 with a survey of relevant concepts from optics and photonics, before considering the gamut of modern distributed fiber-optic sensing technologies. Then, we introduce the DAS measurement principal, as well as aspects of the DAS instrument and method, including sources of measurement noise, strain sensitivity, and potential sources of bias such as ground-fiber coupling. Many of these aspects are on-going research. We conclude Chapter 1 with descriptions of each of the four field experiments conducted and an adjacent list of best field practices for DAS experiments.

2. Permafrost degradation

   In Chapter 2, we begin to apply DAS. We consider how DAS functions in a study of subsurface seismic properties or changes in those properties using the example of permafrost thaw monitoring in Alaska. In 2015-2016, we conducted a field-scale permafrost warming experiment in Fairbanks, AK. The project aim was to investigate geophysical thaw signatures related infrastructure state-of-health monitoring. Body waves produced by passing vehicles and recorded by DAS were used to measure time-lapse changes in seismic velocity across the thawing volume. Chapter 2 presents the permafrost warming experiment, and analysis of thermal and geodetic data to set the stage for the DAS ambient noise imaging problem. We then introduce the ambient noise methodology and DAS observations of vehicle noise. We show results of surface waves and body waves in time-lapse analysis, and place these results in the context of the thaw timeline.

3. Earthquake seismology

   During the thaw experiment, we also made several DAS observations of earthquakes. This led to more experiments targeting topics in earthquake seismology. At this time, we also began testing the use of DAS with telecommunications cables, which very efficiently expanded our array sizes to tens of linear kilometers, but led to new questions related to more complex strain transfer through conduits. In Chapter 3, we introduce a second field experiment (Richmond Field Station). We then discuss DAS earthquake seismology, including subjects of seismic phase identification, stacking procedures, local to regional event array beamforming, source location, and long period DAS recording of teleseismic earthquakes.

4. Instrument response

In 2017, we deployed a high-quality broadband seismometer alongside a DAS-enabled telecommunications cable in Sacramento, CA for the purpose of investigating DAS instrument response. In Chapter 4, we describe this third field experiment, the teleseism and microseism observations from the two colocated sensors, an approach to compare DAS strain-rate and seismometer particle velocity data, and a deconvolution methodology to empirically estimate DAS instrument response, as well as the results of our study.

5. Seafloor faults and nearshore ocean dynamics

In 2018, we had an opportunity to record DAS data offshore Monterey Bay with a science cable that spans the continental shelf. In Chapter 5, we focus on this fourth field experiment and its results, which included calibration of seafloor DAS data using ocean waves, observations of a local earthquake wavefield interacting with seafloor faults, quantification of the reflection of strong primary microseisms, in situ generation of secondary microseism, microseism comparisons between DAS, buoy, and seismometer data through a storm cycle, and broadband records that include ocean hydrodynamic observations down to 1000 second period.

Following Chapter 6, the findings of the thesis are summarized.

Chapter 2

Principles of Distributed Acoustic Sensing

This Chapter contains material that is presently accepted for publication at *Journal of Geophysical Research: Solid Earth* as N. Lindsey, Rademacher, and J.B. Ajo-Franklin 2019, "On the broadband instrument response of fiber-optic DAS arrays", in particular Section 2.2.

Summary As optical fiber technology has matured in the telecommunications industry to conduct digital signals, optical fiber sensors have coevolved as versatile monitoring tools in industries such as manufacturing, civil and aerospace engineering, and oil and gas. In this forerunner chapter, I introduce foundational concepts, mostly from optics and photonics, which may be unfamiliar to a geoscience audience. Fiber-optic sensing is based on the concepts of Snell's Law, optical interferometry based on the coherence of laser light, optical scattering, and time-domain reflectometry. Fiber-optic sensors are commonly distinguished by the measurand or the optical scattering mechanism employed to make the measurement. Distributed Acoustic Sensing, an intrinsic Rayleigh-based fiber sensing method, has its own important set of relevant principles, which bounds its applications inside geophysics and also inform DAS experiment design. I conclude this preliminary chapter by summarizing the five DAS field experiments conducted as part of this thesis, and discuss some best practices.

2.1 Primary concepts

In 1970, a team of scientists (Robert Mauer, Peter Schultz, and Donald Keck) working at Corning Glass in upstate New York discovered that high purity fused silica glass had excellent light transmission qualities, such as low absorption and low intrinsic scattering. This optical fiber enabled transmission of 6.5×10^7 times more information than incumbent copper wires. Optical signals transmitted at 1.65 GHz frequency and near infrared wavelength (1310 or 1550 nm) could travel over 40 km before attenuation degraded the signal below the noise level. The team developed also a method for producing their invention in long fiber wires that

was critical to commercialization. Today optical fiber geometries, dimensions and materials vary, but a common style of single-mode fiber has a 9.125 μm fiber core surrounded by a 62.5 μm diameter cladding, which is insulated by aramid protective wrapping, acrylyte, and a plastic jacket. Fiber-optics are relatively inexpensive to produce ($\sim$ \$1 - 100/m), and robust enough to be deployed underground just like other standard utilities. In the 1980's and 1990's, development and proliferation of global telecommunications led to demand for high bandwidth (1-10 Gb) optical fiber networks. Today, more than $1\mathrm{x}10^9$ m of optical fiber is buried across the continents and oceans, often with hundreds of thousands of kilometers between end-points.

Fiber-optics rely on a few basic principles of photonics. These are described next.

2.1.1 Total internal reflection

Transmission of light in optical fiber can be described using geometrical ray theory with Snell's Law:

$$n_0 Sin(\theta_0) = n_1 Sin(\theta_1),$$

where θ_0 and θ_1 are the respective incident and refracted ray angles describing how light behaves at the boundary between a material with index of refraction n_0 and n_1. Refractive index (n) of a material describes the ratio of the speed of light in vacuum (2.998 $\mathrm{x}10^8$ m/s) to the speed of light in a material. Optical fiber cores are typically 96% amorphous silica glass and have a higher index of refraction (e.g., 1.466) compared with the cladding material (e.g., 1.4584), a difference that is established by the doping process. Commonly used dopants include multivalent metal oxides (titanuium oxide, tin oxide, aluminum oxide), cesium, and rubidium.

As a result of Snell's Law, light propagating inside of the fiber-optic core becomes refracted beyond the critical angle:

$$Sin(\theta_c) = \frac{n_0}{n_1}$$

This is called total internal reflection. In Figure 2.1, the incoming rays are shown to refract into the cladding material for $\theta_0 \approx 45^o$. unless the angle of incidence (θ_0) is greater than the critical angle (θ_C), beyond which angle all light will continue to propagate in the fiber until scattering or attenuation occurs.

2.1.2 Laser light

Lasers are quantum-mechanical devices that emit electromganetic radiation in the optical spectrum through a process of optical amplification based on stimulated emission. The first operational construction of a laser ("Light Amplification by Stimulated Emission of Radiation") in 1960 by Theodore H. Maiman was based on the theory of Charles Hard Townes and Arthur Leonard Schawlow, which was inspired by construction of the maser ("Microwave Amplification by Stimulated Emission of Radiation") by Townes and Alexandr
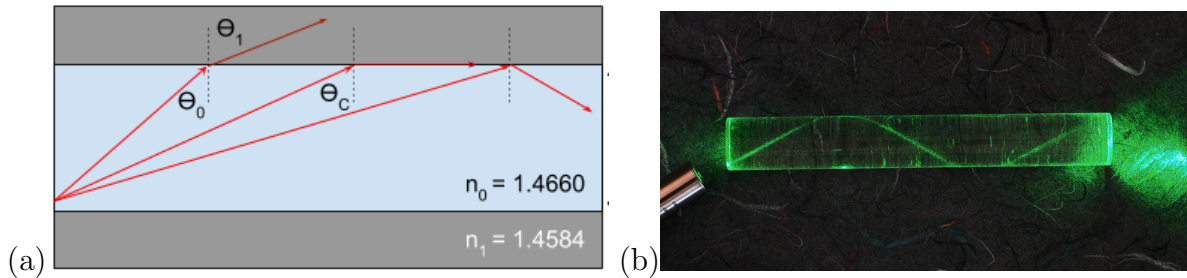
Figure 2.1: (a) Illustration of how Snell's Law inside single-mode optical fibers leads to total internal reflection [Source: N.L.]. (b) Laser light undergoing total internal reflection in a plastic hand sample at the interface between plastic (n_0=1.4892) and air (n_1=1.0003) [Source: Wikipedia].

Mikhailovish Prokhorov and Nikolai Gennadievich Basov in the early 1950s. In 1964, the Nobel Prize in Physics was awarded to Basov, Prokhorov, and Townes "for fundamental work in the field of quantum electronics, which has led to the construction of oscillators and amplifiers based on the maser-laser principle. To date, laser physics has resulted in four subsequent Nobel Prizes.

The difference between lasers and all other light sources is that laser light is coherent, meaning there is a measurable phase relationship of between two emitted waves. Coherent light can be collimated (spatial coherence) into a narrow wavelength band (temporal coherence), enabling many applications from welding and lithography, to laser pointers, printers and LiDAR.
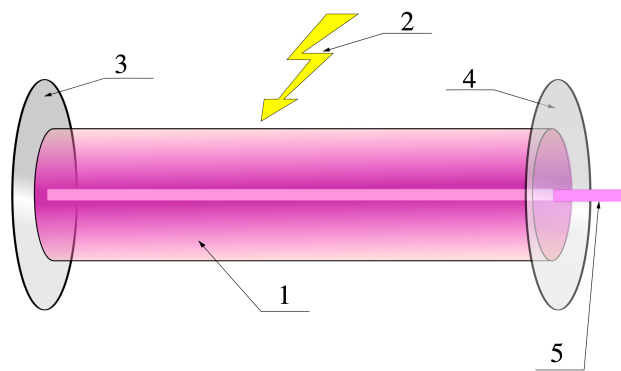
Figure 2.2: Components of a laser: (1) Gain medium, (2) Pump, (3) Mirror, (4) Partial Mirror, (5) Output coupler [Source: Wikipedia].

As shown in Figure 2.2, common lasers consist of a gain medium surrounded by a pair of mirrors forming an optical cavity which is used to achieve oscillating feedback/amplification

(i.e., the lase). A supply of pump light is initiated by a flash lamp or another laser. Typically one of the mirrors is partially transparent, which enables output coupling of a narrow beam. Laser diodes are semiconductor devices that directly convert electrical voltage into light in an analogous fashion. There are many different types of lasers varying by wavelength, line width, power, form factor, and measurement noise (thermal stability, drift, noise).

2.1.3   Optical interferometry

Several DAS instruments are based on measurements of optical phase (or its time-derivative) obtained by optical interferometry. Interferometry will be common to geophysicists, most notably because of the use of space-based geodetic interferometric synthetic aperture radar (InSAR). InSAR measures changes in distance along a line-of-sight path separating the satellite from a position on Earth's surface across a time interval of two fly-overs, and is applied to measure volcano deformation, coseismic/post-seismic deformation, and other surface dynamics. Here, I summarize the basic mathematical definition of interference as described in the context of electromagnetic waves from Hecht 1998 for context on phase-based DAS.

Consider the perspective of linearly polarized light with wave behavior given by:

$$E(x,t) = A cos(kx - \omega t + \epsilon).$$

According to the Principle of Superposition, the electric field intensity $E(x,t)$ arising from two electric source fields E_1 and E_2 is:

$$E = E_1 + E_2.$$

Assuming a homogeneous medium, the irradiance or the optical power (magnitude of electric-field intensity squared), is

$$I = < E^2 >$$

where $< \cdot >$ implies time-averaging. Equivalently,

$$I = < E_1^2 > + < E_2^2 > + 2 < E_1 \cdot E_2 > .$$

The final term, representing I_{12} is called interference, reduces to:

$$I_{12} = 2 < E_1 \cdot E_2 > = A_1 A_2 cos(k_1 x - k_2 x + \epsilon_1 - \epsilon_2)$$

where $\delta = k_1 x - k_2 x + \epsilon_1 - \epsilon_2$ represents the combined phase difference due to initial phase-angle difference and path length differences. In the orthogonal case, $I_{12} = 0$, and the waves are said to not interfere. In the more common case of parallel polarized field components, the total irradiance becomes:

$$I = I_1 + I_2 + 2\sqrt{I_1 I_2} cos\delta.$$

which has a maximum value (total constructive interference) when:

$$\delta = 0, \pm 2\pi, \pm 4\pi, ...$$

. and has a minimum value (total destructive interference) when:

$$\delta = \pm \pi, \pm 3\pi, \pm 5\pi, ...$$

Between these limiting cases the two waves are characterized as exhibiting partially constructive or partially destructively interference.

Michelson interferometer

Historically, the most important type of interferometer for science has been the Michelson interferometer, which was made famous by the Michelson–Morley experiment in 1887 that disproved the aether hypothesis and motivated development of the special theory of relativity. A second important implementation of the Michelson interferometer is the recently constructed Laser Interferometer Gravitational-Wave Observatory (LIGO) stations, which in 2015 confirmed an important prediction of general relativity with the first direct observation of gravitational waves.
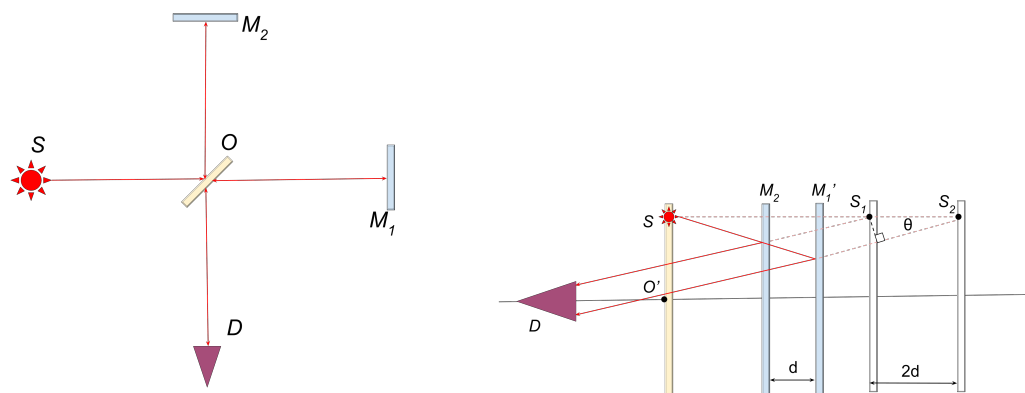
Figure 2.3: (a) Standard setup and (b) conceptual rearrangement of the Michelson interferometer [Source: N.L., after Hecht 1998, Figure 9.25].

The Michelson interferometer (Figure 2.3) uses a single beamsplitter at O to divide light from an extended source at S along two paths. These two waves reflect off of mirrors M_1 and M_2 respectively and return through O to detector at D. The magnitude of irrandiance is measured at the detector. Assume M_1 can move from its location forward or backward, changing the path of the corresponding wave. This standard configuration can be rearranged along a single optical axis defining the position of images and virtual images in terms of

distance from D. It is clear from this redrawing that the polarization of the waves will be plane parallel. Redrawing the diagram also illustrates how the path length differences along paths to virtual image points $D\bar{S}_1$ and $D\bar{S}_1$, formed as a result of separation length d between the two mirrors, leads to an interference pattern at D. The wave traveling to M_1 propagates an additional path length of $2dcos(\theta)$, resulting in a phase lag of $m\lambda$ radians relative to the other wave. This causes destructive or constructive interference based on the conditions outlined above. For standard optical bench setups, a lens detector D will display Newton's rings, where each particular ring corresponds to a fixed order m. The Michelson interferometer enables precise measurements of length. For example, if λ=1550 nm (He-Ne laser) was used in an experiment in which one measured a translation of 7 rings past a point in an Eulerian microscope frame observing at D, we would measure mirror M_1 being displaced 5.425 μm ($\Delta d = N\lambda/2$).

Mach-Zehnder Interferometer

The Mach-Zehnder interferometer is another amplitude-division apparatus in which two separate optical paths are formed using two sets of beamsplitters and mirrors. This transmission type of interferometry is common to many opto-electronic instruments.

2.1.4   Scattering of laser light in optical fiber

According to their 1973 patent, "Fused silica optical waveguide", Mauer and Schultz describe that optical scattering in the fiber core is dominated by the presence of impurities rather than being related to the material itself. Three important scattering mechanisms are widely exploited in fiber-optic sensing. These are Rayleigh scattering, Raman scattering, and Brillouin scattering. Rayleigh scattering is an elastic process, while Raman and Brillouin scattering are both inelastic processes. Rayleigh scattering is used for DAS. Below we describe each of these scattering principles in more detail. For even greater detail, please refer to AH Hartog 2017.

Rayleigh scattering (Figure 2.4ad) in optical fiber occurs when an incident photon encounters a zone of the fiber with a density heterogeneity lengthscale of diameter r< $\lambda/10$ (~100 nm), which results in scattering light in the forward and reverse directions. Light scattered at angles greater than the numerical aperture of the fiber will refract into the cladding. Light scattered back towards the source can be used for DAS measurements. The amplitude of Rayleigh scattering goes as the inverse fourth power of the wavelength of the light. When r> $\lambda/10$, light is unequally scattered in the forward and reverse directions. This is called Mie scattering. Both Rayleigh and Mie scattering are elastic because the wavelengths of the scattered and incident light are the same. For a full discussion of Rayleigh scattering in the context of DAS, see Section 2.2 below and Chapter 5.

Other forms of optical scattering include Raman scattering and Brillouin scattering, which arise from interactions of the incident photon with the vibrational modes of silica molecules (phonons). Raman scattering (Figure 2.4be) is the interaction that leads to either
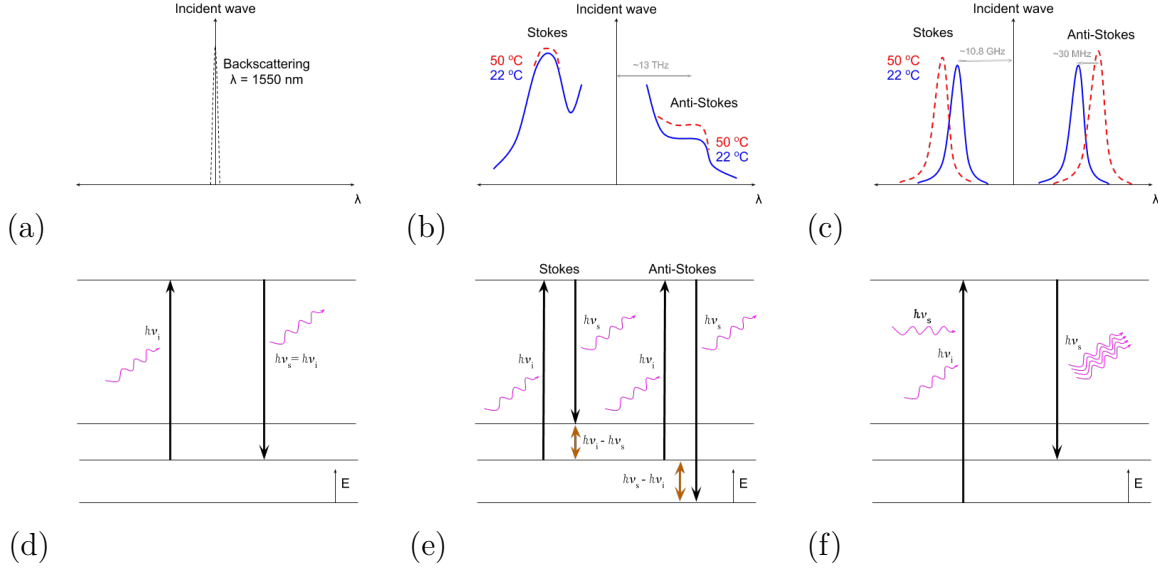
Figure 2.4: Principles of (a) Rayleigh scattering, (b) Raman scattering, and (c) Brillouin scattering. Energy-level diagrams for (d) Rayleigh scattering, (e) Raman scattering, and (f) Brillouin scattering [Source: N.L. after Hecht 1998 and Hartog 2018].

the reduction or promotion of the energy level of an incident photon. After a Raman scattering optical transition, the emitted photon can be analyzed because it will have a wavelength equal to the incident wavelength shifted by a predicatable amount. This anti-Stokes and Stokes wavelength is separated from the incident wavelength by the Raman wavelength shift ν_R (actually a wavenumber, with units of cm^{-1}). These new wavelengths are:

$$\lambda_{AS} = \frac{0.01}{\frac{0.01}{\lambda_0} + \nu_R}; \lambda_S = \frac{0.01}{\frac{0.01}{\lambda_0} - \nu_R},$$

where ν_R is on order 200 - 1500 cm^{-1}. The anti-Stokes wavelength is shorter than the incident wavelength (i.e., promoted energy state; higher energy; higher frequency).

A ratio of the Stokes to anti-Stokes photon intensities over a measurement duration is related to the temperature of the glass, and is the basis for Distributed Temperature Sensing (DTS). The intensity of anti-Stokes scattering (Long 2002) is:

$$I_{AS} = \frac{K_{AS}}{\lambda_{AS}^4} \frac{1}{exp\left(\frac{h \cdot \nu_R \cdot c}{k_B \cdot T}\right) - 1},$$

while the intensity of Stokes scattering is:

$$I_S = \frac{K_S}{\lambda_S^4} \left(\frac{1}{exp\left(\frac{h \cdot \nu_R \cdot c}{k_B \cdot T} \right) - 1} + 1 \right)$$

where h is Planck's constant ($6.62607015 \times 10^{-34}$ Js), c is the speed of light in vacuum (2.998×10^8 ms^{-1}), k_B is Boltzmann constant ($1.38064852 \ 10^{-23}$ m^2 kg s^{-2} K^{-1}), the Raman shift ν_R is expressed in cm^{-1}, with empirical coefficients K_{AS} and K_S. The ratio of the anti-Stokes to Stokes intensities is utilized in Raman-based sensing applications:

$$R(T) = \frac{I_AS(T)}{I_S(T)} = \left(\frac{K_{AS}}{K_S} \right) \left(\frac{\lambda_S}{\lambda_{AS}} \right)^4 exp \left(-\frac{h \cdot \nu_R \cdot c}{k_B \cdot T} \right).$$

At room temperature (293 K), the sensitivity of $R(T)$ is approximately 0.74%/K. Sensitivity is reduced at high temperature (0.27%/K at 593 K) because the Stokes and anti-Stokes signals converge.

Brillouin scattering (Figure 2.4cf) is similar to Raman scattering in that it is an inelastic process which generates new frequencies at a predictable shift to longer and shorter wavelengths on either side of the incident wavelength. One example of the mechanism is Stimulated Brillouin Scattering, which refers to a pump-probe process in which a pump of continuous wavelength light is used to produce an acoustic wave in the lattice of the silica glass, generating refractive index variations, and a probe beam of photons sweeps through a range of wavelengths setting up a matched condition where there exists a characteristic frequency shift, which is equal to the optical wavelength gap between the pump and probe wavelengths and dependent on environmental factors of strain and also temperature. When the wavelength difference between pump and probe is equal to the Brillouin frequency shift a large number of photons are emitted.

The Brillouin frequency shift is less than the Raman shift, on the order of 10×10^9 Hz compared to $13 \times 10^{1}2$ Hz for the Raman shift (AH Hartog 2017). The Brillouin frequency shift ν_B is defined as:

$$\nu_B = 2n_1\nu_0 \frac{V_A}{c} sin(\frac{\theta}{2})$$

for an incident optical frequency (ν_0), acoustic wave speed V_A, and phase angle θ between incident and scattered optical waves, with c referring to light speed in vacuum and n_1 being the index of refraction. A standard Brillouin frequency shift sensitivity coefficient to strain is 0.046 MHz/$\mu\epsilon$. The sensitivity coeffiecient for Brillouin frequency shift to temperature is 1.07 MHz/K, hence the senstivity to temperature is considerably weaker than for Raman scattering (0.36%/K vs. 0.8%/K) (AH Hartog 2017).

Rayleigh and Brillouin measurements are most commonly made using single-mode fibers because the incident and measured optical wavelengths are nearly the same, while Raman measurements are made using multi-mode fibers to transmit the anti-Stokes and Stokes photons back to the instrument.

2.1.5   Attenuation of laser light in optical fiber

Optical attenuation in fiber can be caused by bend losses, splice losses, optical absorption, elastic and inelastic extrinsic scattering. Intrinsic absorption is the loss of light by absorption OH+ ions and dopant, which converts photon energy at 0.85, 1.3, 1.55 μm wavelength to heat. Since the 1970's, multiple material science developments have progressively mitigated these "absorption peaks", reducing the effective loss from around 5 db/km to <0.25 db/km, where the loss of light becomes Rayleigh scattering limited. In the telecommunications industry, opto-electronic repeaters are used every 40-50 km to receive the optical phase, convert it to an electrical signal, gain that signal, and re-transmit the optical signal into the fiber. This is how signals are transmitted across the oceans, for example. Figure 2.5 shows these "water peaks" and the NIR range used for telecommunications and DAS.
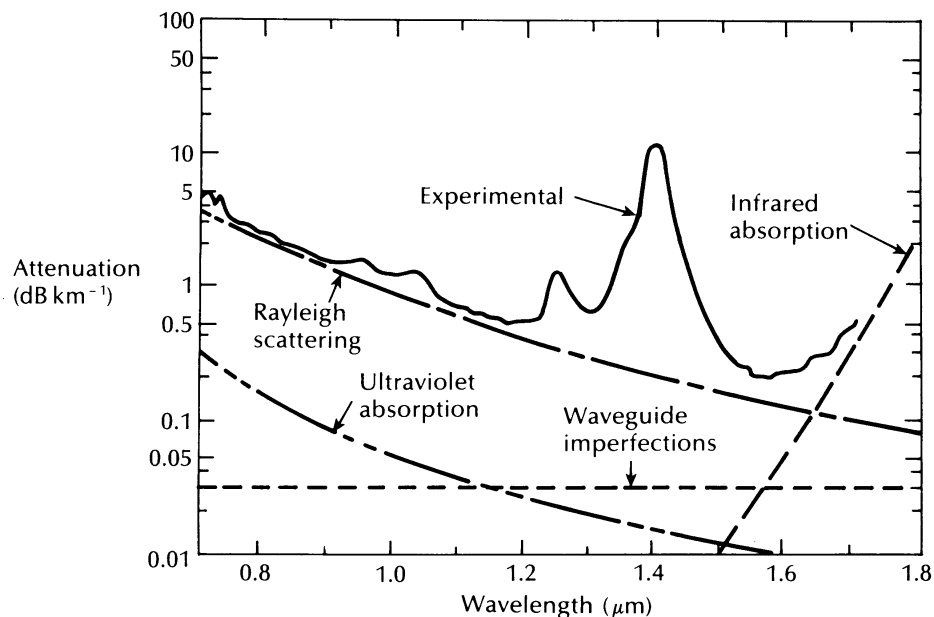
Figure 2.5: Attenuation vs. optical wavelength [Source: Comlab-2, `http://www.pef.uni-lj.si/eprolab/comlab`].

2.1.6   Optical time-domain reflectometry

Optical time-domain reflectometry (OTDR), independently developed by multiple groups in the late 1970's (Barnoski and Jensen 1976, Personick 1977), refers to a fiber-optic telecommunications technique commonly used to measure fiber quality and splice/installation defects. The technique involves injecting a pulse into the fiber, which loses light as it moves into the fiber over time owing to different attenuation mechanisms, including Rayleigh scattering. This backscattered energy is the basis for measuring attenuation as a function of

length in the fiber. A large decrease in the backscattered light correspondes to more loss at that location from where the energy reflected based on two-way time-of-flight. Using OTDR it is straightforward to detect where in the fiber there are normal sections which have linear attenuation profile versus extrinsic scattering loss points due to bends, breaks, instrument connections, or low quality splices (Fig 2.6). The time-for-distance transform principle of OTDR is common to nearly all distributed optical fiber sensors, including DAS (AH Hartog 2017).
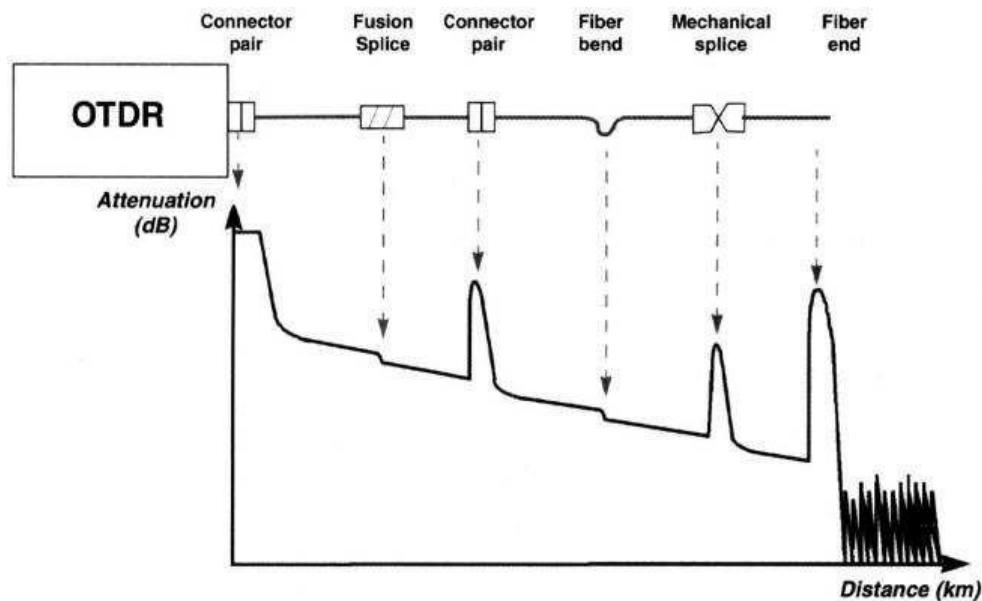
Figure 2.6: Concept of optical time-domain reflectometry illustrated with a cartoon OTDR trace where backscattered power is plotted against fiber length offset [Source: Žgalj, Skaljo, and Kadušić 2011].

2.1.7 Fiber-optic sensors

Fiber sensors can be distinguished as either extrinsic fiber sensors, such as fiber Bragg gratings, or intrinsic fiber sensors, such as the distributed types. Extrinsic sensing either refers to embedding high scattering materials into the fiber at a regular interval (e.g., 10 m) during manufacturing and then using these locations with OTDR to achieve higher signal to noise, or using a single sensing point (end tip) at the far end of the fiber. In this second version, the length of the optical fiber is simply a conductor of light and not actually a sensing element. Intrinsic distributed sensing refers to using the manufactured fiber in its basic form or sensing, without the addition of discrete scattering points. Distributed-based interrogators exist to make measurements of temperature, strain, and vibration (dynamic strain). In the future, the development of distributed sensing might include chemical sensing

and electric field sensing. Presently, we restrict our discussion to the distributed sensors available today, with the next section dealing exclusively with DAS.

Distributed Temperature Sensing (DTS) is the most mature fiber-optic sensing method. Most commonly, DAS employs a spontaneous Raman scattering to record the temperature field with a spatial resolution on order of 1 meter or less (AH Hartog 2017). DTS uses OTDR to measure the ratio of anti-Stokes to Stokes intensity for a known near-infrared incident wavelength at distances up to tens of linear kilometers. The method commonly requires use of multi-mode fibers instead of single-mode fibers due the analysis at a range of wavelengths.

Distributed Strain Sensing (DSS) is achieved using stimulated Brillouin scattering (also called Brillouin Optical Time Domain Analysis, BOTDA) or spontaneous Brillouin scattering (Brillouin Optical Time Domain Reflectometry, BOTDR). Both methods measure the Brillouin frequency shift which is established per fiber location by the condition of acoustic and optical waves moving in the fiber. The spatial resolution of the method is exceptionally tunable down to the millimeter range. DSS is sensitive to temperature, and hence is often measured with DTS for calibration of the mechanical strain data. Compared with DAS, DSS retrieves the absolute strain measurement and is typically used for static strain measurements for bridge, tunnel, and pipeline monitoring (Kechavarzi 2016).

2.2 Distributed Acoustic Sensing

Distributed Acoustic Sensing (DAS) is the generic name given to a process in which a fiber-optic interrogator unit is used to measure the dynamics of a strain field acting on a fiber. This process can be accomplished using several distinct optical approaches; however, all commercial DAS instruments generate, send, and receive coherent laser light pulses to and from the fiber that it is attached to. Most DAS instruments utilize the principles of Rayleigh scattering to measure changes in photon path length (Figure 2.7). DAS has also been performed using optical frequency domain reflectometry with a chirpped-pulse light source (E. Williams et al. 2019). Because DAS is a relatively new form of fiber-optic sensing, the details of DAS sensitivity and calibration are still a subject of on going research. The process referred to here as DAS is also called Distributed Vibration Sensing (DVS), Coherent Optical Time-Domain Reflectometery (COTDR), or phase-sensitive OTDR (ϕ-OTDR) in the photonics community.

The following discussion of the relationship between ground motion and DAS data is a synthesis of many works including: AH Hartog 2017; Kreger et al. 2015; Karrenbach et al. 2018; Grattan and Meggitt 2000; T. Parker, S. Shatalin, and Farhadiroushan 2014; Bakku 2015; Dean, Cuny, and Hartog 2017; Bóna et al. 2017; Willis, Jonathan Ajo-Franklin, and Roy 2017, as well as a number of US patents on the technology. Please see these resources for a superior discussion of DAS photonics, and the implications of alternative optoelectronic architectures. At the outset we note that there are critical differences between some DAS instruments, which include whether the Rayleigh photon scattering phase or amplitude is analyzed, whether the optical phase information is measured digitally or photonically,
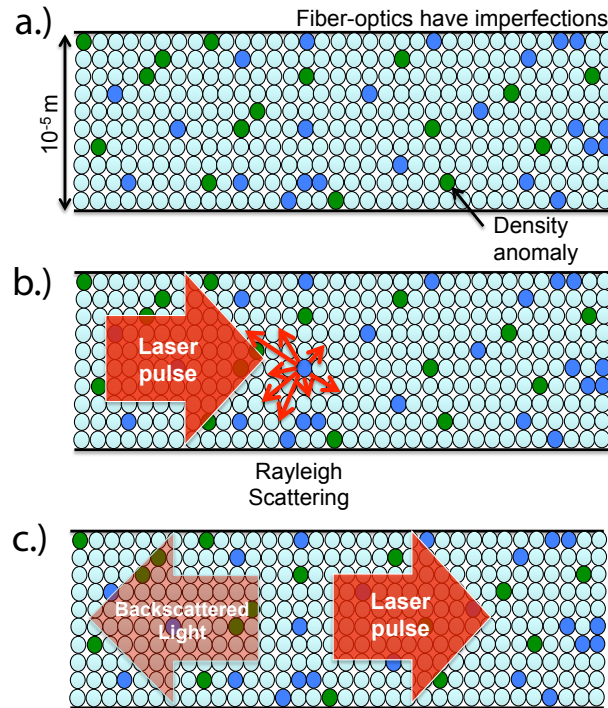
Figure 2.7: Conceptual cartoon of the DAS measurement principle: a.) Density fluctuations arise in the core of standard-grade single-mode fiber-optic cables due to manufacturing impurities; b.) Rayleigh scattering of a coherent laser pulse occurs at any density change; c.) As the laser pulse continues down the fiber, the backscattered light returns to the detector. Photonic time-of-flight provides the mapping between measurements of optical phase change and distributed axial strain acting on incremental fiber sections [Source: N.L.].

and whether such analysis is done in the time- or frequency-domain. In this thesis, we restrict our focus to the formulation of DAS employed in one instrument, the Silixa iDAS v.2, which is a time-domain, phase-based OTDR DAS instrument T. Parker, S. Shatalin, and Farhadiroushan 2014. Presently, the Silixa iDAS is among the more widely utilized instruments in the field of earthquake seismology (Nathaniel J Lindsey et al. 2017; H. F. Wang et al. 2018; Jousset et al. 2018; J.B. Ajo-Franklin et al. 2019; C. Yu et al. 2019).

Consider a DAS instrument connected to one end of a single-mode fiber. The connection is considered position $x = 0$. Assume the fiber has an average core refractive index of $n_c = 1.45$. A laser pulse with wavelength $\lambda = 1550nm$ and pulse width $p = 40ns$ is sent into the fiber ($+x$-direction) at time $t = \tau_0$. In the fiber, the pulse window occupies a few meters and travels at known speed (c/n_c). Fiber manufacturing and handling leads to commercial-grade fibers with core refractive indices that are non-uniform, thus intrinsic and extrinsic photon Rayleigh scattering will occur from unknown positions inside the pulse window. Assume a

homogeneous, dense distribution of scatterers, such that Rayleigh scattering occurs at all fiber positions out to a maximum fiber position, $x = x_{max}$. Beyond x_{max} no light travels because all photons have already scattered, were absorbed along the way, or were muted by a fiber truncation device at $x = x_{max}$. Scattered light is assumed to return to the instrument at a predictable time and is termed the backscattered signal.

2.2.1 Gauge length

The nth backscattered signal from the nth scatterer arrives at the instrument's photodetector at $t_n = \tau_0 + n \cdot dt$. Thus, late-arriving backscattered signals are associated with scattering locations further into the fiber. The position of the nth scatterer ($x = x_n$) can be derived from an accounting of the two-way travel time over the path length, $L = 2x_n = n \cdot dt \frac{c}{n_c}$. This time-for-distance transform ultimately provides positions for channels in the dataset that we say are located at $x_n \pm \frac{x_g}{2}$, where x_g is called the gauge length.

Gauge lengths are conventionally a few meters to tens of meters, and act as a low-pass filter on the strain field (Dean, Cuny, and Hartog 2017). Channel positions must still be located in physical space rather than optical distance; this is commonly accomplished by hammer "tap-test" surveying with input from as-built installation drawings of the fiber-optic route. We will further note that we can use our knowledge of x_{max} and n_c to delay the next laser pulse by the requisite amount of time in order to avoid consecutive pulse interference effects (i.e., $\tau_0 < t_n < \tau_1$).

2.2.2 Relationship between optical phase and strain

Phase-based OTDR DAS instruments employ optical interferometry to measure the optical phase change ($\Delta\Phi$) of all backscattered signals per pulse time, which we represent as:

$$\Delta\Phi(\tau_n, x) = \frac{4\pi n_c x}{\lambda} [\frac{\Delta x}{x} + \frac{\Delta n_c}{n_c} + \frac{\Delta\lambda}{\lambda}]. \tag{2.1}$$

where x represents the distance traveled in the fiber (Grattan and Meggitt 2000).

Optical phase changes result from changes in fiber length ($\frac{\Delta x}{x}$), refractive index ($\frac{\Delta n_c}{n_c}$), or optical wavelength ($\frac{\Delta\lambda}{\lambda}$). We can ignore optical dispersion ($\frac{\Delta\lambda}{\lambda} = 0$), because Rayleigh backscattering measurements are made at the incident wavelength ($\lambda = 1550nm$). Temperature changes can cause index of refraction changes (thermo-optical effect) and/or fiber length changes (thermal strain), but we ignore all temperature effects in cases of seismic wave propagation because the measurement timescale is much less than that of soil thermal fluctuations driven by diurnal or seasonal cycles ($10^{-2} - 10^2$ s $<< 10^4$ s). Stress can also change index of refraction (stress birefringence effect), but we can assume that this reduces to a scalar approximately equal to $\psi = 0.79$ for silica glass with an average Poisson's ratio of $\nu = 0.16$ at $\lambda = 1550nm$. This analysis yields an expression for $\Delta\Phi$ that depends only on the dynamic mechanical strain (dilation or contraction) of an original fiber gauge length in

the axial direction of the fiber, ϵ_{xx}, as in:

$$\epsilon_{xx}(\tau_n, x) = \frac{\lambda}{4\pi n_c x_g \psi} \Delta\Phi = \frac{1550 \cdot 10^{-9}[m]}{4\pi \cdot 1.45 \cdot 10[m] \cdot 0.79} \Delta\Phi = 11.6 \cdot 10^{-9} \cdot \Delta\Phi[rad]. \qquad (2.2)$$

The term 'dynamic' arises from the fact that $\Delta\Phi$ is measured from a reference signal. It is not possible to retrieve the true DC strain component with dynamic DAS measurements. Such measurements can be made with Brillouin-based fiber-optic strain techniques (e.g., kechavarzi2016). Choice of the reference signal turns out to have important consequences. One implementation of DAS uses a baseline reference, $\Delta\Phi(\tau_n) = \Delta\Phi(\tau_n) - \Delta\Phi(\tau_0)$, which results in DAS strain records that are relative to the baseline measurement (e.g., beginning of experiment, beginning of day). The commercial DAS we evaluated, on the other hand, treats the previous laser pulse as the reference signal, $\Delta\Phi = \Delta\Phi(\tau_n) - \Delta\Phi(\tau_{n-1})$. This means that the measurement is a record of strain-rate, or the strain accumulated since the previous pulse divided by the pulse time-step. The laser pulse rate in a conventional instrument is greater than 1e5 Hz.

In summary, the DAS system we consider injects laser light pulses into a fiber-optic cable, and measures the backscattered signal's optical phase change over time by applying optical interferometry to consecutive backscattered signals, which yields array measurements of dynamic strain-rate for individual fiber gauge lengths on the order of 10 m with a spatial sampling at 1 m or finer.

2.2.3 Ground-to-fiber strain transfer

It is most common to assume DAS fiber-optic cables are rigidly and uniformly coupled to the Earth (Albena Mateeva et al. 2014; T. Parker, S. Shatalin, and Farhadiroushan 2014). This convenient formalism is not necessarily true. Exploration of DAS strain transfer issues first appeared in vertical seismic profiling experiments where free-hanging, clamped, and grouted fibers inside of oil and gas wells showed that data quality can depend systematically on the degree of rigid coupling (J Mestayer et al. 2011; Kuvshinov 2016; Arthur Hartog et al. 2014; Munn et al. 2017).

Horizontally-trenched direct burial and dark fiber installations face at least as many complications as vertical fiber installations, including the strain transfer through the fiber and cladding material; cable packing style (e.g., aramid synthetic fiber wrapped versus gel-filled with loose-tube); outer cable coating; conduit deployment versus direct burial; conduit material; degree of contact between the fiber and the conduit; occupancy of the conduit; number of conduits per trench; age; trench depth; drained versus undrained conditions. More work is required to understand these potential impacts, which certainly vary between dark fiber DAS experiments, and likely also vary within each DAS array.

Laboratory studies are also beginning to provide a bottom-up understanding of how the isolated fiber-optic, or fiber cable package act as a sensing element (Becker, Ciervo, and T Coleman 2018; Papp et al. 2017). A few models have been proposed to upscale these

results to seismic field data (Kuvshinov 2016; Reinsch, Thurley, and Jousset 2017). Reinsch, Thurley, and Jousset 2017 proposesd a simple multilayer model of one gel-filled/loose-tube fiber-optic embedded in a telecommunications grade cable buried in sand. The authors suggest that the small strain excited by earthquakes ($1\mu m/m$) is within an elastic regime of both the ground-to-cable and cable-to-fiber systems. No conduit is considered. Based on the cable materials chosen, they calculate that seismic waves propagating at speeds in excess of 100 m/s (minimum soil V_s) are rigidly coupled to their surroundings below T $\sim 2s$ period.

2.2.4   Azimuthal sensitivity

When recorde with straight fiber, DAS data represent the axial strain acting on the cable. As this is a single component measurement, the variation in sensitivity with wave azimuth is critically important. Azimuthal sensitivity represents one important difference between DAS and more traditional inertial sensors.

Due to the fact that fused silica glass is relatively rigid, linear fiber sensors are often conceptualized as multiplexed linear strainmeters (T. Parker, S. Shatalin, and Farhadiroushan 2014; Kuvshinov 2016). Benioff 1935 described the main differences between a seismometer and a linear strainmeter (Figure 2.8). Seismic wave solutions to the one-dimensional wave equation propagating in the r direction with speed c take the form $u(x,t) = f(t \pm r/c)$. r is related to the sensors component orientation x by angle β as $r = x \cdot cos(\beta)$. u in this context is generalized, but let's take it to mean particle velocity. For a longitudinal seismic wave, a seismometer records the component of velocity parallel to x, as in $y(t) = u \cdot cos(\beta)$, whereas a linear strainmeter records $y(t) = \frac{du}{dx}cos(\beta)$. Substituting $\frac{d\zeta}{dx} = -\frac{cos(\beta)}{c}\frac{d\zeta}{dt}$, we have $y(t) = -\frac{L}{c}cos^2(\beta)\frac{d\zeta}{dt}$. Thus the azimuthal difference between a seismometer and a linear strainmeter is one additional $cos(\beta)$. The same is true for transverse waves, where the direction of wave propagation is rotated by $-\pi/2$.

This expression also shows how strainmeter recordings depend directly on the length of the strainmeter L, and represent rates of particle motion. For example, strain is a measurement of displacement over a reference length but strain recordings are proportional to velocity; strain-rate is proportional to acceleration. This is discussed more below in "Relationship between DAS data and seismometer data".

The relatively strong azimuthal sensitivity of DAS is more of an issue for horizontal applications than for vertical applications, because of the tendency for vertical body wave propagation. On horizontal DAS broadside-arriving vertically-polarized P-wave energy is, in principle, hardly detectable, but P-SV Rayleigh waves are ideally polarized. DAS becomes most sensitive to S-waves and Love waves at 45° to the axis of the cable.

2.2.5   Spatial resolution

A basic question for any geophysical instrument is, "What is the spatial resolution of the measurement?". As described above, DAS is based on the gauge length principle. According to this principle, the displacement of a fixed length is measured. DAS data are often presented
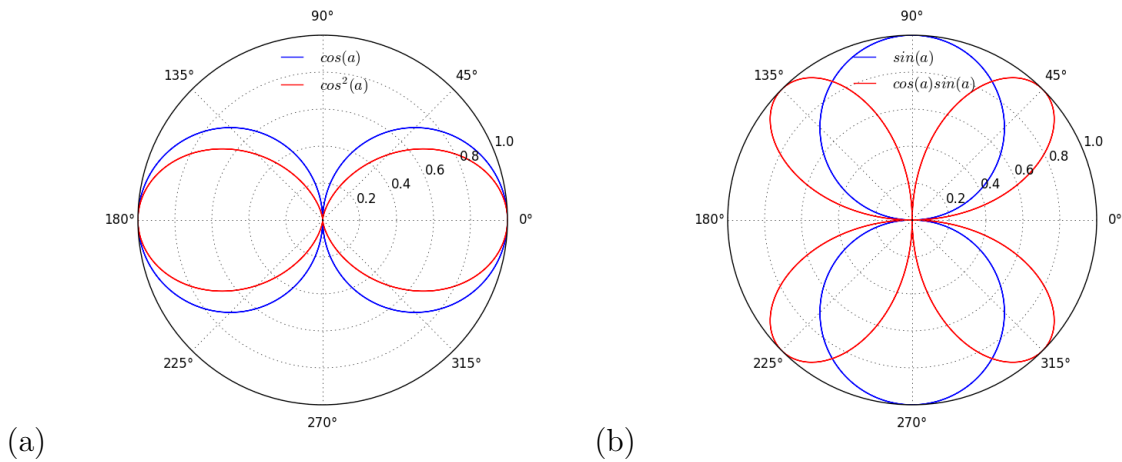
Figure 2.8: (a) Longitudinal wave response. (b) Transverse wave response. Sensor aligned with $0 - 180^o$ [Source N.L. after Benioff, 1935]

as an array of channel measurements, where a channel spacing is the increment between two gauge length measurements along the axis of linear fiber length. In the experiments conducted as a part of this thesis, the gauge length was always 10 m. Common gauge lengths range from 1 - 30 m. The channel spacing is commonly set to 1 or 2 m, but can less than a meter or can be the average of several gauge lengths.

A useful definition of spatial resolution might be the length scale at which DAS can reliably separate two independent seismic sources. For this definition we ignore amplitude information and assume that the two sources are identical in character. For example, if two seismic sources are separated by 1 m, then a 10-m gauge, 0.25-m channel DAS measurement will smear the two sources into one unseparated feature. As the intersource distance increases, the retrieved DAS feature will broaden and then separate into two. This distance depends on data processing parameters, in particular the shaping function of the channel data. For the rectangular shaping function (i.e., channel data equal to the value of a "rect"-function of length equal to the gauge length centered about the channel), two seismic sources become separable at an intersource distance of the gauge length plus one channel increment. For more complicated shaping functions ("Gaussian", "triangle") in which the data from greater than a single gauge length are used to smooth and ultimately optimize the DAS signal-to-noise ratio, the spatial resolution of DAS is likely less than this quantity.

2.2.6 Relationship between DAS data and seismometer data

Propagating elastic waves are measured at the Earth's surface using a fiber-optic cable connected to a DAS instrument and a colocated seismometer. The seismometer is oriented in the fiber cable direction and records the wavefield particle velocity v_x convolved with its known instrument response function $g(t)$. The DAS records the strain-rate of the wavefield

in the direction of the fiber axis ($\dot{e}_{xx}$), which we assume is convolved with an unknown DAS instrument response function $h(t)$. After integrating the DAS data to strain, the two measurements are related through c, the apparent phase velocity of the wave (Aki and Richards 2002):

$$v_x(t) * g(t) = -c_x(x,t) * e_{xx}(x,t) * h(t). \tag{2.3}$$

After removing $g(t)$ from the seismometer data through standard instrument response removal, a Fourier transform is applied to all quantities. We then can express the DAS instrument response function in the frequency domain as:

$$H(\omega) = \frac{V_x(\omega)}{-c_x(k_x,\omega)E_{xx}(k_x,\omega)}. \tag{2.4}$$

where $\omega = 2\pi/T$, $k = 2\pi/\lambda$, $X(\omega) = \mathcal{F}\{x(t)\}$.

2.2.7   Known sources of instrument noise

Like a seismometer, the threshold for measuring ground vibration is based on the instrument self noise level. DAS instrument self noise has not been rigorously evaluated at present. However, based on the known components involved in DAS it is likely that a few sources of noise must be controlled. As the instrument's temperature is not regulated in the field, fluctuations in the instrument's temperature will cause significant thermal strain of any optical components, causing a non-seismic noise.

A second type of DAS noise commonly observed in DAS data as a random infinite-velocity spike is attributed to laser frequency drift or laser noise, that is the non-idealized emission of photons (Zhirnov et al. 2016). This source of optical noise should be ameliorated over time as laser quality increases, but can also be removed in postprocessing with a median filter (Bakku 2015).

A third type of optical noise manifests as a reduced amplitude pattern that is quasi-random in space but time-invariant. This common problem in ϕ-OTDR measurements is called optical fading (Zhou et al. 2013; Gabai and Eyal 2016). Generally-speaking, fading results from destructive interference in the interferometry, which can happen when the random electric fields from scatterers within the fiber sum to a very small total (see Section 2.1.3). This effect depends on the wavelength of light, gauge length and pulse width, but will be time-invariant for a chosen set of recording parameters. Reduced amplitude channel noise can also result from sub-optimal fiber-ground coupling (Willis, Jonathan Ajo-Franklin, and Roy 2017; Becker, Ciervo, M. Cole, et al. 2017; Reinsch, Thurley, and Jousset 2017; J.B. Ajo-Franklin et al. 2019). Note that photonic fading noise and sensor coupling noise are indistinguishable except at the scale of the array, where sensor coupling is usually identifiable by its systematic pattern or from field installation information.

At present, a low-frequency drift has been observed in several experiments, and recently was reported on by Becker and Thomas Coleman 2019 in the amount of 2000 nm/day displacement rate. Additional testing is required to understand the cause of this drift.

Presently, it can be removed by highpass filtering to isolate the usually higher frequency signal of interest.

2.2.8 Dynamic range

The limits of DAS strain sensitivity are not presently publicly known. In principle, the lowest possible measurement is set by the self noise of the optical detector (see previous section). In situations in which the measurement is phase-rate, and not a phase, the minimum measurement must be above the self-noise over the time-step of the measurement. Thus, when measuring a low frequency seismic wave the amount of strain per pulse rate because an important quantity. Maximum strain-rate saturation level is fixed by the optical phase unwrapping algorithm applied inside of the instrument to recover the phase-rate value, or if this is very large the elasticity of the fiber itself (AH Hartog 2017). In Figure 2.9, first and second order phase-rate unwrapping algorithms have been applied to the measured values of a synthetic seismic wave increasing in amplitude over time ("True"). The result is an estimate of the maximum possible recorded strain-rate amplitude. Again, for a phase-rate measurement system, the measurement limit depends on the pulse repetition rate. Additional research is required to clarify these two limitations that bound the dynamic range of the DAS technique in the context of various DAS applications.
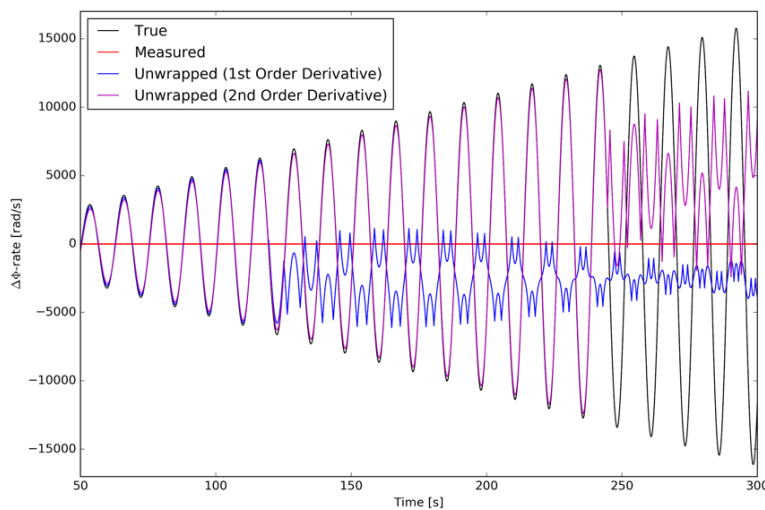
Figure 2.9: First and second derivatives of the phase-rate measurement, applied before unwrapping algorithm. At higher phase-rates the algorithms breakdown, with the 2nd order derivative providing 2x higher maximum strain-rate [Source N.L.].

2.3 Best practices for DAS experiments

- Direct burial depth

  The coupling dependence of fiber DAS is achieved in direct burial experiments by using a ditch width or another trenching machine to exacavate a shallow trench and then backfill after the cable is deployed. The requisite depth of installation was tested over several different experiments. For the applications of vehicle noise and earthquake recording, we found no considerable differences between a cable deployed at 1 meter depth (Richmond Field Station), 0.5 m (Fairbanks 2015), or 0.2 m (Fairbanks 2016). L. Parker et al. 2018 and H. F. Wang et al. 2018 used a fiber-optic cable for DAS that was installed at 10 cm depth. Spikes et al. 2019 succeeded in recovering usable seismic information from DAS recorded on surface cables deployed by simply draping the cable on the ground.

- Choice of fiber-optic cable

  The type of single-mode optical fiber cable package refers to a large number of qualities, including fiber-core doping material, cladding material, jacketing material, strength member material, gel-filled or aramid-wrapped differences, and the exterior pacakaging material. These qualities were briefly evaluated for four different fibers connected to the same DAS instrument by Dou et al. 2017, and found to present a minimal impact on the record of seismic noise from a nearby road. Additional study of this topic for low frequency monitoring was performed in a controlled laboratory setting by Becker, Ciervo, and T Coleman 2018, and additional tests are underway. A significant component in direct burial installations can be the handling and ease of working with the fiber, depending on the complexity of the fiber geometry. Thus, it may be important to consider ease of handling as a component of the cable decision.

- Dark fiber access and coordination

  The use of DAS the telecommunications cables requires recording from an end-point or node on the network. These facilities commonly have conventional power supplies and rack space available to install the instrument, but substantial planning and coordination with the facility operator is required. The delicacy of optical switching stations can limit frequency of access. Furthermore, GPS timing may also not be available due to the secure setting.

- Establishing geometry with tap testing

  The location of fiber channels in real coordinate space requires registration, commonly called tap-testing. During a tap test, a simple source like a hammer is used to make a characteristic impulse while the DAS is recording. Analysis of the DAS recording is used to establish the location of the source in channel space, while a GPS position at the active source location is used to establish the true location in latitude and longitude. Depth information is either known from directly burying the cable or is provided by

the cable laying company. Typically end- and mid-points of a direct burial experiment are enough to register the dataset to within a precision of +/- half the gauge length. At trench ends or corners there is often slightly less precision. In dark fiber experiments, there is typically less information available. The uncertainty can be greater depending on the quality of documentation provided by the current operator.

- Limit one pulse in fiber per time

  For the purpose of phase-based interferometric measurements, it is necessary to maintain a single out-going reference phase at all times. Thus, the longest sensible fiber length given pulse repetition rate f_R and average refractive index of n is:

  $$L_{max} = \frac{1}{f_R} \frac{c}{2 \cdot n}.$$

  The corollary of this becomes critical in experimental designs. For a known fiber length L, the maximum pulse repetition rate is

  $$f_R = \frac{1}{L} \frac{c}{2 \cdot n}.$$

  For 1 km well-based experiments, f_R can easily be set to 100 kHz based on the relation above. At this exceptionally high pulse rate, the method reaches a practical recording limitation. At 100 kHz the Nyquist frequency (50 kHz) exceeds the probable active source seismic frequency range (1000 - 5000 Hz depending on the experiment). For a 5 km fiber typical of direct burial installations, $f_R \sim$35 - 50 kHz, which is still high compared to ambient, earthquake, and environmental seismic frequency ranges (0.002 - 200 Hz). In both of these experimental types, there is still photonic energy at the far end of the fiber and thus fibers must be properly terminated to reduce backend reflection. For long haul dark fiber telecommunication fiber, which can exceed 40 or 50 km, $f_R \sim$1 - 2 kHz so Nyquist is 500 - 1000 Hz. which becomes potentially problematic for some applications.

- temperature stability Standard operating temperature conditions for silica-based optical fiber are typically around -40°C to +85°C. Specialty grade silica-based optical fibers are available with ratings up to 600 K, but at this high temperature regime there are many restrictions as to coatings, glass composition and other conditions for operation (AH Hartog 2017).

2.4 DAS experiments

Between 2014 and 2019, several DAS experiments were conducted by LBNL to understand validate DAS data quality and sensitivity, explore applications, and as our understanding and practice of the method became more sophisticated, use DAS to address open questions

in earth science. Here we summarize four of the DAS experiments conducted during this time. These are referenced by number or name across the following chapters, often with additional details provided. Figure 2.10 shows all four experimental arrays, which together highlight the range of possible geometries and apertures available.
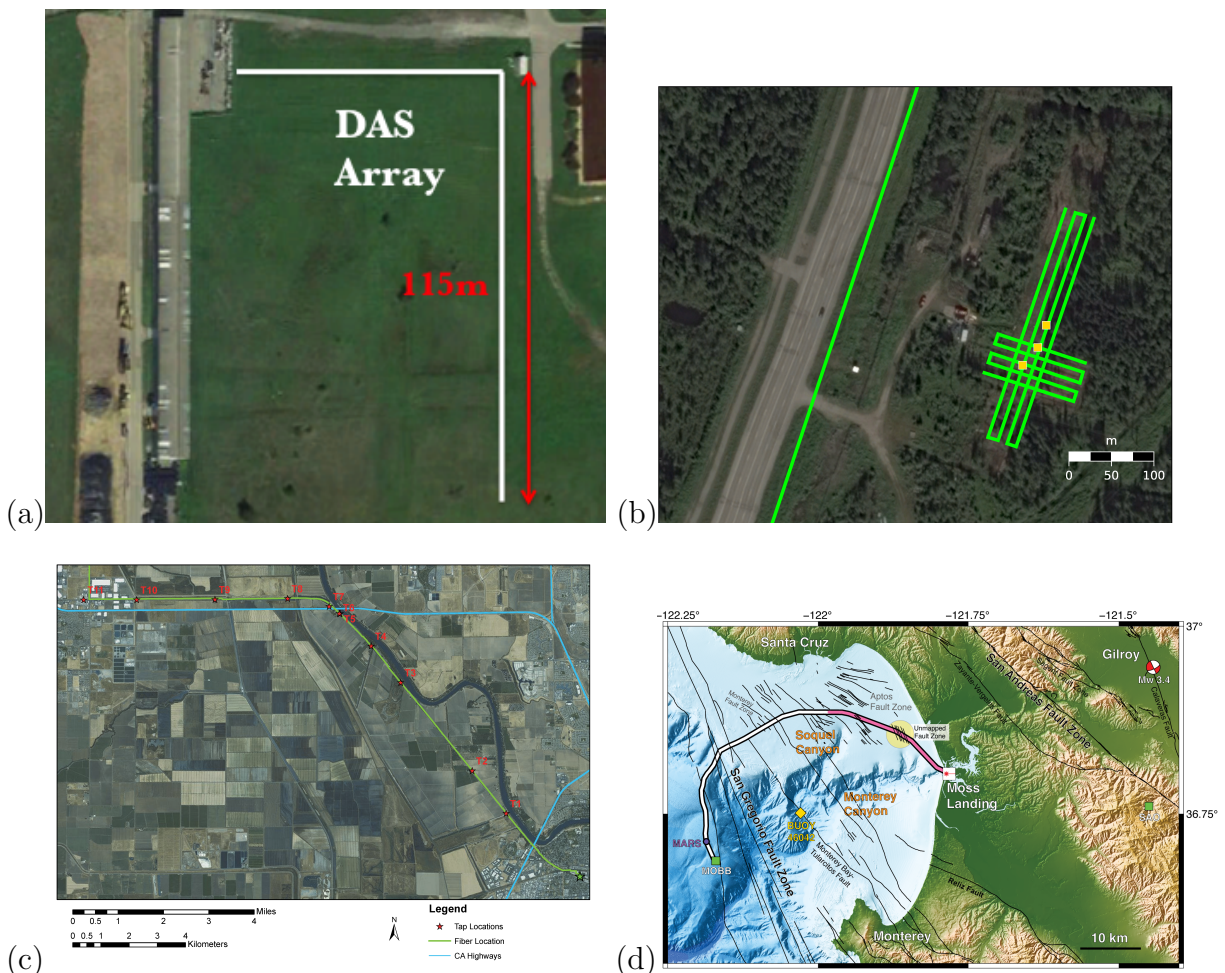
Figure 2.10: (a.) Experiment 1: 100 x 100 m, L-shaped, horizontal, direct burial DAS array at the Richmond Field Station, Richmond, CA; (b.) Experiment 2: rectilinear Warming array and Farmer's Loop Road array installed by direct-burial at the US Army Corps of Engineers' Permafrost Warming Station in Fairbanks, AK; (c.) Experiment 3: 22 km-long, horizontal, ESNet long-haul, unused telecommunications DAS array used in West Sacramento, CA; (d.) Experiment 4: 20 km-long submarine MARS cable DAS array used in Experiment 4 in Monterey Bay, CA [Source N.L.].

2.4.1   Experiment 1: Richmond Field Station, Richmond, CA

Richmond Field Station is located in Northern California on the eastern side of San Francisco Bay. Richmond Field Station is an auxiliary campus for the University of California with a history of geophysical experimentation and existing well-log information (L. R. Johnson and Silva 1981). The region lies within the Coast Ranges, a northwest trending series of ridges and valleys composed of marine sedimentary, volcanic and metamorphic rocks of the Franciscan melangé (e.g., chert, sandstone, basalt, serpentinite, blueschist). In the depositional bay setting of our experiment in Richmond, the Franciscan Formation is buried by unconsolidated fine-grained alluvial and estuarine deposits of interbedded clays, silts, gravel, and sands called the Old Bay Mud and Young Bay Mud. Well logs from the site of our experiment show a depth to the Franciscan bedrock of 35 m (L. R. Johnson and Silva 1981). The site is at sealevel and the measured water table is at a depth of 1 - 4 m. The San Andreas Fault System runs through the area, with the local Hayward Fault running between the University campus 5 miles to the east. As a result of this tectonic activity, the region experiences many earthquakes each year. A high concentration of seismic events occurs to the north less than 75 km in The Geysers geothermal system, some fraction of which are induced by the injection of water from surrounding communities in order to balance reservoir pressure.

In December 2014, we tested the DAS method with several different single mode fiber types in a 100 m x 100 m L-shaped horizontal trenched array located at the Richmond Field Station (RFS) in Richmond, CA. The purpose of this experiment was to record and then analyze a preliminary dataset for algorithm development around the method of near surface monitoring with vehicle noise and DAS, and understand the influence of cable packaging on DAS sensitivity. RFS is beside Interstate-80, a major Amtrak railway, and Regatta Boulevard, so it was an ideal location which also provided ease of access from Berkeley, CA. In addition to this passive recording we conducted a few active source experiments at the beginning of the experiment using a hammer and strike plate. In total, we tested four different fibers: (1) a gel-filled, polyethylene-coated hybrid cable containing both single-mode and multi-mode fibers manufactured by Optical Cable Corporation (OCC); (2) a tight-buffered, polyethylene-coated tactical cable manufactured by AFL Telecommunications LLC; (3) a gel-filled, steel-armored cable manufacturedby OCC; (4) a tight-buffered, steel-tubing encapsulated cable manufactured by Draka. All cables were buried in the same trench and connected in series to form one continuous sensing element. The depth of the fiber was 1 m. We used a ditch witch for the excavation and a small steam shovel and hand tools to backfill. The far end of the fiber was terminated so as to prevent a large amplitude backreflection. We conducted a tap test with a hammer and strike plate and GPS theodolite to survey in the geometry and the DAS dataset. For the experiment, we used a Silixa iDAS v.2 interrogator unit to record at a 1000 Hz sample rate (500 Hz Nyquist) with a 10 meter gauge length and 1 meter channel spacing. The instrument was attached to one end of the single-mode fiber inside the sensing cable inside a small research container with a wall feed-through that led to the fiber optic trench. A GPS antennae provided accurate timing. DAS strain-rate

measurements were made between 01-Dec-2014 and 12-Feb-2015, with a multi-week period of no recording in January 2016. A total of 9.7 TB of data were collected. Additional details about this experiment are published in Dou et al. 2017.

2.4.2 Experiment 2: Permafrost Research Station, Fairbanks, AK

The next experiment was conducted over two summers in Fairbanks, AK in collaboration with the US Army Corps of Engineering, Cold Regions Research and Engineering Laboratory. The purpose of this experiment was to artificially thaw the frozen ground and measure the geophysical signals of thaw related to subsidence hazards to infrastructure, one thaw-related seismic wave speed changes. The thaw experiment was located at the CRREL facility near Fort Wainwright called the Permafrost Research Station, 5 km NW of Fairbanks town.

Tectonically, Central Alaska exists in a a broad zone of crustal deformation produced by collision and flat slab subduction, which is accommodated by slip on right-lateral strike-slip faults, such as the Denali fault (Mw 7.9 in 2002), as well as smaller-scale fold-and-thrust belts and a set of left-lateral strike-slip fault zones that produce a transtensional setting (Tape et al. 2015). The broad flood plains of the Tanana and Chena Rivers dominate the landscape with meandering streams and oxbow lakes bounded by low hills and flat-bottomed valleys. This depositional environment from the Alaska Range means Quaternary fluvial and glaciofluvial sediments blanket Fairbanks. Sand and gravel transported by glaciers are covered with finer silt and sand-silt sediments and organic material of varying thickness. Permanently frozen soils are present in the basin, discontinuously covering one-third to one-half of the area. Where present the soil is frozen below approximately 0.3 - 10 m below the surface depending on the time of the year, and forms a seasonally-frozen active layer that promotes frost heave and ground subsidence.

In June 2015, we buried 1.5 km of OCC hybrid optical fiber along Farmer's Loop Road at a depth of 50 cm. In August 2015, we used the Silixa iDAS to record preliminary noise dataset during the daylight hours over 6 days (01-Aug-2015 to 07-Aug-2015; 500 GB) at 1000 Hz with a 10 m gauge length and a 1 m channel spacing. In July 2016, we returned to Fairbanks, AK for the thaw experiment. We deployed an additional rectilinear fiber array above the artificial permafrost warming experiment, which was located 75 - 100 m east of Farmer's Loop Road at the Permafrost Research Station. The 2016 array consisted of 4 x 180 m roughly NNE-SSE (road parallel) and 5 x 60 m ESE-WNW (road orthogonal) lines directly buried at a depth of 20 cm. Fiber was run from one trench to the neighboring trench through adjoining connector trenches to form one continuous sensing element. The far end of the fiber was terminated so as to prevent a large amplitude backreflection. Connecting the 2016 and 2015 fiber arrays, the total linear fiber length was 4 km. The instrument was located in the central operations building where the warming system was controlled. The Silixa iDAS v. 2 used in this experiment was placed on a vibration isolation table designed to isolate the optical interferometer from local vibration noise. GPS timing was not enabled

during this experiment due to a miscommunication. DAS strain-rate measurements were made from 28-Jul-2016 through 04-Oct-2016. A total of 51 TB of data were collected during this period in a continuous fashion. Additional details about this experiment are published in A. M. Wagner, Nathaniel J Lindsey, et al. 2018.

2.4.3 Experiment 3: CenturyLink cable, Sacramento, CA

The site of Experiment 3, our first dark fiber experiment, was a transect located in the Sacramento River flood plain, north and west of Sacramento, CA. The geology of the site consists largely of Quaternary sediments including a sequence of silts and clays underlain by fine sands. Prior regional studies (e.g., Gutierrez 2011) have mapped the surface sediments as a mixture of poorly sorted Holocene alluvium near the Sacramento and finer-grained Holocene basin deposits deeper in the flood plain. Partially lithified sediments from the Tehama formation have been mapped from approximately 50 m to greater depths (Olmsted and Davis 1961). The segment of dark fiber we utilized for this study, shown in Figure 2.10c, runs from West Sacramento CA to the small town of Woodland CA. As can be seen from the fiber network map, the recording profile extends from an urban environment into a section of farmland near the Sacramento River, crossing Interstate 5 before bending westward towards Woodland. For the length of the fiber route shown in Figure 2.10c, installed cables utilize the right-of-way associated with a rail line and are roughly co-linear with the train tracks. The agricultural areas sampled by this profile are partially irrigated through a variety of methods and groundwater is actively extracted from both the shallow surficial aquifer as well as deeper sources.

In July 2017, we began recording DAS data on a telecommunications cable in West Sacramento, CA. This multi-month experiment ran from 04-Jul-2017 through 08-Mar-2018 and utilized an unused long-haul (> 50 km) fiber from the US Department of Energy's Energy Sciences Network (ESNet) group based on LBNL. The purpose of this experiment was first to quantify the conditions around recording DAS with unused telecommunications cables, but also represented an opportunity to scale up our previous field experiment designs to now operate over multiple kilometers and multiple months. The major science aims were hydrological imaging with infrastructure and urban noise and also earthquake recording. The Silixa iDAS v. 2 used to record the data was installed on a vibration isolation table on a server rack-mounted shelf inside a Point of Presence (PoP) telecommunications switching station owned by CenturyLink located in West Sacramento. GPS timing was not available during this experiment due to the location inside the PoP room, but Network Timing Protocol was accessed weekly via an internet connection. Knowledge about the fiber's location and packaging were provided by CenturyLink. In total, the full linear fiber length was 22 km, which covered an aperture of approximately 18 km. The fiber route consisted of an urban segment as the route departs the PoP under the road and then crosses a busy bridge, and a less busy 10-km NW-SE segment along the Sacramento River, as well as an E-W segment as the route enters Woodland, CA. DAS data geometry was established by tap testing. Based on as-built drawings provided from the operator, fiber installation conditions varied from

cable mounted to the side of a bridge, to the most common style of trenched cable in HDPE conduit, to cable in HDPE conduit that had been pulled through directionally-bored HDPE or in some cases steel casing. The average depth was assumed to be 1 - 3 m. The instrument recorded strain-rate measurements at 500 Hz with a 10 m gauge length and a 2 m channel spacing. The far end of the fiber was determined to be beyond the maximum sensible length of 22 km. A total of 172.8 TB of data were collected during this period in a continuous fashion. Additional experiment details are published in J.B. Ajo-Franklin et al. 2019.

2.4.4 Experiment 4: MARS cable, Monterey Bay, CA

The site of Experiment 4 was a bending North shelf transect of Monterey Bay south of Santa Cruz, CA where the submarine Monterey Accelerated Research System (MARS) science cable was installed in 2006-2007. The San Andreas Fault System traverses the setting of our study in a northwest-southeast orientation in a series of sub-parallel faults forming the boundary between the Pacific and North American tectonic plates. In this area, the San Andreas Fault System is comprised of several major faults, including the Monterey Fault Zone directly beneath our array extending from Monterey to Santa Cruz within Monterey Bay, the San Gregorio Fault extending from Monterey to Half Moon Bay predominantly offshore, the San Simeon Fault, and the San Andreas Fault. The shallow-dipping continental shelf in Monterey Bay is a submerged extension of the continent with a maximum water depth of 120 m, but was approximately 30 - 50 m water depth for our experiment. Recently multibeam mapping from the California Seafloor Mapping Program has identified that the shelf is comprised of fine-grained mud, sand, gravel and rocky outcrops that provide ecological niches for marine species. Close to shore and at the edge of the continental shelf pebble to cobble-sized clasts and a coarser-grained sediment (e.g., sand or gravel) makes up the seafloor.

In early March 2018, we conducted a DAS experiment from the shore of Moss Landing, CA in Monterey Bay using the submarine MARS cable. We were permitted to use this cable during a four day period of routine maintenance and testing on the MARS science node that is supported by the MARS cable. From 09-Mar-2018 until 14-Mar-2018, a Silixa iDAS v.2.3.3.5 instrument was positioned on a vibration isolation table in the shore station where the cable emerges onshore. Continuous DAS recordings of strain-rate were acquired with a limited number of brief interruptions due to power outages associated with cable maintenance. An optical time domain reflectometry measurement of the optical fiber used for DAS showed 0.19 dB/km of loss from shore and the MARS node at 52 km, with minimal losses at the instrument connection point. This DAS instrument used a 10-m gauge length. Laser pulse timing parameters were set to ensure only one outgoing laser pulse was inside the fiber at a time. Channel spacing was set to 2 m, which resulted in 9,984 channels spanning the first 19.968 km of cable length. Data were digitized at 500 samples per second to preserve seismological and oceanographic signals below 250 Hz. A GPS antennae provided accurate timing. DAS data were written continuously via USB 3.0 at 250 MB/s to an external hard disk. In total, 3.2 TB of raw optical phase rate data (proportional to strain-rate) were

recorded during the 4 day experiment. Additional experiment details are provided in N J Lindsey, T C Dawe, and J B Ajo-Franklin 2019.

2.5 Concluding remarks

Fiber-optic DAS has developed across multiple industries. Although there exists, at present, a wide instrumentation knowledge gap related to the photonic details and calibration of any DAS instrument, the basic principles of optical fiber transmission, fiber sensing, Rayleigh scattering, optical interferometry, OTDR, as well as details related to measurement noise are all known. The background presented in this Chapter sets the stage for applications of DAS (Chapters 2, 3, 5) and further calibration (Chapter 4).

Chapter 3

Permafrost degradation

The thaw experiment piece of this Chapter was published in A. M. Wagner, Nathaniel J Lindsey, et al. 2018, "Permafrost degradation on demand: observations from a controlled warming experiment", *Scientific Reports*, **8**, 10908 doi:10.1038/s41598-018-29292-y.

Summary Global climate change has and will continue to disproportionally warm high latitude regions, whose landscapes have been characterized by a presence of permafrost in historical times. In a warmer Arctic, the thermal, hydrological, and mechanical physics of permafrost thaw and degradation including ground subsidence have been hypothesized to couple in a complex fashion. However, data collection efforts to study these feedbacks in the field have been limited. As a result, laboratory and numerical models have largely outpaced field calibration datasets. This includes application of geophysical methods in permafrost terrain to calibrate our understanding of the signals of permafrost degradation.

We present the design, execution, and results from a decameter-scale controlled thawing experiment, targeting the coupled thermal/mechanical response and temporal sequence of surface subsidence relative to permafrost degradation at depth. The warming test was conducted in Fairbanks, AK, and utilized an array of in-ground heaters to induce thaw of an 11 x 13 x 1.5 m soil volume over 63 days. The 4-D temperature evolution demonstrated that the depth to permafrost lowered 1 m during the experiment. The resulting thaw-induced surface deformation was ~ 10 cm as observed using a combination of measurement techniques. Surface deformation occurred over a smaller spatial domain than the full thawed volume, suggesting that gradients in cryotexture and ice content were significant. We then develop a seismological methodology based on fiber-optic DAS sensing of vehicle noise with the aim to assess subsurface seismic velocity changes in a time-lapse fashion. The methodology is tested using data from the warming experiment and our results are evaluated in the context of the known warming experiment's timeline.

Key Findings

- A permafrost zone containing approximately 30% ice content was artificially warmed

over two months. During this time, the warming front advanced by 1 m beginning from a depth of 4 m, which resulted in thaw-induced subsidence of $\sim$ 10 cm over a smaller spatial domain than was warmed. This suggests cryotexture and ice content gradients were significant, and that mechanical deformation accounted for some of the volume change.

- Vehicle-generated seismic noise produced along nearby Farmer's Loop Road and recorded by a 2-D horizontal DAS array delivered time-lapse repeatable noise correlations on a daily basis despite observed spatial and temporal source field nonstaionarity.

- Rayleigh waves (f = 5 - 25 Hz) extracted from noise show large traveltime delays across the entire site (3-6% dv/v), which correlate temporally with precipitation events. Late arriving phases show larger delays; an attenuation effect is also observed. This process dominates the hypothesized changes in dispersive surface waves, rendering them unusable for tracking the permafrost thaw process.

- Refracted SV waves (f = 2 - 4 Hz) extracted from noise show large traveltime delays (> 50% dv/v) across the warmed zone and coevolve in a predictable manner with the thaw experimental results. Seismic slow-down is observed to begin as early as the second or third week of the experiment, prior to or coincident with subsidence, however the measurement noise may prevent its usefulness in realtime subsidence early warning system.

3.1 Background

Recent and forecasted global climate change trends have led to observations and predictions of increased thermal degradation of frozen ground (M. T. Jorgenson, Shur, and Pullman 2006; Romanovsky, Smith, and Christiansen 2010). At Earth's high latitudes, this transition threatens one of the largest carbon sinks on the planet, an estimated 2.7 B metric tons of frozen organic soil stored in permafrost (Schuur et al. 2015). Additionally, permafrost thaw modifies landscapes, affects ecological and biological systems, and destabilizes arctic infrastructure, which has led the United Nations Environmental Program to identify thawing of permafrost as one of the most significant yet least studied environmental hazards (Nelson, Anisimov, and Shiklomanov 2001; S V Kokelj and M. Jorgenson 2013; Schaefer et al. 2014; Steven V Kokelj et al. 2017; Vincent, Lemay, and Allard 2017). More than 40% of Earth's high latitude permafrost will be lost by 2100 (Chadburn et al. 2017) where damage to future arctic infrastructure is of great concern. Permafrost environments are a unique setting for built infrastructure where minor surface or subsurface thermal perturbations can lead to significant substrate consolidation. Permafrost warming and thaw subsidence can occur slowly as prograde thaw fronts deepen the seasonally-unfrozen "active" layer year-upon-year, or rapidly as thermokarst (surface subsidence) features that degrade deep zones of previously ice-rich soil over weeks to months (S V Kokelj and M. Jorgenson 2013; Ge et al. 2011).

An individual thaw zone may only span ten meters, but tessellate over multiple watersheds (Frohn, Hinkel, and Eisner 2005). Structural foundation damage and even catastrophic failure of roads, bridges, and runways due to permafrost degradation have been documented across Canada, Alaska, and northern portions of Europe and Asia (Fortier, LeBlanc, and W. Yu 2011; Harris 2019; Ladanyi and Andersland 2004; Fortier, LeBlanc, and W. Yu 2011; Hayashi 2013). One cumulative estimate of the expense from climate-related damage to Alaskan public infrastructure for the period 2015-2099 is \$5.5B (Melvin et al. 2017). Infrastructure failure often occurs without precursory observations of the escalating risk, because the pan-arctic extent of the hazard and the resolution required to "catch" any single nascent thaw zone is ill-posed for conventional monitoring strategies. Ideally, infrastructure would involve sensing network elements to provide "awareness" of environmental changes that could provide warnings to infrastructure managers before failure.

In order to understand the role of permafrost thaw in future trends of global climate change and the related arctic infrastructure hazard, it is necessary to develop numerical, laboratory, and field-based approaches that are capable of capturing the relevant physical processes, including important spatial and temporal dynamics (J. C. Rowland, Travis, and CJ Wilson 2011; Atchley et al. 2015; Grosse et al. 2016). For example, understanding how soil bulk and shear modulus evolve as permafrost thaws could facilitate development of a permafrost thaw early warning system using dense seismic sensors along critical infrastructure like railways and pipelines. Predicting how effective stress and heat transport will evolve at an interface in low permeability silt and clay given a possible range of environmental conditions, and specifically how these processes upscale to a useful global climate model input is another important topic of research (Schuur et al. 2015; H. M. Wainwright et al. 2015). Complicated thermal, hydrological, and mechanical feedbacks with multiphase freeze-thaw dynamics have been hypothesized using realistic parameters and timescales (McKenzie, Voss, and Siegel 2007; Rempel 2012; Uchida, Soga, and Yamamoto 2012; Bense et al. 2012), yet field-scale calibration is difficult resulting in that laboratory and numerical studies presently outpace instrumented observational datasets.

The majority of permafrost thaw observations are campaign-based or utilize historical remote sensing datasets. This approach to field calibration has two challenges. First, although remote sensing and ergodic field campaigns have generated a set of geophysical observations that can be used to test hypotheses (Hubbard et al. 2013; Walvoord, Day-Lewis, et al. 2015; Walvoord and Kurylyk 2016; Liu et al. 2015; Baptiste Dafflon et al. 2016), the massive scale demanded by atmospheric models and available parameter space involved in coupled thermo-hydraulic-mechanical (THM) feedbacks requires development of innovative ways to effectively capture sub-grid cell processes and calibrate all of the possible models. A second problem with the present limited inventory is that the rate and impacts of anthropogenically-driven warming still require decades of observation to conclusively characterize a process; surface subsidence is a difficult target due to superimposed seasonal cycles. Examination of the impact of warming magnitude and timing on processes is also complicated by the coupling of temperature gradients with secondary variables (e.g. soil moisture) across time-for-space comparison transects.

These limitations have motivated development of a variety of artificial warming approaches to allow exploration of the impact of temperature on relevant biological, biogeochemical, and physical properties at a range of length and time scales. A range of studies examining surficial alteration, particularly those involving small (meter to sub-meter) plots have utilized infrared lamps to induce controlled heating on the order of 1-10 ^{o}C (Beyens et al. 2009). Other warming experiments have explored the use of snow fences to provide semi-controlled warming through use of winter snow accumulation as an insulating driver. Starting with the work of Hinkel and Hurd Jr 2006, a sequence of studies have used snow fences to increase permafrost temperature by as much as 14 ^{o}C at seasonal peaks, in some cases generating subsidence on the order of 10-20 cm over 8 years of installation. Recently, the CiPHER project (Susan M Natali, Schuur, Trucco, et al. 2011; Susan M Natali, Schuur, and Rubin 2012; Susan M. Natali et al. 2014) combined snow fence treatments, spring snow removal, and surface warming to provide year-round modifications to soil temperature. Despite their success, several limitations of snow fence alterations exist, including the substantial duration of the resulting experiments (multi-seasonal, often spanning 3-5 years), complicated seasonality of the driving force (winter, relative to snow depth), and coupled impacts on hydrology. For this study we instead adopted a strategy that was originally proposed by Hanson, Childs, et al. 2011; Hanson, Riggs, et al. 2017, M. Krassovski et al. 2015 and A. M. Wagner, Beede, and Zufelt 2013, but had not been fully implemented. Our approach utilized an array of subsurface electric heaters installed in a tight grid to manipulate subsurface temperature over a decameter scale during a single field season. The advantage of this approach is the ability to precisely probe the coupling between energy flux, thermal alteration, and resulting mechanical alteration or permafrost degradation over short duration. Although natural permafrost degradation usually occurs more slowly, a controlled-warming experiment allows one to accelerate the near-surface environment and thus quantify the important relationship between subsurface thaw and surface topography, capture the geophysical signatures of the advanced thaw process, and test novel sensing modalities such as low-cost instruments, distributed fiber-optics, and remote imaging methods which might someday be combined in a permafrost early warning system.

Problem formulation

Use of DAS receivers and vehicle noise for time-lapse near surface monitoring generally, or permafrost thaw infrastructure hazard monitoring in particular, requires demonstration of the methodology in a permafrost zone. In 2016, we performed a permafrost controlled-warming experiment in Fairbanks, Alaska. The aim of this project funded by the Department of Defense Strategic Environmental Research Development Program was to capture the coupling between deep soil thermal perturbations and surface subsidence in cold regions using a wide variety of traditional and novel remote sensing, geophysical, and hydrological techniques. My involvement in this project led to the use of these data as the demonstration experiment.

In Section 3.2, we present the warming experiment results which demonstrated that artificial warming arrays can be utilized for (a) extensive soil column heating over short duration, (b) permafrost table ablation representative of decades of warming, and (c) surface subsidence over the decameter range of lateral extent. This capability has immediate utility for validating coupled thermal-mechanical models of permafrost, testing geotechnical monitoring systems, and exploring the biogeochemical impacts of warming scenarios. The core problem in this part of the chapter is method development to configure and demonstrate a system that enables simulation of the fieldscale effects of warming.

Then in Section 3.3, we present the data, methodology, results and discussion of the time-lapse ambient noise seismic imaging experiment. This experiment was conducted during the warming experiment. It utilized fiber-optic DAS as the central recording technology and vehicles as the source of seismic waves. The core problem in this part of the chapter is to determine the onset of soil softening through seismic velocity analysis relative to known observables such as input heat flux and soil warm-up, ice loss, and surface subsidence. A related task is to consider how such a "seismic precursor" may be incorporated into a permafrost early warning system to detect and monitor thaw subsidence hazard in cold regions. The use of vehicle noise from the road infrastructure itself and a continuous passive recording system already are address that problem.

During analysis, we observed major swings in surface wave speeds that were strongly correlated with near surface ground moisture due to precipitation. While interesting on its own, for the purposes of this experiment it meant the proposed time-lapse dispersion imaging methodology had to be replaced with a seismic refraction methodology that utilized body wave refracted phases which arrive before the surface waves. In this scenario, the refracted/diving S-wave is less sensitive to the shallow unfrozen zone due to its propagation through the deeper permafrost.

3.2 Artificial permafrost warming experiment

3.2.1 Site selection

Our experiment was conducted at the Fairbanks Permafrost Experiment Station (Figure 3.1), located about 4 km northeast of Fairbanks, Alaska on Farmers Loop Road. Fairbanks is located in the interior region of Alaska at 64.80^{o}N, and has a continental sub-Arctic climate with a mean annual air temperature of -2.9 ^{o}C (1971 – 2000) with a range of -23.2 ^{o}C to 16.9 ^{o}C. This region is characterized as having discontinuous permafrost on the cusp of stability. The Permafrost Experiment Station was established in 1945 by the Field Operations Branch of the Permafrost Division of the U.S. Corps of Engineers St. Paul District and is currently operated by the Cold Regions Research Engineering Laboratory (CRREL). The study site was previously disturbed and cleared for an ecosystem prototype warming installation system in 2010. The objective of that study was to develop an in-ground warming system that could artificially simulate soil-warming. Components of the present heating system are pictured

in Figure 3.5. The heating elements were re-purposed and reinstalled for this study during the summer of 2016 in the geometry shown in Figure 3.1B.
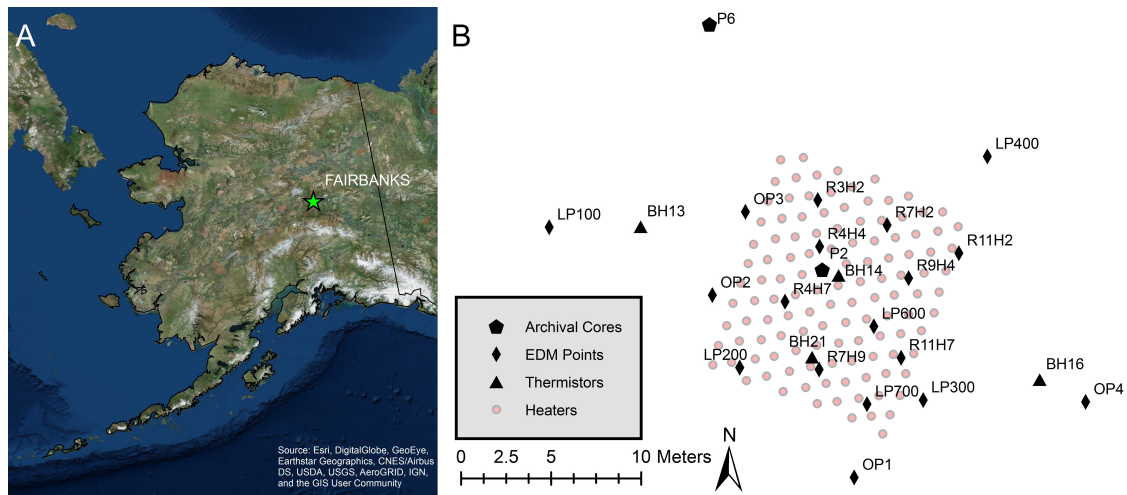
Figure 3.1: Site Overview. (A) Location of Fairbanks, Alaska. (B) Map of warming experiment at Fairbanks Permafrost Research Station showing heater layout (red circles), archival borehole locations (black hexagons), borehole temperature monitoring locations (black triangles), and EDM monument locations (black diamonds) [Source: A.W.].

Core Location	Depth (m)	Coarse Sand (500-1000 microns)	Medium Sand (250-500 microns)	Fine Sand (100-250 microns)	Very Fine Sand (50-100 microns)	Silt (2-50 microns)	Clay (< 2 microns)	Soil Type (USDA)
P2	4.04	0%	0%	8.95%	25.98%	64.63%	0.44%	Silt loam
P2	4.52	0%	0.11%	11.18%	36.89%	51.46%	0.37%	Silt loam
P2	4.85	1%	4.62%	11.67%	22.63%	59.88%	0.43%	Silt loam
P2	7.01	0.20%	2.01%	12.77%	33.22%	51.35%	0.45%	Silt Loam
P2	8.18	0%	0%	2.81%	29.86%	66.78%	0.55%	Silt loam
P6	6.25	0%	0.44%	9.98%	31.64%	57.19%	0.75%	Silt loam
P6	6.63	1.47%	5.60%	17.62%	29.02%	46.33%	0.12%	Silt loam
P6	7.01	0%	0%	5.32%	19.06%	74.91%	0.72%	Silt loam
P6	7.47	0%	0.43%	10.01%	20.90%	68.13%	0.54%	Silt loam

Figure 3.2: Grain size and soil texture results from P2 and P6 cores as obtained by laser particle size analysis [Source: J.A-F.].

Soil texture and conditions

Preliminary coring and geophysical exploration was conducted prior to the warming test. The subsurface was found to consist of both ice-rich and discontinuous warm permafrost soils. Tan silts were encountered at the surface and grey silt are located at depths exceeding 1.4 m. Soil grain size analysis of cores collected at multiple locations revealed the site was dominated by relatively homogeneous silt loams with a small fraction of very fine sand (Figure 3.2) at all sampled depths. X-ray computed tomography (CT) analysis of recent cores has shown laminar ice features and some disseminated ice in silt sections (Figure 3.4). Soil saturation is normally within 0.3 m or less of the surface and moisture contents range from 26% to 41% by mass for silts with peat down to a depth of 9.5 m at the Linell plots. Modern permafrost table depths vary across the heating plot, ranging from 1.5 m to the east to ~6 m to the west; this variability is due to historical changes in vegetation coverage.

Soil texture characteristics were evaluated at the site. Small samples were obtained from archival cores P2 (center of heated zone) and P6 (northwest of heated zone). Sub-samples were weighed, dispersed in Sodium Hexametaphosphate, and analyzed using a laser particle size analyzer (Malvern Instruments Inc, Mastersizer 3000). Depths between 4.04 m and 8.18 m were sampled, corresponding to the primary thaw zone. As can be seen in Table S1, all samples are classified as Silt loams under USDA soil classification guidelines with the majority of each sample by volume consisting of particles between 2 and 50 microns (silt). Clay fractions were surprisingly small (<1% by volume) and the sand fractions were dominated by very fine material (50-100 micron). Figure S1 shows the results on the US Department of Agriculture: Natural Resources Conservation Services soil triangle. In summary, the analyzed samples are consistent with the relatively homogeneous wind-blown Fairbanks silt deposits common in the region.

Cryotexture texture

To better understand dominant cryotexture and ice distribution, core was obtained for location OP4, to the east of the thaw experiment plot. X-ray computed tomography (CT) of
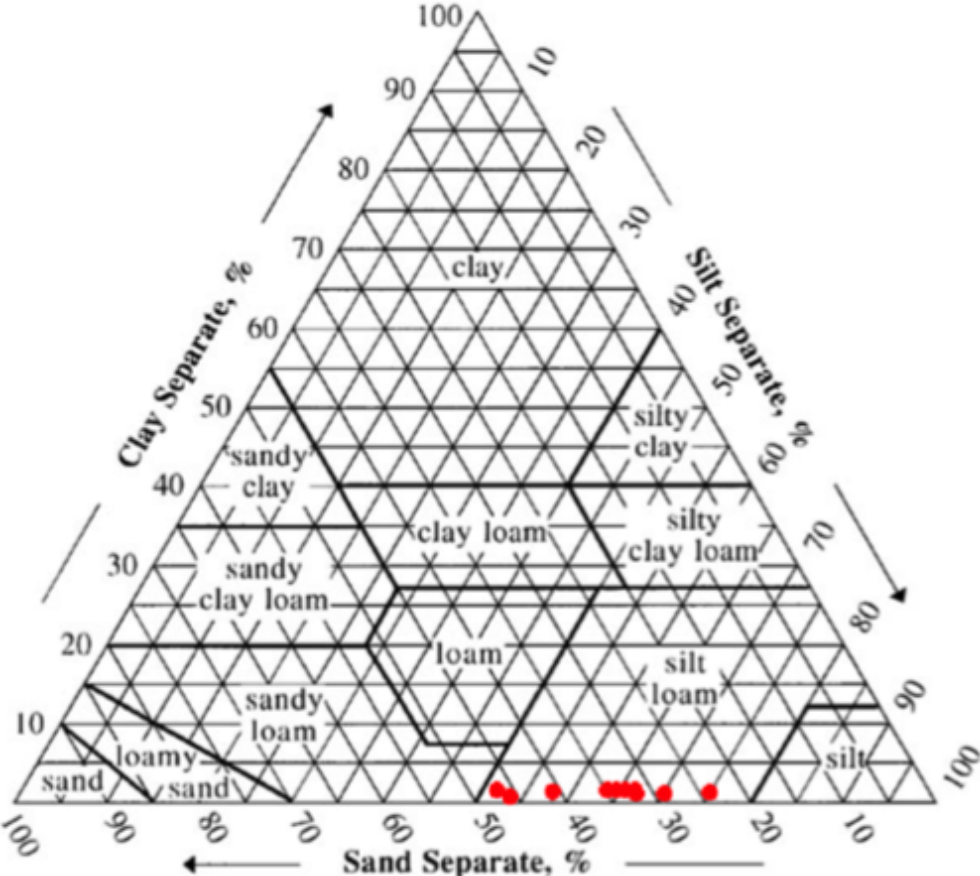
Figure 3.3: Grain size analysis for samples obtained from core locations P2 and P6. All soil analyzed were silt loams. Background soil triangle image courtesy of the US Department of Agriculture : Natural Resources Conservation Service. [Source: J.A-F.].

extracted cores was conducted at Lawrence Berkeley National Laboratory. The scanning was performed using a modified medical GE Lightspeed scanner, with 16 slices using an energy of 120 kV and a current of 160 mA. Attenuation data from the CT scan is converted to Hounsfield Units which are correlated to density through calibration obtained by scanning known density objects. Each voxel from the scan was 625 micron dimension oriented in the axial direction, and depending on the sample the voxel in the radial dimensions ranged from 193 to 250 microns, depending on sample diameter. To prevent thawing, samples were kept cold until placed in the CT scanner. As can be seen in Figure 3.4, ice distribution was laminar with several zones of higher ice fraction. Figure S2 panels A and B show central slices of sequential cores acquired through the permafrost table and below with blue colors corresponding to lower density zones of ice rich material. Panel C shows depth slices of the core shown in panel B.
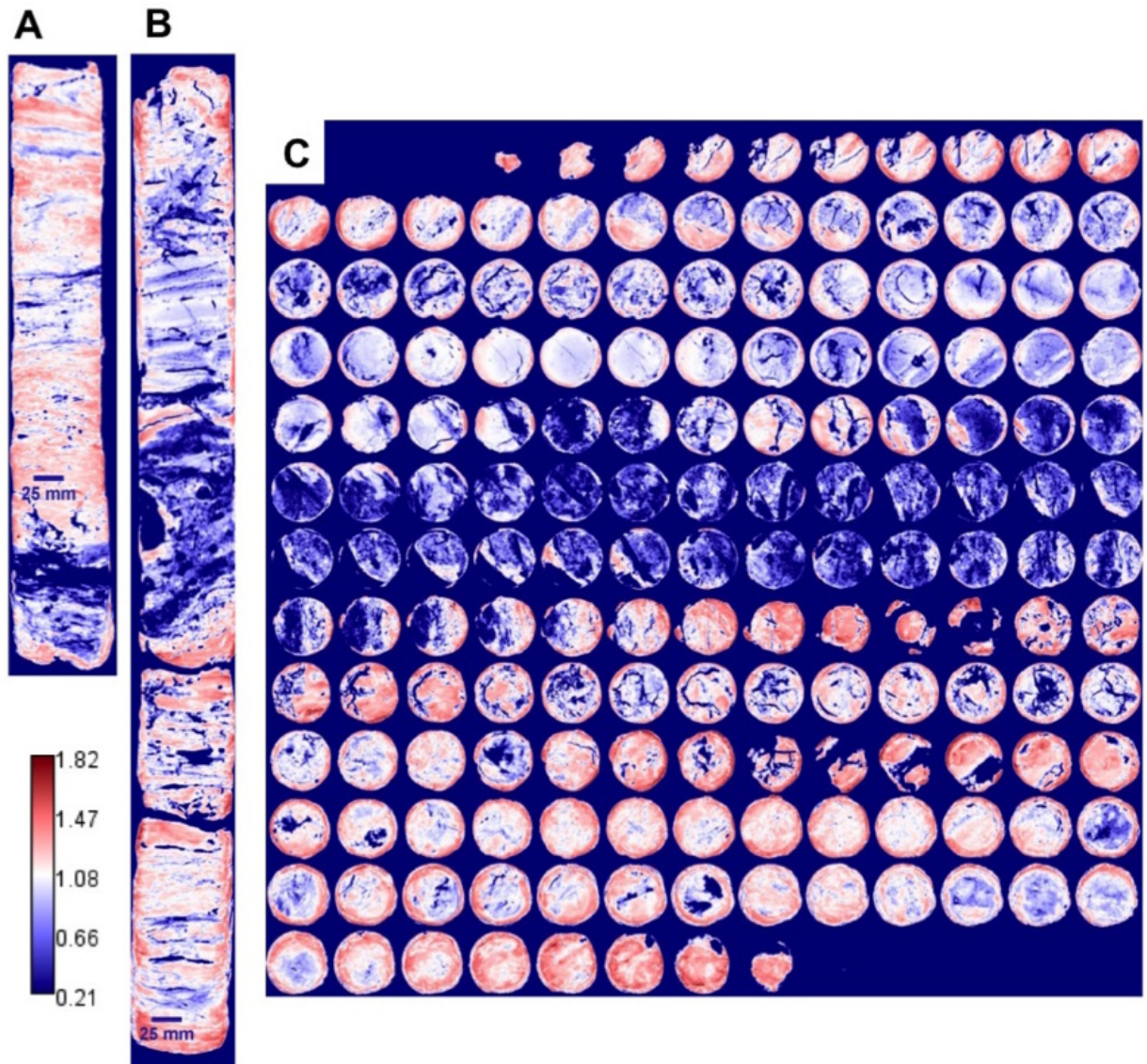
Figure 3.4: CT scans of permafrost cores from location OP4. Panels A and B are length-oriented slices of depth sequential cores. Panel C shows depth slices of the core section in panel B. [Source: C.U.].

3.2.2 Warming system and protocol

Figure 3.1B and Figure 3.5D,F show the geometry and installation pattern of the heating array. A total of 121 heaters were emplaced in 11 rows over a 133 m2 area (10.5 m 12.7 m). Each row was installed with an offset resulting in a distance between each heater of about 1.2 m. The vertical heaters (Indeeco Industries) had an outer diameter of 33.3 mm and measured 4 m in length. Each heater used 120 V, 50/60 Hz power and injected 60 W continuously into the ground. Only the bottom 1 m section of each element was actively heating, by design. The heaters were installed using a track-mounted, direct-push drill rig (GeoProbe 7822) where a 5.7 cm solid-stem drill pipe was first pushed into the ground until the required depth was reached, and then the drill pipe was removed. The 42.2 mm outer diameter steel heater casings (1 1/4" schedule 40) were then placed in the resulting holes and pushed with the drill rig to the required depth leaving about 0.15 m exposed above the ground surface. Figure 3.5B shows the push process. Silica sand was used to backfill between the native soil and the heater casings. When all the heater casings had been installed the heater elements were placed in the heater casing. The heaters were wired in series using 12-gauge solid wire and the wire was protected using armored flexible conduit. Each row had a total of 11 heaters and they were wired into a single circuit that resulted in 11 circuits. All circuits were wired into two breaker boxes (Figure 3.5G) and the heaters were monitored using standard data loggers (Campbell Scientific CR1000). The heaters were turned on August 5, 2016 and subsurface heating continued through November 11, 2016.
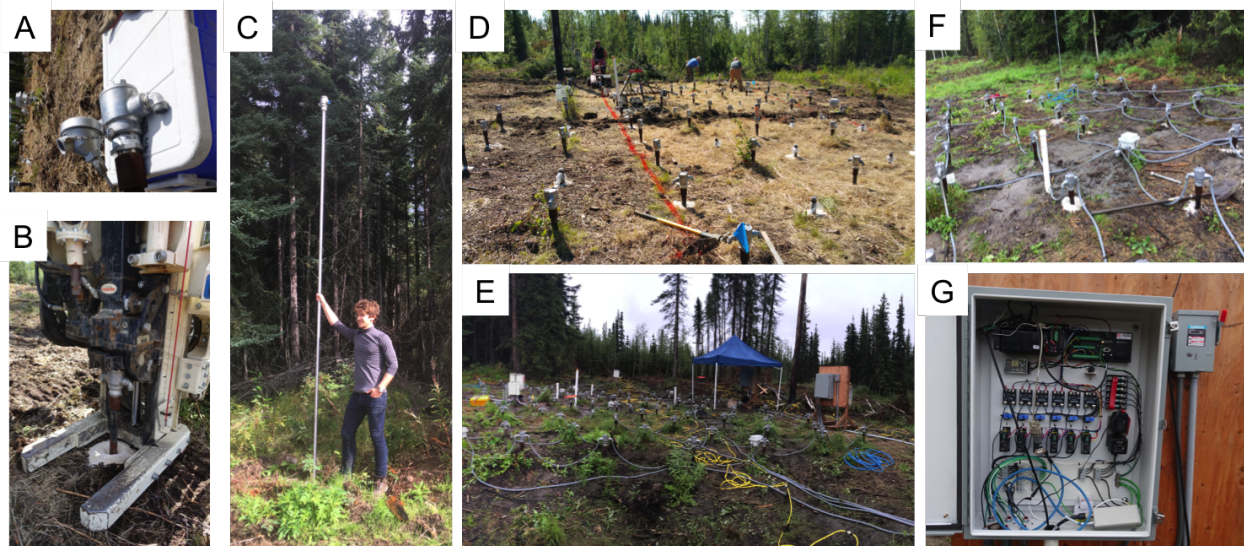
Figure 3.5: Photographs of the heating system installation and components. (A) Heater head assembly. (B) Push install of heater casing. (C) Full heater assembly. (D) Array after initial installation. (E) Site after completion. (F) Serial heater wiring configuration. (G) Heater control system. [Source: A.W., N.L., J.A-F.]

3.2.3 Data

During the warming experiment, near-continuous measurements captured the thermal and mechanical property evolution of the subsurface. These data included heater array recordings made by the system controller, soil temperature data recorded above, inside, and below the warming volume using thermocouples and thermistors in vertical boreholes, surface deformation recorded using dense two-point electronic distance measurement surveys, weekly-biweekly lidar surveying, and continuous (1 photo/5 minutes) multi-angle photogrammetry.

The heater array temperature and soil temperature at a few selected depths and locations were recorded using thermocouples (W.H. Cooke Co., Inc.; see Figure 3.1B for locations). Eight thermocouples were attached to heater casings throughout the plot during drilling operations. Soil temperatures were recorded at six locations throughout the heated area using multi-sensor T-type thermocouple strings (W.H. Cooke Co., Inc). Near-surface soil temperatures were recorded at 0, 0.05 m, 0.20 m, 0.40 m, 0.80 m, 1.60 m, and 2.00 m. Schedule 80 PVC pipe with a nominal diameter of 19 mm, were installed to provide locations for more precise temperature measurement by way of thermistor strings. Two 6-m long PVC pipes (BH14, and BH21) were installed in the heated section of the plot and four 10-m PVCs were placed outside the heated area. One of the PVCs outside the plot was installed in the shallow permafrost to the east of the heated area (BH16) and three strings (BH13, BH19, and BH20) were installed to the west of the heated plot approximately 6 to 7 m from the heaters. The four PVCs outside the heated area were remaining infrastructure from the ecosystem heating prototype experiment. Soil temperatures outside the heated area were measured at 2, 4, 6, and 9 m depth and the soil temperatures inside the heated area was recorded every 0.5 m to a depth of 5.5 (BH14) and 6 m (BH21). Temperature probes (Campbell Scientific 107) and loggers (Campbell Scientific CR1000) were used to measure the soil temperatures in the PVC pipes at a temporal interval of 10 min throughout the experiment.

The ground surface deformation related to subsidence was measured across the heating experiment using a combination of techniques. Traditional two-point electronic distance measurements (EDM) were acquired using a manual total station (Leica Flexline TS06) and a survey-grade global positioning system (Trimble R8). Survey control was established with a static survey using the GPS, for an occupation time of a minimum of two hours, and receiving corrections using the Online Positioning User Service (OPUS) for stated accuracies of ¡2 cm. Benchmarks were established throughout the site (see Figure 3.1B) that were used both during the EDM and DGPS surveys. In addition to the benchmark surveys the heater elements and ground surface at the heater/ground surface boundaries were also surveyed throughout the heating experiment. Prior to starting the heating experiment, a terrestrial based LiDAR scanner was used to capture the initial ground topography on August 5th, 2016. The LiDAR surveys were collected using a Leica ScanStation C10 and were performed approximately once a week (depending on weather), for a total of nine scans during the heating phase, with the final scan acquired on October 7th, 2016. A minimum of four scan positions were occupied to ensure complete coverage of the heater plot. Additionally, color

photographs were taken from 8 different perspectives above the warming plot using a camera array every 5 minutes.

In addition to the thermal and mechanical measurement campaigns, we made nuclear magnetic resonance (NMR) measurements in three vertical wells every day, continuous electrical resistivity tomography measurements along two horizontal arrays, sampled the water chemistry using a central well, recorded conductivity, temperature and water depth with a single HOBO data-logging probe, recorded distributed fiber-optic temperature, strain, and acoustic sensing data, and used three three-component Trillium posthole compact 120-s seismometers to record ground motion. The DAS and inertial seismic sensors recorded passive vehicle noise from Farmer's Loop Road as well as active source surveys conducted periodically using a hammer source, and each night using a surface orbital vibrator installed 100-m to the south of the warming zone. In the following sections we will analyze the DAS and seismic data.

3.2.4   Results of warming experiment

Warming system results

The heating array functioned as designed from 05-Aug to 11-Nov-2016 with no major shutdown periods except for one brief power outage. Figure 3.7 shows total energy usage for the 11 heater sub-arrays which varies between 6.5 and 6.8 kW over the course of the experiment. The heating system was operated in close to constant energy flux mode rather than at a constant borehole temperature; as a result, heater casing temperature increased over the duration of the experiment, peaking near 45 ^{o}C before termination of the experiment. Diurnal fluctuations in energy input yielded small variations in heater casing temperatures (< 0.2 ^{o}C) as well which were not observed in any interwell measurements. Tight monitoring of current draw and heater surface temperature provided excellent energy flux constraints for coupled thermomechanical modeling; heater casing surface temperatures reached 45 ^{o}C immediately before the end of the experiment (Figure S3, lower panel).

Temperature results

Figure 3.7 shows downhole temperature acquired during each week of the experiment in monitoring boreholes BH14 and BH21 in the center and southern side of the heating plot respectively. As expected, the heating protocol effectively increased temperature at monitoring locations between the heating elements; temperature values at the heating interval increased from slightly below 0 to 25 ^{o}C over the course of 14 weeks of heating (Figure 3.7 and Figure S3). The applied thermal load deepened the permafrost table between 1.25 and 1.5 m, depending on measurement location as can be seen by the highlighted regions in Figure 3.7. Interestingly, the thermal load was not visible at the surface due to the concurrent seasonal cooling, visible at depths shallower than 2 m. Heating was not observed in zones of shallow permafrost off the plot. Monitoring borehole BH16, located 7 m west of the
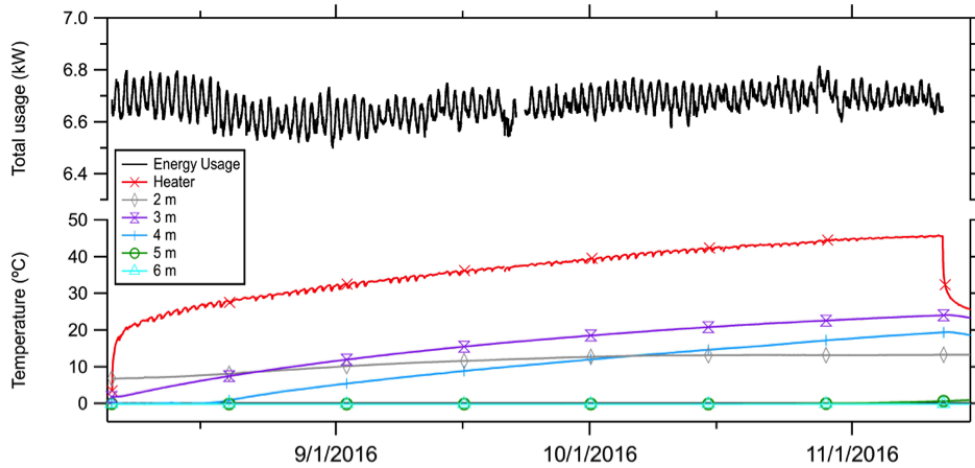
Figure 3.6: Heater stability and casing temperatures. [Top] Total power usage of the heater array over the duration of the experiment. [Bottom] Thermocouple-measured temperature at a single heater as well as temperature in the interwell region (thermistor well BH14) over the same time duration. [Source: A.W.].

heating plot, remained below 0 ^{o}C during the heating pilot at 2, 4, and 6 m depths as can be seen in Figure 3.7. Advective heat transport was visible off the plot at unfrozen downslope monitoring locations (Figure 3.7), likely driven by hydrologic coupling to thermal transport. Thaw was not observed in upslope thermal measurements.
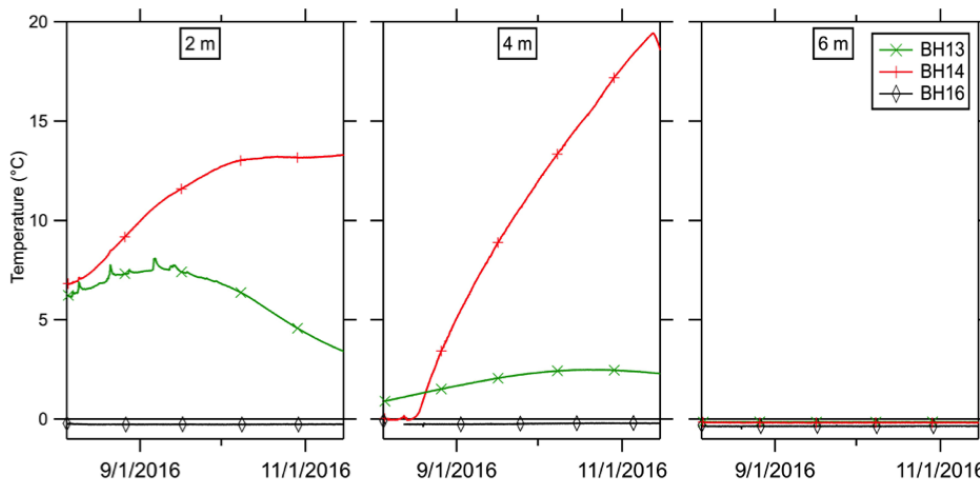
Figure 3.7: Temperature histories for on and off-plot thermistor monitoring locations at 2 (left), 4 (center), and 6 (right) meter depths [Source: A.W.].

Figure 3.8 shows the main long-term borehole thermistor datasets from one central mea-
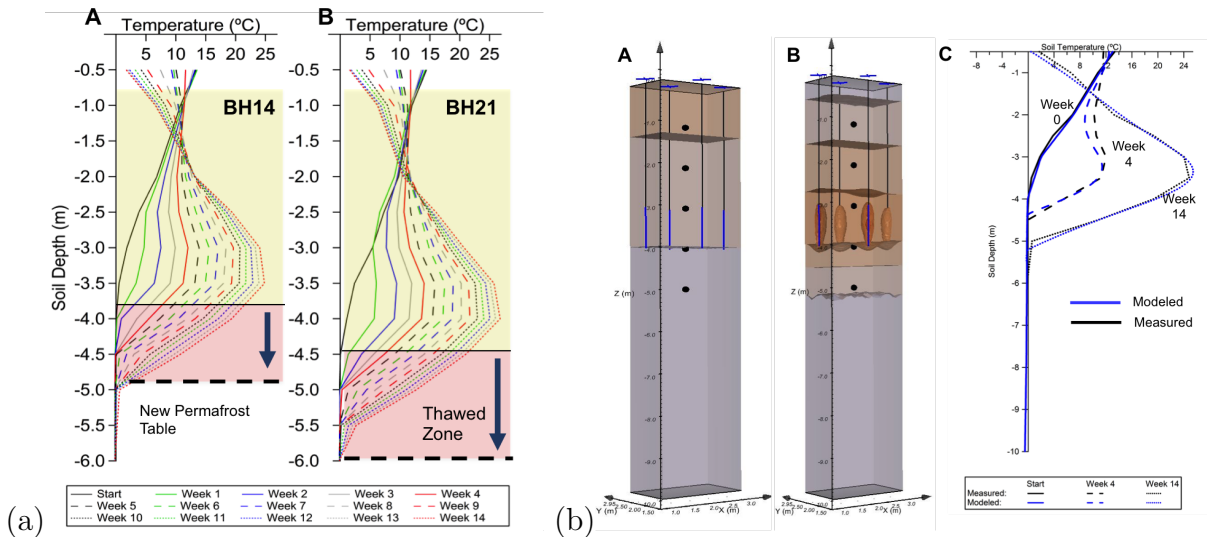
Figure 3.8: (a) Thermal history during heating experiment using BH14 (left) and BH21 (right) borehole thermistors. Weekly depth-dependent temperature variation curves are shown. Pick highlight shows descent of permafrost table boundary (0 ^{o}C) [Source: A.W.]. (b) Thermal model and validation with thermistor data. Panels A and B (left) depict baseline and final 3D thermal states, respectively, as predicted by a finite-element thermal transfer simulator for a small sub-section of the heater plot surrounding monitoring well BH14. Panel C (right) shows a comparison between the modeled (blue lines) and measured (black lines) thermal profiles at BH14 for weeks 0, 4 and 14 [Source: A.W.].

surement borehole (BH14) located within the warming plot, a second located to the east off of the heater array (BH16) in a zone of shallower permafrost, and a third downslope to the west (BH13) in a zone of deeper permafrost. At 2 m depth, seasonal variations are visible for both BH14 and BH13 while BH16 remains slightly below 0°C. BH14 also measures the heater pulse at 2 m, superimposed on the seasonal cycle. At 4 m, the thermal pulse from the heating is quite strong on the plot (BH14) and is also weakly observed via advective transport downslope off of the plot at BH13 (center panel). BH16 (upslope, off plot) remained below 0°C during the experiment. At 6 m depth, all three locations remain below 0°C.

Geodetic results

Ablation of the permafrost table resulted in localized surface subsidence. Figure 3.9 shows the results of sequential EDM measurements quantifying the change in surface elevation over the course of the experiment. The central panel shows the difference between the baseline elevation and the elevation measurements at day 54 of the heating experiment. Measurements were conducted at surface monuments shown as red squares; the resulting differences were interpolated. As can be seen, subsidence with magnitudes between 4 and 10

cm were observed, with the largest deformation on the northern border of the heating plot. The measured onset of surface subsidence at station R7H2 was approximately 20 days after heating initiation (Figure 3.9A) and exhibited a nearly linear rate, potentially suggesting ablation of distributed rather than highly localized ice. In a real-time monitoring scenario it is necessary to place these findings in the context of measurement uncertainty, which is +/- 1-2 cm for an EDM type survey due to measurement errors; hence, an obvious subsidence signal was not apparent from the EDM results until after Day 30.

A higher resolution map of the same surface subsidence process was provided by repeat LiDAR surveys. The dense point clouds from the baseline survey on 05-Aug-2016 and the final survey on 07-Oct-2016 were differenced using an open-source software tool (CloudCompare) to yield the image shown in Figure 3.10A. Isolated points with large positive differences, corresponding to growing vegetation, were removed before point cloud visualization. The zone of subsidence appears to be localized to the heating plot, but again on the northern section. The magnitude of the EDM and LiDAR-derived vertical deformations are quite similar, showing maximum values of approximately 10 cm. Figure 3.10B shows the tight spatial correspondence of the LiDAR (colored) and EDM (contoured) subsidence measurements. Note that in Figure 3.9 and 3.10, the northward extent of the subsidence zone is slightly exaggerated to the north because of the larger spacing of EDM benchmark measurements between the heater plot and monuments LP400 and LP500, a linear interpolation artifact that is corrected in the dense LiDAR image. LiDAR surveys were conducted once every 2-3 weeks due to the time required to make a full scan of the experimental site.
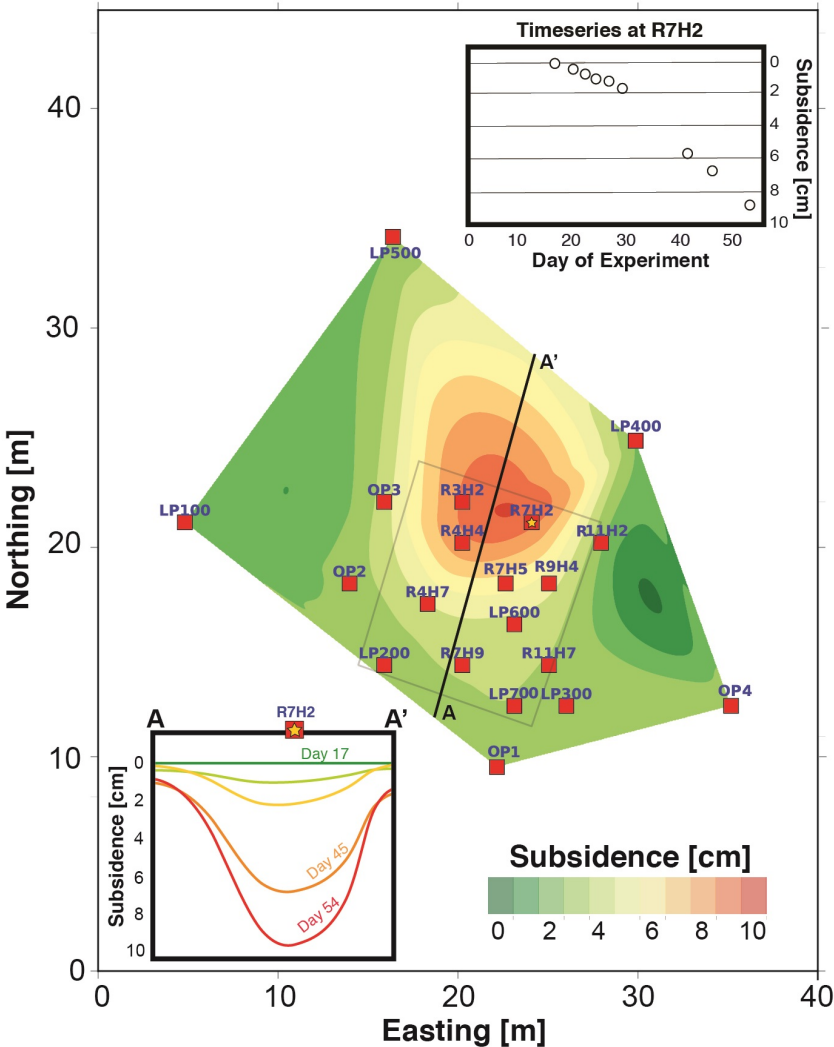
Figure 3.9: Electronic Distance Measuring (EDM) survey results for surface subsidence during the heating experiment. Central plot depicts difference in surface elevation between baseline and week 14. Colors are interpolated from measurements at fixed monuments (red squares). Top right panel shows time-history of subsidence measurements at monument R7H2. Bottom left panel shows a cross-section of elevation change from points A to A' [Source: N.L.].
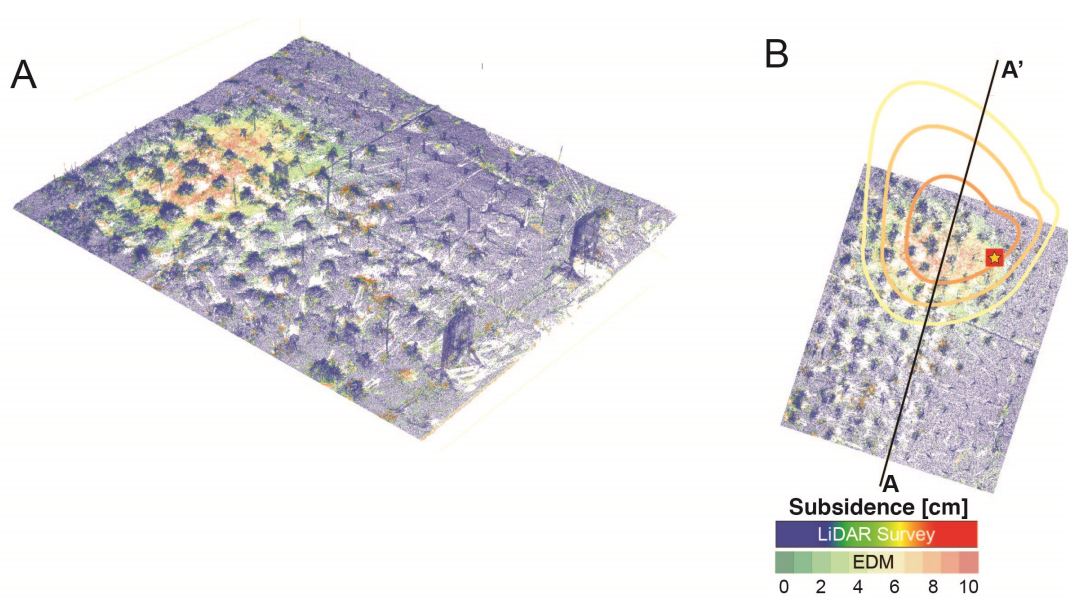
Figure 3.10: Differential LiDAR measurements spanning the heating experiment. Panel A shows a perspective view of the difference in surface elevation between baseline and week 14 as measured by LiDAR over the heater plot. Panel B shows a top view of the same dataset with superimposed contours showing co-located EDM subsidence measurements [Source: N.L.].

3.3 DAS Data

As an additional component of the Fairbanks warming experiment, we deployed a horizontal 2D fiber-optic sensing array across the warming site, and used this as the distributed sensing array for DAS. DAS recordings were made continuously for over 60 days beginning on August 4, 2016 and ending October 3, 2016.
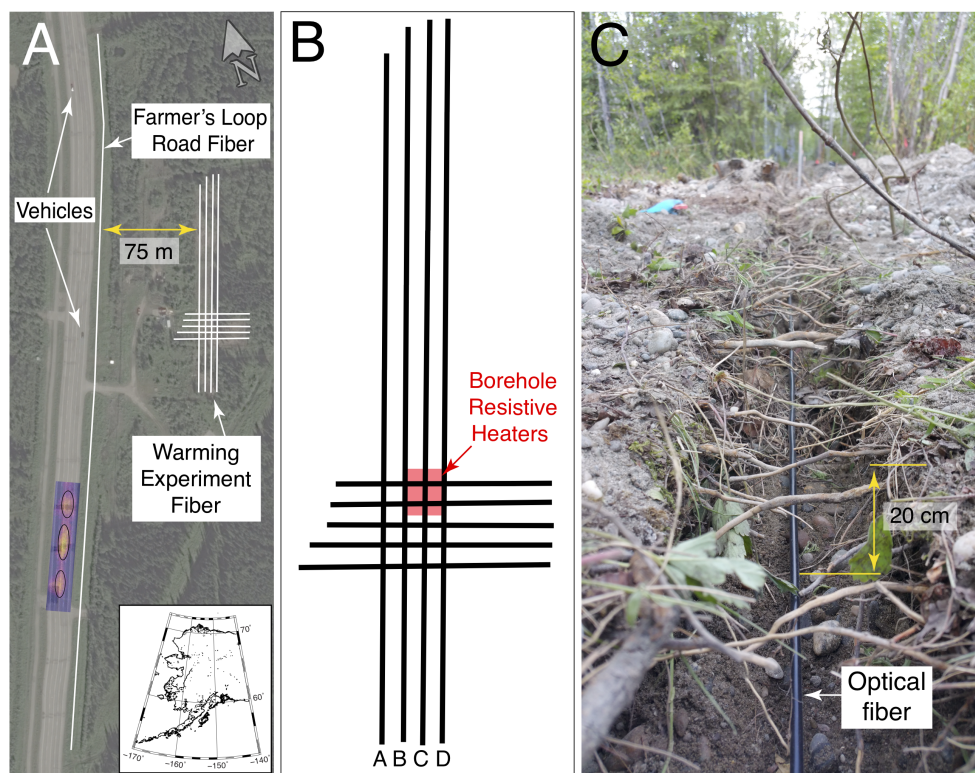
Figure 3.11: (A) Map of fiber-optic array approximately 75 m ESE of Farmer's Loop Road in Fairbanks, AK. (B) Proximity of warming experiment ("Borehole Resistive Heaters") to the fiber-optic array Lines ABCD run approximately NNE-SSW. (C) Trench in fiber shows how the fiber was laid 20 cm below the surface before backfilling. [Source: N.L.].

The fiber array is shown in map view in Figure 3.11a. The full fiber array used for monitoring was a combination of two subarrays. In June 2015, we deployed the "Farmers Loop Road Fiber" array, a 1.5 km loop of OCC hybrid optical fiber along Farmer's Loop Road trenched in at a depth of 50 cm. The Farmer's Loop Road Fiber had both a road line on the

east side of the shoulder approximately 1-2.5 meters from the center of Farmer's Loop Road, and a back line (not shown in map). into the shoulder of of Farmer's Loop Road ("Farmer's Loop Road Fiber" Figure 3.11a). No field splices were made. The far end of the fiber was terminated inside the research building so as to prevent a large amplitude backreflection. In 2016, we deployed an additional rectilinear fiber array ("Warming Experiment Fiber") above the artificial permafrost warming experiment described above. The Warming Experiment Fiber is located 75 - 100 m east of Farmer's Loop Road, and consisted of 4 x 180 m roughly NNE-SSE (road parallel) and 5 x 60 m ESE-WNW (road orthogonal) lines directly buried at a depth of 20 cm. Figure 3.11c shows a trench view of the fiber lying below the surface layer of thick roots prior to backfilling. Fiber was run from one trench to the neighboring trench through adjoining connector trenches to form one continuous sensing element. Fiber-optic connections between lines were by arc fusion splices housed inside the research building for maximum protection. Connecting the 2016 and 2015 fiber arrays, the total linear fiber length was 4 km. DAS data were recorded using a Silixa iDAS, v.2. DAS strain-rate measurements were made from 28-Jul-2016 through 04-Oct-2016. Additional Details about the experimental procedure can be found in Chapter 2.4.2.

3.4   Methodology

3.4.1   Theory of ambient noise seismology

Ambient noise seismology is a set of empirical techniques whose aim is to retrieve information about the Green's function of the Earth's elastic impulse response from passive noise recordings (Michel Campillo and Paul 2003; Weaver and Lobkis 2005; Curtis et al. 2006). In this chapter we refer to any estimate of the Green's function developed through ambient noise interferometry as a noise correlation function (NCF). When the NCF is computed between two seismic receivers it is referred to as a 1D NCF (vector), meaning the impulse response recording at one receiver (virtual receiver) due to a unit-force impulse source at the other receiver (virtual source). As a result of reciprocity, the NCF includes both this causal time series and an acausal time-reversed time series that represents the Green's function estimate from the virtual receiver to the virtual source. When a set (more than two, but in practice a straight DAS line) of consecutive seismic receivers are used to compute the Green's function estimates with one common virtual source, the result is referred to as a 2D NCF (array).

For nearly 15 years, ambient noise seismology has been applied to develop images of the planet's interior at a range of scales, but predominantly at the scale of the continental crust (see Snieder and Larose 2013 for review). Surface waves from ocean microseisms (f=0.05 - 0.3 Hz) are a dominant ambient signal with adequate long range coherent strength and wavelength for the crustal scale. In general, turning ocean microseism noise into crustal information is accomplished by traditional surface wave dispersion analysis, also called frequency-time analysis. In this technique, regional (5 - 200 km) broadband stations are used to form 1D NCFs between station pairs over daily recordings. Before computing the 1D NCFs, pre-

processing routines are applied to remove distortion related to high-amplitude earthquakes, instrument filters, and site effects, and also rebalance the frequency content through spectral whitening (Bensen et al. 2007; Seats, J. F. Lawrence, and German A Prieto 2012). Dispersion analysis retrieves seismic phase and group velocity curves by analysis of the arrival times at a given period divided by the known interstation path length (N. M. Shapiro et al. 2005). Finally, on a per period basis, models of seismic velocity structure are estimated through least-squares inversion and volume averaged to produce 3D shear velocity structural images (Sabra et al. 2005; Bensen et al. 2007; M. Moschetti, M. Ritzwoller, and N. Shapiro 2007; Yang et al. 2007). For dense Large-N array experiments, it is possible to track individual seismic phase moveout within 2D NCFs, and then by solving the eikonal equation retrieve 3D isotropic and anisotropic shaer-wave phase velocity images F.-C. Lin, D. Li, et al. 2013. NCF amplitude information has also been used to estimate attenuation and site amplification (German A Prieto et al. 2010; J. F. Lawrence and Germán A Prieto 2011; Germán A Prieto et al. 2011; Viens et al. 2017; Bowden, Tsai, and F.-C. Lin 2017).

A slightly more advanced ambient noise technique uses the seismic waves arriving after the ballistic surface waves, commonly called seismic coda. Coda waves sample the subsurface more completely than body and surface waves based on their diffusive timescale of propagation. This volume-averaging effect is are often cited as the basis for studying dynamic processes in time-lapse analysis using coda wave interferometry (CWI). CWI involves computation of NCFs from consecutive epochs, and then measuring the amount of waveform dilation or sub-cycle time shift observed dt/t at late NCF times, an observable that is linearly proportional to a change in velocity with respect to a reference velocity, dv/v (Mikesell et al. 2015). CWI has been applied to measure volcano deflation/inflation cycles (**duputel2009; donaldson2017**), the response of fault zones after earthquakes (Taira et al. 2018), the response of aquifers to precipitation/drought (Sens-Schönfelder and Wegler 2006; Clements and Denolle 2018), and the seasonal migration of the permafrost active layer in central Alaska (James et al. 2017). The resulting seismic velocity changes are often on the order of less than a percent, but in cryosphere applications the seasonal freeze/thaw cycle in the near surface leads to major NCF coda time shifts, cycle-skipping, and velocity changes of as much as 75%.

In principle, noise-based interferometry of two surface records retrieves the complete Green's function (Wapenaar and Fokkema 2006), however in practice relatively weak body waves are less-commonly observed. If it were routinely feasibly, body waves typically have higher frequency content, and thus provide a basis for higher resolution imaging. However, to-date, NCF body wave observations have been limited, typically in two radically different scales: 1) the upper crustal reservoir scale (Roux et al. 2005; Draganov et al. 2009; Draganov et al. 2013; Nori Nakata et al. 2015); and 2) the planetary scale including reflections off of the Moho (PmP, SmS) and outer core (ScS) and twice-refracted inner core phases (PKIKP^2) (Z. Zhan et al. 2010; Poli et al. 2012; F.-C. Lin, D. Li, et al. 2013). It is common to create average 1D NCFs by stacking the results, or filtering the raw noise data and only analyzing those data when there is evidence of body wave-like wave propagation. In the case of Large-N experiments, such as the Long Beach Nodal Experiment, 3D P-wave travel time tomography

was conducted using body waves around 3 - 10 Hz, suggesting a model resolution around $\lambda \sim 250$ m (Nori Nakata et al. 2015).

Elastodynamic Green's function representation of noise interferometry

Consider the displacement time series u recorded at location x^r due to a unit-force source of elastic waves, as described by the representation equation (Aki and Richards 2002):

$$u_i(x^r, t) = \int_D G_{ik}(x^r, x^s, t) * F_k(x, t) dx.$$

Here F_k represents the individual forces applied at an arbitrary location in space x and time t over domain D at the free surface. $G_{ik}(x^r, x^s, t)$ represents the Green's function, or the solution to the wave equation at x^r for a unit-force point source at x^s. Subscripts i and k denote displacement seismogram components, and Einstein notation is adopted to compactly consider all three translation components.

When averaged over a long time period, denoted by $< \cdot >$, seismic waves from unit-force sources become uncorrelated and the source field becomes equal to the long term power-spectral density (PSD), $S(\omega)$ as in (see Wapenaar and Fokkema 2006 for details):

$$S(\omega) = < F(x, \omega) F^*(x', \omega) >$$

where superscript $*$ denotes complex conjugation.

Cross-correlation of two displacement time series is thus equivalent to (in the frequency domain):

$$< u_i^*(x^s, \omega) u_j(x^r, \omega) >= S(\omega) \int_D G_{ik}^*(x^s, x, \omega) G_{jk}(x^r, x, \omega) dx$$

where x is generalized to any location in D. This expression is called the noise correlation function (NCF). In practice, the term NCF refers to all flavors of the cross-correlation, including cross-coherency and deconvolution. The NCF expression can be simplified and transformed into the time domain (see Snieder 2004; F.-C. Lin, M. P. Moschetti, and M. H. Ritzwoller 2008 for details):

$$< u_i(x^s, t) u_j(x^r, t) >= S(t) \left(\frac{G_{ij}(x^r, x^s, t)}{i\omega} + \frac{G_{ij}(x^s, x^r, -t)}{i\omega} \right)$$

$$< v_i(x^s, t) v_j(x^r, t) >= S(t) \left(G_{ij}(x^r, x^s, t) + G_{ij}(x^s, x^r, -t) \right)$$

where $v_i(x, t) = i\omega u_i(x, t)$.

To summarize, under the presence of a homogeneous, uncorrelated seismic sourcefield, the time-averaged mathematical cross-correlation of two velocity seismograms at the free surface is equal to the sum of the displacement source-to-receiver Green's function and the time-reversed displacement receiver-to-source Green's function. This result can be confirmed numerically by comparing the cross-correlation of two velocity noise records with

the equivalent synthetic displacement Green's function (Figure 3.12). 900-s duration noise synthetics are computed at a line of receivers by summation of the time-histories from 1000 randomly-oriented, randomly-located, randomly-timed unit-force impulse sources located at the free surface. A 1D velocity model is used. The data are then subdivided into 30-s duration windows and averaged. The average cross-correlation of velocity is equivalent to the displacement Green's function. We compute displacement Green's functions using the frequency-wavenumber integration approach (Herrmann 2013). The result has errors related to an inhomogeneous noise source distribution. If we stacked over longer intervals and perhaps filtered the data differently the noise cross-correlation might have smaller errors, but the major surface wave arrival and dispersion is reproduced in the 1 - 3 Hz range.

Complications due to vehicle noise sources

Although it is less common than the classic microseism noise studies, the proliferation of Large-N seismic arrays has enabled observation and study of the coherent seismic waves produced by automobiles, trains, wind turbines, and other urban objects/motions (Norimitsu Nakata et al. 2011; Riahi and Gerstoft 2015; Quiros, Brown, and Kim 2016; Dıaz et al. 2017; Inbal, Cristea-Platon, et al. 2018). Both Rayleigh waves and body waves have been observed.

Ambient noise techniques have been applied at scales up to MHz (Hadziioannou et al. 2009), and hence the noise interferometry described in Chapter 3.4.1 is assumed to work in the vehicle noise band with elastic frequencies in the range of 1 - 50 Hz. Attenuation of higher frequencies is considered the major concern in practice, but at the fieldscale apertures of many DAS experiments vehicle noise is observed to be strongly coherent. In 2015, our group recorded train and automobile noise with DAS in Richmond, CA in the experiment discussed in Chapter 2.4.1 and in Sacramento, CA in the experiment discussed in Chapter 2.4.3. With the Sacramento experiment a fiber in the rail/roadbed measured the long range coherent seismic waves from vehicles up to 5 km from the array for trains, and approximately 0.5 km for automobiles/trucks.

One important complication with vehicle noise is the moving source problem. Ideal source positions are assumed to be uncorrelated, but vehicle motion has been described as a moving vertical force at each contact point between the vehicle and the ground (L. Li, Nimbalkar, and Zhong 2018; Brenguier et al. 2019). Pavement undulations or mechanical breaks/potholes in the pavement may introduce additional seismic wave components.

A second complication is that the road is often positioned on one-side of the seismic array experiment. Ideal source positions are assumed to surround receivers on a closed surface. Wapenaar 2006 considers this case explicitly and proposes that subsurface heterogeneity leads to scattering of many different wave components which suppresses any minor errors involved in single-sided illumination. More complicated heuristic techniques such as multi-dimensional deconvolution (MDD), in which the effects of a unbalanced source-side wavefield are removed from the NCF, have also been proposed for this type of problem but have not been successfully demonstrated in practice. Our attempts to use MDD were also unsuccessful.
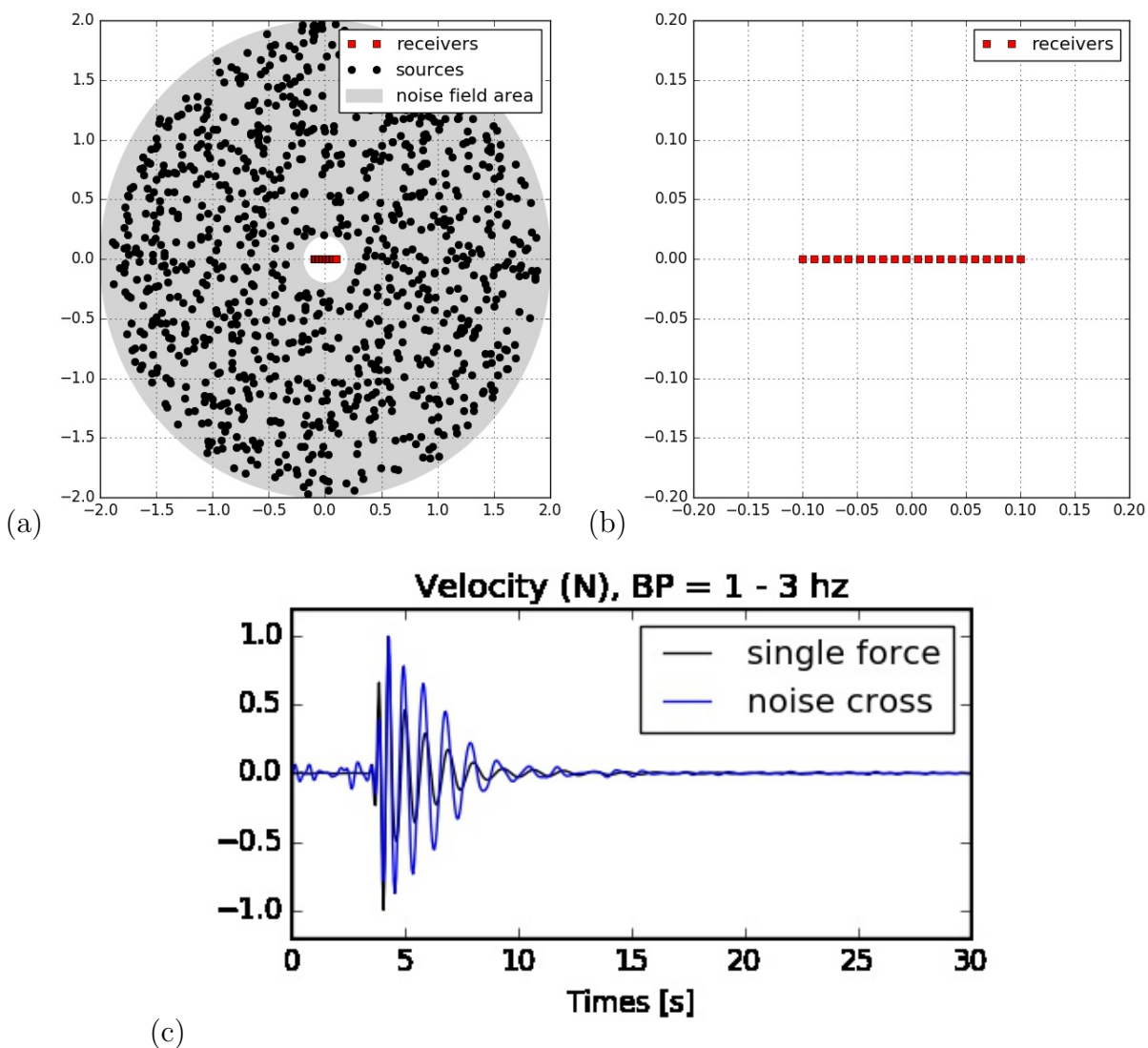
Figure 3.12: (a) Map view of synthetic experiment geometry (units are km). (b) Expanded view of receivers at center of (a). (c) Average North-North cross-correlation (blue) of first and last line of receivers shown in (a) and (b) plotted with the complete 1-D unit-force transverse-transverse synthetic displacement Green's function (black). Computations were done with Computer Programs in Seismology 3.30 Herrmann 2013 [Source: N.L.].

Complications due to DAS receivers

DAS-based noise interferometry, using fixed gauge strain or strain-rate sensor data to form the NCFs, has been successfully demonstrated to retrieve accurate subsurface group velocity estimates (Xiangfang Zeng et al. 2017; Dou et al. 2017; J.B. Ajo-Franklin et al. 2019), however the exact phase velocity, waveform, amplitude and frequency content is likely biased by not considering the DAS-DAS correlation as a strain-strain correlation. Full waveform inversion, for example, would require explicit consideration of this fact (Paitz, Sager, and Fichtner 2018).

Eileen Rose Martin 2018 (PhD thesis) pointed out that cross-correlation of DAS sensor data (difference of two velocity sensors separated by a fixed gauge length) results in important radiation pattern sensitivity. This sensitivity depends on wave type, orientation of each DAS sensor, azimuth between the sensors (θ). It is less pronounced for near surface vehicle noise (or microseism noise) than for high frequency noise, because the seismic energy from vehicle propagates with wavelengths that are many times the 10 m gauge length (c=1000 m/s; f=50 Hz; λ=200 m). Geophone-geophone correlations have dipole sensitivity for both Rayleigh and Love waves. Rayleigh wave DAS-DAS correlations have dipole sensitivity with a maximum in-line (radial-radial correlation) like geophone-geophone correlations, but transition to be four-lobed at higher frequencies. Love wave DAS-DAS correlations are four-lobed maximizing at $\theta = 45 - 60^o$. This means that a linear fiber is optimally oriented for 2D NCF Rayleigh wave noise imaging, but has no sensitivity to Love waves, while a 2D NCF computed with a virtual source and virtual receivers on two fibers that are either co-linear or orthogonal will show Love waves with an additional node in the radiation pattern.

3.4.2   Noise correlation process

Pre-processing

To analyze the continuous vehicle noise recording, we first computed 2D NCFs for segments of the DAS array in a modified DAS-based NCF data processing workflow developed by Dou et al. 2017, ultimately based on Bensen et al. 2007. In this workflow, raw 1-minute DAS strain-rate records are first pre-processed by fitting and then subtracting a linear trend to remove any static component. Then, we despiked the data to remove photonic noise. Despiking involves applying a moving median filter that replaces outliers with the median value of a window with length of a few seconds (Bakku 2015). Next, we apply a zerophase, two-corner, bandpass filter between 1 and 40 Hz to isolate the vehicle noise identified in the data, and then apply a cosine taper to each end of 5% of the 60 s record (3 s). To reduce any potential bias due to earthquake ground motions and potentially also unquantified large optical noise, we removed full 1-minute windows containing samples larger than 10 times the record's standard deviation. In the next phase of the workflow we correlate the data across DAS channels to obtain the NCF.

Cross-correlation vs. Deconvolution vs. Coherency

Noise correlation can be computed in a number of different ways, most commonly cross-correlation, coherency, and deconvolution, with or without one-bit normalization (see Bensen et al. 2007; Viens et al. 2017 for more details). The formulae are all very similar. The cross-correlation function is defined above as:

$$C(x^r, x^s, \omega) = < v_i(x^s, \omega)v_j^*(x^r, \omega) >$$

where the $< \cdot >$ operator means time-averaging.

A cross-correlation that has been normalized in the frequency domain by a smoothed version of the product of the source and receiver spectra is called the coherency or cross-coherency function:

$$H(x^r, x^s, \omega) = \left\langle \frac{v_i(x^s, \omega)v_j^*(x^r, \omega)}{\{|v_j(x^s, \omega)|\}\{|v_i(x^r, \omega)|\}} \right\rangle$$

where the operator $|\cdot|$ means the absolute values, and $\{\cdot\}$ means the spectra are convolved with a boxcar of a chosen sample length in order to avoid small numbers in the denominator.

When the cross-correlation is normalized by only the source spectra it is called the deconvolution function:

$$D(x^r, x^s, \omega) = \left\langle \frac{v_i(x^s, \omega)v_j^*(x^r, \omega)}{\{|v_j(x^s, \omega)|\}^2} \right\rangle.$$

Spectral shaping, spectral normalization, spectral smoothing or pre-whitening all refer to a filtering process commonly applied during pre-processing before computing the cross-correlation; this is assumed to be equivalent to including this filter in the denominator of the coherency or deconvolution definitions. One-bit normalization, another common pre-processing step that changes all time samples to either +1 or -1 based on polarity of the value, has been shown to improve the speed of convergence in limited cases Bensen et al. 2007; Eileen Rose Martin 2018.

We found remarkably consistent NCFs with only minor amplitude discrepancies between the three different approaches. No one-bit normalization was applied. Figure 3.13a shows the 1D NCF result for an inline, road-orthogonal DAS-DAS receiver pair. The offset is 60 m. The largest components are all at positive lags, because seismic energy is moving from Farmer's Loop Road to the warming array and the virtual source and receiver are positioned in this direction (waves move from source to receiver). All three 1D NCF estimates identified the same phases:

1. a first arriving phase around $0.15 - 0.3$ s;

2. a large-amplitude dispersive surface wave packet around 0.5 s;

3. a late arriving relatively long period surface wave.
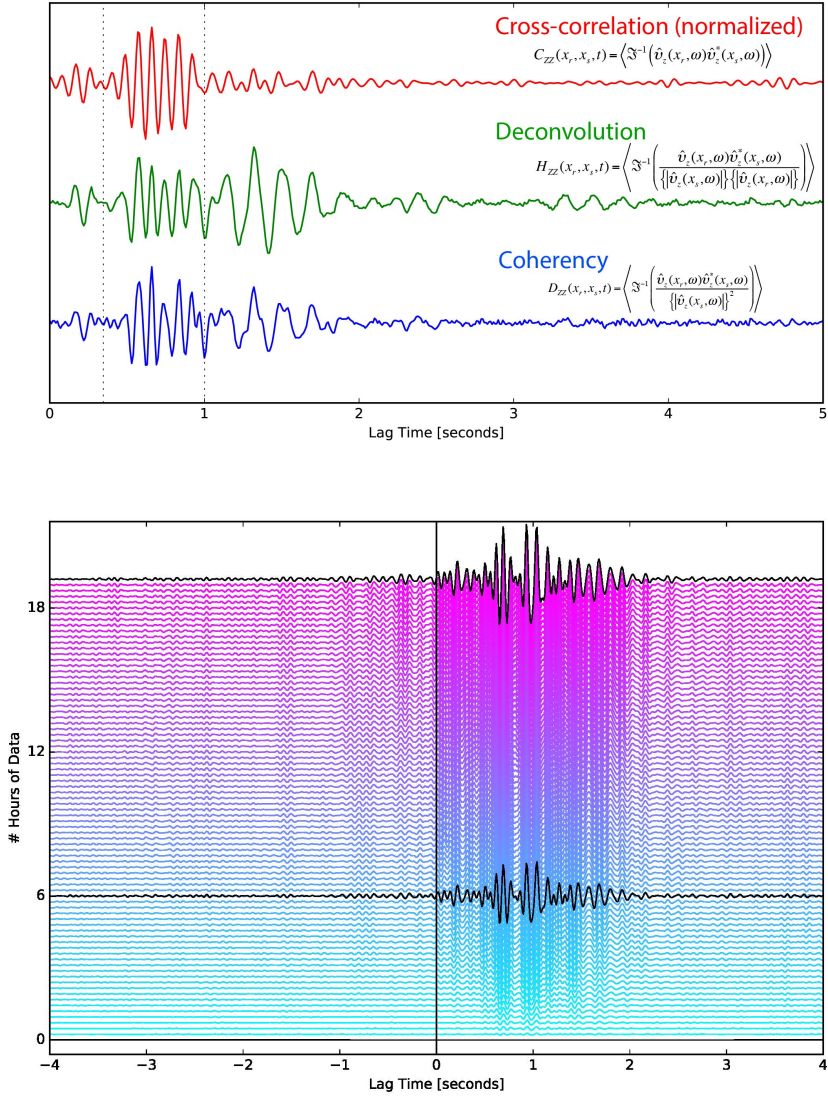
Figure 3.13: (a) Results of three different methods to compute the NCF for two DAS receivers located on Line 2 (road orthogonal warming array). The filter is BP 2- 40 Hz. Data have been stacked over 6 hours. The energy is all at positive lags because of the road orthogonal geometry with Farmer's Loop road to the west. The largest differences are in late arriving surface waves. (b) Effect of applying a linear stacking protocol to 1-minute NCF (Coherency) estimates over several hours for the same DAS receivers used in (a). The signal-to-noise ratio of the NCF seismic phase arrivals increases with the number of minutes stacked. [Source: N.L.]

The largest differences pertain to the late arriving surface waves and coda waves, which we do analyze in this study. The deconvolution and coherency estimates both have lower noise around zero time compared with the cross-correlation estimate. The body wave signal-to-noise ratio is highest for the deconvolution estimate. For these reasons we use the deconvolution form of correlation to compute all NCFs in this study. Future analysis to understand why the virtual source and receiver spectra so dramatically affect the late arriving surface waves and code waves may have implications for other near surface noise studies.

Stacking

Smoothing soucefield non-stationarity is accomplished by time-averaging, or stacking individual 1-minute NCFs together. The most common method of stacking is a simple average or mean stack. Alternative approaches use the median instead, or a phase-weighted approach (Schimmel et al. 2011). Figure 3.13b shows an example of how seismic phase quality (signal-to-noise ratio) improves with the number of 1-minute NCFs averaged together during stacking up to 20 hours. Note that the major seismic phase information available at 20-hours is visible after just 6 hours.
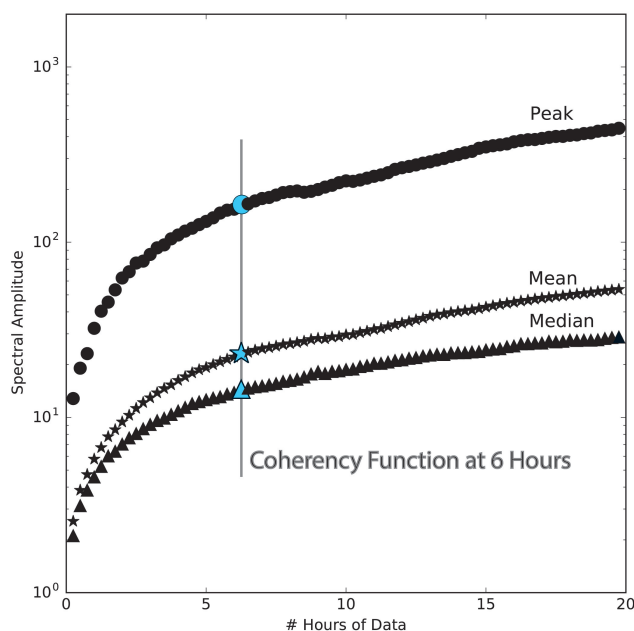
Figure 3.14: (c) Linear stacking protocols lead to a stable NCF estimate after approximately 6-hours, meaning the maximum, mean and median spectral amplitude does not change substantially with additional data. [Source: N.L.]

After stacking the NCF is said to have "converged". This terminology was originally meant to suggest that the empirical qualities of the NCF have converged to the true Green's function (Bensen et al. 2007), but now has more of a heuristic sense in that the NCF has stopped changing due to changes in the sourcefield. In practice, the NCF and true Green's function are rarely compared. The impact of stacking NCFs in a heuristic sense has been previously analyzed in only a couple of studies (Seats, J. F. Lawrence, and German A Prieto 2012; Dou et al. 2017). One way to quantify NCF convergence or measure the efficiency of a stacking routine is to analyze how the NCF stacked result (called the NCF) changes as incremental data are averaged. This requires a metric, and we use the signal-to-noise ratio of the maximum spectral amplitude from the FFT of the positive-lag NCF normalized by spectral amplitude at 1 Hz ('Spectral Amplitude' in Figure 3.13b). An alternative metric is the average root-mean squared difference between the stack before and after the new data are averaged as in Dou et al. 2017. Figure 3.15 shows the result of this convergence analysis for a simple mean averaging routine at Fairbanks. We also analyzed a median stacking routine, a mean stacking routine where each incremental 1-minute NCFs are weighted by a peak value, and a phase-weighted stacking routine. We find that increases in the spectral amplitudes begin to level off around 6 hours, but continue to improve up to 20 hours. An equivalent range of signal-to-noise ratio is achieved after just 3.75 hours when we used a phase-weighted stacking routine, but was not pursued here because this routine is known to distort amplitude information because of its use of the instantaneous phase via Hilbert transformation (Schimmel et al. 2011). Based on the analysis here we can assume NCF stacks at 6-hours or longer are converged.

For the purpose of time-lapse noise imaging, a critical disadvantage of stacking is that temporal resolution decreases. By the Nyquist sampling theorem, subsurface dynamics are aliased when the change operates on a timescale shorter than twice the stacking timescale. For example, if soil velocity changes over minutes, daily NCF stacks will not be able to resolve the details of the process. In this study, we analyze either 6-hour or 20-hour NCF stacks and aim to resolve long term multi-day changes in the subsurface.

3.4.3   Dispersion analysis

Surface waves propagating at the free surface have a unique dispersion solution, barring any destructive interference between modes. Having observed surface waves on linear DAS 2D NCF, we can use the *tau*-p transform to estimate the dispersion and modal summation technique to estimate the velocity structure of the subsurface.

$\tau-$p transform

A 2D NCF image commonly shows surface wave phases radiating out from the virtual source location. In global analysis of ambient microseism noise, it is common to apply frequency-time analysis to the NCF to obtain a group velocity. Instead, the density of DAS receivers enables direct transformation of the 2D NCF from time-distance to frequency-

velocity by way of the τ-p transform. This is a decomposition of a wavefield assuming plane-wave components, each with a unique frequency and angle with respect to vertical. "τ" in this context refers to a vector of delay times that are used to shift through the lag-time axis of the 2D NCF; "p" refers to the ray parameter or 1/horizontal phase velocity. The τ-p transform is also referred to as the slant-stack. An underlying assumption of slant stacking is that of a horizontally layered earth model. Algorithmically, the τ-p transform is achieved by applying linear moveout and summing amplitudes over the offset axis for each value of the ray parameter. A Fourier transform along the τ axis returns the familiar dispersion result with velocity (1/p) as a function of frequency.
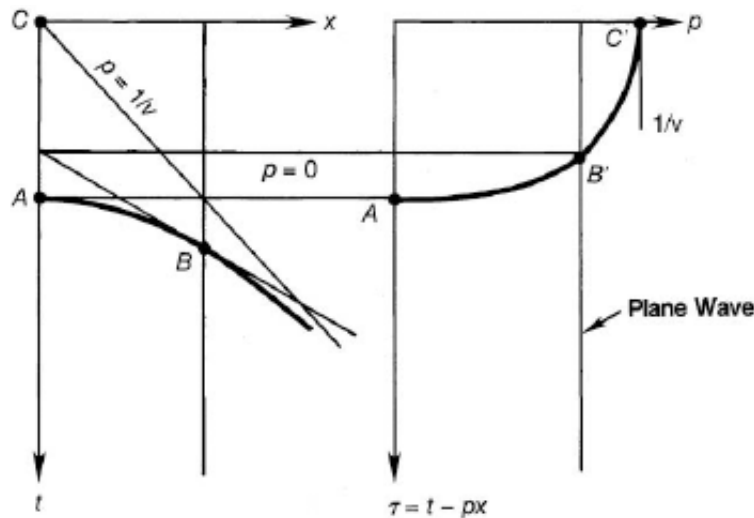
Figure 3.15: Slant-stack transform mapping from x-t space where plane-waves plot as lines to $\tau-$p space where plane-waves plot as points. Dispersive wave analysis, specifically the interpretation of fundamental and higher order modes, is difficult in x-t space, but modes separate as smooth functions in $\tau-$p space. This diagram also shows reflected waves which plot as hyperbolas in x-t and ellipses in $\tau-$p. [Source: Wikipedia].

1-D Vs forward modeling by modal summation

The surface wave modes for a given 1-D (vertically heterogeneous) isotropic, elastic medium occupying a half-space are solutions to the eigenvalue problem for the displacement-stress vector (Aki and Richards 2002, Ch. 7.2). We can use mode superposition, or modal summation technique)Herrmann 2013). In modal summation, a propagator matrix method (Thomson 1950; Haskell 1953; Gilbert and Backus 1966) is adopted and iteratively solved by trial-and-error for a vector of possible plane waves using their wavenumber value (see Aki and Richards 2002, Eqn. 7.59). Forward modeling of the dispersion data using a set of 1D layer geometries and elastic parameters is one of the synthetic seismogram methods

implemented in Computer Programs in Seismology (Herrmann 2013). This method is the basis for the Monte Carlo inversion method used in (Dou et al. 2017).

3.4.4 Refraction analysis

Noise data selection for body wave analysis

As a direct result of the longer coherence length of surface waves ($1/r$ versus $1/r^2$ for P- and S-waves), and likely also as a result of the source physics of microseism noise generation, surface waves dominate over body waves in almost every noise study published to date. Hence, the use of body wave refraction techniques with seismic noise is less common. Some of the first surveys demonstrating body wave existence in 2D NCF microseism observations suggested that body waves have higher frequency content and deeper sensitivty to structure (Roux et al. 2005; Draganov et al. 2009; Norimitsu Nakata et al. 2011; Poli et al. 2012; F.-C. Lin, D. Li, et al. 2013). To enhance the signal-to-noise ratio of body waves in NCF observations, Nori Nakata et al. 2015 proposed selectively filtering the raw data used to create the stacked NCF based on a statistical selection criteria, such as amplitude thresholding in a window of body-wave slowness or array-derived backazimuth slowness information.

If we can treat a single vehicle as a vertical point source of seismic waves (L. Li, Nimbalkar, and Zhong 2018), then we should improve the 2D NCF fidelity by stacking over only those 1-minute windows that contain a high level of road activity. We tested the effectiveness of data selection at our experiment in Fairbanks in order to improve the fidelity of body wave observations and potentially also reduce the computational burden of the task of computing NCFs across multiple virtual source positions.

To perform data selection, we employed a sentinel DAS receiver (channel 3310, 310m from the north end of the Road Array) as a proxy for road activity. Figure 3.16 shows the distribution of energy versus hour in UTC time (local AKST = UTC - 8:00). Figure 3.17 shows different 1-minute observations from this sentinel channel across this distribution, including times when there were no vehicles present, only one small car present, when many vehicles were present at the same time as one big truck, and from a time during rush hour when 7 vehicles passed the receiver point during 1 minute. These observations are made using DAS data only and from qualitative field observations of the general visual observations of DAS recordings with individual vehicles on Farmer's Loop Road. No recorded visual evidence of vehicles was available for side-by-side confirmation. Next, we measured the mean raw DAS energy (counts/timesample) for the sentinel receiver over all 1-minute records for Aug-15 (20.83 hours). To load and compute the sentinel data statistic for 1 day required 24 CPU hours (2 x 12 CPU), but would likely be faster if the data were distributed over more than one disk or stored in a sliceable format such as HDF5.

Comparison of NCF results from different data selection criteria was used to inform the noise correlation workflow used to obtain 2D NCFs for the purpose of body wave analysis. When we stack over the full day using the workflow described above the result is high signal-to-noise arrivals over the DAS Road Array (Figure 3.18a). Surface waves and body waves
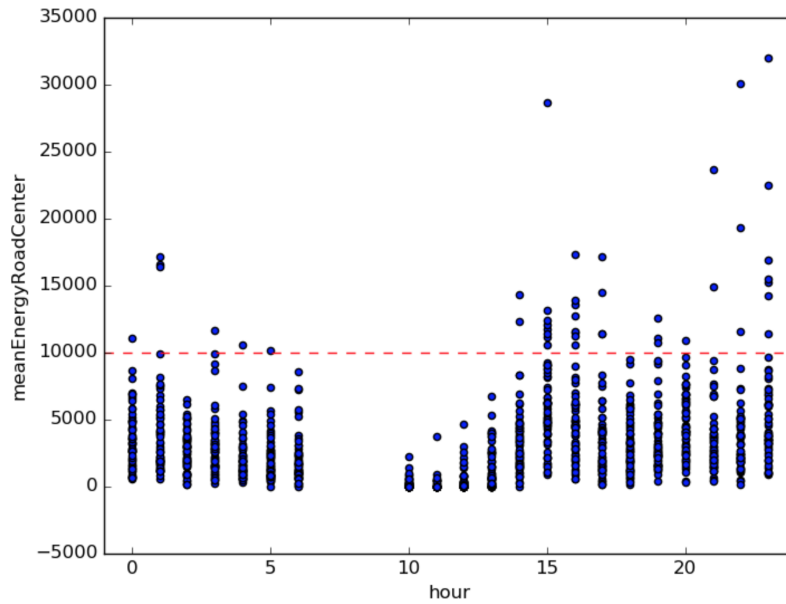
Figure 3.16: Distribution of sentinel DAS receiver energy on Aug-15-2016 by UTC hour (local AKST = UTC - 8:00). After the initial tabulation of energy on the road, we can filter the minutes used in noise correlation to only include a particular energy range in our stack [Source: N.L.].

are identified with moveout of 100 - 200 m/s and 800 - 1200 m/s, respectively. The NCF has been computed using a virtual source position near the sentinel channel (channel 3220, 90 m north of the sentinel channel) This NCF result required 48 CPU hours (4 hours x 12 parallel processors). Figure 3.18b shows the result of stacking over only the minutes when there was a mean sentinel energy level of 10,000 or greater (0.8 hours of data included; 1 CPU hours). Figure 3.18c shows the result of stacking over only the minutes when there was a mean sentinel energy level less than 1,000 (5.2 hours of data included; 16 CPU hours). 3.18c shows the result of stacking over times when there was a mean sentinel energy level between 6,000 and 10,000 (5.96 hours of data included; 17 CPU hours). A bandpass filter of 1 - 8 Hz (n 2 p 2) has been applied to display the final 2D NCF here. Surprisingly, a high level of road activity produces very little body wave energy in the NCF result, perhaps because only 39 minutes of data are included in the computation. Similarly, it is surprising that the low energy level actually produces very little surface wave energy in the 1 - 8 Hz range, and high signal-to-noise ratio body wave observations along Farmer's Loop road. However, there is little evidence of this body wave energy on the Warming Array for the same data selection process, potentially because of the low energy signal (normalized in the figure).

A medium level of road activity was determined to optimally achieve a strong body wave signal while also reducing the overall compute time by 65% (not including the pre-compute phase). Based on this result we modified our workflow for body wave analysis, but kept the

original full-day recording workflow for surface wave analysis. For the purposes of time-lapse body wave analysis over the full experiment we pre-compute and store the values of mean sentinel energy level for each minute of passive DAS recording for the entire experiment. For each day, we then only compute noise correlations for those minutes when there was a medium level of road activity (mean sentinel energy level = 6,000 - 10,000 counts/timesample).

First-break picking

Traveltime tomography is an inversion of scalar-valued data representing the "first break" arrival times of a seismic phase of interest. To obtain these arrival times we have a choice of several different picking algorithms. The simplest and most traditional method would be to hand-pick each arrival. In expectation of wide deployment to DAS datasets with thousands of virtual sensor and virtual receiver points this approach is not efficient enough. A simple semi-automatic method is to use a "short-term average over long-term average" (STA/LTA) algorithm to find the first onset of a wave at each sensor. STA/LTA is called "semi-automatic" here because the threshold of the algorthm must be adjusted across the large array depending on variable noise levels and virtual source-receiver geometry. This algorithm works well for virtual source-receiver separations >400-500 m, when there is a significant "pre-event" time with no ground motion to establish the LTA, but does not work as well for shorter paths especially when there is energy at negative lagtime. To improve the performance of the STA/LTA algorithm in the context of shorter offset noise we will mask the negative lagtime arrivals prior to running the algorithm.
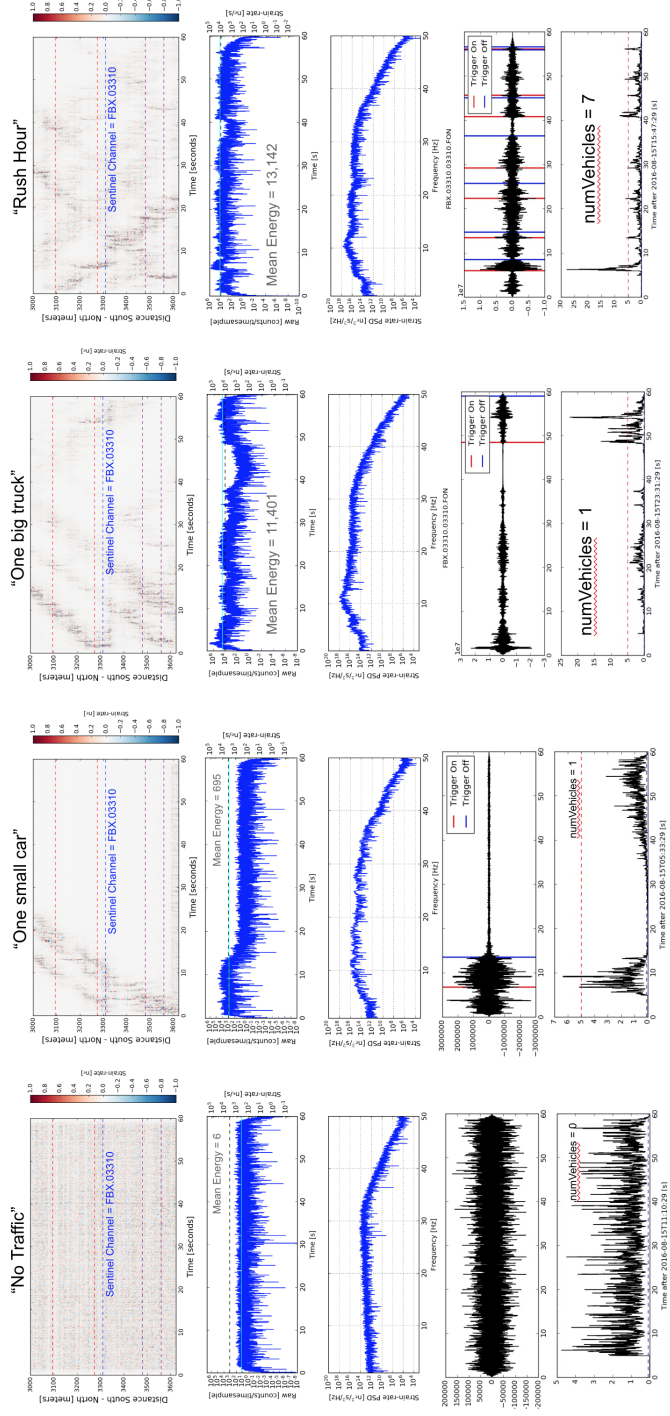
Figure 3.17: Example 1-minute observations from sentinel DAS receiver (channel 3310, 310m from the north end of the Road Array). We use the sentinel DAS receiver as a proxy for road activity. Each column show observations and data statistics for a minute when there was (Far left) No activity, (Center left) low activity, (Center right) and (Far right) high activity. The top row shows time-distance data for the DAS Road Array. Center two rows with blue lines show raw energy time series and strain-rate spectra. Lower two rows with black lines show raw time series and STA/LTA threshold to detect the number of vehicles. The mean sentinel energy level is printed in the middle row [Source: N.L.].
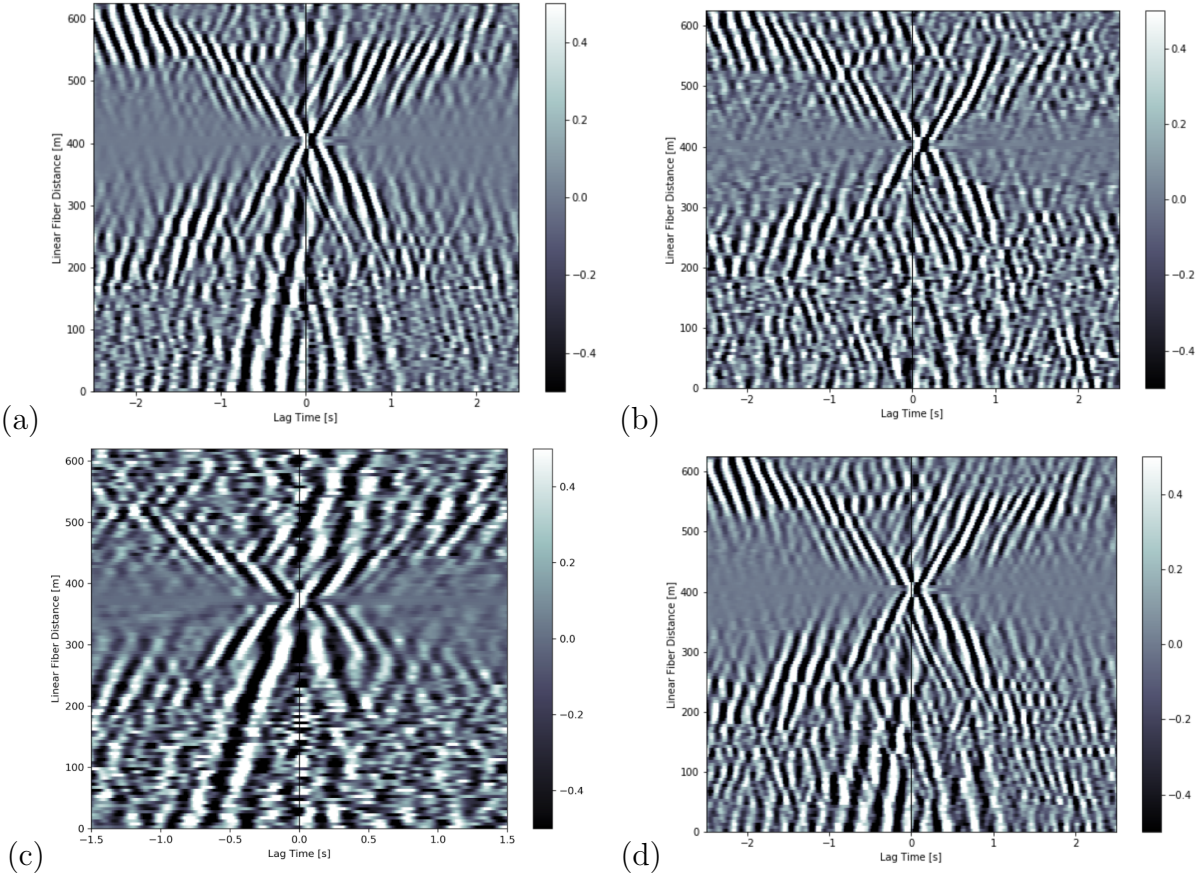
Figure 3.18: Data selection results for the Road Array from Aug-15 based on different data selection criteria: (a) All times included; (b) High activity; (c) Low activity; (d) Medium activity. A sentinel DAS receiver positioned on the Farmer's Loop Road Array was used for the data selection. The NCF has been computed using a virtual source position near the sentinel channel [Source: N.L.].

Plane-wave refraction analysis

In a near surface seismic refraction survey, P- and S-waves are treated as plane waves that propagate from surface sources into the subsurface and refract at layer interfaces (Figure 3.19). Seismic impedance contrasts define the geometry of the problem according to Snell's Law (see Chapter 2, Section 2.1.1). In the simplest form of seismic refraction analysis, traveltime observations of separate seismic waves moving with different speeds are used to estimate layer velocities and thicknesses based on geometrical principles. Three observations are required to properly constrain the simple layer over a half-space problem. To find the required information, seismic array recordings are plotted in time-distance space and independent seismic phases are identified. The slope (called the slowness=1/velocity, $1/V_i$) of the arriving direct wave and refracted wave and the zero-position y-intercept ($T0_1$) or cross-over distance (X_{cross1}) are used to find the critical angle:

$$i_c = arcsin(\frac{V_0}{V_1})$$

and solve for the layer thickness:

$$h_0 = \frac{T0_1 V_0}{2cos(i_c)} = \frac{X_{cross_1}}{2}\sqrt{\frac{V_1 - V_0}{V_1 + V_0}}$$

Multi-layer and dipping layer problems have similar geometrically-derived formula (Lay and Wallace 1995).
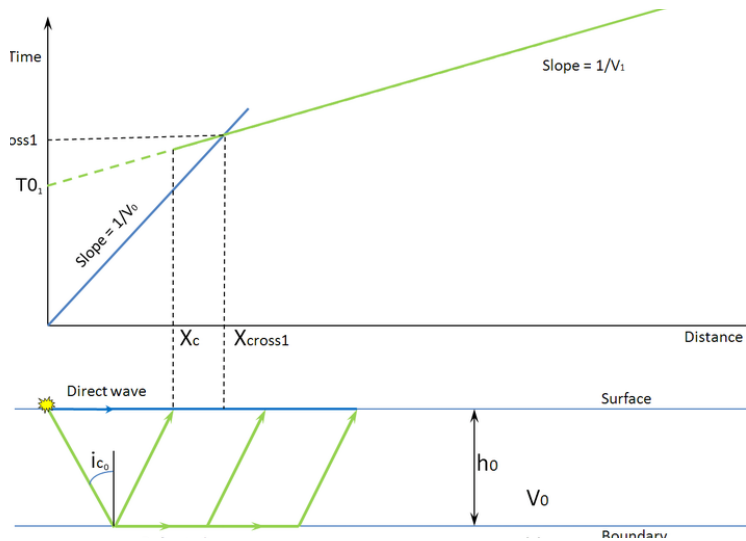
Figure 3.19: Geometry of seismic refraction through the simple layer over a half-space problem. [Source: Wikipedia]

Traveltime tomography

Alternatively, plane-wave propagation can be posed as a linear inverse problem wherein traveltime observations (d) are related to a slowness model (m) given the set of raytracings (G) which map data to model parameters, as in (Aster, Borchers, and C. H. Thurber 2018):

$$d = Gm.$$

There are many advantages to a tomography approach, not least of which is the flexibility to perform imaging in more complicated 2-D and 3-D model geometries.

Due to the common limitations of nonuniqueness for seismic surveys conducted at the surface of the planet, we will adopt a least-squares minimization approach to traveltime inversion in which we seek a best-fitting near-surface model that both fits the data constraints and is smooth. We acheive this by minimizing the regularized objective function:

$$\Psi = ||d - G(m)||^2 + \lambda||L(m)||^2.$$

λ is a tunable parameter that weights the model smoothing operator L (typically zero, first or second order Laplacian of model parameters). Small values of lead to models which overfit the data, while large values of λ diminish the contribution of the observable to the solution and are "overly-smoothed". Cross-validation or L-curve analysis is used to heuristically determine the appropriate regularization parameter.

In practice, we will not focus on mesh generation, ray tracing, or the numerical inversion methodologies in this project. Aspects of these techniques are still on-going research topics in the field of computational geoscience, but have been demonstrated in a basic form in previous work and are included in the seismic refraction package called PyGimli (Rücker, Günther, and F. M. Wagner 2017). Thus, we feel it is fine to proceed with this "black-box" tool of seismic imaging. We will use a form of the Dijkstra algorithm (Dijkstra 1959) to determine the G matrix for any given model interpolated using a Delauney triangular mesh with a cell size threshold based on the array geometry. A pre-conditioned iterative nonlinear conjugate-gradient method will be used for inversion (Rücker, Günther, and F. M. Wagner 2017).

3.5 Results

3.5.1 Noise from a single vehicle

Passive DAS recordings across the site were dominated by seismic energy in the frequency range between 3 and 50 Hz. Subarray correlations of single vehicle passes confirmed that the source of this seismic energy was vehicles driving on Farmer's Loop Road.

The seismic 'vehicle band' has previously been used for imaging (Louie 2001; Dou et al. 2017). Before using this noise it is appropriate to consider the variability in the noise field, especially because the noise is high frequency. We first consider what the noise from a single
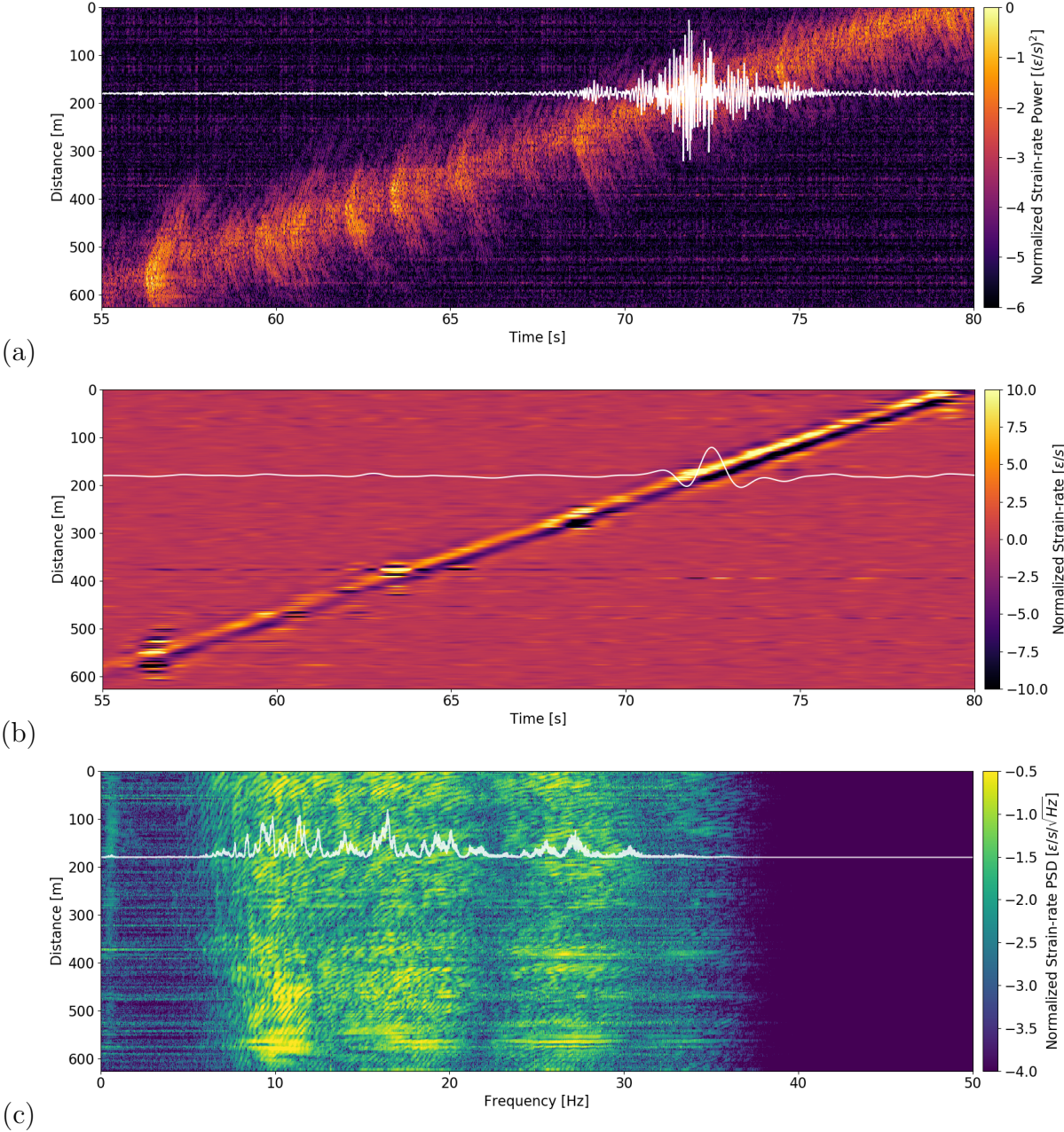
Figure 3.20: (a) DAS recording of a vehicle driving on Farmer's Loop Road using the Farmer's Loop Road Array shown in Figure 3.11a. Channels are ordered North to South (0-615). Channel 180 is highlighted. The Warming Experiment Array is located due east of channels 20-200, at a distance 75 m. (b) Same as (a) plotting strain-rate instead of power with a lowpass filter with corner at 1 Hz to show low frequency strain response of roadbed. (c) Power Spectral Density highlights spatial variability [Source: N.L.].

vehicle looks like, and then expand to average over many vehicles to treat Farmer's Loop Road as a line array each day.

Figure shows a number of observations common to recording DAS data along busy roads (e.g., Jousset et al. 2018). First, the vehicle speed is evident from the envelope move-out. Here the vehicle is traveling at approximately 24.6 m/s or 55 mph (speed limit on Farmer's Loop Road is 55 mph). Second, at each moment, seismic waves are being produced from the vehicle's position. The waves are coherent for more than 100 m, and appear to radiate outwards in all directions, but the Farmer's Loop Road Array records them only to the north and south. This energy appears to have a speed of 200 m/s, but it is highly likely based on the move-out that these are surface waves and so are dispersive. A third observation is that the amplitude of seismic wave production is variable along the road – not all locations generate the same level of seismic noise.

An additional, remarkable feature of recording vehicles with DAS near roads is highlighted in Figure 3.5.1b. This image shows the same vehicle recording used in Figure 3.5.1a, but after a 1 Hz lowpass filter. What remains after removing the elastic waves produced by the vehicle is the quasi-static strain response of the vehicle load in the direction parallel to the road. This observation was first made by Jousset et al. 2018 using DAS data along a road in Iceland, and modeled using the Flambert-Boussinesq approximation. We will not use this energy for the purposes of permafrost imaging, because it does not propagate. Use of the Flambert-Boussinesq approximation for monitoring of Poisson's ratio or vehicle classification are interesting future directions.

3.5.2   Spatial nonstationarity of noise field

Next, we consider the state of noise field nonstationarity on Farmer's Loop Road. A nonstationary process is one whose mean and variance are not constant. This is important in ambient noise analysis, because the presence of a nonstationary noise field will bias our velocity image **wapaneer2011** We find strong spatial noise variations along the ∼615 m segment of the Farmer's Loop Road array, and strong temporal variations in noise from night to day. Although we have designed our method to average the noise field over daily intervals, thus issues pertaining to gaps between vehicles or the spectral holes identified for a single vehicle are avoided, it is important to consider the degree of nonstationarity.

For example, Figure 3.5.1c shows the spectra for the vehicle DAS recording. The south (400-610) and north (0-80) parts of Farmer's Loop show relatively stronger noise around 10 Hz when compared to the rest of the array. This same observation persists when we average over many hours on a busy day. One possible explanation for stronger response to the south is a series of topographic undulations over the southern portion of the Farmer's Loop road observed in the data recorded by a LiDAR survey in June 2016. LiDAR identified multiple 20 cm peak-to-trough amplitude variations with a 30 m horizontal wavelength (shown in Figure 3.11a). These road bump features, common across central Alaska in summer time, are caused by localized thaw subsidence within and beneath the roadbed. North of the Permafrost

Experiment Station Farmer's Loop Road turns sharply to the west. We hypothesize that both road bumps and sharp turns cause higher amplitude seismic noise.

L. Li, Nimbalkar, and Zhong 2018 suggested that road noise can be thought of as a superposition of vehicles, each represented as a moving vertical unit force. Our observations suggest that road shape and topography may also play a role. Road bumps cause vertical chassis oscillation potentially resulting in a higher amplitude vehicle vertical force for vehicles traveling over this part of the road. Sharp turns will potentially partially rotate the vehicle vertical force into the horizontal plane, resulting in excitation of a larger horizontal component. The fact that we see strong seismic energy with a horizontal sensor less than 1 wavelength away suggests the vehicle source type may have both vertical and horizontal forces. P, SV, SH, Love, and Rayleigh waves were observed in this study in daily noise correlations using different orientations of the fiber-optic array (see below), which suggests that vehicles may produce both surface and body waves. Fully characterizing how vehicles act as seismic sources is an interesting future direction of this research, however for the purposes of this study we will not consider this any further and simply assume that Farmer's Loop Road in the vicinity of the Permafrost Experiment Station acts as a line array of seismic energy.

3.5.3 Temporal nonstationarity of noise field

Vehicle noise is time-dependent due to diurnal commuting times, weekday/weekend differences in traffic, and variations in vehicle type. An additional temporal noise characteristic is the uneven level of activity on the warming array site. At the beginning of the experiment there was more activity as we setup experiments and calibrated all of the system components compared to the end of the experiment when we were out at the site for only a few hours each day. We also conducted an active surface orbital vibrator source survey each night for 3 hours and periodically performed hammer tests during the day. All of these data were removed from ambient analysis. Earthquake ground motions are an additional source of nonstationarity, but this will be removed during pre-processing.

Figure 3.21 shows the temporal variability in Farmer's Loop road noise level over the two month warming experiment. High noise level around 5 - 50 Hz on the Road array and 5 - 15 Hz on the Line B of the Warming array occur during the day between 7:00 am and 11 pm. The lowest energy time period is from 2:00 - 5:00 am each morning. Differences from weekdays to weekends were less obvious.

Energy decay from Road array to Warming array

The Warming array is offset from Farmer's Loop Road a distance of about 75 - 100 m depending on the measurement points. We observed that the Warming array showed a reduction in seismic amplitudes of frequencies above 12 Hz compared to the Road array. Energy at lower frequencies (5 - 15 Hz) was mostly found to be preserved with less than 1 dB power loss (Figure 3.21 a-b). This is consistent with the frequency dependence of how
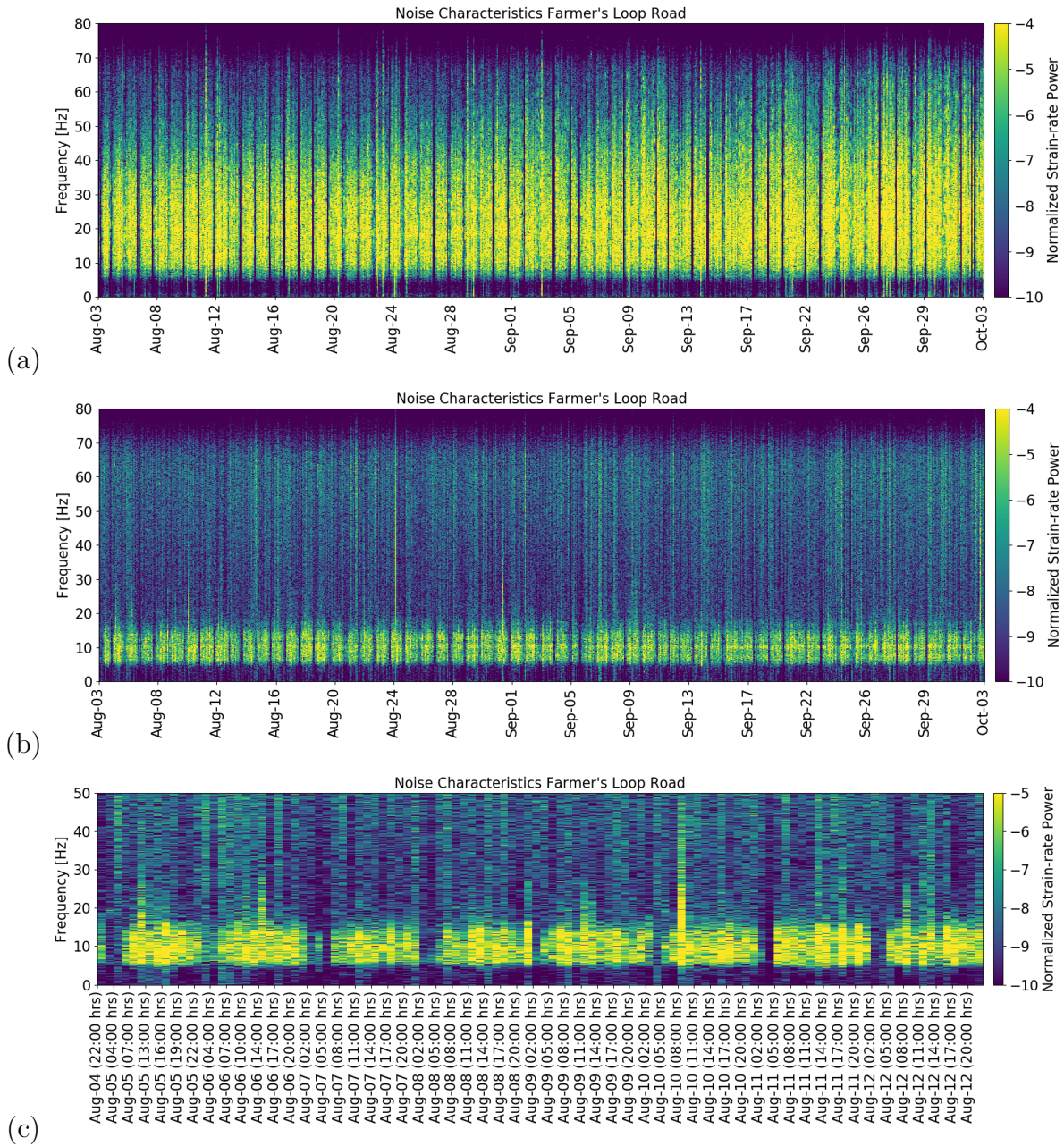
Figure 3.21: (a) Vehicle noise spectra from the north end of Farmer's Loop Road (channel 0 shown in Figure 3.5.1) divided into 90 minute windows. (b) Same as (a) but for a channel on Line B (channel 600). (c) An expanded view of 1 week from (b) highlighting the high energy and low enegy time periods. [Source: N.L.].

surface waves decay with distance, which results in an additional phase term, $exp[\frac{-\omega x}{2c(\omega)Q(\omega)}]$ (Aki and Richards 2002, Eqn 7.93).

3.5.4 2D Noise Correlation Functions

Daily deconvolution NCFs computed using DAS recordings of Farmer's Loop vehicle noise showed a high level of reproducibility. We use the term "daily NCF" to refer to the average over the duration of passive recording excluding when the instrument was turned off for testing, the 4-hour period each night of the experiment when an active shear-wave orbital vibrator source imaging experiment was in operation, and times of earthquake arrival or other impulsive sources which are automatically excluded by the data processing workflow.

Figure 3.22 shows two example 2D NCF results for two DAS lines: Line A and Line 1 (see map in each figure for indication of the data used in the figure). These NCF results have been filtered using two different bandpass filters in order to highlight the surface waves, which are between 5 and 25 Hz, and the lower frequency body waves. The background images are resolved every 5 meters along the DAS array (1 channel every 5 channels, or 2 channels per gauge length). For the road orthogonal Line 1, most of the observed seismic energy occurs on the negative lag side, and has an apparent phase velocity in the range 50 - 500 m/s. This is predicted from knowledge of the noise coming from Farmer's Loop Road. In the case of the road parallel Line A, the noise is coming predominately from the road, with a bias to the north and south ends of the road where we found stronger concentration of persistent noise sources. This distribution of noise leads to a more homogenous source distribution for Line A, and so there is more equitable energy at both positive and negative lag times. Note that the road orthogonal lines are 60% shorter than the road parallel lines, which means there is not as much phase separation for the observations made using Line 1 relative to Line A. Next, we analyzed the robustness of the NCF results to develop our understanding of uncertainty.

Note that the later Rayleigh wave observations (and also the coda waves) appear to eminate from 0 m offset and a Lag Time intercept of up to 0.5 - 2 s. What is this energy and why does it exist? Given the geometry of the problem, it is possible that noise is arriving at both DAS sensors simultaneously at a range of times. To consider this case, think of a car moving on Farmer's Loop Road. When the vehicle is located at the midpoint position between the two sensors' colinear positions, there will be a NCF arrival at Lag Time of 0 s. As the vehicle moves from the midpoint to the northern sensor's colinear position the NCF arrival time will increase. Not until the car reaches a far field location such that the noise source is considered inside the Fresnel zone of the two sensors will the NCF arrival approach the true velocity of the subsurface. Thus, moving vehicle noise sources in parallel geometries can be potentially problematic. Nevertheless, there is significant energy concentrated at approximately the correct arrival times and it is this energy that we interpret. Secondly, in an effort to not overinterpret the experimental results, we will be investigating relative changes in velocity, not absolute velocities.

Reproducibility of results

Spatial nonstationarity, as observed along Farmer's Loop Road, is smoothed by wave propagation from Farmer's Loop Road to the Warming array due to attenuation of short wavelength energy. However, there is a different source of nonstationarity due to variability of installation conditions between trenches, creating inherent differences between side-by-side DAS profiles. To assess this variability, we overlaid traces from 2D NCFs for the same day for all road orthogonal trenches (Lines 1,2,3,4,5) on the warming array (Figure 3.23). NCF results show that all five colinear trenches recover approximately the same waveform and travel time. The most significant waveform trench-to-trench variations occur in the later surface wave and coda wave arrivals. The warming site is 3D, and some variability at these high frequencies is expected due to structural heterogeneity.

Figure 3.24 compares weekday and weekend results for four different instances for Line 1 using a virtual source at the east end of the line. The blue plots are for weekend daily NCFs and the magneta plots are for weekday daily NCFs. Trace spectra are compared in the lower plot.

Comparison with hammer source

Figure 3.25 compares one 2D NCF from Aug-12 for a road orthogonal DAS segment of the Warming array (Line 1) with a hammer survey conducted on the same day for the same DAS segment. The choice of the virtual source position has been made to be colocated with the hammer shot position, both at the east end of Line 1. As disclosed in the Data and Methodology sections, the hammer survey data was not included in the NCF computation.

The hammer survey data show a fast arriving phase moving at approximately 1000 m/s with relatively higher frequency content (15 - 30 Hz), and a second slower and more dispersive phase (50 - 600 m/s) with lower frequency content. In the time-distance domain these arrivals have different move outs, while in the frequency-wavenumber domain the surface waves are broad and slow speed (low f/k) while the body waves are more accurately localized (in plane wave theory they would plot as a point) with at a faster speed (high f/k). The hammer shot wave conducted atop a wooded area and so some of the coupling is evident in the lower coherency from 0 - 20 m offset.

The colocated 2D NCF results show the same seismic phases but as a result of the high frequency road noise components being attenuated during propagation from the road to the warming array, both wave types are shifted down in frequency content. One consequence of this is that the waves do not clearly separate in the time-distance domain for the 1 - 40 Hz range. If we change the bandpass filter to a higher band from 15 - 40 Hz (compare Figure 3.25c with Figure 3.25e) it is clear both fast and slow seismic waves exist. In the frequency-wavenumber domain (Figure 3.25d) this manifests as a low-passed version of the hammer result.

Due to the significant frequency differences we did not attempt to compare the fundamental forumlations of the empirical Green's function and a unit force impulse from the

hammer. This would be an interesting future direction.

To summarize, noise variability analysis suggested that NCF records, when stacked over 1-day intervals, could be analyzed in a time-lapse repeatable fashion to understand subsurface changes.

3.5.5   1D Rayleigh wave dispersion model before warming

The aim of the thaw experiment was to understand the time-lapse seismic velocity changes due to thaw process. One way to develop a seismic image of the thawing permafrost velocity structure is to analyze the dispersive properties of the surface waves observed in the daily 2D NCF. However, as we will show next, the time-lapse inversion of surface waves would in fact not be useful for thaw imaging in this case because the noise records were dominated by rainfall signatures.

Application of the slant-stack method to extract dispersion from the 2D NCF from Line A on Aug-15, before substantial warming had occurred, retrieved the dispersion image shown in Figure 3.26. The slant-stack technique utilized the causal side only, however the results were found to be very similar if we used the acausal side, or if we averaged both causal and acausal sides. Using CPS 3.30 (Herrmann 2013) we then predicted the group velocity dispersion curves for Rayleigh waves using a reasonable 1-D layer-over-halfspace velocity model based on the soil samples taken from the site, available thermal measurements taken from the center of the warming array on Aug-15, and a basic understanding of how density and seismic velocity change during freezing (Figure 3.26d). This simple model predicted two Rayleigh wave modes in the observed frequency range (f=10 - 25 Hz) that fit the observed dispersion image (Figure 3.26c). There was larger misfit between predicted and observed energy in the higher mode, but in the general characteristics were preserved. We found a strong dependence of results on the model layer interface depth (set at 4 m) and the velocity contrast. This suggested that dispersion of high frequency noise from vehicles may be useful for monitoring structural changes such as permafrost thaw.

To develop this idea further, we could pick the observed maxima of the dispersion image and then invert the data in a methodology described by Dou et al. 2017. To explore this possibility we plotted the 2D NCF observations for each day as described in the next section.
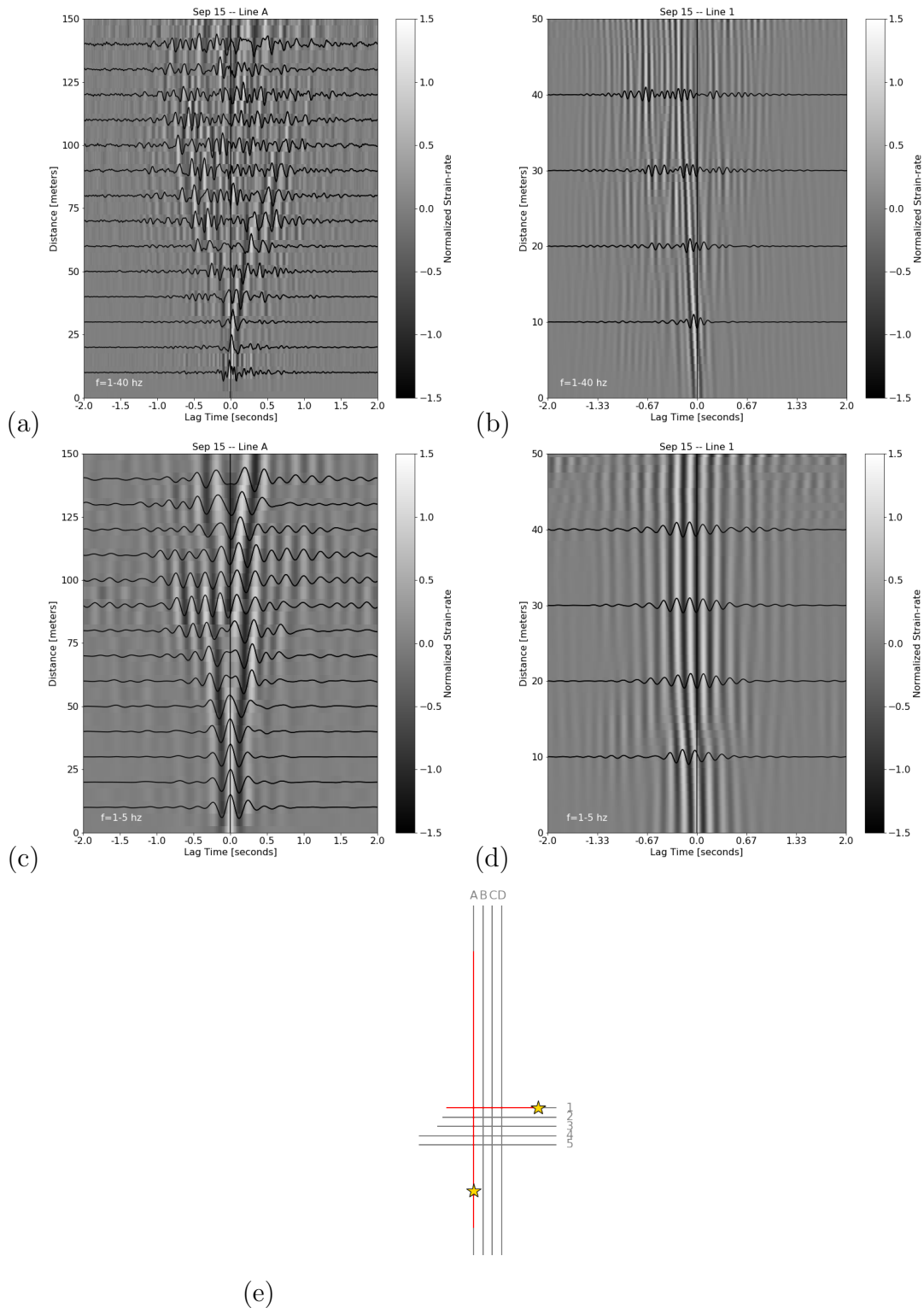
Figure 3.22: 2D NCF results for Warming array DAS Lines A and 1 from Sep 15, filtered in two different pass bands to highlight body waves at low frequency. (a) Line A for f = 1 - 40 Hz. (b) same as (a) for Line 1. (c) Line A for f = 1 - 5 Hz. (d) same as (c) for Line 1. Virtual source positions are indicated by stars in (e) [Source: N.L.].
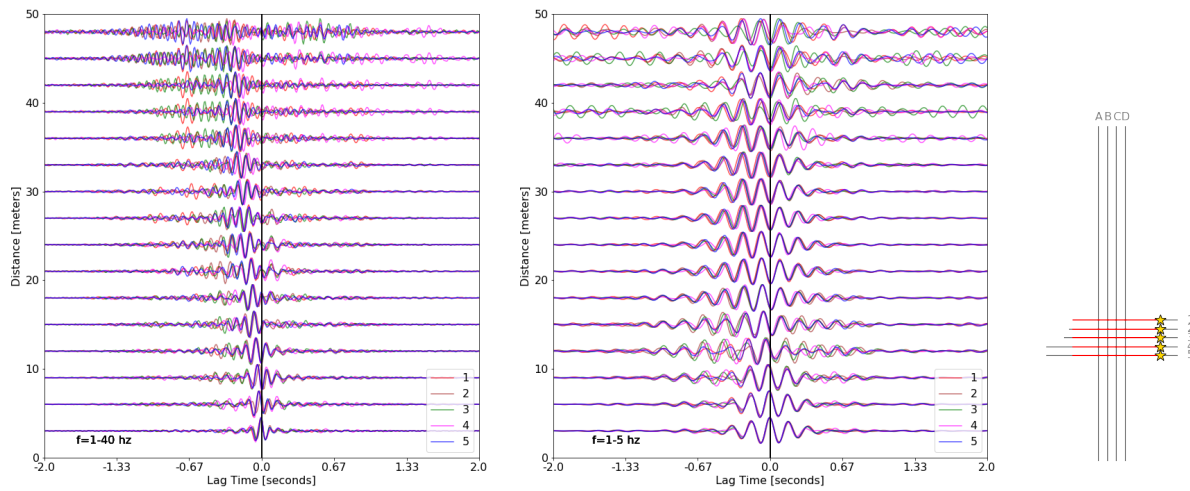
Figure 3.23: Comparison of daily NCF result for Lines 1, 2, 3, 4 and 5 for 15-Aug-2019 with virtual receiver at east end of each DAS line [Source: N.L.].
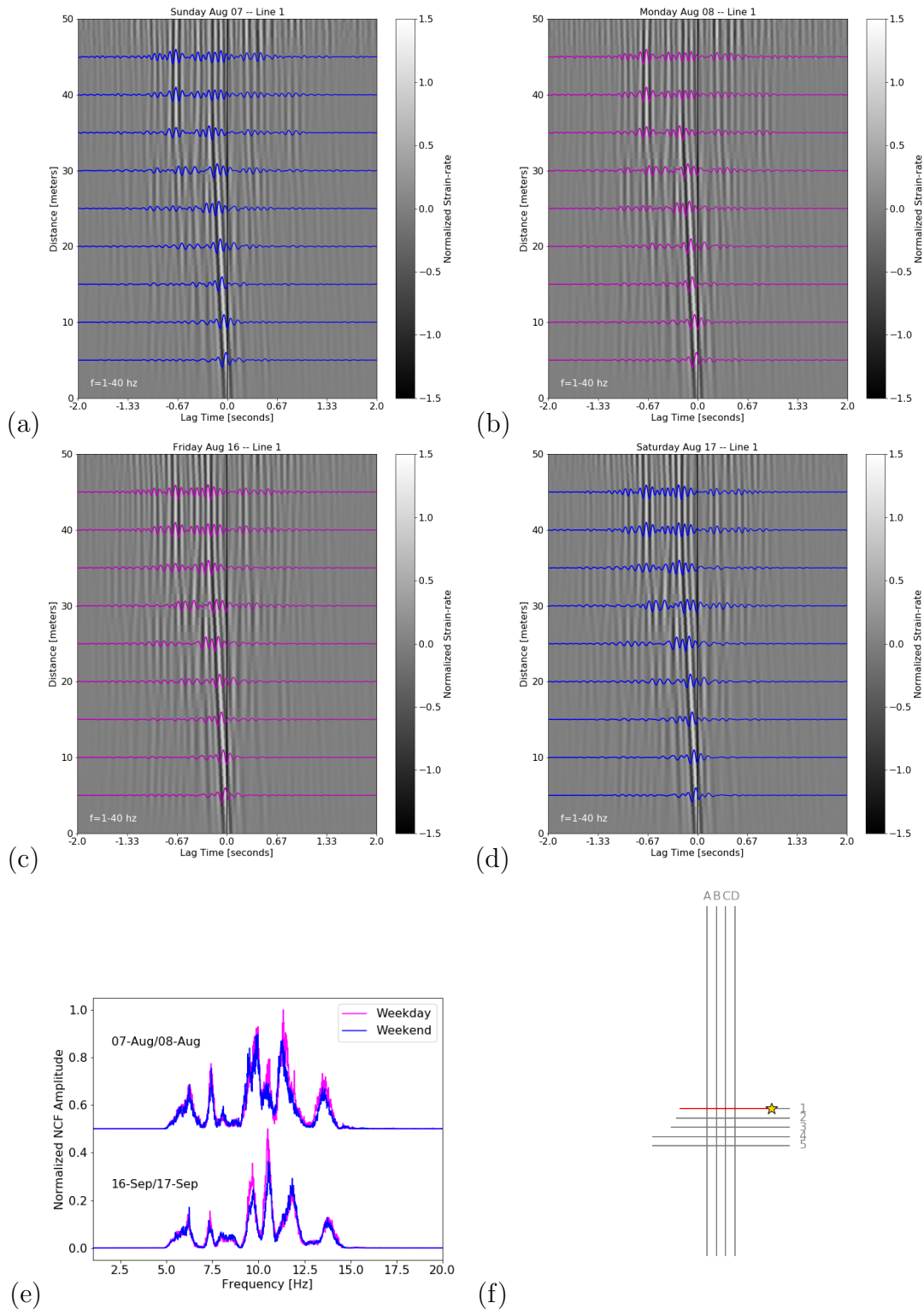
Figure 3.24: Comparison of weekday and weekend 2D NCF results for Line 1 with virtual source at east end. (Top left) Friday 07-Aug-2016; (Top right) Saturday 08-Aug-2016; (Center left) Sunday 16-Sep-2016; (Center right) Monday 17-Sep-2016; (Bottom left) Comparison of PSD for virtual receiver 30 (highlighted) color-coded by day; (Bottom right) Warming Array map [Source: N.L.].
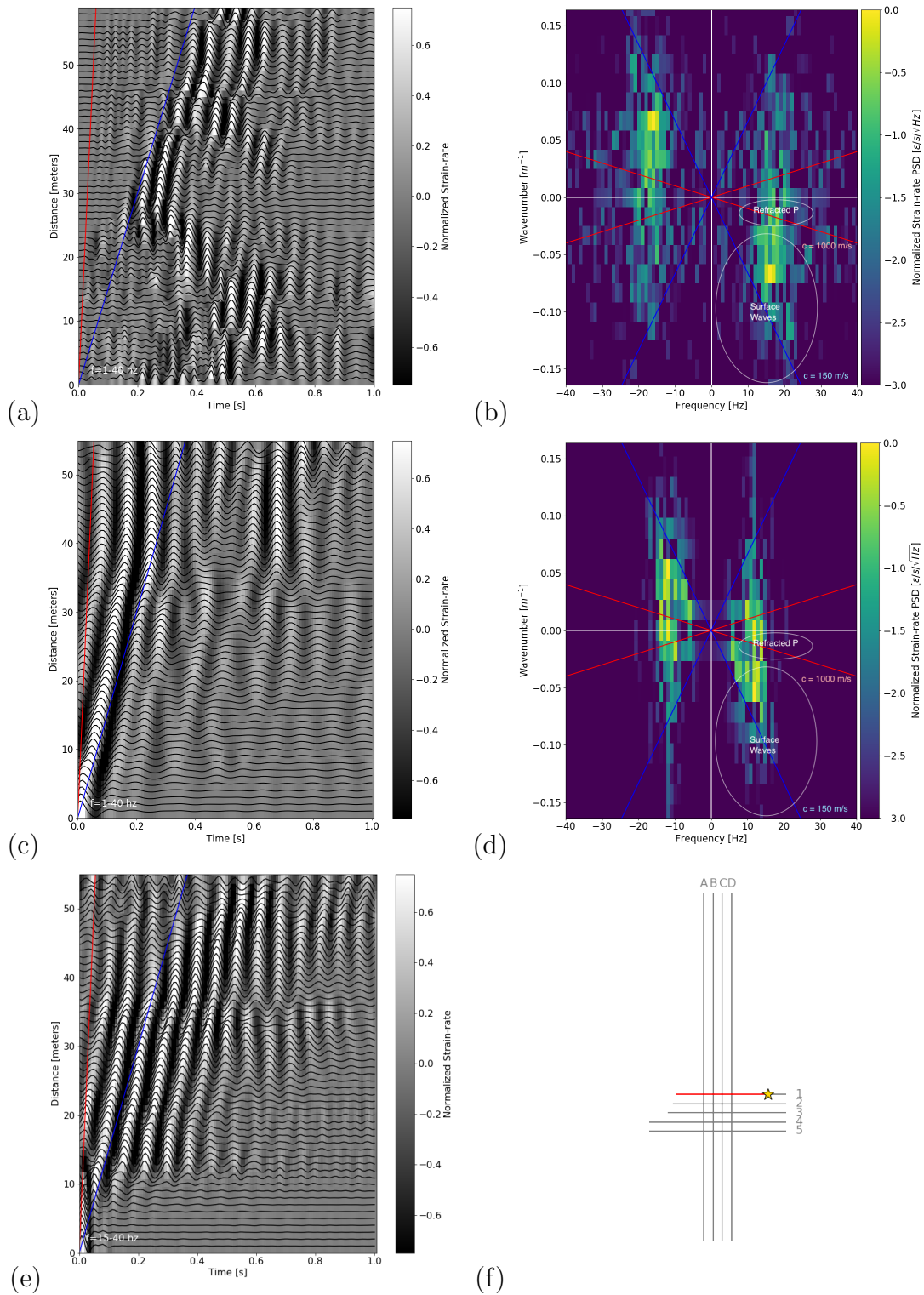
Figure 3.25: Time-distance and frequency-wavenumber observations for (a-b) the Aug-18 Line 1 hammer survey and (c-d) the colocated 2D NCF for Line 1 from Aug-18. A bandpass filter was applied to both datasets from f=1-40 Hz. (e) same as (c) but filtered f=15-40 Hz to show surface waves. (f) Warming Array map. Two phase arrivals are observed in f-K, but NCF data have lower frequency due to attenuation from the road. [Source: N.L.].
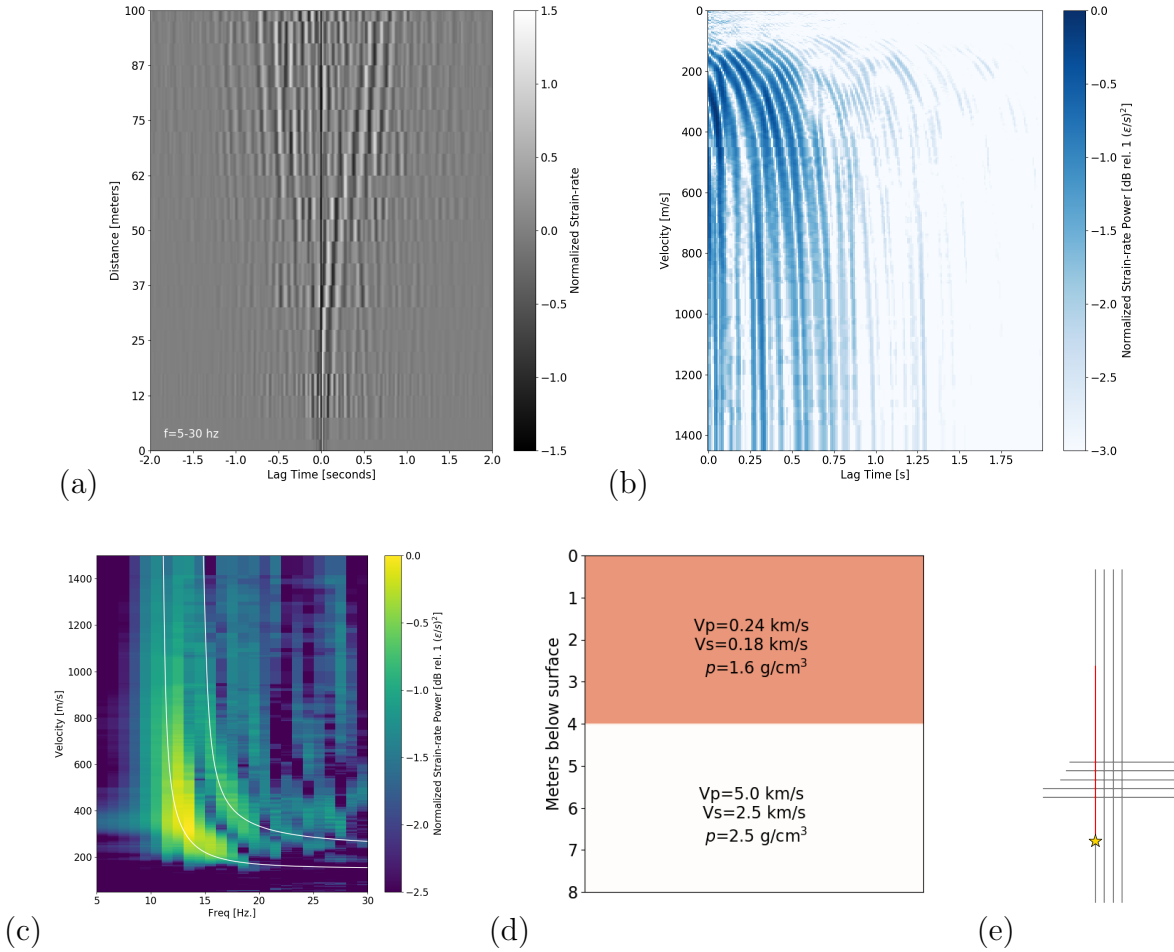
Figure 3.26: (a) Time-distance plot of 2D NCF for DAS segment shown in (e). (b) τ-p analysis for causal 2D NCF branch shown in (a). (c) Dispersion observations (image) with 1D synthetic dispersion (white lines). (d) 1D velocity model used to generate synthetic dispersion curves by modal summation (e) Warming Array map showing DAS segment (red) with virtual source at star [Source: N.L.].

3.5.6   Time-lapse Rayleigh wave observations during warming

Figure 3.27a shows an example 2D NCF from Line 1 with velocity ranges color-coded according to main Rayleigh wave phase (>100 m/s), later-arriving Rayleigh wave phases (50 - 100 m/s), and late scattered waves or coda waves (15 - 20 m/s). We picked the maximum energy arrival for these three velocity ranges for a trace spanning the warming plot with a source-receiver offset of 40m, highlighted in Figure 3.27a and the map by the blue circle (Figure 3.27c). The phases appeared to slowly speed-up over a few days and then slow-down in less than one day. This effect was more pronounced in the late surface waves than in the main Rayleigh wave arrival. There is also a correlated amplitude effect, which suggests attenuation properties may be changing. In the Discussion we consider possible reasons for why the 2D NCF arrivals do not move-out from a time of 0 seconds; this effect is especially apparent for the later arriving phases shown in Figure 3.27a.

We used the picks to compute the change in velocity for each range as compared to a reference mean velocity, dv/v, for each day. Figure 3.28 shows dv/v (red line plots) from each day aligned with volumetric water content measurements from a sensor installed on the warming plot at the 20 cm fiber depth. Major VWC increases are identified as blue lines which correlate with timing of major precipitation events. These sharp increases are referred to as apparent instantaneous events, but which in reality were observed to last several hours up to a day in duration and consist of multiple smaller rain showers. VWC was observed to vary inside the range 40 - 55 %, which would be considered partially- to fully-saturated in Fairbanks silt.

Large dv/v decreases strongly correlated with sharp increases in soil water content. The full peak-to-peak magnitude of the seismic velocity change was approximately $3 - 6\%$ for the main Rayleigh phase, $3 - 5\%$ for the late Rayleigh phase, and $2 - 3\%$ for coda, with some variability perhaps due to size of rainfall event or time since last rainfall event. The bottom panel of Figure 3.28b plots the total energy of the causal side of the 1D NCF trace as a proxy for the energy in the trace. This metric increases with water content.
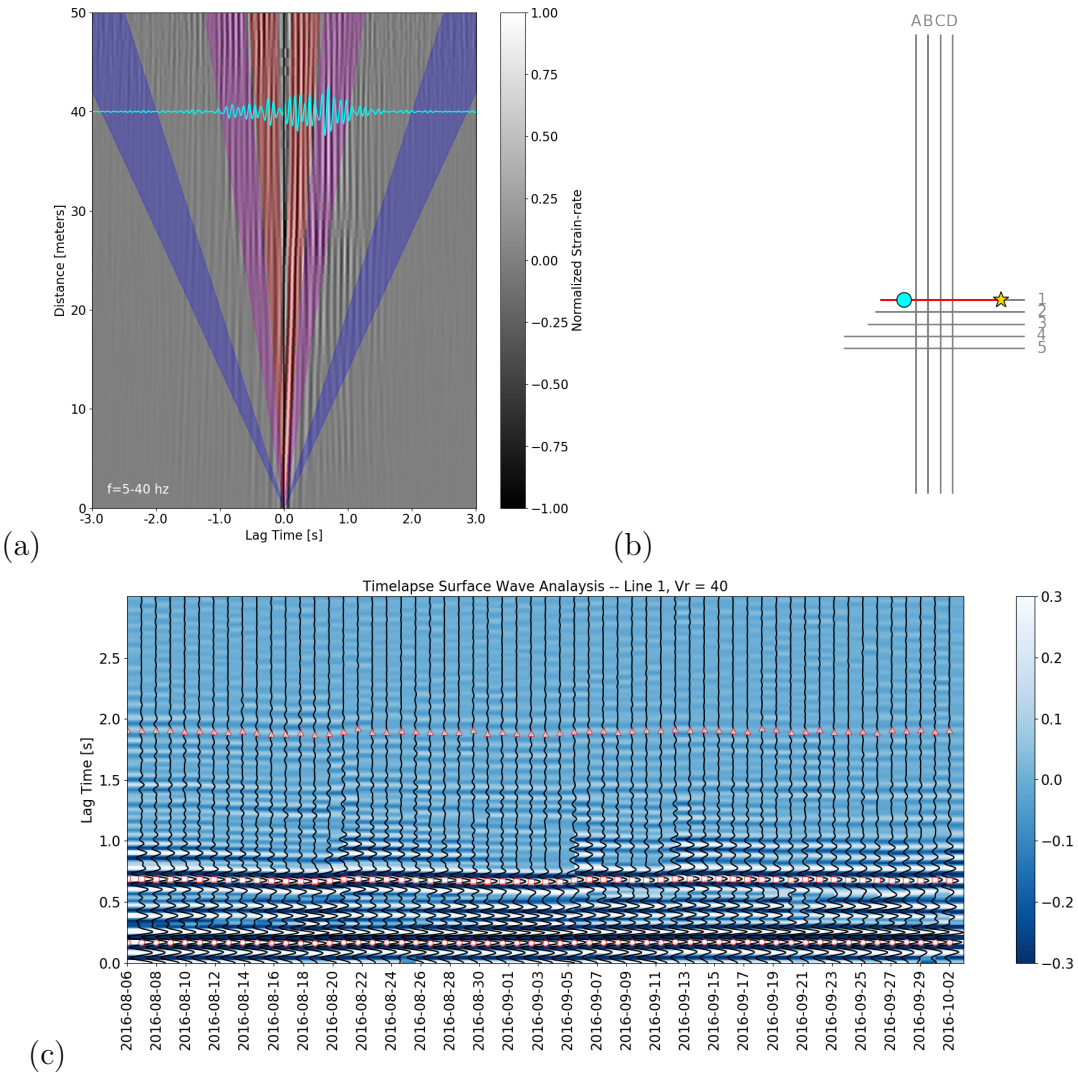
Figure 3.27: Road parallel Warming array time-lapse analysis of surface waves for an example virtual source-receiver pair. (a) Time-distance NCF for Line 1 on 09-06-2016 with virtual source at distance 0 m (to East) and virtual receiver at distance 40 m to the West across the warming plot (cyan line). (b) Map of Warming array showing Line A (red), virtual source (star), and virtual receiver (cyan circle). (c) Folded DAS-DAS virtual source-receiver pair trace from each daily NCF between 8/06/2016 and 10/04/2016 during the warming experiment. Individual surface wave and coda phases appear to migrate in lag time, and have been picked for further anaylsis [Source: N.L.].
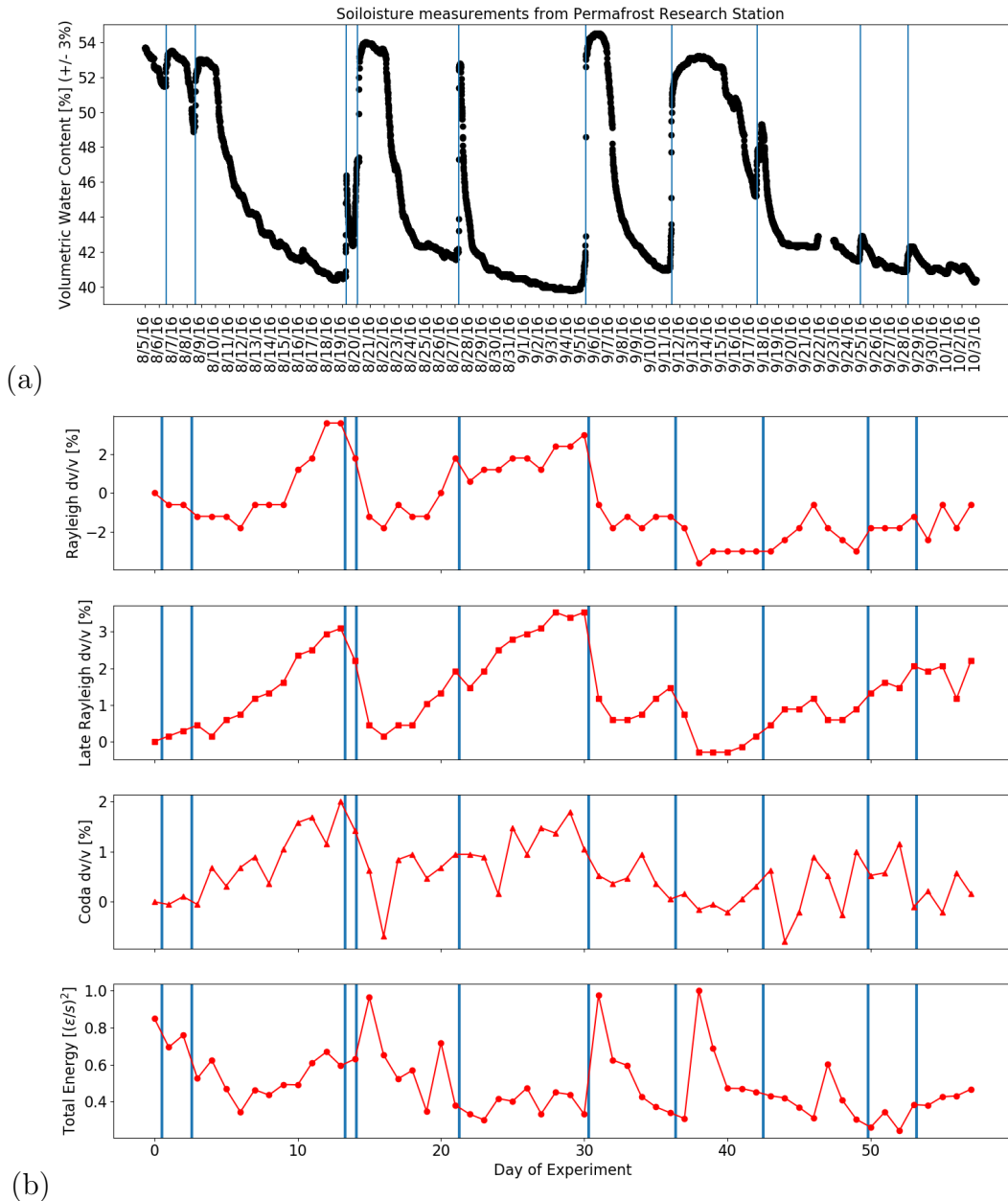
Figure 3.28: (a) Measurements of volumetric water content [%] made every 10 minutes on warming plot using a Campbell Scientific moisture probe installed at 20 cm depth prior to the experiment. Vertical blue lines indicate precipitation events, which increase soil moisture and are followed by dry-out. (b) 2D NCF surface wave and coda wave picks from Line 1 virtual source-receiver geometry shown in Figure 3.27 after mean removal. Rayleigh, Late Rayleigh, and Coda picks are related to the window used to make the picks as explained in the text [Source: N.L.].

3.5.7 Time-lapse SV refraction analysis during warming

Body waves arrive before surface waves and sample deeper, providing an alternative opportunity for seismic imaging. We observed a strong, low frequency arrival with velocity of $\sim$ 950 - 1400 m/s, appropriate for an SV refraction off the top of the permafrost. The strongest energy was in the 2 - 4 Hz frequency range. 2D NCFs developed each day showed this phase on both the road parallel and perpendicular directions. Hammer results confirmed the existence of this phase, but the NCF results had much lower frequency content. An additional surface orbital vibrator dataset collected during the experiment also identified body waves at high frequency.

To analyze SV refracted waves, we first picked the observed refractions at each DAS channel on the road-parallel lines using a virtual source at the south end of each of these lines (Figure 3.29). To make the picks we isolated the causal phase moveout in the energy domain for a window range based on a straight-ray phase velocity of 900 - 1600 m/s, and then used a subset of consecutive DAS channels to evaluate the time shift from a subset template to each consecutive trace. The process was repeated for each subset in the DAS line. As the number of subsets decreases, the correlation length is allowed to increase and the picks become less smooth. For the observed phase moveouts on road parallel lines we typically used 1 - 3 subsets, which is an averaging over 5 or more gauge lengths. Using this parameter choice, the picking algorithm was found to be insensitive to small phase velocity variations. Picks between Lines A, B and C were very similar prior to heating (Figure 3.29C). Line D was less regular and so was excluded from further analysis.

SV refractions for Line A,B,C showed a very fast arrival from 0 - 50 m, which then slowed down, and then increased in velocity toward the end of the profile. This unusual velocity pattern was possibly due to a 2D variation in permafrost, however, electrical resistivity tomography as well as surface orbital vibrator waveform analysis suggested the permafrost continued at its shallow depth to the north. This meant it is more likely that the observed velocity pattern was due to the ambient noise source field distorting the observed velocity pattern in te 2D NCFs because they are located on Farmer's Loop Road, outside the Fresnel zone for road parallel receiver pair geometries. 2D straight-ray traveltime inversion of these picks using the PyGimli code confirmed the observations of strong lateral heterogeneity, which we do not believe is physical (Figure 3.30). Further analysis and testing using additional 2D NCF paths as well as the active hammer shots from the north and south is required to clarify the accuracy of the velocity structure in absolute terms. Despite this uncertainty in the true velocity structure, the time-lapse changes from the beginning of the experiment (Aug-15) to the end of the experiment (Oct-03) are very clear. Figure 3.31 shows the change in the raw pick domain.

The warming experiment resulted in a slowdown of the observed SV refracted wave for a 10 - 20 m portion of Line C, and about 5 - 10 m of Line B, with no change in travel time observed on Line A. The zone of slowdown overlays the warming experiment. The wavefront appears to heal back after this disturbed zone. When the traveltimes per DAS channel are viewed in time-lapse as in Figure 3.32, the changes that are at the offset of the warming

array (red circles) begin to show a systematic delay of more than 0.025 s from Aug-20 - Aug-25.
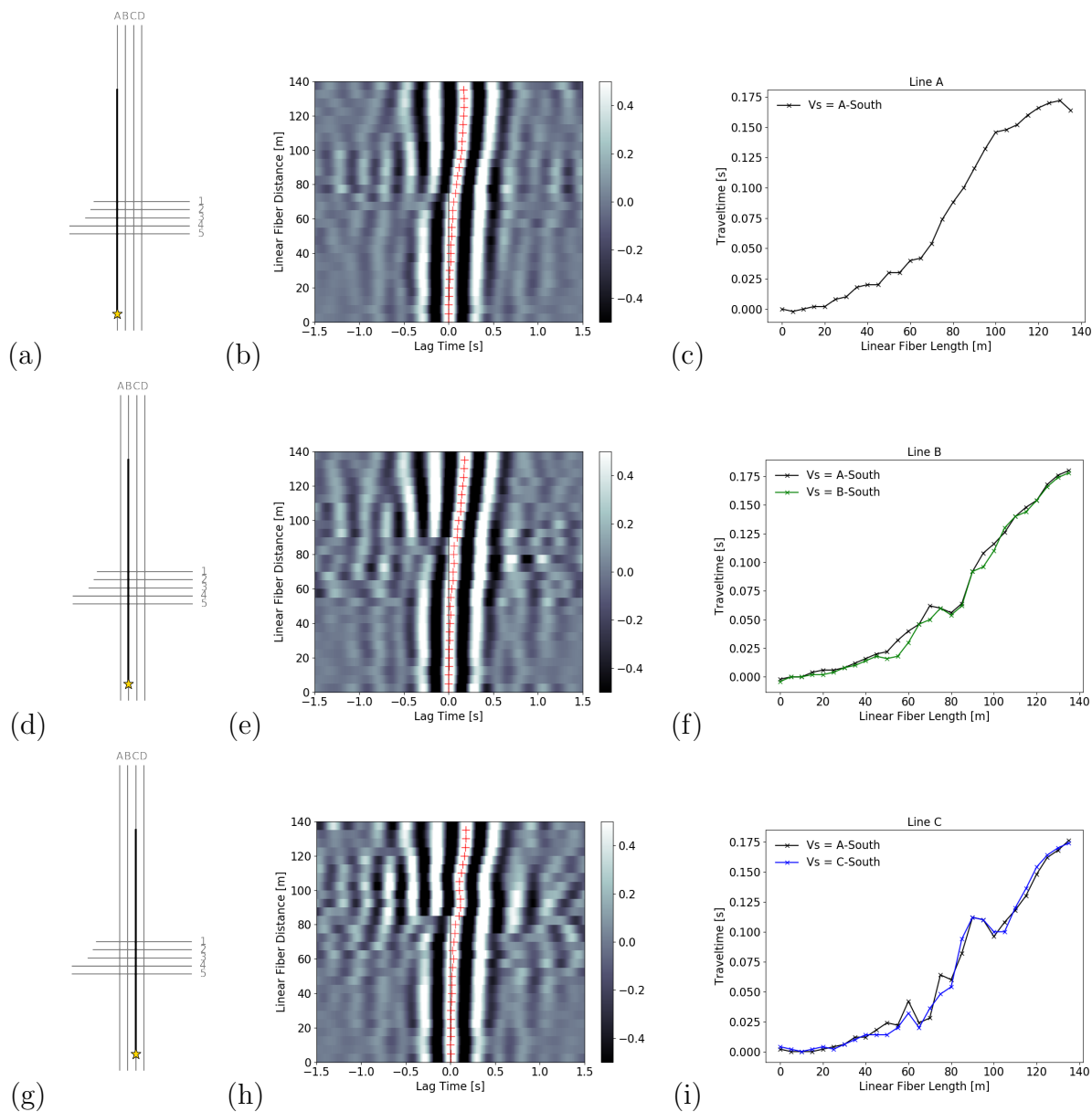
Figure 3.29: (a) Line A map with Vs=A-south; (b) Corresponding 2D NCF data from Aug-15-2016 with picks shown as red "+". (c) 2D NCF first break picks (black). (e) Line B with Vs=B-south; (f) Corresponding 2D NCF data for B. (g) 2D NCF picks (green) plotted with 2D NCF picks computed for Vs=A-south (black). (h) Line C with Vs=C-south; (i) Corresponding 2D NCF data for C. (j) 2D NCF picks (blue) plotted with 2D NCF picks computed for Vs=A-south (black) [Source: N.L.].
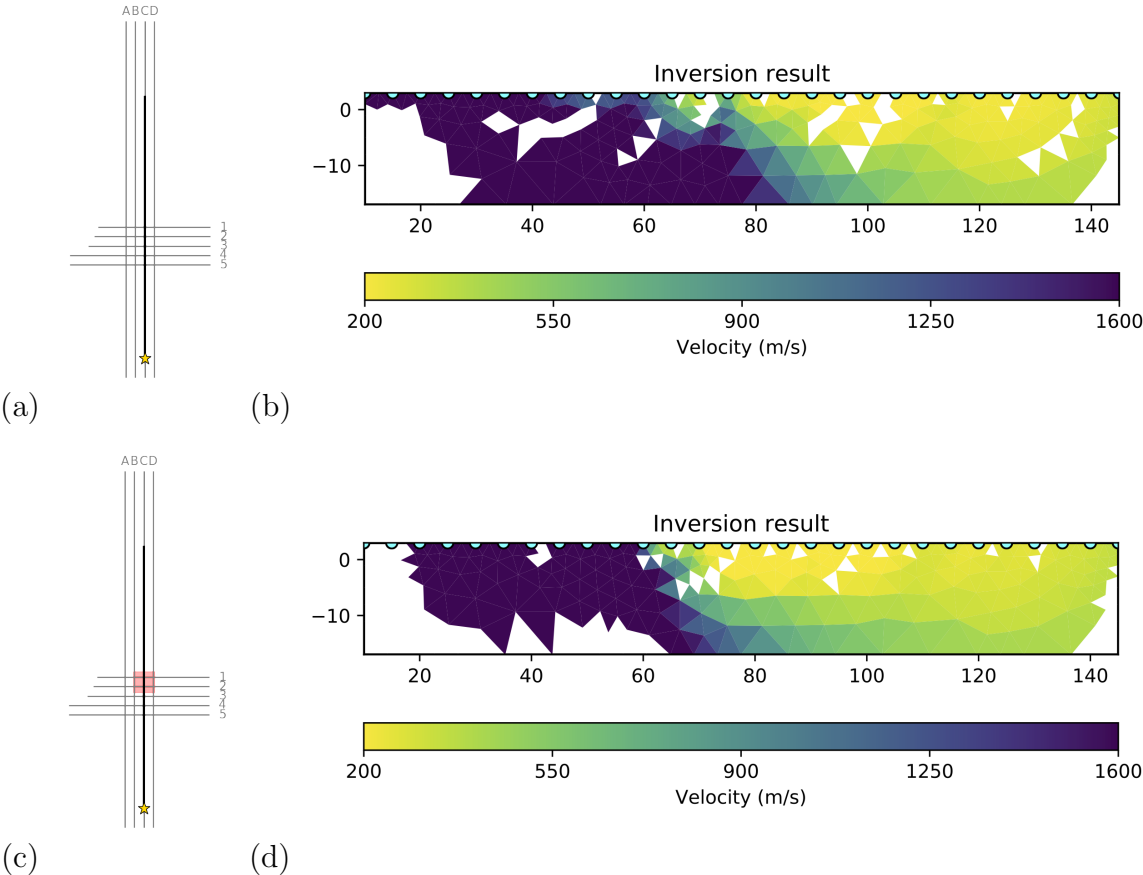
Figure 3.30: (a) Map of DAS Line C with virtual source to south; (b) Inversion result for straight-ray traveltime tomography of Line C picks for Aug-15 shown in Figure 3.29i. (c) Map of DAS Line C with heater array as red zone. (d) Inversion result for straight-ray traveltime tomography of Line C picks for Oct-03 shown in Figure 3.29i. The zone beneath the warming array has decreased in velocity, although there is a large lateral velocity contrast that is possibly an artifact of the ambient noise source field [Source: N.L.].
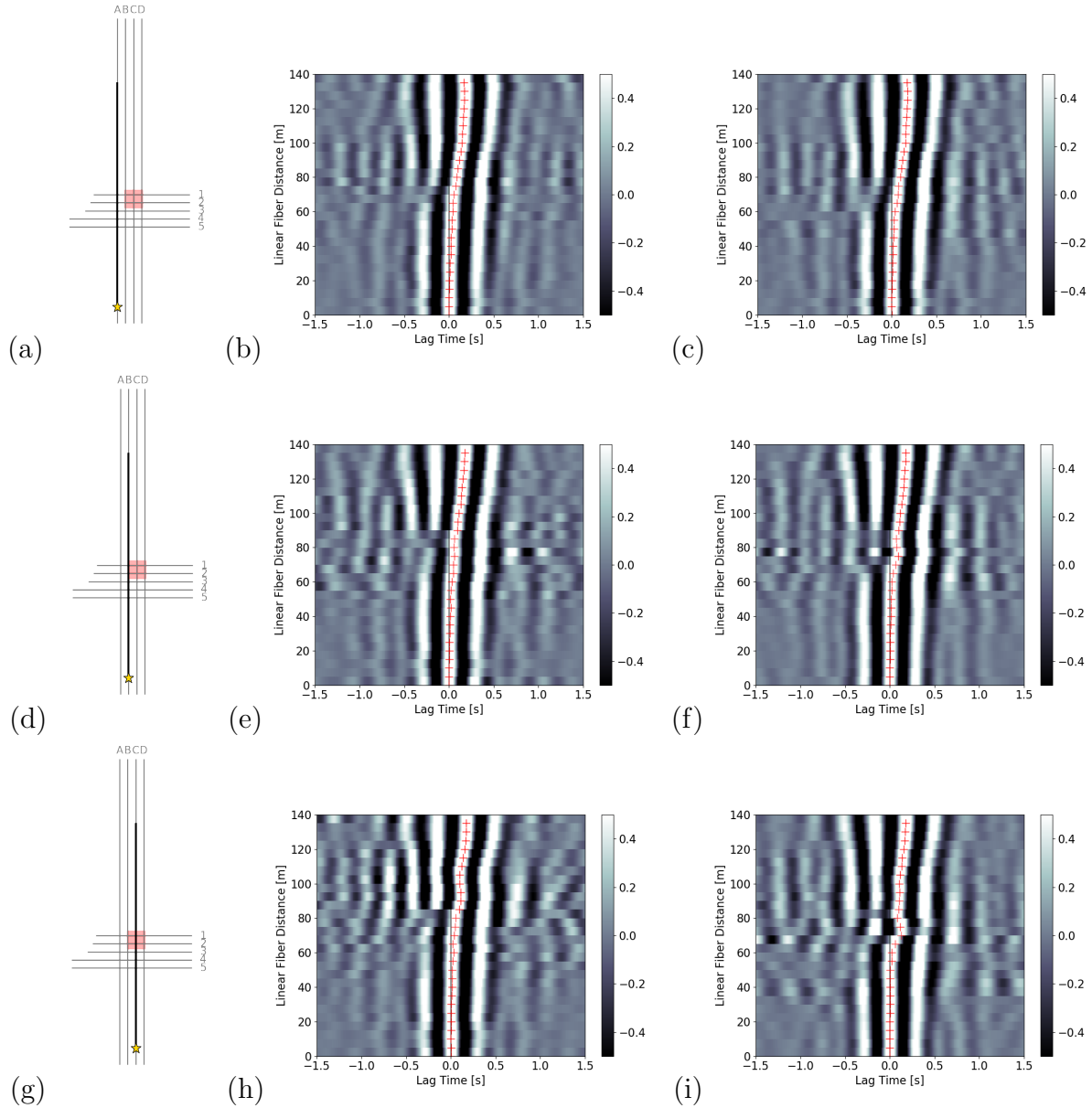
Figure 3.31: (a) Map of A with Vs=A-south and warming array; (b) Corresponding 2D NCF data from Aug-15-2016 with picks shown as red "+". (c) 2D NCF data from Oct-03-2016. (d) Map of B with Vs=B-south and warming array; (f) Corresponding 2D NCF data for B from Aug-15. (g) Corresponding 2D NCF data for B from Oct-03. (h) Map of C with Vs=C-south and warming array; (i) Corresponding 2D NCF data for C from Aug-15. (j) Corresponding 2D NCF data for C from Oct-03 [Source: N.L.].
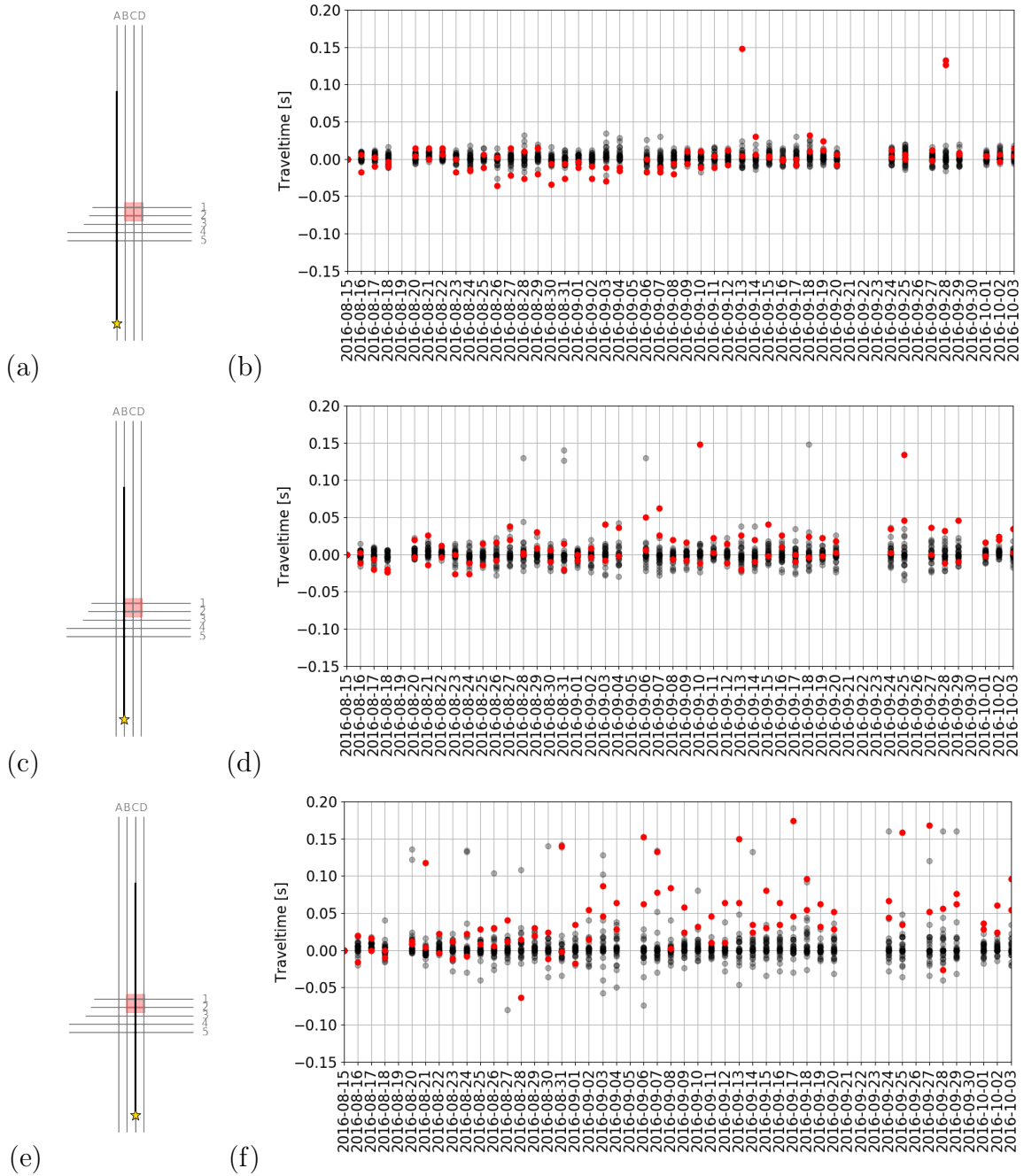
Figure 3.32: (a) Map of A with Vs=A-south and warming array; (b) SV refraction picks for all DAS channels on Line A plotted per day. Two channels at offset of heater array are plotted as red circles. (c) Map of B with Vs=B-south and warming array. (d) Same as (b) for Line B. (e) Map of C with Vs=C-south and warming array. (f) Same as (b) for Line C [Source: N.L.].

3.6 Discussion

3.6.1 Permafrost warming experiment

According to the results of the warming experiment, dense borehole heater arrays can be utilized to effectively thaw large zones of permafrost and trigger surface subsidence at a scale relevant to understand civil infrastructure performance, evaluate thaw hazard monitoring approaches, and validate numerical models of coupled processes in permafrost environments. While prior studies have generated subsidence through snow fences over multiple seasons, the present approach provides the practical advantage of a rapid timescale where permafrost thaw features operating at multi-decade timescales can be evaluated in a single field season. This approach thus provides opportunities to study and design systems that target the response to such processes, such as infrastructure retrofit and early detection systems. The heater array design, combining industrial resistive heaters housed in rugged well casings, was straightforward to install using a small direct-push rig and proved reliable over extended periods.

Multi-year and multi-decade Alaskan permafrost degradation monitoring (Liu et al. 2015) suggests that thawing the permafrost by 1 meter in this artificial experiment was the equivalent of secular warming of 2 - 10 decades with large uncertainty, or more appropriately a case of thaw slump thermal run-away. This is obviously unrealistic for accurately modelling the kinetics of permafrost thaw, but provides opportunity for experimental observation of secular permafrost degradation signals.

An outstanding question resulting from the early stage of this work is the concentration and asymmetry of the observed surface subsidence. The dominant known gradient at the site is the dip of the permafrost table, which deepens to the west and is close to the surface immediately to the east of the warming plot. We hypothesize that lateral variations in ice content, shown to be layered lenticular from nearby cores, generated this heterogeneity. Computed tomography (CT) scans of cores acquired at location OP4 reveal both laminar and more concentrated regions of ice-rich material; coring at alternate off-plot locations will be required to confirm the ice variability hypothesis.

To further evaluate the likely 3D temperature distribution of the site, a commercial finite-element thermal transport code (SVOffice5, SoilVision Systems Ltd.) was used to model a small portion of the heater array. We assumed a homogeneous soil column with a dry soil density of 800 kg/m^3, a thermal conductivity of 0.55 W/mK, and a 40% volumetric water content, broadly consistent with soil texture analyses conducted on archival core. Four heaters surrounding BH14 were modeled using known temperatures at the heater elements as Dirichlet boundary conditions. Surface temperature boundary conditions were also imposed to capture seasonal cooling effects. Figure 3.7b depicts the modeling results for both the baseline state (left panel A) and the thermal state at 14 weeks (center panel B). Predicted and measured temperature profiles at baseline, 4, and 14 weeks are also shown (right panel C). As can be seen, the measured data were closely matched given these relatively simplistic assumptions, which did not include advective heat transport, nor geomechanical processes

(e.g. subsidence). Most importantly, the predicted permafrost table ablation is reasonably uniform between heaters despite thermal gradients in the unfrozen soil column.

Several advantages of the deep warming approach should be mentioned. While the areal energy flux (55 W/m^2) used in this study is substantial, this relatively large input allows completion of subsidence studies in short periods, compatible with summer arctic field deployments. The use of borehole heaters installed at the permafrost table also enables energy to be directly delivered to the region of interest rather than heating a much larger volume of soil from the surface; a similar heating experiment using IR lamp arrays would have required a dramatically higher power consumption.

A final advantage to the instrumented deep thawing approach is the combination of control of input energy, measurement of internal/surface temperature boundary conditions, and spatial quantification of deformation, parameters required for validating coupled THM models currently under development. A variety of approaches have been considered but no field validation datasets at the decameter scale are available. As a result, validation often relies on a combination of analytical solutions, laboratory studies, and field measurement which often lack constraints on energy fluxes. We view this intermediate scale of thaw deformation test as a transformational step in confirming the validity of new solution schemes and permafrost constitutive models. We should note that the higher subsurface temperatures generated during rapid thaw experiments would complicate biogeochemical studies due to both the thermal scaling of chemical kinetics and rapid shifts in microbial population to a mesophilic domain; neither of these problems are present for THM model calibration and monitoring validation.

3.6.2 Ambient Noise workflow using vehicle noise and DAS

Analysis of the continuous DAS recordings of ambient seismic noise with frequency content in the 1 -40 Hz range produced along Farmer's Loop Road by passing vehicles provided evidence of the warming experiment time series. Despite observed spatial and temporal patterns of nonstationarity observed along the road and through the diurnal cycle, we retrieved stable results by averaging daily 2D NCF records evaluated across the warming area at a distance of 75 - 100 m away from Farmer's Loop Road. For the purposes of body wave analysis in the 2 -4 Hz range we were able to recover similar results with substantially less data by only stacking the times when the road had a medium level of activity as determined by the seismic power of a sentinel channel located on the Road Array.

The 24 hour window used in our workflow was overly conservative based on NCF convergence tests. An active source running at night meant that each 24 hour period was limited to actually only 20.7 hours of continuous ambient seismic noise. Although only approximately 6 hours of noise was required to achieve a 2D NCF where additional stacking made noticeably little difference to the results, stacking over 20.7 hours provided confidence that we were not biasing our interpretation by unforeseen source field variability. One consequence of this extended stacking approach is a coarsening of the minimum temporal window across which subsurface changes may be evaluated.

The location of the target thaw zone (the Warming Array) at a distance of about 100 m off of Farmer's Loop Road also had consequences. Ideally, we would have conducted a thaw experiment immediately beneath the line source of seismic energy, and while this would be the use case for this style of infrastructure monitoring it was impractical. As a result of the experimental geometry all seismic energy arrived from the road first at the Warming Array's west side and propagated eastward. Thus, the 2D NCF observations for the road perpendicular DAS fiber segments (Lines 1 - 5) were strongly one-sided, while road-parallel DAS segments (Lines A-D) were exceptionally fast. However, this apparent velocity distortion appeared to be relatively minor as the road perpendicular dispersion images still obtained realistic velocities for the unfrozen zone (180 - 500 m/s) and the road parallel 2D NCFs had positive move out unlike an earlier DAS trial experiment which was oriented along a road at an offset of about 25 m. One explanation for this result is based in the observations that there were stronger seismic noise produced in two road patches to the north and south of the latitude of the warming area, hypothetically caused by observed road topography. Hence, Farmer's Loop Road potentially acted like a line source with two strong source locations superimposed near the edges of the Fresnel zone for road parallel lines in the warming area. Although this bias is critical for imaging, when the goal is time-lapse monitoring the absolute velocity is unnecessary.

Data selection in the case of body wave imaging provided a means to mitigate the computational burden of processing every minute of the two-month experiment. The 'lookup table' method to evaluate the road noise using a single sentinel road DAS channel was convenient, but not readily generalized to other DAS-based imaging or monitoring experiments. A superior approach would involve use of an alternative array-based statistic, such as the power at a given backazimuth-slowness vector or a complementary data stream such as a video tracking of vehicles moving on the road. In this second approach, a statistic as simple as number of cars on the road each minute would likely be enough to classify the seismic data containing vehicle noise from the empty road background noise.

The use of DAS instead of geophones in this experiment meant an availability of more sensors. We processed data in 2D NCF arrays with a sensor spacing of 5 meters, which meant we were decimating the 1-meter recorded dataset by a factor of 5 and still using two points per 10-meter gauge length. Sensor density along the road and warming arrays enabled identification of source field differences along Farmer's loop Road, and smooth 2D NCF body wave picks. One consequence of DAS was that we interpreted our results in terms of shear wave velocity because of the orientation of the DAS sensor in the horizontal. There were also minor coupling differences between sections of the warming DAS array that may have been different if each sensing point had used a separately installed inertial geophone sensor.

3.6.3   Surface waves slowdown in silt during precipitation events

We observed a strong dependence of Rayleigh wave speed on soil moisture, driven by precipitation events at the site during the two month warming experiment. The slowdown

was as much as 3 - 6 % dv/v, and can be seen in both road parallel and perpendicular orientations.

If we consider the Aug-15 dispersion velocity model as a reference model, then these dv/v departures in Vs of +/-3% can equivalently be thought of as the upper unfrozen layer stiffening and softening with Vs=175 - 185 m/s. One possible explanation for this is that silt has low permeability and high porosity, hence the groundwater infiltrating during and immediately after major rain storms is held in the silt, which reduces shear modulus and leads to reductions in Vs. An alternative hypothesis is that the impermeable permafrost at a depth of about 4 m acts as an infiltration barrier, and thus the water must slowly drain laterally (very low permeability in silt) and/or dry-out from the top side.

This effect dominated the hypothesized observation of wave speed delay induced by permafrost thaw. Hence, we investigated a different seismic phase – refracted body waves – to study the thaw process, because body waves propagated deeper into the permafrost than Rayleigh waves trapped in the unfrozen zone.

3.6.4 Refracted waves slowdown during thaw

We observed a wave speed delay change in refracted SV waves during the thaw experiment. The change of 50 - 350% as measured relative to a 950 - 1400 m/s wave was observed along Lines C and Line B, but not along Line A, suggesting subsurface warming occurred inside the intended area with tangential effects in the neighboring zone <5 m from the perimeter heaters. We have confidence in this measurement because of the timing of the delay which does not begin until approximately Day 14 (Aug-20) of the experiment, consistent with preliminary analysis of surface orbital vibrator DAS refraction data. The wavefield appears to heal beyond the warming array because the change is occurring at the unfrozen/frozen layer interface over a relatively small zone, and therefore the refracted wave arrivals before or after the warming zone are not as sensitive to it.

The thaw delay analyzed for one virtual source location is not statistically significant until Sep-02 when it exceeds 0.025 s for the ray paths to the heater area. This is based on the traveltime variance of all ray paths. Additionally, there is a large scatter in travel times due to picking errors for this particular virtual source. By using additional virtual source positions we plan to reduce these uncertainties.

3.6.5 Experimental timeline of thaw and subsidence

Based on the one warming path used to analyze the body wave evidence of slowdown, the seismic evidence of thaw appeared no later than coincident with subsidence, and perhaps a few days before subsidence. Temperatures recorded by vertical thermistor sensor arrays in BH-14 and BH-21 in the warming area were observed to begin to increase within the first week of warming following Aug-05 initiation. By week 2 (Aug-20) the original unfrozen/frozen interface was warmed 3-5°C from its original temperature and the 0°C isotherm deepened 50 cm (more than 2 sensor levels). At the surface, subsidence was not apparent until Day

30 (Sep-04) when the two-point EDM survey registered greater than - 2 cm of change from baseline. 2cm is the measurement error of the EDM technique employed and thus is taken as the minimum threshold for statistical significance in this case. LiDAR scans of the site would provide sub-centimeter precision, however our experimental procedure did not allow for scans of the site with the required weekly frequency to provide such a constraint. Thus, if a seismological technique can provide evidence of subsurface warming before Sep-04 it is defined as a seismic precursor to thaw subsidence. As described in the preceding sections, the body wave refraction through the warming area registered a delay above the background variance on Aug-30, and thus we identify a seismic precursor. Soil softening has been observed in ultrasonic lab experiments and in

3.7 Concluding remarks

In conclusion, the artificial warming technique demonstrated in this study provides a methodology for field testing a wide range of future climate scenarios on permafrost behavior. In particular, similar systems could be utilized to test permafrost subsidence monitoring approaches as well as the performance of resilient or adaptive civil infrastructure in a warming Arctic.

Second, vehicle noise recorded along roads using DAS sensors embedded in horizontal trenches successfully recovered near surface changes in the unfrozen-frozen warming interface. To achieve this result we analyzed time-lapse deviations in daily averages of seismic noise correlations in linear arrays. Relatively high frequency (5 - 40 Hz) Rayleigh waves propagating at 200 - 600 m/s in the upper 4 meter thick unfrozen zone slowed down by 3 - 6 % dv/v after rainfall events, and required days to recover to the original velocity, likely because the permafrost acts an infiltration barrier. Faster refracted SV waves around 2 -4 Hz arriving around 950 - 1400 m/s before the surface waves provide a more robust indicator of the permafrost interface thaw process because they are less sensitive to the rainfall effect in the upper layer as a consequence of traveling through the top side of the permafrost. These body waves slowed more than 50% over the warming area before subsidence occurred.

This study is not complete. We have developed a methodology and experimental dataset to test the seismic precursor hypothesis, and identified its existence in body wave analysis. The remainder of the task involves replicating the time-lapse body wave analysis at additional virtual source positions across the warming array, and then statistically quantifying the thaw time line for the body wave observations.

Chapter 4

Earthquake Seismology

Summary Our understanding of subsurface processes suffers from a profound observation bias: seismometers are sparse and clustered on continents. A new seismic recording approach called fiber-optic Distributed Acoustic Sensing (DAS), transforms telecommunication fiber-optic cables into sensor arrays enabling meter-scale recording over tens of kilometers of linear fiber length. In this brief observationally-oriented Chapter, we analyze cataloged earthquake observations from four horizontal DAS arrays with different geometries for the purpose of demonstrating some of the advantages, disadvantages, and possibilities of using DAS as a tool for earthquake seismology. In Fairbanks, Alaska, we find that stacking ground motion recordings along 20 meters of fiber yields a waveform that shows a high degree of correlation in amplitude and phase with a co-located inertial seismometer record in a narrow frequency band, 0.8 - 1.6 Hz. Using an L-shaped DAS array in Northern California, we record the nearly vertically-incident arrival of an earthquake from The Geysers Geothermal Field and estimate its backazimuth and slownesses via beamforming for different phases of the seismic wavefield.

In a follow-on experiment located in Sacramento, CA, we utilize an existing but unused telecommunications cable to record earthquake ground motions related to regional and teleseismic earthquakes. We use this dark fiber experiment to investigate the sensible low frequency range of DAS. Recording of the M8.1 Chiapas, Mexico 2017, Sep 8th event over a 1 km aperature of the cable is found to recover energy from 1 - 100 s period (0.01 - 1 Hz). This suggests that DAS can be used to both record the arrival of short period seismic waves

like those used in an active oil and gas experiment, but also seismic waves that are relevant to crustal imaging and planetary interior research problems.

Key Findings

- Earthquake observations indicate DAS channel sensitivity is on order with a co-located inertial seismometer, but also has a higher noise floor, and directionality challenges, resulting in a lower overall signal-to-noise ratio.

- Telecommunication single-mode fiber, commonly installed underground in conduit, shows sensitivity to propagating seismic waves.

4.1 Background

Massive seismometer arrays in Large-N geometries have quickly become a fundamental tool for modern earthquake seismology (Brandon Schmandt and Clayton 2013; F.-C. Lin, D. Li, et al. 2013; Rost and C. Thomas 2002); however, such experiments are difficult to maintain over months to years (so-called "large-T"), especially in offshore and urban settings. Low-cost sensors and smartphone arrays have the potential to circumvent many of these logistical limitations, but are currently much less sensitive than seismometers (Kong et al. 2016; Laine and Mougenot 2014). Here we consider how a new type of seismic measurement approach, fiber optic based Distributed Acoustic Sensing (DAS), might be used in earthquake seismology to deliver meter-scale seismic wavefield information over tens of kilometers with a single instrument operating at one end of the fiber.

DAS repurposes standard telecommunication fiber-optic cables as a long series of single-component, in-line strain or strain-rate sensors, with sensing point separations as fine as 1 m or less. The DAS method employs a laser interrogator unit located at one end of the fiber whose purpose is to illuminate the fiber with short pulses and then perform high-rate optical interferometry of the Rayleigh backscattered light. Backscattered photons return to the interrogator unit at a time proportional to the linear fiber distance traveled by the photon. The retrieved phase-shift from interferometry is quasi-linearly proportional to the change in strain (Grattan and Meggitt 2000). This means that DAS essentially probes the motion of the entire fiber optic at each time sample. The time sampling corresponds to a minimum spatial sampling, called the gauge length of the system, which is often set around 8-10 m for seismic applications (Posey, G. Johnson, and Vohra 2000). For more details on DAS methodology see Chapters 2 and 5.

Fiber optics make ideal sensors because they yield inherently distributed measurements over tens of kilometers without additional components, while also using a sensing element that is inexpensive (on the order of $1 per meter), flexible (typical minimum bend radii are a few inches), and insensitive to electrical noise. Fiber is easily deployed in tight spaces and can be left in the ground virtually-undisturbed for large-T studies. An additional advantage is that the DAS interrogator probes the fiber sensing array from one end, meaning, for

example, that offshore seismic data would be available for rapid earthquake early warning with minimum data latency.

DAS technology has evolved in the oil and gas industry to solve a range of reservoir imaging and monitoring challenges, both onshore and offshore (T. M. Daley et al. 2013; Webster et al. 2013; D. Miller et al. 2016; G. Zhan, Kommedal, and Nahm 2015; Albena Mateeva et al. 2014; Verliac*, Lesnikov, and Euriat 2015). Applying DAS with to the problem of local, regional and teleseismic earthquake characterization requires different metrics, such as sensing ground motions that are characteristically lower amplitude and lower frequency content than active source methods. There is an additional complication of using horizontal fiber to detect earthquake wavefields where conventional earthquake seismology is based on three-compnent recording, or at least vertical component recording in the case of a single-component experiment. We study DAS sensitivity to incoming seismic energy from natural and induced earthquakes and the capacity of DAS to quantitatively characterize that energy. We utilize two different DAS instruments (Silixa iDAS, v.2; OptaSense ODH-3) and three 2-D horizontal fiber optic arrays of varying geometry to analyze seismic events (M 1.0 - M 5.8) at local to teleseismic distances. We compare DAS records with a co-located inertial seismmeter, and find comparable estimates of ground motion (acceleration vs. time), including body wave and surface wave travel time, peak ground acceleration, and coda envelope shape. We show how the array-nature of DAS, as opposed to a single seismic point sensor, enables identification of the backazimuth and slowness of arriving earthquake energy. One fiber array installed inside of telecommunications conduit demonstrates how existing fiber optic networks might also provide useful information, in spite of reduced signal-to-noise from ground coupling.

4.2 Data

Here we utilize earthquake recordings from DAS Experiments 1, 2 and 3 described in Chapter 1) and also from the Stanford campus array (Eileen Rose Martin 2018). To summarize, these experiments are all horizontal arrays in which a DAS instrument was connected to one end of a single-mode fiber that had been laid inside of a trench. As a result, we have in theory lower sensitivity to near-vertical incident particle motions present during P-waves.

As an aside, Lellouch et al. 2019 recently showed an interesting advantage of recording earthquakes in vertical well geometry, namely the applied to measure vertical velocity gradients from up/down wavefield separation of both the P-wave and S-wave. This represents an interesting use case of earthquakes in well-based DAS imaging experiments

The cables from Experiment 1 and 2 at the Richmond Field Station and the Fairbanks Permafrost Research Station were directly buried using a small ditch witch and backfilled by hand, while the cable in Experiment 3 and Stanford were pulled through a plastic composite conduit which is in contact with the surrounding soil. The presence of a conduit and installation mode will be explored, but likely damp or otherwise reduce the strain transferred to the fiber-optic sensor. The Silixa iDAS, v.2 was used to record data for Experiments 1, 2 and 3.

An OptaSens ODH-3 instrument was used to record data at Stanford. No direct instrument comparisons are available at this time, nor is there information available about instrument response details in absolute units (as opposed to a few signal-to-noise ratio comparisons made at different wells). Below we add a few additional details about each experimental dataset. In the case of Experiment 1 and 2, DAS data were collected as continuous strain-rate measurements at 1000 Hz at a 1 m channel spacing with a 10 m gauge length along the fibers. For Experiment 3, because the cable was so long, we reduced the temporal sampling rate to 500 Hz and the channel spacing to 2 m, but again strain-rate data were collected. The Stanford DAS data were written as phase before being converted to strain, and used a 50 Hz sampling rate with a 7.14 m gauge length and 8.16 m channel spacing.

In Experiment 3, we demonstrate the application of DAS utilizing dark fiber for measurement of seismic wavefields at the sub-basin scale with an extremely fine spatial sampling (2 m) over long time periods. We utilized dark fiber components of ESnet's Dark Fiber Testbed. ESnet, a US Department of Energy (DOE) user facility, provides high-performance unclassified network infrastructure to connect DOE research sites including high performance computing (HPC) facilities and data-intensive instrumentation e.g. x-ray, neutron, and nanoscience facilities. The Dark Fiber Testbed is a 20,920 km (~13,000 mile) network of short and long haul telecommunication fiber designed for testing novel network communication equipment and protocols. The network consists of single mode telecommunication fibers of varying age and installation technologies and hence is an excellent proxy for existing commercial network components. This study is one of the first experiments that utilizes this massive network for sensing purposes. Figure 4.2A, depicts the long haul regional sections of the Dark Fiber Testbed in California, as well as the segment exploited for our test (4.2B), which runs from West Sacramento, CA to Woodland, CA.
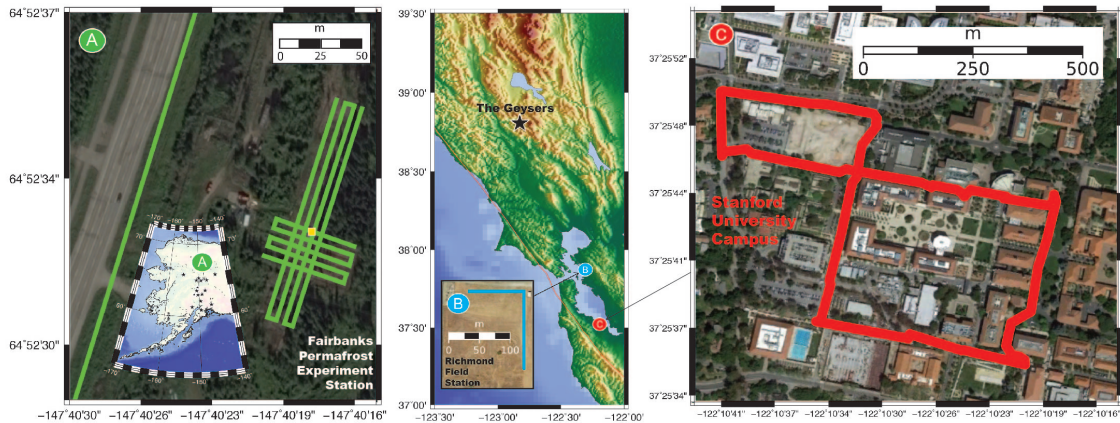
Figure 4.1: Color-coded fiber-optic array maps used for the experiments at (A) The Fairbanks Permafrost Experiment Station, AK, (B) Richmond Field Station, CA, and (C) Stanford University, CA. Colored lines indicate fiber cables directly installed in shallow trenches or conduit. Figure 2 and Figure 4.4 used data recorded at the intersection of the two orthogonal lines in (A) where a Trillium Posthole Compact 120-second inertial seismometer was installed (gold square). Regional maps locate the arrays with respect to observed earthquake epicenters (black stars), including the site of The Geysers Geothermal Field used in Figure 4.9.
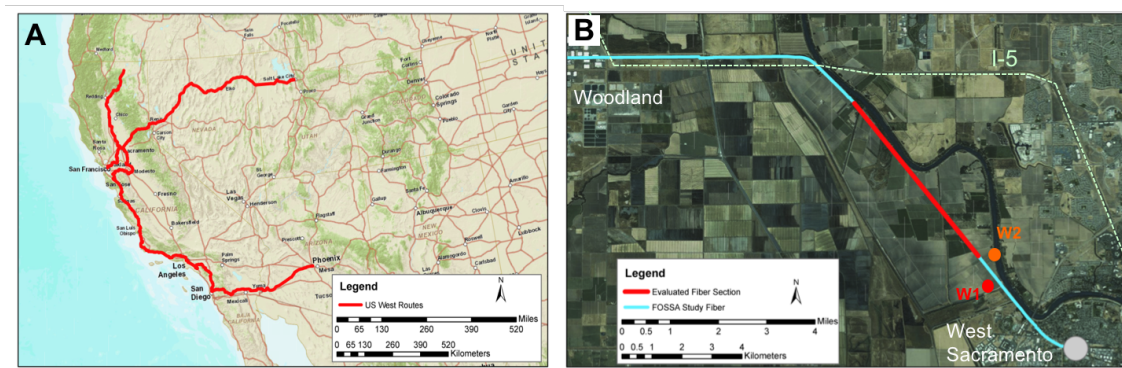
Figure 4.2: Map of a section of the ESNet Dark Fiber Testbed (https://www.es.net/network-r-and-d/experimental-network-testbeds/100g-sdn-testbed/terms-and-conditions/). (A) Regional network; zone of panel B shown in black dashed box. (B) Network subsection used in this study. The study fiber (blue) is approximately co-linear with an active rail line. Dashed green line labeled I-5 is Interstate 5, a major source of ambient noise beyond the rail corridor.

4.3   Results

4.3.1   Regional earthquake observations

Figure 4.3a shows example DAS recordings of the 26-Aug-2016 M3.8 Central Alaska earthquake observed by 160 channels over 160 meters, or one NE-SW trenched segment, of the Fairbanks, AK fiber-optic DAS array. This earthquake occurred approximately 150 km SSW of Fairbanks. Main P- and S-wave arrivals are clearly registered above the noise level on the DAS. 10 m average trace stacks are plotted on top of the image. Figure 4.3b compares the normalized Fourier amplitude spectra for a four-minute window of DAS data around the event and the background noise level recorded during a four-minute window without an earthquake. Figure 4.3c shows the equivalent Fourier amplitude spectra for a horizontal component of the co-located seismometer. For the DAS instrument, signal amplitude in the 0.5 - 2 Hz band rises approximately one order of magnitude above the noise. At frequencies lower than 1 Hz and higher than 10 Hz the sensitivity of the DAS measurement falls off more steeply than the inertial sensor, but is still above the noise level. The stacked DAS data shows a modest gain in signal-to-noise ratio above the single DAS channel measurement, particularly at longer periods where the incident seismic wavelengths are more coherent.

Figure 3 compares DAS and inertial seismometer waveform records for the 26-Aug-2016 M3.8 Alaska Range earthquake. Raw iDAS strain-rate amplitudes were converted to equivalent phase of acceleration prior to filtering. A triaxial Nanometrics Trillium Posthole Compact 120-second inertial seismometer was buried at a depth of 1 m at the intersection point of two orthognal fiber-optic lines to provide a co-located ground motion estimate. The two horizontal components of the seismometer were mathematically rotated into the two fiber array directions, prior to removing the instrument and digitizer responses. Bandpass filtering was applied to the inertial and DAS records is zerophase, two-pole, and applied to the records in the same way. For this earthquake backazimuth (200 degrees SSW), the two trenched fiber directions, NNE and ESE, approximately decompose into radial and transverse ground motion orientations. To compute a seismometer-equivalent ground motion using the DAS records, we applied a median stack to 20 fiber sensing points (1 channel per meter) in each of the two fiber directions centered on the inertial seismometer location, prior to applying the bandpass filter described above. The DAS stacked traces were then normalized to the peak amplitude of the seismometer data by component – equivalent to applying a uniform sensor gain with a factor of approximately five.

We find nearly equivalent phase estimates of main body wave arrival times, peak ground acceleration values, and coda shape between DAS and seismometer, however there are important differences. P-wave phases are not recorded with the same fidelity as S-wave and surface wave phases, and many other phase arrivals are not recorded by the DAS as well as the inertial instrument. The dominant factor may be that DAS measurements on horizontal fibers have minimum (theoretically zero) sensitivity to vertically-incident P-wave energy, and fall-off steeply with azimuth when compared with traditional seismometer component sensitivity (Kuvshinov 2016). Soil coupling differences likely also play a role. The way a
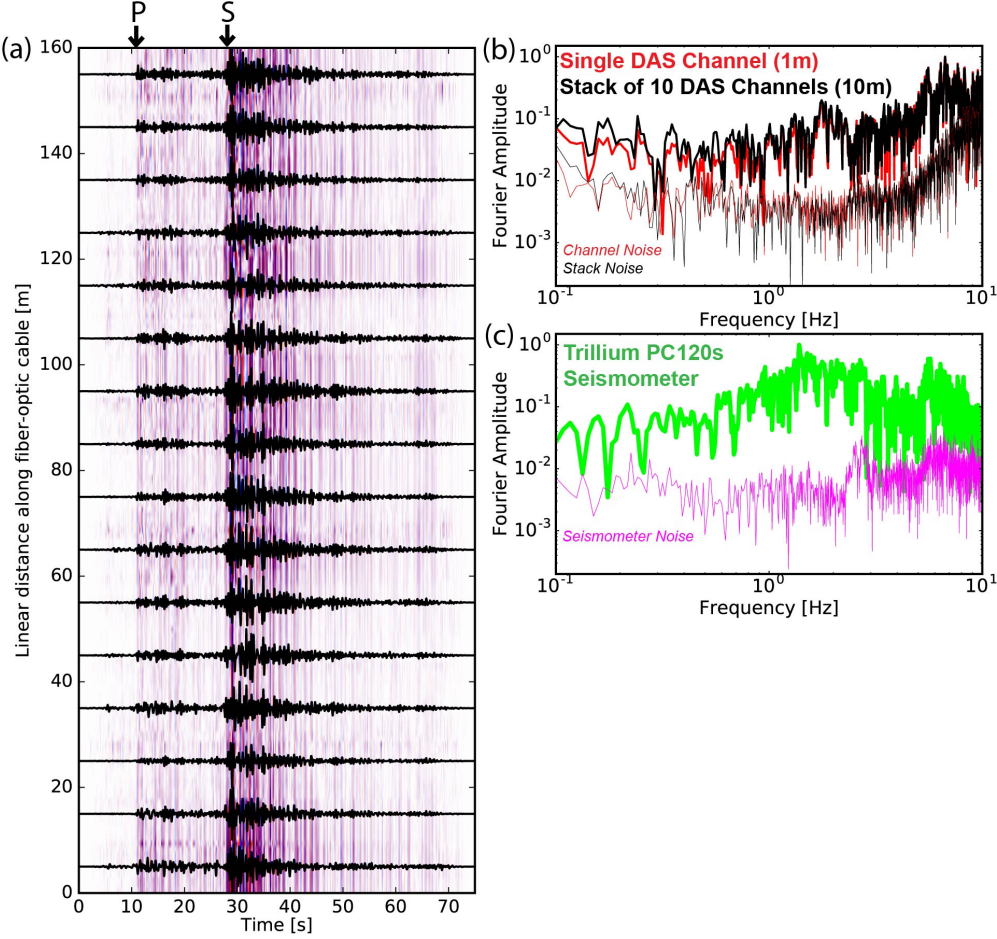
Figure 4.3: Example Fairbanks DAS array recording of the 2016-08-26 M3.8 Central Alaska earthquake (distance= 150km). (a) DAS data from a trenched 160m long fiber with a 1m channel spacing recorded with a 10m gauge length, overlaid with 10m averages (black traces). Filtering is zerophase, four corner, 0.5-2 Hz bandpass following detrending and edge-tapering. Main P- and S-phase arrivals are labeled. Spatial signal variability of individual traces may indicate near surface site response or uneven sensor coupling. (b) DAS Fourier amplitude spectra from a four-minute time series around the earthquake signal (thick lines) compared with a background noise window (thin lines) measured by one DAS channel (red) and the 10-channel DAS stack. Spectra are normalized to the single DAS channel peak signal value. (c) Signal and noise as in (b) for the horizontal channel of a co-located Trillium Posthole Compact 120-second inertial seismometer. Spectra are normalized to the peak signal value of the seismometer.
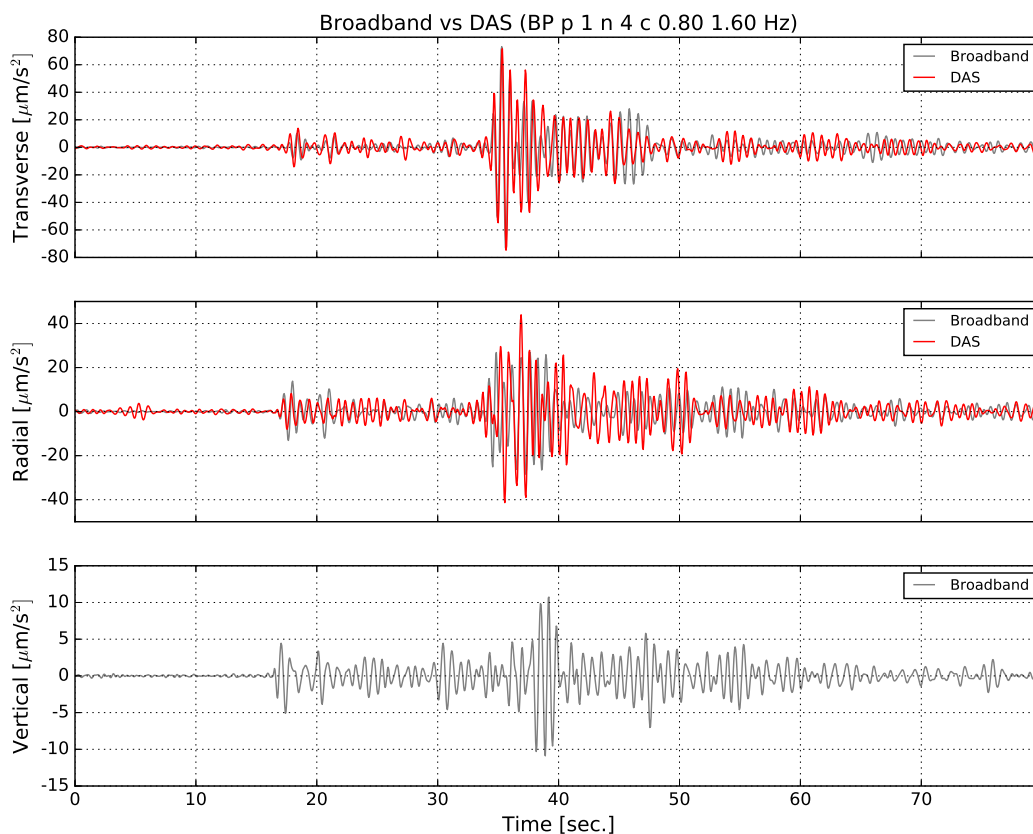
Figure 4.4: Normalized comparison of earthquake ground motion phase (2016-08-26 M3.8 Central Alaska) recorded by the Silixa iDAS (red, horizontal components only) with fiber installed horizontally in two orthogonal trenches and a colocated Trillium Posthole Compact 120-second inertial seismometer (black, 3C), the location of which is shown in Figure 4.1A. Distributed fiber optic records in transverse (Top) and radial (Center) directions were gained to peak sample of seismometer (a factor of ~5), and then averaged over 20m (1 channel/m) centered on the location of the seismometer shown in 4.1A using a median stack. The two horizontal seismometer components were rotated into the fiber array directions, following removal of the instrument and digitizer responses. A zero-phase four corner bandpass filter was applied in the 0.8-1.6Hz range.

well-coupled inertial seismometer responds to ground motion is well-characterized, but how that ground motion strains a shallowly-buried fiber optic cable and how the strain on the outer cable jacket couples into the actual strain imposed on the fiber optic sensor inside the cable package is less understood. Despite these considerations, our observations suggest that the information required for earthquake detection and hypocenter relocation, traveltime tomography, phase velocity studies, and many other flavors of seismology could use inexpensive DAS just as well as an inertial type sensor to study this particular event in the frequency range shown (0.8 - 1.6 Hz).

After the network geometry was established, DAS signal strength, amplitude, and periodicity were examined to evaluate noise characteristics along the array. Dominant noise features include several regional highways, diffuse urban noise, and energy from local railroad activity. Qualitatively, the highest quality data was observed on a straight section of fiber starting beyond West Sacramento and extending to the noise field of Interstate 5, shown as the highlighted red profile in Figure 4.2B. Zones to the Southeast of this section suffered from non-optimal installation conditions (e.g. the fiber was attached to surface structures including a bridge) as well as incoherent noise in the urban transition zone around West Sacramento. Zones to the North and West suffered from both optical fading, insufficient return photons which decreased measured S/N, and broadside noise interference from Interstate 5. This illustrates the potential heterogeneity of signal quality across the existing telecom network.

We hypothesize that the method of installation (direct-burial, single conduit, conduit inside a larger conduit, conduit attached to infrastructure) has a significant effect on DAS recorded ground motion (see Figure 4.11). The fiber-optic cable itself (gel-filled, aramid wrapped vs. loose-tube, polyethelene-jacketed vs. steel-armored, polyethelene vs. steel exterior) has each been shown to have only a small effect on recording quality at high frequencies (Dou et al. 2017).

4.3.2 Teleseismic earthquake observations

Waveforms

Seismic network detection thresholds are highly heterogeneous, even across regions known for dense seismic monitoring like the western United States and Japan (Wiemer and Wyss 2000; Nanjo et al. 2010), in part because broadband seismic stations are sited in hard-rock locations where background noise is low (Pasyanos, Dreger, and Barbara Romanowicz 1996; B Romanowicz, Gee, and Uhrhammer 1992). Areas of less-competent geology, like sedimentary basins, therefore correlate with poor catalog completeness; the magnitude of completeness is Mc ~ 2 – 3 in the Sacramento and Southern San Joaquin Basins compared to Mc ~ 0.5 – 2.4 in the San Francisco Bay Area or Mc ~ 0.5 – 1.8 in Southern California (Felzer 2008; Hutton, Woessner, and Hauksson 2010). Thus, despite the greater Sacramento area hosting significant gas production, underground gas storage, and high-volume waste water disposal, all of which can impact seismicity, the Sacramento Dark Fiber DAS array is located
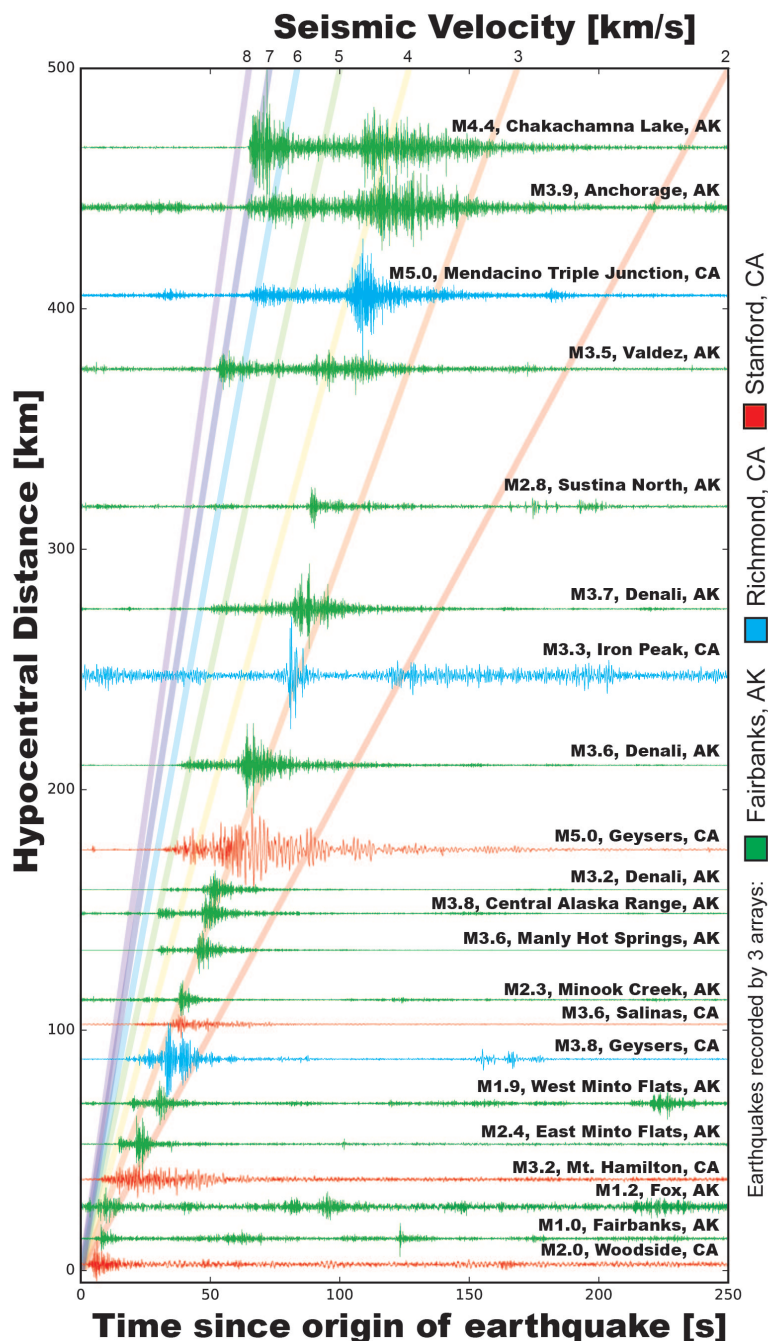
Figure 4.5: Composite catalog of fiber-optic earthquake observations plotted as a function of hypocenter-array offset. Seismic traces are color-coded by array of observation (green=Fairbanks; blue=Richmond; red=Stanford). Bandpass filtering was applied around 1-5 Hz. Seismic velocity values are shown for reference.

30 km away from the nearest networked short-period seismometer (NDH) and 62 km away from the nearest broadband seismometer (AFD).

A relevant question when examining seismic events on telecommunications networks in contrast to fit-for-purpose installations is the impact of installation conditions. As recently demonstrated (Nathaniel J Lindsey et al. 2017; Eileen R Martin et al. 2017; Jousset et al. 2018), fiber installation in a standard plastic conduit does not preclude sufficient sensor coupling required for the detection of earthquakes, but the case of recording DAS data with repurposed telecommunications fiber is yet untested at regional scales. To explore this question with the Sacramento Dark Fiber DAS experiment we extract raw strain-rate waveforms for major global and regional earthquakes that occurred during the continuous recording interval (Figure 4.7). We again use the linear quiet portion of the array shown in Figure 4.2B and process the data by averaging 100 seismic traces (200 m section) and applying a bandpass filter to isolate the appropriate earthquake signals. To plot the raw strain-rate data in a more familiar unit we multiplied the data by a reference length equal to the gauge length (10m) to convert to a unit that is proportional to velocity. We observed broadband DAS sensitivity to ground motion from earthquakes of varying magnitudes (M4.4 – M8.1) and distances (100 – 7757 km). For example, in the case of the M7.5 Honduras event there is clear evidence of short period body waves and longer period surface waves over the two hour window following the origin.
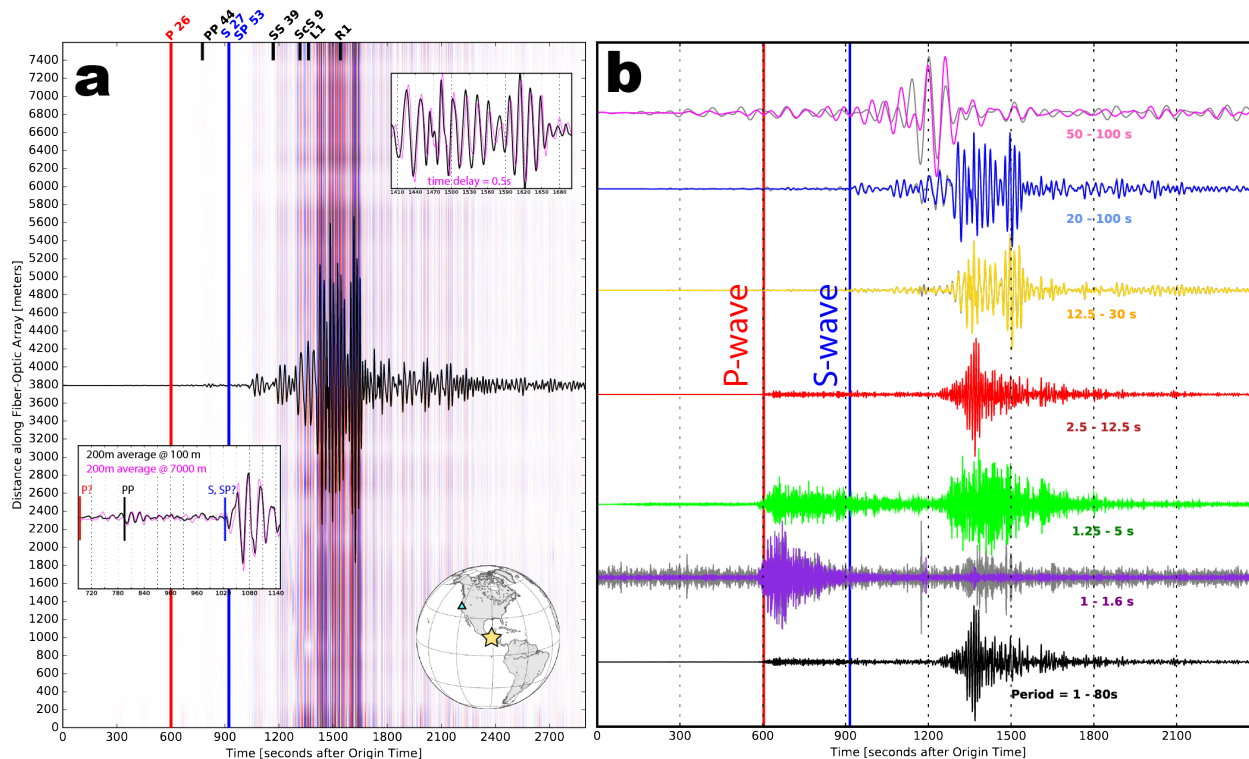
Figure 4.6: Teleseismic DAS recording of the M8.1 Chiapas, Mexico 2017-Sep-08 earthquake. (a) Seismic data for [black trace] one location and [red and blue] all locations from 0.0-7.6 km at a 2 m spacing (4001 traces total); top right inset shows surface waves arriving at the [black] south and [pink] north end locations of the array (backazimuth   120o), bottom left inset shows body waves arriving coincidently at both locations. A two-corner, zerophase, f= 0.01 – 0.5 Hz bandpass filter was applied. (b) Stacking 400m or 200 consecutive DAS channels, color-coded by the bandpass filter applied to emphasize the broadband observation (1-100 seconds). Gray background traces show the single trace recording for cases that make a significant difference. Each of the traces is normalized to peak amplitude.

Spectra

While long period sensitivity is a major limitation of many inertial seismic sensors (e.g., accelerometers, short-period geophones, smartphone sensors), the long period response of DAS is currently a topic of active research with only limited available data (Becker, Ciervo, M. Cole, et al. 2017; Becker and Thomas Coleman 2019); teleseismic earth motion (strains near 1×10^{-8}), for example, may be dominated by thermal expansion of the fiber-optic cable (strains on the order of 1×10^{-6}) depending on the frequency studied as well as the depth, composition, and condition of the fiber-optic cable and conduit. Recent studies (Becker, Ciervo, M. Cole, et al. 2017) have used shallow hydrogeologic pump tests in a well with a fiber-optic cable to show that DAS has sensitivity to 9.4×10^{-3} Hz (period = 1080 seconds) oscillations in strain induced by the variable confining pressure, presumably due to Poisson effects. This subject is complicated by the known directionality of DAS cables (Kuvshinov 2016; X. Wu et al. 2017), which for the horizontal geometry of telecommunications dark fiber cables is theoretically insensitive to vertically-incident compressional motion (P-waves).

To explore the long period sensitivity of the Dark Fiber DAS array to teleseismic events, we extract raw strain-rate seismograms from the largest earthquake recorded during the experiment, the M8.1 2017-Sep-08 Chiapas, Mexico earthquake (Figure 4.6). We observe broadband dispersive surface waves with strong energy at periods from 50 – 100 seconds. P-wave signal amplitude is lower than S-wave amplitude, perhaps because the sensor has minimal sensitivity to compressional particle motions for waves with incidence angles approaching 0° with respect to vertical (i.e. perpendicular to the fiber "broadside arrivals"). Nonetheless, the arrival times of major seismic phases are detected because of free surface scattering. Incidence angles of seismic phases are given in Figure 4.6A. Differences in incidence angle also likely affect recorded amplitude, and appear to result in more coherent surface wave arrivals across the array (incidence angle=0°) and as much as a 0.5 second delay time across the record section.

4.3.3   Event detection

In an urban setting like Sacramneto, CA, the level of ground noise commonly exceeds the conventional level of site noise McNamara and Buland 2004. Telecommunications cables are commonly routed along railways, roads, and through high noise urban areas. We find that major regional earthquakes ($M \approx 4$) generate ground motions on the Sacramento array that have equal or lesser amplitude than local moving vehicles, however anthropogenic seismic signals typically are dominant in a higher frequency band (5 – 30 Hz). Figure 4.8 shows two examples of the site noise along the Sacramento DAS experiment at the time of two regional earthquakes (M4.22 Geysers 2018-Jan-18 and M4.38 Berkeley 2018-Jan-04). The background noise is mostly due to cars and trucks driving along River Road northwest of Sacramento, south of I-5. This noise has energy in the frequency range 1 - 40 Hz, but are characterized by symmetry in the time domain as the vehicle approaches and then moves away from the sensor. The two earthquakes were found to have similar ground motion amplitudes to the
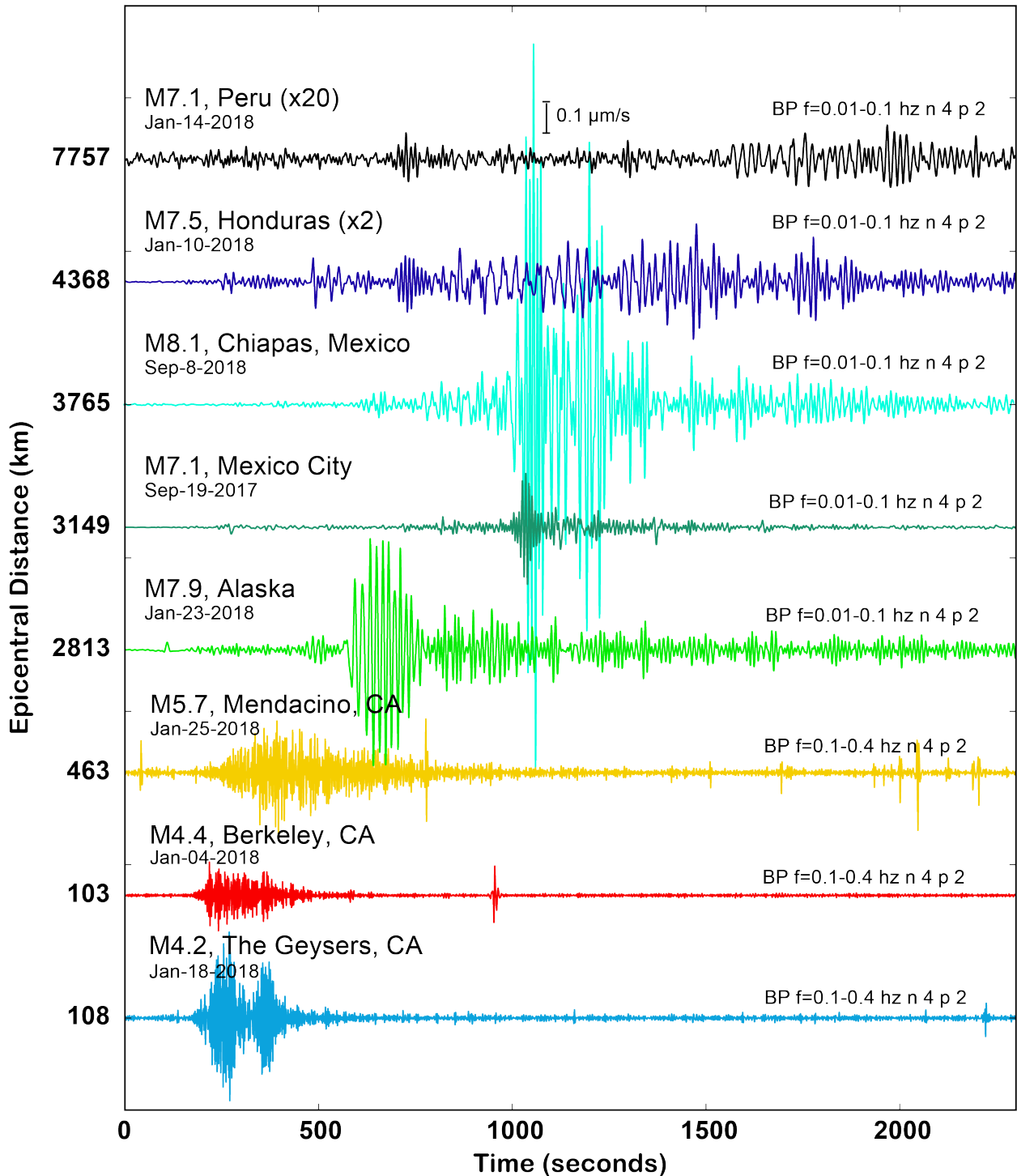
Figure 4.7: Example earthquakes recorded by the Sacramento Dark Fiber DAS array. The recorded data are plotted as strain-rate after multiplying by the gauge length (10 m) to convert to units proportional to velocity (1e-6 m/s), and have been averaged over 100m of linear fiber length (50 traces) and then bandpass filtered in the 0.1-0.4 Hz range for regional events, and 0.01-0.1 Hz for teleseisms. Events are sorted by increasing epicentral distance from Sacramento. Earthquake amplitudes for the Peru and Honduras events are scaled by the factors in parentheses.

largest vehicles but can be detected by their impulsive waveform in the time domain. Higher frequencies of interest for local small magnitude and microearthquake analysis (f $\leq$ 50 Hz) are not expected to be as easily separated.

The two earthquake records shown in Figure 4.8 differ in peak strain-rate ground motion amplitude by more than a factor of 2 different despite having been generated in similar sized ruptures and traveling similar distances to the fiber in Sacramento. This may be due to source rupture depth differences (z=2.4 km for The Geysers, z=12 km for Berkeley), but we should expect the shallower of the two events to generate more surface waves. Opposite observation if that were the case, or the major differences in geologic structure along the raypath, but could also be the result of strong DAS axial sensitivity to energy in the direction of the fiber axis. Orientation of the earthquake and the sense of fault motions with respect to the DAS fiber axis are also important to DAS event detection, because the sensitivity to arriving motion falls off with angle from the axis of the fiber like $\cos^2(\theta)$ for compressional waves and $\cos(\theta)\sin(\theta)$ for shear motions. For example, in Figure 4.8, two events are shown with similar offsets to the Sacramento DAS array, however The strike-slip focal mechanism of the Berkeley M4.4 event radiated shear waves (SH and Love waves) that were $\sim 20 - 30^o$ out of maximum sensitivity for the NW-SE oriented DAS array in Sacramento, while the oblique normal faulting M4.2 event in The Geysers produced a shear wave radiation pattern with a minimum amplitude node near the fiber axis. P-wave ground motions were not strongly recorded by either event due to the horizontality of the array. See Chapter 2, Figure 2.8 for details about DAS sensitivity to ground motion with azimuth.

4.3.4   Array beamforming

The availability of a single-instrument array measurement with DAS, as opposed to a single point inertial sensor, introduces the opportunity to record information about the propagation backazimuth and slowness (1/apparent velocity) of the seismic wavefield.

Figure 4.9 showcases this concept using a small DAS array that was installed in 2014 at the Richmond Field Station (RFS) in Northern California. As outlined in Figure 4.1b, fiber optic cables at Richmond Field Station were directly buried at 0.5 m depth in an L-shaped horizontal trench measuring approximate 100 m on a side (Dou et al. 2017). The trench was backfilled with the excavated soil using hand tools. A Silixa iDAS instrument with a 10 m gauge length and 1 m channel spacing was used to make continuous DAS measurements at a 1000 Hz sampling rate.

Using 192 DAS channels from the RFS DAS array recording of the 2016-04-08 M3.8 Geysers Geothermal Field earthquake we perform a frequency-domain grid search over possible values of backazimuth and slowness to compute the beam solution (i.e., the peak energy estimate given the data) for various seismic phase arrivals. The frequencies used in this calculation ranged from 0.25 Hz to 1 Hz. Beamforming results for different time windows are shown as individual heatmaps in Fig 4.9 beneath the seismograms. Arriving phases register opposite polarity signals on orthogonal fiber segments for approximately co-located channels (see Supplementary Materials), thus we apply a polarity flip to one of the array
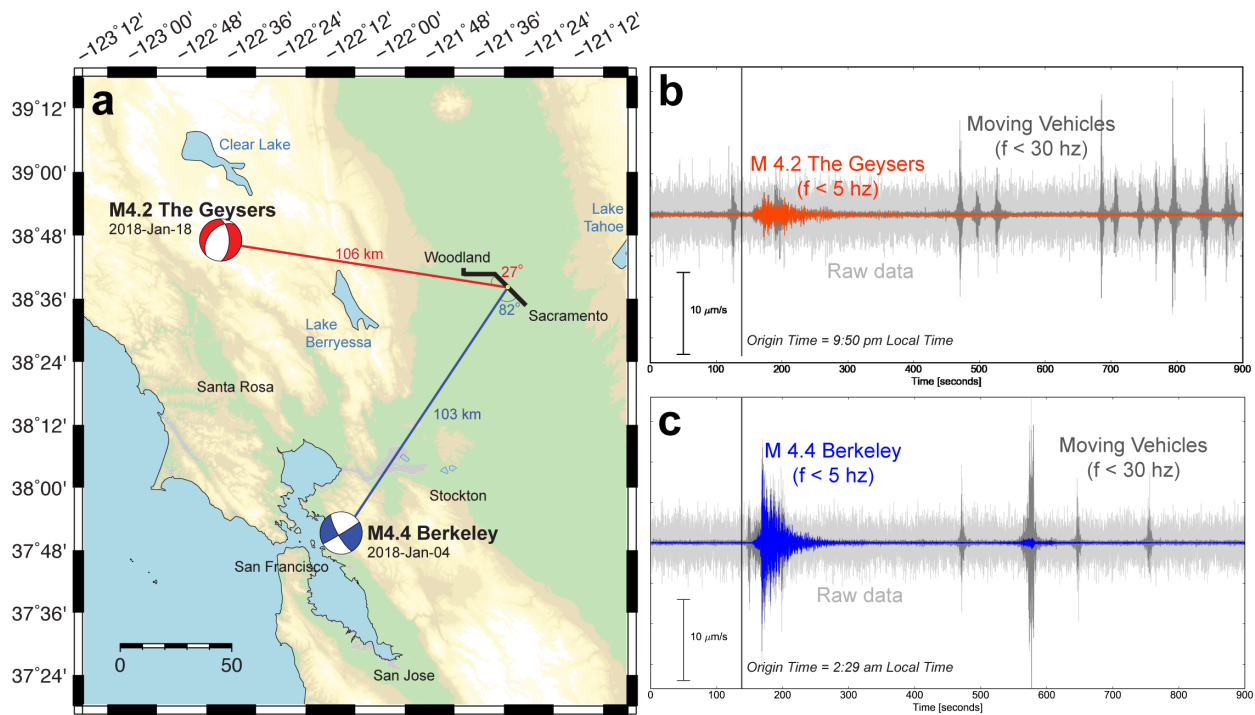
Figure 4.8: (a) Locations and focal mechanisms of the M4.2 2018-Jan-18 Geysers (red) and M4.4 2018-Jan-04 Berkeley (blue) earthquakes, which occurred approximately 100 km from the Sacramento Dark Fiber DAS array (black line). (b,c) Raw and lowpass filtered DAS strain-rate waveforms for these events averaged over 100 m (50 channels) at the yellow circle position shown in (a) (channel 4975 +/- 50 channels). Note the similarity between seismic and non-seismic signal amplitudes and the differences in frequency content.

components during preprocessing. Linear subsets of north-south or east-west traces provide poor constraint on the earthquake beam, however, when all 192 DAS traces are employed we find good agreement with 1-D theoretical ray tracing predictions.

Generally, the RFS DAS array beamforming of the M3.8 Geysers earthquake record shown in Figure 4.9 accurately estimates values of backazimuth and slowness. For example, the observed P-wave beam is found to have vertical to sub-vertical incidence (¡10 degrees with respect to vertical), and later arriving s-P and S phases shallow toward 65 degrees with respect to vertical. However, some details of the beamed result are not explained by the predictions.

The most prominent observation is that the P-wave distribution of energy in the beam spreads out in both the east and north directions. Considering the beam energy as the uncertainty in backazimuth, the reader may infer that the DAS array may not be doing a good job because the true backazimuth is to the NW. Such an error could be due to the DAS array geometry, fiber-optic DAS directionality of the sensor, or seismic wave propagation effects
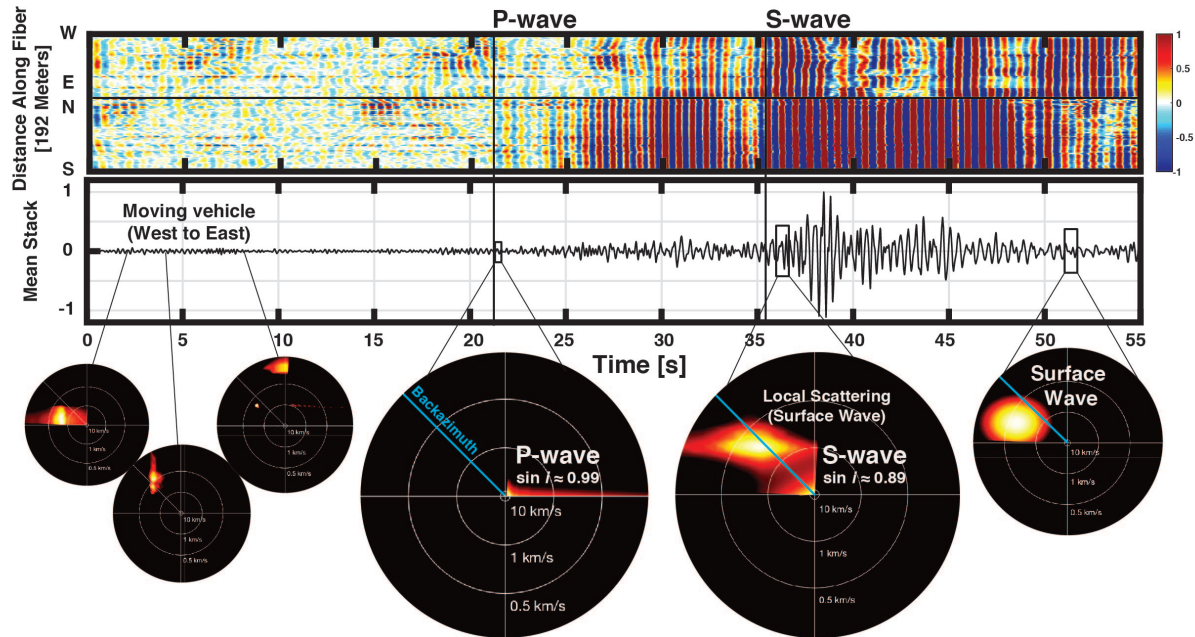
Figure 4.9: Beamforming the 2016-04-08 M3.8 Geysers, CA earthquake observation on the Richmond, CA DAS array. (Top) The full 192 seismic array recording shown in Figure 4.1B from west-east and then north-south. Bandpass filter is in the range 0.25 - 1 Hz. (Center) Stack of the seismic array records shown. (Bottom) Polar diagrams showing the peak beam as a function of backazimuth and slowness for different windowed times corresponding to (in order, right-to-left) a moving vehicle, the main P-wave arrival, the main S-wave arrival, and subsequent seismic phase arrivals. The blue lines one each beam plot show the backazimuth to The Geysers Geothermal Field, approximately 315 degrees (see Figure 4.1B).

like P-to-S scattering at the surface, multipathing, and/or 3-D velocity structure. Figure 4.10 shows the modeled array response for the Richmond Field Station array assuming each meter of the fiber optic cable is a separate sensor without directionality sensitivity. Theoretical slowness predictions are shown in Figure 4.10b, which enlarges the center part of Figure 4.10a. All theoretical P-wave energy lies within the maximum power response for this array, and therefore this array geometry if believed to have good coverage for the slowness and frequency considered. Note that the L-shape of the array is responsible for the elongation of maximum power in the SW-NE direction. Seismic wave propagation effects are likely given the structural complexity of the San Francisco Bay and the high frequency considered in this example.
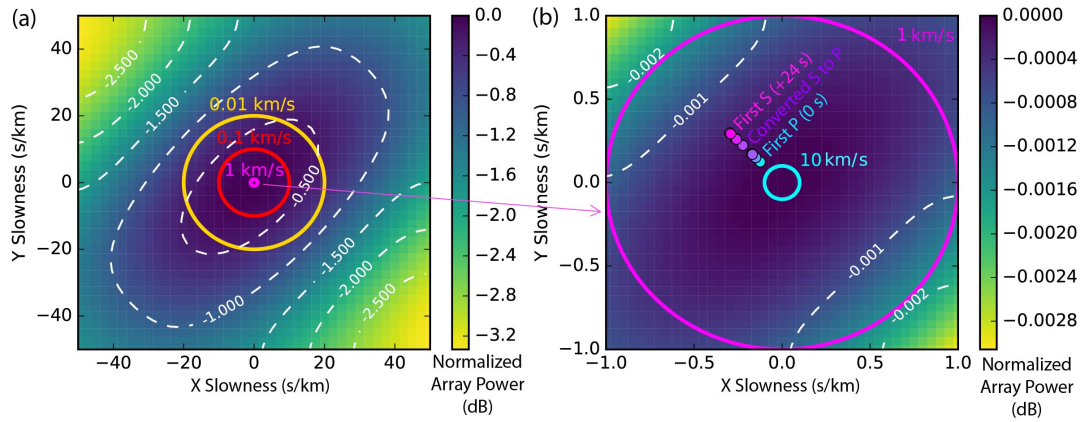
Figure 4.10: (a) Array response for Richmond Field Station (f = 0.5 - 1 Hz). White contour lines describe array power at points in X-Y slowness space. Concentric colored contours describe arbitrary values of apparent velocity in this space. (b) Zoom of the center of (a) showing predicted beam values based on a 1-D straight-ray theoretical iasp91 model path between the Geysers, CA and Richmond, CA. The predicted backazimuth is 314.55 degrees for all phases. The first P arrival is predicted to have a high incident angle very near to vertical (88 degrees), and later arriving seismic energy should have higher slowness values.

4.3.5 Empirical evaluation of installation geometry

Installation information for the Sacramento Dark Fiber DAS array provides clues as to the heterogeneity of fiber-soil coupling across our experimental profile. Cable installation occurred in 1999-2000. Most of the fiber was pulled through one of 12 high-density polyethelene (HDPE) conduits (ID = 3.5 − 4cm, wall thickness = 0.5 cm) that were buried together in a trench at 1 − 1.5 m and backfilled with soil before installing the fiber cable inside. Each fiber cable contains 84 gel-filled, loose-tube Corning LEAF fibers that are polythelene jacketed and steel-armored. The DAS data were recorded using a single 9/125 μm single-mode fiber from one of these cables. In a few locations, trenching was not possible so directional boring was used to install a large casing conduit (ID = 20-25 cm, wall thickness = 0.4 cm), inside of which the 12 smaller conduits were pulled. Depth of boring varied between one meter and a few meters when navigating around various culverts, sections of road and railway, and other obstacles. In some instances the casing was not required, or a steel casing may have been used. A third mode of installation used for approximately 300 m of the dark fiber array involved attaching a 20 − 25cm diameter steel casing directly to the elevated rail line where it crosses a section of protected wetlands, the Sacramento Bypass Wildlife Area. Inside this attached conduit, the 12 HDPE conduits were installed as the boring method described above.

Figure 4.11 shows DAS strain-rate earthquake waveforms (BP 0.5 − 2 Hz n 4 p 2) and
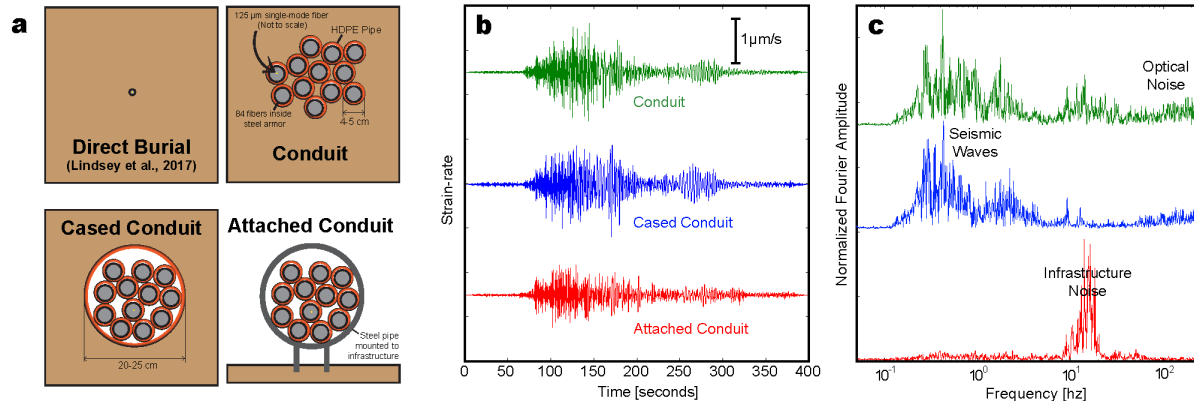
Figure 4.11: (a) Illustration of different installation geometries. (b) Earthquake (M4.2 Geysers 2018-Jan-18) trace comparison for each installation mode at Sacramento – trenched conduit (green), cased conduit (blue), attached conduit (red); strain-rate data are stacked over 100m and filtered (BP 0.5 – 2 Hz n 4 p 2). (c) Normalized Fourier amplitude spectra for the waveforms shown in b.

normalized Fourier amplitude spectra for the M4.2 Geysers 2018-Jan-18 event stacked over 100 m of each of the three install modes. Any phase shifts between traces are due to these install locations being separated by as much as 7 km along the array. The conduit and cased conduit data show very similar seismic wave response to the ground motion centered in the f=0.1 – 10 Hz range. Seismic signal amplitudes are observed to be on order with the optical noise at f $\geq$ 100 Hz. Data from attached section are noisier in a narrow frequency band centered on 12 Hz +/- 3 Hz, perhaps caused by interaction of the incident seismic energy with the infrastructure and/or tube waves traveling in the attached conduit at air velocity. The trenched conduit shows a broader spectral response to near-surface scattering into surface waves, while the cased conduit is relatively insensitive to it. We should note that three installation conditions discussed in this study are certainly not a comprehensive survey. A large variety of techniques are used for fiber installation, ranging from direct cable burial to installation on utility poles; the impact on DAS recording for many have yet to be evaluated.

4.4 Discussion

DAS instruments enable acquisition of spatially dense recordings of propagating seismic wavefields by sampling the strain field along fiber-optic cables. The DAS method sends and receives laser pulses in the fiber, and measures how the optical phase of coherent Rayleigh

backscattering from positions along the fiber changes through time. DAS instrument response has not been rigorously analyzed, especially at T > 1 s.

We find nearly equivalent phase estimates of main body wave arrival times, peak ground acceleration values, and coda shape between DAS and seismometer, however there are important differences. To properly measure these differences it is necessary to convert the strain or particle velocity data into the same units of measure. This is the subject of the following Chapter.

According to the results of analyzing teleseisms, we find that the DAS amplitude response is exceptionally flat to true ground velocity at periods longer than 10 s. At T<10 s, both the teleseism and microseism methods find that the DAS amplitude response increases and the standard errors also increase. We interpret this as a coupling or optical noise effect. The

Additional field and laboratory studies are necessary to clarify the full range of DAS response and sensitivity, separate photonic and cable effects, and characterize other important aspects of this new form of seismometery. The instrument comparison methodologies proposed in this work could be applied to other DAS experiments with other DAS instruments as means of inter-array calibration, specifically to understand the experimental gain coefficient or the difference between the recorded DAS amplitude and true ground motion.

4.5 Concluding remarks

The possibility to leverage pre-existing telecommunications fiber optic networks as seismic arrays with tens of thousands of sensing locations in areas where seismologists have traditionally lacked access represents an exciting future potential for many areas of earth science. A variety of basic and applied science topics could benefit from DAS including urban seismic hazard analysis, global seismic imaging, offshore submarine volcano studies, nuclear explosion monitoring, and microearthquake characterization. In studies of the near surface, the high spatial density and extensible range afforded by DAS could be used in tandem with ambient noise methods to characterize groundwater hydrology and study permafrost thaw with meter-scale resolution and basin-scale aperture. Recent nodal seismic array experiments exemplify the benefits of studying the Earth in densely-populated zones, but nowhere is it more difficult to install a seismometer longterm than in our cities. Lastly, DAS could complement earthquake early warning systems, in particular in regions with offshore hazard by addressing high cost and latency challenges through the leveraging the millions of meters of fiber optic cables that presently extend across the ocean floor as a distributed sensor network while writing the data on-shore.

Acknowledgements

Chapter 5

Instrument Response

This Chapter is presently accepted for publication at *Journal of Geophysical Research: Solid Earth* as N. Lindsey, Rademacher, and J.B. Ajo-Franklin 2019, "On the broadband instrument response of fiber-optic DAS arrays".

Summary Unlike classic inertial seismometers, DAS instrument response is presently unquantified. This topic includes a variable sensing element – the fiber, including packaging and installation – which changes between experiments. Ignoring this element, one DAS record should yield ground motions similar to fixed-length stainmeter, which exactly measure Earth's motion down to quasi-static frequencies relevant to geodesy. In this chapter, we test this hypothesis using three M > 7 teleseismic earthquakes as well as microseism noise recordings. These sources of seismic waves are selected because they span the broadband spectrum from periods of 1 to 200 seconds. We use a commercial DAS interrogator unit connected to an optical fiber previously used for telecommunication and a colocated broadband seismometer to estimate the DAS transfer function.

Key Findings

- Colocated broadband seismometer and telecommunications DAS records can be used to successfully quantify experimental instrument response of DAS.

- At periods of 10 - 200 s, there is a 1:1 correspondence between DAS and actual ground motion (phase response is flat), but amplitude response is reduced by -12.75 dB.

- At shorter periods of 1 - 10 s, the DAS responds more strongly. over this range of periods. We interpret the recovered DAS response function in terms of hypothesized fiber coupling and photonic effects, and propose this calibration methodology for future DAS experiments where seismic amplitude information is desired.

- DAS instrument response for a telecommunication cable is quantified empirically using a colocated broadband seismometer.

- We provide an approach to calibrate DAS arrays in order to extract absolute ground motion amplitudes.

5.1   Background

The goal of all seismic measurements is to determine the true motion of the ground in response to mechanical vibrations. To be truly useful in studies of Earth's interior, seismic instruments must be able to record fine vibration amplitudes at the level of 1e-6 m/s ground velocity or smaller.

Such precision is inherently difficult. Only various types of strainmeters, mechanical or optical, and GNSS sensors can determine this movement directly (Agnew and Wyatt 2003; Blum, Nooner, and Zumberge 2008; Hohensinn and Geiger 2018). In contrast, all inertial seismometers, by far the most common instruments used in seismometry, record the relative motion between the ground and a known internal inertial mass in response to vibrations (Lay and Wallace 1995).
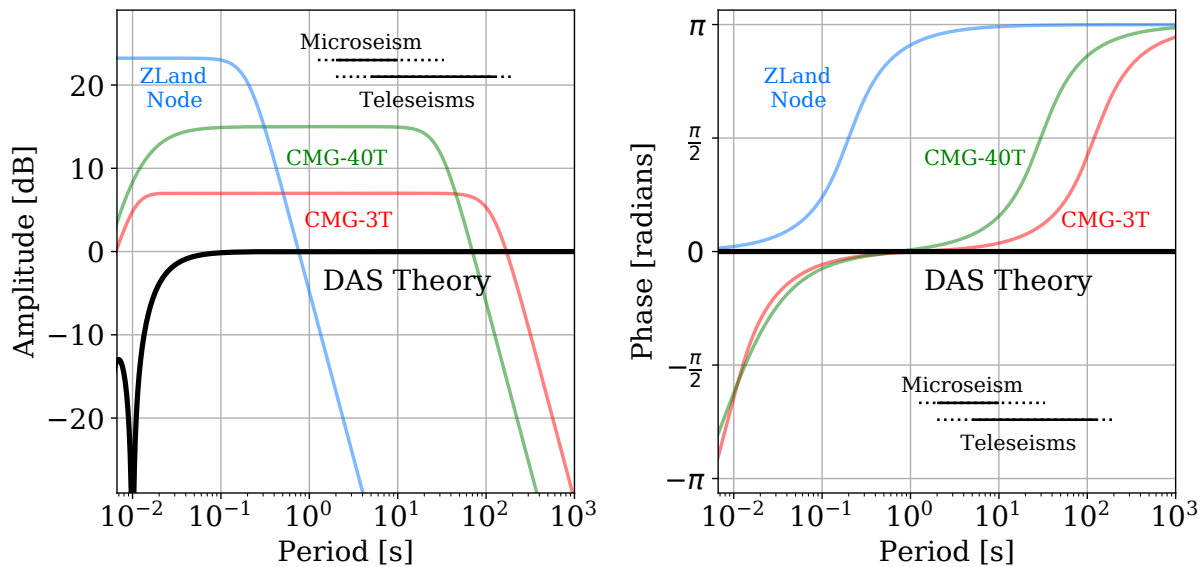
Figure 5.1: Instrument response functions for commonly-used seismic instruments and DAS, including the CMG-3T (red) used in this study, CMG-40T (green), and ZLand Nodal geophone (blue). Amplitude functions are offset along the vertical axis for clarity; seismometers are plotted as dB with respect to V/m/s; the DAS is plotted as dB with respect to strain. Treating DAS as a strain-meter yields a theoretical DAS amplitude response which falls to zero due to the gauge length effect, and is flat at the low frequency limit.

In order to relate these measurements to physical units of ground motion, the response

characteristics of the inertial mass system must be known with as much precision as possible. Modern open-loop geophones and other short-period instruments, as well as electromechanical force-feedback broadband seismometers, are precisely described by empirical formula or as the numerical coefficients of a transfer function, commonly known as the instrument response function (see review by Collette et al. 2012). Depending on the type of mechanical connection to the seismometer's frame, usually a leaf spring or another elastic device (Wielandt and Streckeisen 1982), the system response can also show a phase shift with respect to the ground motion. Hence inertial seismometer transfer functions commonly are documented in two parts, an amplitude response and a phase response.

Instrument response functions are commonly derived from analytical methods or through calibration testing on shake and tilt tables (Hutt et al. 2009). Today, such response functions are well established for commercial instruments, and typically are included in a parameterized form in the seismic recording metadata (IRIS-PASSCAL 2019). Instrument response removal, a process akin to digital filtering, is a common numerical procedure available in open source libraries such as SAC (Goldstein et al. 2003) and ObsPy (Beyreuther et al. 2010). This description only reflects the ideal case of a perfect coupling of the seismometer to the ground.

Figure 5.1 shows the instrument response functions for four seismic instruments in common use today.

Distributed Acoustic Sensing (DAS) interrogators probe fiber-optic cables buried in the ground to measure the vibrations of their surroundings. While all manufacturers of inertial seismometers provide instrument response calibration information with each of their sensors, DAS system manufacturers do not presently conform to this standard. This has resulted in the assumption that DAS measurements are equivalent to an array of virtual fixed-dimension optical strain gauges popularized in the study of earth motion at geodetic frequencies (Blum, Nooner, and Zumberge 2008). The implication of this is that DAS data directly measure true ground motion at all frequencies subject to notches related to multiples of the gauge length (see Figure 5.1). In this paper we seek to test this hypothesis at a single installation.

The broadband nature of DAS has largely been overshadowed by the use of DAS in active source experiments at frequencies f>10 Hz (T<0.1 s). DAS records of teleseismic earthquakes (Jousset et al. 2018; J.B. Ajo-Franklin et al. 2019) and hydrological pump tests (Becker, Ciervo, M. Cole, et al. 2017) have demonstrated the long period frequency response of the method. To date, the longest period earthquake signal observed with DAS used a dark fiber DAS array in the Mojave Desert to capture surface waves recordings down to T=200 s (C. Yu et al. 2019). Recently, Becker and Thomas Coleman 2019 observed a tidal period response (T=4.3x10^4 s) with DAS in a laboratory setting, albeit with a strain amplitudes 7x10^3 times greater than the solid Earth tide.

Generally, DAS studies have focused on seismic wave phase information, which is sufficient to model seismic wavefield velocities, for example in vertical seismic profiling (Albena Mateeva et al. 2014; TM Daley et al. 2016), ambient noise velocity inversions (Dou et al. 2017; Xiangfang Zeng et al. 2017; J.B. Ajo-Franklin et al. 2019), and earthquake phase identification (Nathaniel J Lindsey et al. 2017; Jousset et al. 2018; J.B. Ajo-Franklin et al. 2019;

C. Yu et al. 2019). However, true ground motion amplitudes are necessary for many other seismological processing tasks, including full-waveform inversion, AVO analysis, moment tensor inversion, and attenuation analysis, which the DAS community will likely investigate in the near future (Paitz, Sager, and Fichtner 2018; S. Cole et al. 2018).

This paper investigates how a telecommunications fiber-optic DAS array and a broadband inertial seismometer respond to the same input ground motion. We utilize a number of large (M>7) teleseismic earthquakes and strong ocean microseism noise as the signals for the instrument comparison. Such an experiment enables estimation of DAS instrument response over the signal period range from T = 1 - 200 s with overlap of the two different types of seismic energy around 10 s. In the next section (Section **??**), we detail how photonic DAS measurements are made and the assumptions involved. Section 5.5 describes two different DAS instrument response estimation methods, one using a propagating earthquake signal and one using ambient noise in the microseism band. Both methods require DAS unit conversion from strain to velocity, related through phase velocity. In Section 5.1 we describe the field experiment, data processing procedure, and observations. Earthquake and noise results (Section 5.6) suggest that absolute DAS amplitude response is complicated by ground coupling of the fiber-cable system.

5.2 Data

For a period of three months beginning in November 2017, a three-component broadband inertial seismometer (Guralp CMG-3T; 750 V/m/s) was installed near a linear section of the Fiber-Optic Sacramento Seismic Array (FOSSA) experiment (Figure 5.2) documented in J.B. Ajo-Franklin et al. 2019 (see Chapter 1, Experiment 3). FOSSA utilized a commercial DAS instrument (Silixa iDAS, v.2, S/N 14033, T. Parker, S. Shatalin, and Farhadiroushan 2014) with a 10-m gauge length. The DAS was connected to the southern end of an unlit single-mode long-haul telecommunications fiber-optic cable running from West Sacramento, CA northwest to Woodland, CA. Continuous DAS recordings at 500 Hz sampling rate and 2-m channel spacing were made over the first 24 km of this fiber, resulting in a 12,000 horizontal strain-rate component array. For additional details about FOSSA experiment please see the experiment description in (J.B. Ajo-Franklin et al. 2019).

As described in detail in J.B. Ajo-Franklin et al. 2019, the FOSSA optical fiber was installed in 1999-2000 and some information about the fiber-soil coupling profile can be obtained from the as-built installation notes. The occupied 9/125 μm single-mode used to record DAS is one of 84 gel-filled, loose-tube Corning LEAF fibers inside one polythelene jacketed and steel-armored cables. This cable was pulled through a 4 cm diameter high-density polythelene (HDPE) conduit (wall thickness = 0.5 cm) buried at $1 - 1.5$ m depth in soil (backfilled and mechanically-tamped). This cable and conduit were one of 12 in the same bundle. The section of the fiber presently analyzed was from channel 4545 (9.09 km linear fiber length from the DAS instrument) to channel 5045 (10.09 km).

The seismometer was installed on a concrete foundation inside the Elkhorn Fire Station
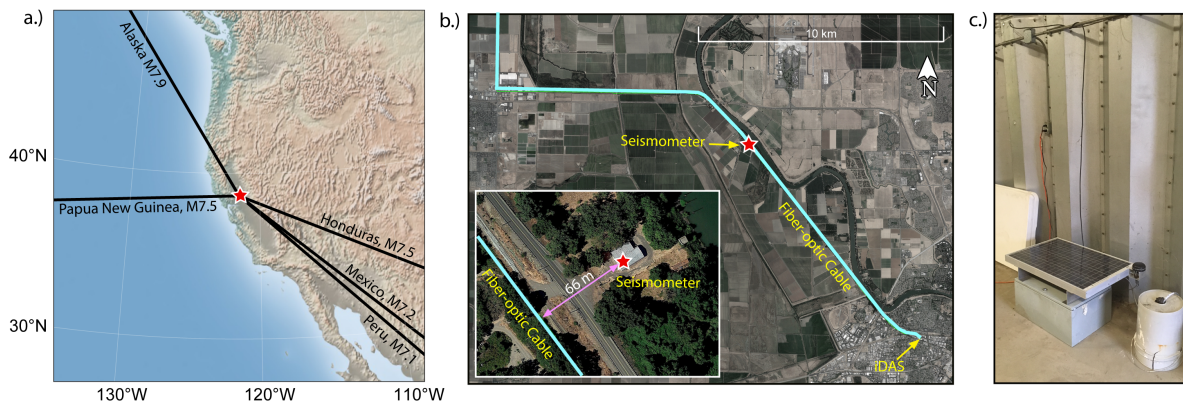
Figure 5.2: a.) Equal azimuth map projection of Western US showing experiment location in Northern California with black lines indicating teleseism backazimuths (see Table 5.1). b) Fiber-optic cable path or DAS array geometry for the FOSSA experiment showing location of the DAS instrument (Silixa iDAS) in West Sacramento, the seismometer (red star) about 9 km NW of the DAS instrument and 66m NE of the fiber-optic cable. c.) Seismometer (Guralp CMG-3T) recording inside Elkhorn Fire Station. Sensor is sitting on a concrete pad, beside the gray box that contains the digitizer and battery.

southeast of Woodland, 66 m northeast from the midpoint of this fiber section. A digitizer and data-logger (Guralp Minimus) were used to record the continuous inertial ground motion records at a 200 Hz sampling rate.

Unfortunately, both instruments experienced clock issues during the experiment. A 1 pps NPT time signal was provided to the DAS, but we could not obtain a GPS signal due to the location of the instrument inside of a telecommunications point of presence facility. The time difference between the two instruments was bounded at +/- 30 minutes using earthquake recordings from the Northern California Seismic Network. For the teleseismic earthquake records, time series synchronization via cross-correlation of seismic energies prior to data processing provided a simple means to correct this issue. It was not possible to adopt the same procedure for non-impulsive microseism noise records, because of potential cycle-skipping errors with weak signals. Thus, we analyzed the microseism noise in the Fourier amplitude spectra per night. This prohibited calculation of DAS phase response using the microseism noise.
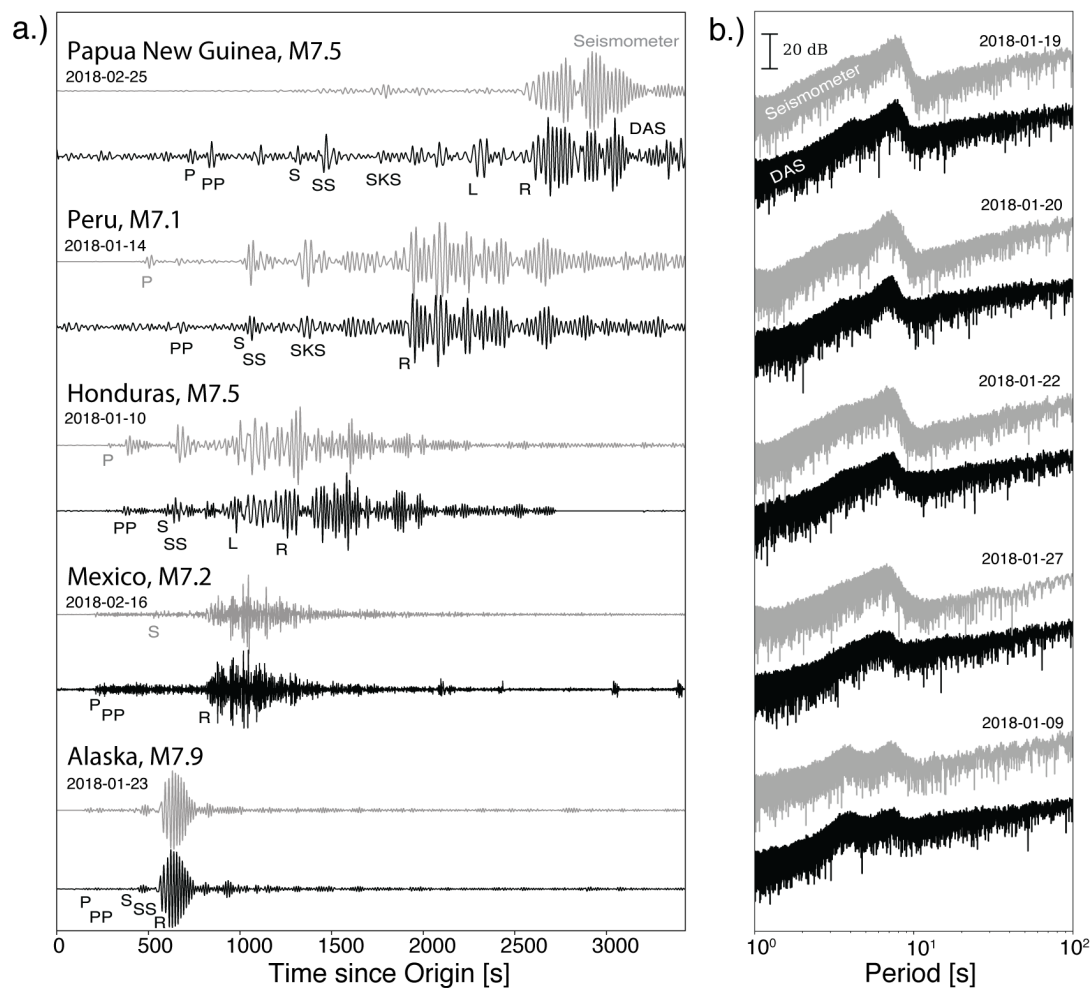
Figure 5.3: Teleseism and microseism ground motions highlight the general similarity between DAS and broadband seismometer signals over a wide period range. Note that DAS data are strain and seismometer data velocity. a.) Teleseismic event waveforms with dominant period range 20 - 100 s normalized by event (black=DAS, strain; gray=seismometer, velocity). b.) Nightly microseism noise power spectral density with peak period around 5 - 8 s (black=DAS, velocity; gray=seismometer, velocity; 23:00 - 07:00 local time). DAS record earthquake phase picks are labeled below the DAS trace, unless the phase was only visible on the seismometer.

Region	Mw	Origin Time (UTC)	Distance	Backazimuth
Alaska	7.9	2018-Jan-23T09:31:43	2778 km	302°
Mexico	7.2	2018-Feb-16T23:39:39	3357 km	139°
Honduras	7.5	2018-Jan-10T02:51:31	4355 km	130°
Peru	7.1	2018-Jan-14T09:08:45	7088 km	141°
Papua New Guinea	7.5	2018-Feb-25T17:44:44	10804 km	231°

Table 5.1: Teleseismic event catalog used in the DAS instrument response analysis.

5.3 Observations

5.3.1 Teleseismic earthquake observations

Global $M > 7$ earthquakes occurring during the FOSSA experiment (Table 5.1; Figure 5.3a) provided coherent, body and surface wave phase arrivals in the period range T = 2 - 200 s, with the strongest amplitudes occurring at periods longer than T = 20 s. Event backazimuths ranged from near the axis of the fiber-optic cable to orthogonal to the fiber (Figure 5.2a). Due to the proximity of the FOSSA dark fiber DAS experiment to a road and railway, local automobile and train noise limited the utility of the Papua New Guinea and Mexico teleseismic arrivals.

5.3.2 Ambient noise ocean microseism observations

To corroborate the analysis of DAS response around T=10 s period and expand the spectral range to shorter periods, we analyzed observations of ambient microseism noise. At our site, microseism noise has higher frequency content than the teleseismic signals, covering the range from T = 2 - 20 s. We restrict our analysis to the five nights of peak microseism noise during the FOSSA experiment time period based on a survey of probabilistic power spectral density across the Northern California Seismic Network. Data from 20:00 - 02:00 local time (UTC+7) were chosen in order to reduce the level of anthropogenic noise. Figure 5.3b shows the noise records for both instruments (DAS, 1 channel = black; seismometer, rotated into fiber azimuth = gray). Nightly spectral characteristics and night-to-night amplitude variations are consistent between the two sensing approaches. For example, there is a systematic fall-off in power spectral density away from the secondary microseism peak around 4 - 8 s. Note how the DAS shows a stronger spectral response to the ambient noise at high frequency.

5.4 Data Processing

5.4.1 Earthquake data processing

Seismometer data processing involved a linear detrending step, followed by mean subtraction and application of a symmetric Hanning window taper. Next, we removed the calibrated instrument response function and digitizer bitweight provided by the vendor to transfer the seismometer data from raw units of V/m/s into ground velocity units. This included accounting for the seismometer's sensitivity. This seismometer's transfer function is characterized by a flat response in amplitude and phase over the period range 0.02 - 120 s (see curves for CMG-3T in Fig 5.1). Then, we rotated the data from the recording frame orientation (NEZ) into the fiber-oriented reference frame (TRZ; radial $= 142^o N$) to retrieve the true horizontal ground velocity component aligned with the fiber. Finally, we applied a zerophase, two-corner, bandpass filter. For teleseismic analysis we filtered the data from T = 2 - 200 s. For microseism noise analysis we filtered the data from T = 2 - 20 s.

DAS data processing involved converting raw optical phase change to strain-rate using a conversion value of $11.6 \cdot 10^{-9}$ nanostrains/radian (see Eq. 2), followed by linear detrending, mean subtraction, and tapering, identical to the seismometer workflow described above. Next, we integrated the DAS data to convert from strain-rate to strain units, and applied the same bandpass filter described above. We then applied the FK-rescaling algorithm described in Section 5.5.1. For the teleseismic waves explored, we experienced no issues when very low wavenumber vertically-incident waves were utilized in the analysis. The effect of these processing steps on the recorded spectra for an example earthquake record are illustrated in Figure 5.4. Rescaling and then averaging the raw DAS data over 500 channels or 50 gauge lengths yields a single DAS velocity record that can be directly compared with the velocity spectra recorded by the seismometer. This processing step reduces spatial information, but has the advantage of decreasing decorrelated noise and increasing fidelity of the long wavelength signals that are the subject of interest in this study.
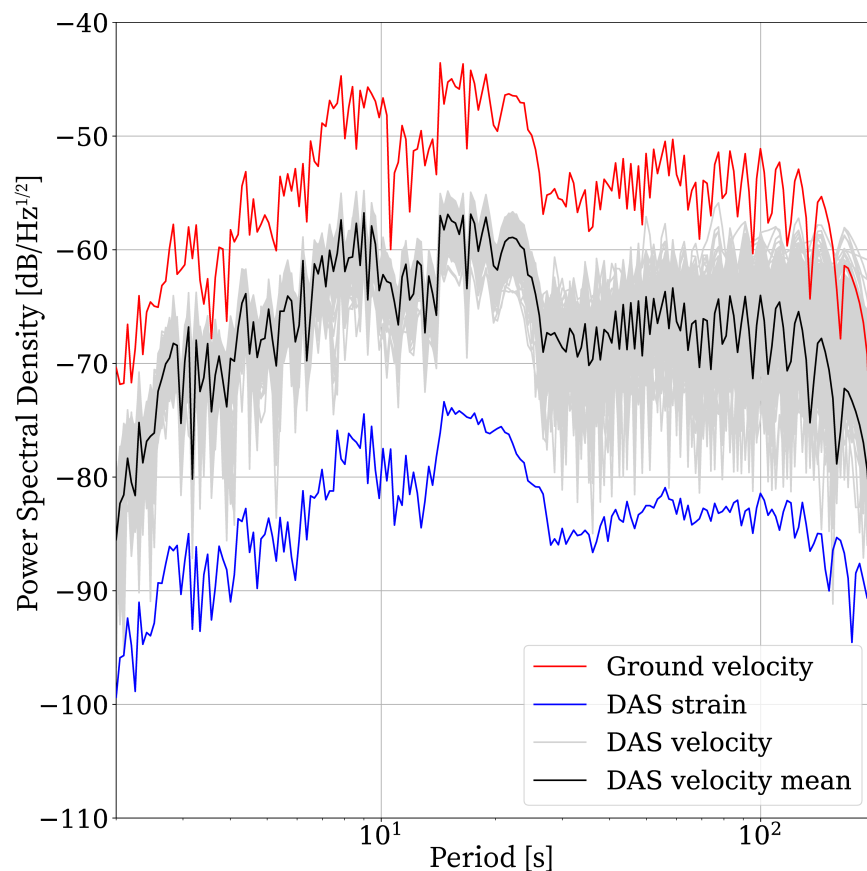
Figure 5.4: Effect of FK-rescaling on DAS recorded amplitude spectra for the 23-Jan-2018 Alaska M7.9 event. Blue line = DAS strain record from the channel co-located with the seismometer. Grey lines = 500 DAS velocity records from +/- 500 m of the seismometer's location. Black line = DAS velocity record from the mean stack of +/- 500 m of the seismometer. Red line = true horizontal ground velocity as measured by a broadband seismometer component in the direction of the fiber-optic cable.
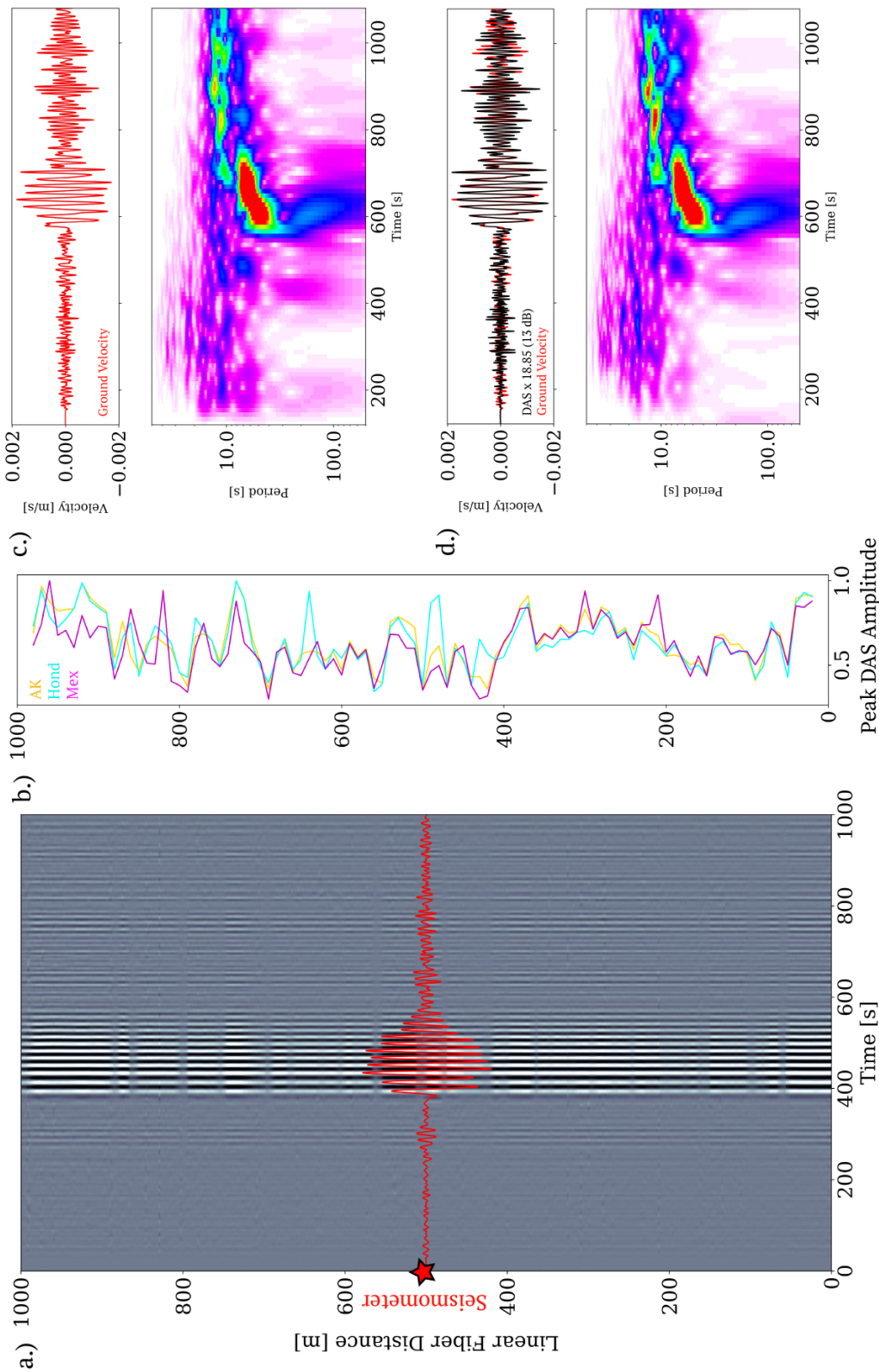
Figure 5.5: Observed ground motion velocities for 2018-Jan-23 Alaska M7.9 event. a) 500 DAS velocity records after FK-rescaling from the 1 km section (black/white image) around the seismometer (red star); bandpass filter = 10 - 100 s, p 2, n 4. b.) Maximum DAS amplitude versus position in a. after gauge-averaging for three separate teleseismic earthquakes (gold=Alaska; cyan=Honduras; magneta=Mexico). Systematic amplitude variability is interpreted as photonic fading. c.) Horizontal ground velocity record and time-frequency spectrogram from the fiber-oriented seismometer component; no filter. d.) Same as c. but for the average of DAS velocity records shown in a. Both instruments retrieve the strong dispersive Rayleigh wave with long period airy phase arriving at 550 s; DAS shows a stronger response for $T \leq 10$ s.

Common-mode noise issues appeared to be minimal for our experiment, however photonic fading was problematic. For the Alaska event recording shown in Figure 5.5, time-invariant amplitude reductions of more than 50% of the peak amplitude were registered at some DAS channels with a quasi-random pattern. Similar fading patterns were observed for two different teleseismic events that occurred weeks later (Figure 5.5b). Alternatively, the observed localized amplitude reductions could result from insufficient coupling or local geology, but we hypothesize that such effects would exhibit a more ordered pattern than was not observed. For example, coupling effects would be expected to correlate with install condition (e.g., steel versus plastic conduit), or manifest with a fixed length scale related to the twist of the cable inside the conduit; local geology effects might correlate with distance from the river. Based on the resolution of information provided in as-build drawings, there is no expected variation in coupling or local geology over this kilometer. We will return to these amplitude reductions when we discuss DAS array calibration in Section 5.6.

Distant earthquakes excite long period ground motions with wavelengths in excess of λ=5 km. Therefore, we can safely stack neighboring DAS records up to 1 km, or 500 DAS channels, without sacrificing fidelity. Indeed, Figure 5.5 demonstrates that the 2018-Jan-23 Alaska M7.9 teleseismic earthquake wavefield propagates with coherence length scales much greater than 1 km at T>10 s. To mitigate the impact of fading, we stacked the remaining channels over 1 km centered on the seismometer. This process retrieved a single representative DAS time-series for comparison with the inertial seismometer.

5.4.2   Microseism data processing

Comparing DAS strain records with seismometer velocity records requires knowledge of the apparent phase velocity, however ambient noise arrives with a low absolute amplitude and typically is not recorded as a coherent phase, hence there is often difficulty determining arrival azimuth. The absence of a dominant propagating phase velocity is overcome in this study according to the technique described in Section 5.5.2 with the use of a regional phase velocity dispersion model. We constructed a composite phase velocity model illustrated in Figure 5.6 by fitting a cubic spline to available Rayleigh wave velocity dispersion models for the Sacramento and greater Northern California area. This model combines phase velocity dispersion from surface waves generated by global earthquakes in 2000 - 2009 in the period range 25 - 250 seconds (Göran Ekström 2011), with dispersion derived from the shorter-period US Array stations and ambient microseism noise (G Ekström 2017), with a recently recovered model of train noise dispersion from 2017-2018 with the FOSSA DAS array which bounds the shortest periods (T < 1 s) (Verónica Rodrıguez Tribaldos et al. n.d.).

We used the composite dispersion model above to convert each nightly DAS strain observation to velocity, prior to inverting for a solution for $H(\omega)$ using Equation (7) with 50 spectral coefficients. Nightly microseism noise observations were considered independent observations, meaning we aimed to use 5 observations to determine the 50 unknown parameters, thus we introduced the smoothness regularization constraint. We chose a solution through a trade-off selection of λ by balancing reduction in fit with smoothness (Figure 5.7).
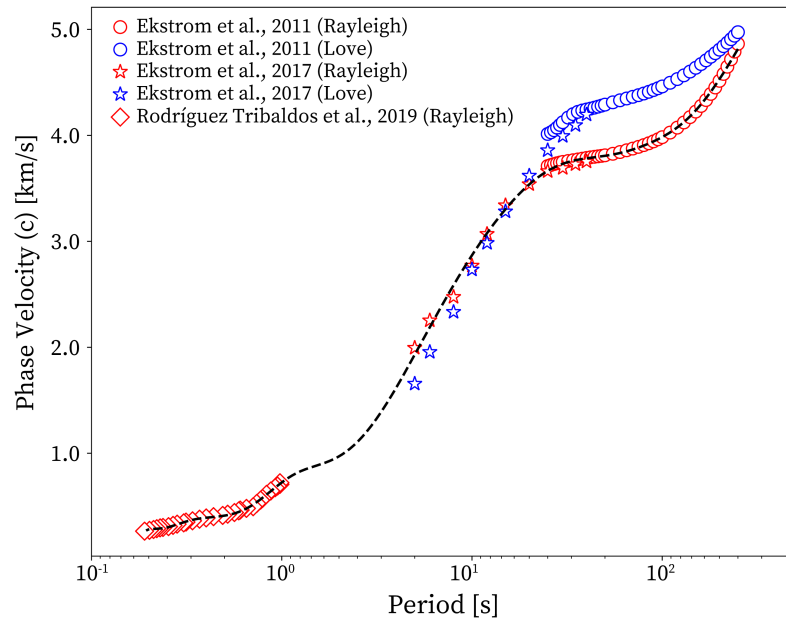
Figure 5.6: Phase velocity model for Western Sacramento. The best-fit spline interpolation to labeled Rayleigh wave phase velocity observations from Göran Ekström 2011, G Ekström 2017, Verónica Rodrıguez Tribaldos et al. n.d. is shown as the black dotted line.
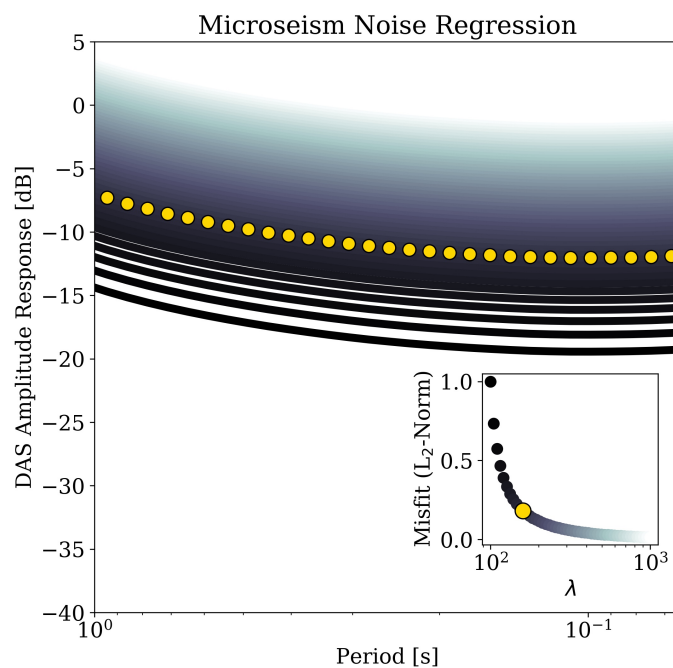
Figure 5.7: Best-fit smooth least-squares solution (yellow circles) for DAS amplitude response spectra based on five nights of microseism noise. Results complement teleseismic analysis and suggest DAS is more responsive to ground motion at T<10 s than at longer periods where the response has zero slope (a flat response). Grayscale curves show how regularization affects the solution. Inset shows selection criteria of color-coded regularization operator (λ).

5.5   Methodology

Propagating elastic waves are measured at the Earth's surface using a fiber-optic cable connected to a DAS instrument and a co-located seismometer. The seismometer is oriented in the fiber cable direction ($+x$-direction) and records the wavefield particle velocity v_x convolved with its known instrument response function $g(t)$. The DAS records the strain-rate of the wavefield in the direction of the fiber axis ($\dot{e}_{xx}$), which we assume is convolved with an unknown DAS instrument response function $h(t)$. After integrating the DAS data to strain, the two measurements are related through the apparent phase velocity of the wave, c_x (Aki and Richards 2002):

$$v_x(t) * g(t) = -c_x(x,t) * e_{xx}(x,t) * h(t). \tag{5.1}$$

After removing $g(t)$ from the seismometer data through standard instrument response removal, a Fourier transform is applied to all quantities. We express the DAS instrument response function in the frequency domain as:

$$H(\omega) = \frac{V_x(\omega)}{-c_x(k_x,\omega)E_{xx}(k_x,\omega)}. \tag{5.2}$$

where $\omega = 2\pi/T$, $k = 2\pi/\lambda$, $X(\omega) = \mathcal{F}\{x(t)\}$.

The aim of this paper is to compare DAS and seismometer records to estimate $H(\omega)$. We focus on two different classes of seismic signal: 1) regional and teleseismic earthquakes with surface waves occupying a broad period range from 10 - 200 s, and 2) weak ambient microseism noise excited by ocean-solid earth interactions and commonly recorded in continental interiors at periods shorter than the teleseism range (2 - 20 s). Other seismic wave types could also be utilized. Next, we describe how to estimate $H(\omega)$ using earthquakes or weak ambient noise signal.

5.5.1   Deconvolution of DAS instrument response using teleseismic signal

The waveforms of seismic signals can easily be compared between DAS and seismometer instruments, however the native units are different. To determine the DAS instrument response we must first convert the DAS strain (strain-rate) and seismometer velocity values into one consistent format. TM Daley et al. 2016 showed how the array-nature of DAS can be used to convert strain into particle velocity values in the frequency-wavenumber domain for cases of high signal-to-noise utilizing the phase velocity relation $c = \omega/k$. This FK-rescaling technique reformulates (4) as:

$$H(\omega) = \frac{V_x(\omega)}{-(\frac{\omega}{k_x})E_{xx}(k_x,\omega)}. \tag{5.3}$$

daley2016 applies the FK-rescaling technique to an active-source vertical DAS dataset far from the free-surface and find a very good comparison with a vertical borehole geophone array. H. F. Wang et al. 2018 applied the technique to surface recordings of earthquakes where the propagating wavefield was observed to be strongly dispersive. Both studies assumed $H(\omega) = 1$ over the period range of interest ($T < 1$ s). Note how (5) may become unstable when the seismic wavefield is dominated by a small value of k_x, such as when teleseismic body waves arrive with near vertical incidence, leading to a case of division by zero. In practice, we did not find this to be an issue in this study.

5.5.2 Inversion for DAS instrument response using microseism noise

Microseism noise occupies a higher frequency range than teleseismic wavefields, typically 2 - 20 s, and therefore provides a complementary source of seismic waves to analyze the DAS instrument response. However, readily converting DAS noise recordings from strain to velocity as described above for an earthquake is not possible when using microseism noise because the energy does not manifest in the continents with a clearly observable propagating phase (McNamara and Buland 2004; N. M. Shapiro et al. 2005).

Continentally-recorded microseism noise, including the primary and secondary microseism noise, is associated with ocean - solid earth interaction (Longuet-Higgins 1950a; Ardhuin, Gualtieri, and Eléonore Stutzmann 2015). Amplitude variations and directionality can vary with geography, season, and even surface sea state changes due to storms (Retailleau and Gualtieri 2019). These complications are simplified in most ambient noise studies by assuming that noise arrives from all directions equally. Previous efforts to pinpoint ocean microseism sources have retrieved smoothed images of average wavefield backazimuths over months to seasons, but this information is not directly applicable to the present strain-velocity conversion (Schimmel et al. 2011; Ermert, Villasenor, and Fichtner 2015).

In order to use microseism noise to study DAS response, we employ knowledge that the microseism wavefield is dominated by large wavelength surface waves ($\lambda_{min} = c_x \cdot 1/\omega = 2.5$ km/s $\cdot$ 2 s = 5 km). We assume that the sources are isotropic and time-invariant over the experiment. These assumptions remove the wavenumber dependence from the apparent horizontal phase velocity, $c_x(k_x, \omega) \approx c(\omega)$, and enable reformulation of (4) using a generalized 1-D regional phase velocity dispersion model, $c(\omega)$, as in:

$$H(\omega) = \frac{V_x(\omega)}{-c(\omega)E_{xx}(\omega)}. \tag{5.4}$$

to estimate the coefficients of $H(\omega)$.

Earthquake records were time-synchronized for deterministic deconvolution using cross-correlation, however weak noise signals are more difficult to synchronize in the time-domain, an issue further complicated by clock drift (see Section 5.1). Instead, we frame the estimation of $H(\omega)$ using microseism noise as a linear inverse problem, in which we seek to minimize

the objective function:

$$||V_x(\omega) - (-c(\omega)H(\omega)E_{xx}(\omega))||_2 + \lambda H(\omega)'', \tag{5.5}$$

where $|| \cdot ||_2$ represents the L2-norm. We will see in the next section, that the problem is underdetermined. We expect $H(\omega)$ to vary smoothly in frequency so we regularize for smoothness through introduction of the term on the far right, which is comprised λ, a regularization constant that is determined empirically, and $H(\omega)''$, which is the second derivative of the solution with respect to ω.

5.6 Results

After the data have been converted to comparable velocity units, DAS and seismometer recordings of the 2018-Jan-23 Alaska M7.9 earthquake show many important similarities. First, time-frequency analysis (Figure 6c-d) shows that the shape of the highest-energy fundamental Rayleigh wave is captured by both instruments. This includes the long period airy phase down to T=300 s. In general, the timing and relative energy of body wave phases before the dominant Rayleigh wave as well as subsequent scattering are well matched. However, the DAS record of the P-wave amplitude is almost a factor of ten lower than the inertial record, as predicted from azimuthal sensitivity differences of the two instruments (Kuvshinov 2016). Note that these records have been trace normalized, which is equivalent to multiplying the DAS by 18.84 to match peak amplitudes.

Deconvolution of the DAS record by the seismometer's record of true ground motion yields an empirical estimate of DAS instrument response for the dominant period range of the teleseism record, between T = 2 - 200 s (Section 5.5.1). This processing technique quantifies how DAS phase response is approximately identical to the broadband seismometer, but DAS amplitude response is lower by a factor of 18.84 or -12.75 dB (Figure 8). Amplitude spectra shown in Figure 8b on an absolute scale document this scalar difference as a function of period.

We obtained independent empirical estimates of DAS instrument response from the 2018-Jan-10 Honduras M7.5 and 2018-Jan-14 Peru M7.1 events (see Supplementary Information for additional earthquake records), and found similar results. DAS response is flat from T = 10 - 200 s at a level -12.75 dB +/- 1 dB below true ground motion. At shorter periods (T<10s), the response estimate and variance increases to -10 dB +/- 3 dB (1-sigma at T = 5 s). We observe a zero phase response at all periods for all events. 2-sigma distributions in amplitude and phase are represented with a single box-and-whisker plot in Figure 9.

We obtain an additional independent estimate of DAS amplitude response at shorter periods (T = 1 - 20 s) by inverting 5 nights of ambient microseism noise as described in Section 5.5.2 (Figure 10). Figure 10 shows the range of solutions to $H(\omega)$ color-coded by the regularization parameter λ. The solutions are of a similar shape with flat response at periods below $T \approx 10 - 12s$ but increase at shorter periods, which agrees with the teleseismic analaysis. The absolute difference between the DAS response and true ground motion is approximately -7.50 dB +/- 1 at T = 2 s and -12 +/- 1 dB at T = 10 s. These results are plotted in Figure 5.11 as yellow circles with error bars representing our regularization uncertainty.
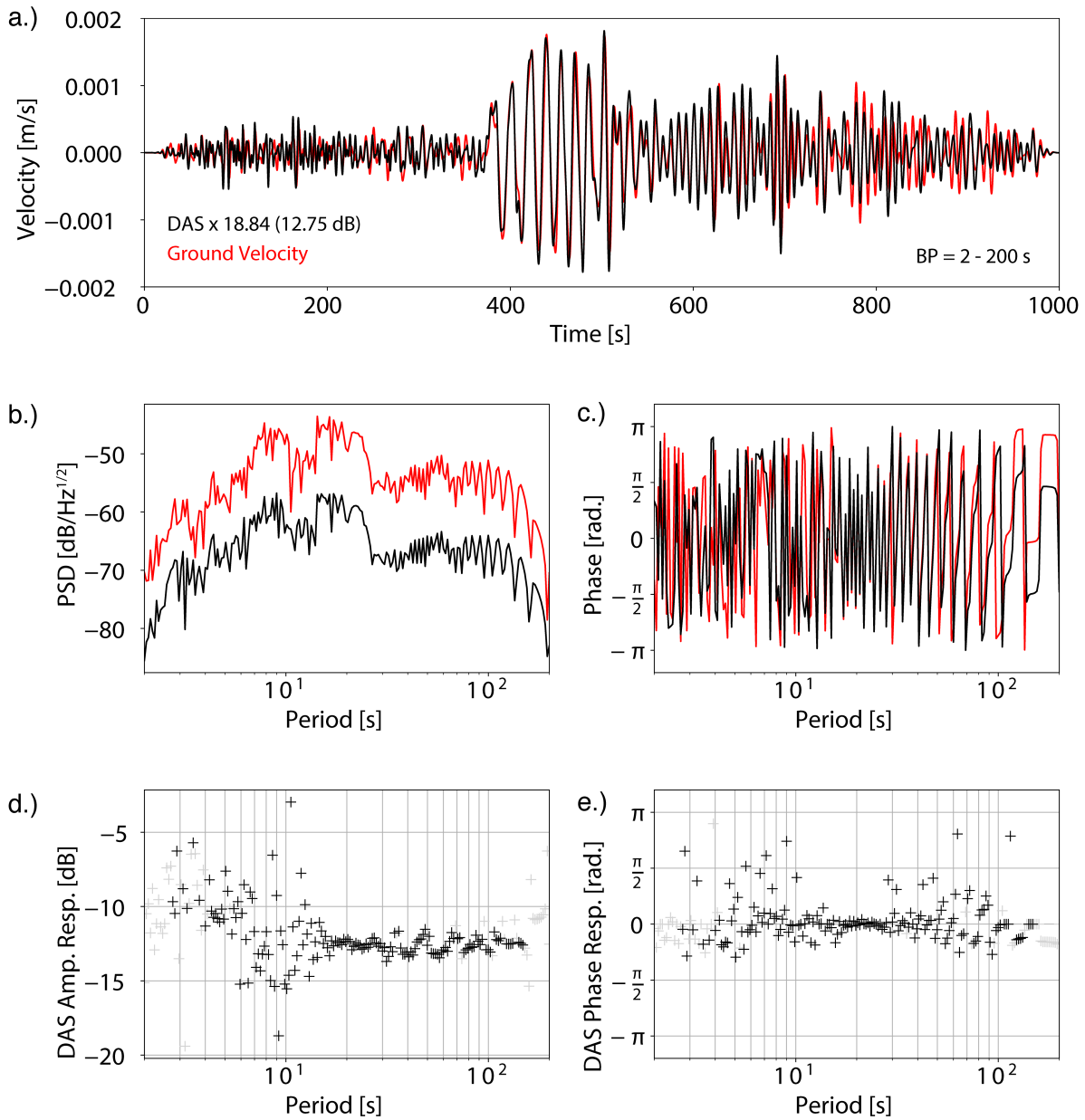
Figure 5.8: DAS instrument response deconvolution analysis for the 2018-Jan-23 Alaska M7.9 event records. a.) Waveform comparison of seismometer ground velocity (red) and DAS equivalent velocity scaled by a factor of 18.84 (12.75 dB) to match the amplitude of the seismometer. b.) Unscaled power spectral density and c.) phase comparison of the two instrument records before deconvolution. d.) Resulting DAS amplitude and e.) DAS phase response spectra after deconvolution of the ground motion.
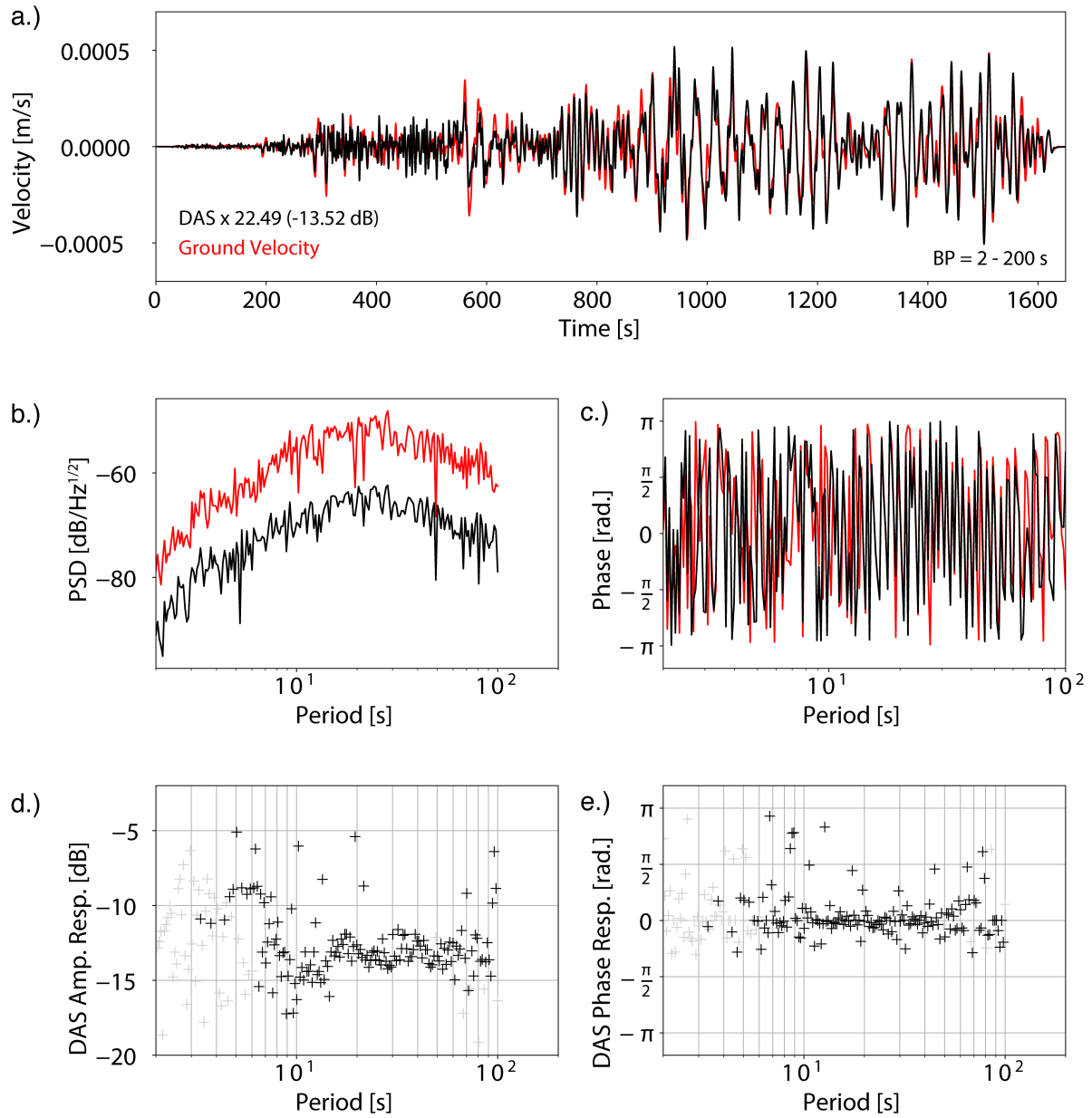
Figure 5.9: Teleseismic deconvolution for DAS instrument response using the .
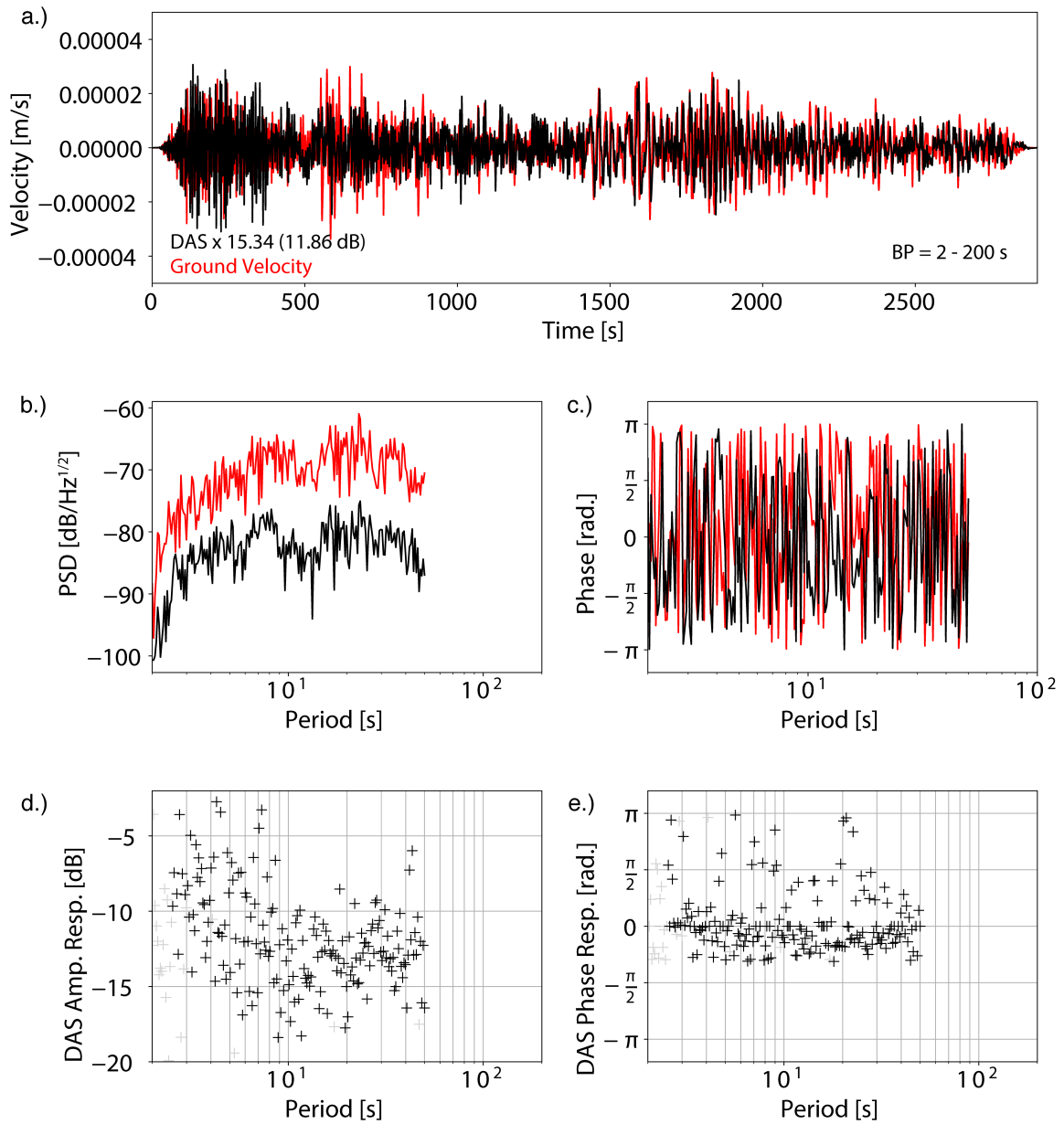
Figure 5.10: Teleseismic deconvolution for DAS instrument response using the .
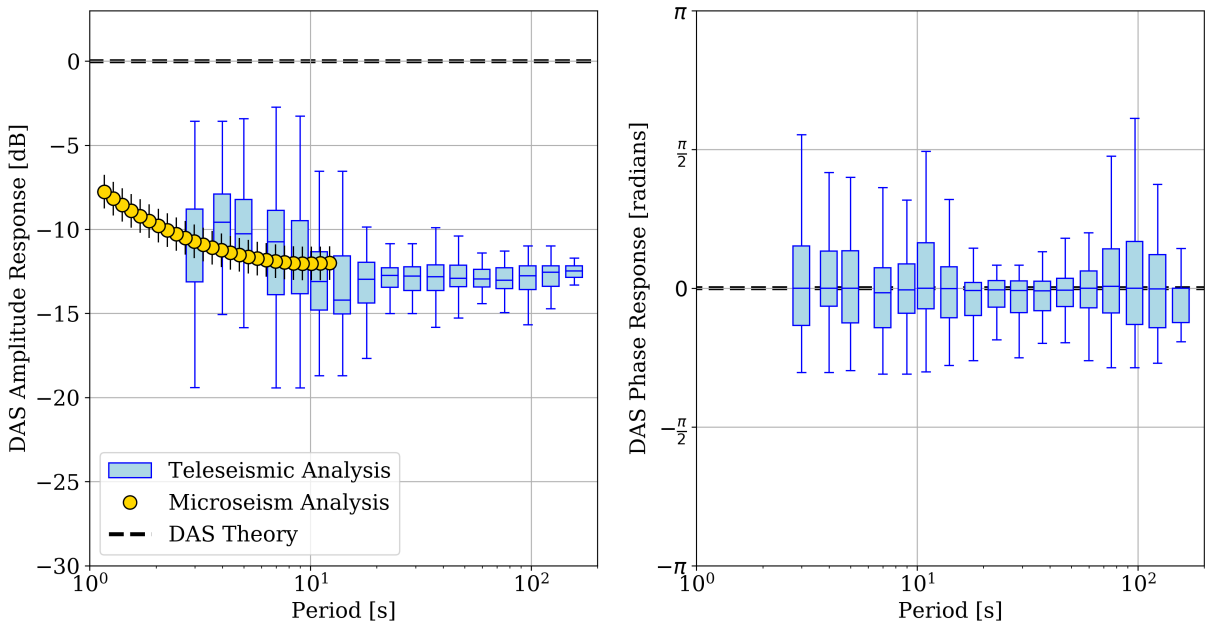
Figure 5.11: (a) Amplitude and (b) phase parts of the empirically-determined DAS instrument response function. Results from teleseismic record comparisons for Alaska M7.9, Peru M7.2, Honduras M7.5 are plotted as blue box-and-whisker to illustrate the mean and standard deviation of the each period's distribution. Results from microseism noise analysis are overlaid as yellow circles. Black dotted line indicates theoretical DAS instrument response shown in Figure 5.1.

5.7 Discussion

DAS studies to-date have mostly analyzed high frequency seismic signals (T<1s), but only a few have presented evidence of long period DAS response. The present analysis of teleseismic earthquakes and ambient microseism noise successfully documents the broadband spectral coefficients of this DAS amplitude and phase response on an absolute scale. In terms of frequency range, DAS is found to be as broadband as the broadband seismometer used for calibration. Usable teleseismic energy falls off at periods longer than T = 120 s, but the DAS continues to show energy in time-frequency analysis down to T = 300 s (for the purposes of analysis we consider T = 200 s as a cutoff). This is more than twice as long as the longest period DAS signals previously documented by Becker, Ciervo, M. Cole, et al. 2017 in a hydrogeological pump test and in earthquake studies on dark fiber DAS arrays (J.B. Ajo-Franklin et al. 2019; C. Yu et al. 2019). One reason for this may be the DAS data processing approach employed here in which we stack over a window of 1 km or 500 consecutive DAS sensors, all falling inside of the seismic wave's coherence length, which serves to mitigate uncorrelated channel noise and improve recovery of the lower frequency signals.

In terms of instrument response, the DAS amplitude spectra for three different earthquakes were found to be flat over the period range T = 10 - 200 s, which agrees in part with theoretical predictions. However, at these long periods the absolute amplitude level of the DAS response function was found to be -12.75 dB lower than true ground motion. We refer to the absolute amplitude difference as the long period gain, which is required to scale the DAS data to the true level of ground motion. The excellent relative amplitude response in the period range T = 10 - 200 s suggests that dark fiber DAS experiments can be relied upon for accurate wavefield amplitude measurements, in addition to phase (traveltime) measurements, following a simple array calibration test like that described in this paper to determine the gain coefficient. At shorter periods (T < 10 s), DAS amplitude response increases from -12.75 dB to -7.50 dB, a feature reproduced by multiple earthquakes and noise processed with a different estimation technique.

We hypothesize that the long period gain factor could result from two underexplored effects of the DAS measurement. One potential contributing factor is the style and degree of fiber-ground coupling. Rigid ground coupling is a necessary condition for any seismometer(Lay and Wallace 1995), yet many DAS studies have concluded that mechanical coupling of the fiber-optic to the ground had an impact on their results (Nathaniel J Lindsey et al. 2017; Becker, Ciervo, M. Cole, et al. 2017; Willis, Jonathan Ajo-Franklin, and Roy 2017; H. F. Wang et al. 2018; Jousset et al. 2018; C. Yu et al. 2019). Coupling is a static feature of a DAS experiment (fiber array; DAS recording parameters) that should be assumed to not change over the duration of a typical geophysical campaign (days to months). In vertical wells, grouting the fiber behind the well casing or using a pressurized permeable sleeve in uncased wells has been shown to improve strain transfer for DAS measurements (Becker, Ciervo, M. Cole, et al. 2017). The topic of coupling horizontally-oriented dark fiber experiments that involve a wide-diameter fiber cable bundle and PVC or HDPE conduit

surrounding the fiber has received less attention. J.B. Ajo-Franklin et al. 2019 observed that in the FOSSA experiment three different conduit styles described by the telecommunications company drawings had a first order impact on regional dark fiber DAS earthquake waveform recordings. However, Hooke's Law predict >99% strain transfer for a simple fiber embedded in sand excited by a long period ground motion with wavelength 20 m (Reinsch, Thurley, and Jousset 2017). We expect that the HDPE conduit material used at FOSSA would modify the amplitude response uniformly over the period range considered, but may impact the response at shorter wavelengths where the length scale of the wave approaches that of the conduit. A flat phase response suggests the fiber-conduit system behaves in a linear elastic regime of strain transfer. We find no evidence for a viscoelastic rise time required to activate the DAS cable as proposed by (Kuvshinov 2016). This may be due to the aramid-wrapped fiber or drained soil conditions surrounding the conduit in the FOSSA experiment. Gel-filled fibers or subsea or undrained cable conditions may act differently. Calibration of DAS instrument response in a direct fiber experiment may clarify the conduit's effect. The uptick in DAS amplitude response at T<10 s could be related to the mechanical coupling of the fiber-conduit-ground system.

A second contribution to the gain coefficient may be related to the photonic system itself. Figure 6b documents how photonic fading reduced amplitudes at specific channels in the array. Averaging over the full record will result in a net underestimation of the true amplitude response. Yet, fading is not expected to lead to amplitude reductions as large as -12.75 dB. We hypothesize that other details of the photonic system and the interferometric measurement, which are yet unexplained may lead to this gain coefficient. Future work will investigate dark fiber DAS array noise sources – both photonic and coupling-related – in order to better quantify the contributions to the experimental gain coefficient.

Future evaluation of other DAS arrays and other DAS instruments is necessary to understand the wider applicability of the present conclusions about DAS instrument response. An ultimate aim of future laboratory and field experiments will be to summarize DAS instrument response as a set of poles and zeros representing the instrumental transfer function. The present study shows that the instrument response should include both the photonic and fiber characteristics as a single system, with potentially important factors including the particular optical interferometry setup, fiber type, cable packaging, and conduit coupling.

5.8 Concluding remarks

DAS instruments enable acquisition of spatially dense recordings of propagating seismic wavefields by sampling the strain field along fiber-optic cables. The DAS method sends and receives laser pulses in the fiber, and measures how the optical phase of coherent Rayleigh backscattering from positions along the fiber changes through time. DAS instrument response has not been rigorously analyzed, especially at T > 1 s. In this study, we used a precisely-calibrated broadband inertial seismometer (Guralp CMG-3T) located along a dark fiber DAS transect to measure the true ground motion exciting the fiber and use these

measurements to solve for the broadband (T = 1 - 200 s) amplitude and phase response of a widely-used commercial DAS interrogator (Silixa iDAS v.2). We used teleseismic earthquakes and multiple periods of unusually high amplitude ocean microseism noise as the input signals to probe the DAS instrument response function. As demonstrated by our results, the DAS frequency range is as broad as the broadband seismometer used in the analysis. The amplitude and phase response is flat with respect to true ground velocity in the range T = 10-200 s, but the absolute amplitude level is reduced from true ground motion by a gain factor of -12.75 dB. At T<10 s, DAS phase response is again flat but amplitude response increases and the standard errors also increase. We hypothesize that the amplitude gain factor is related to coupling or an unexplained effect related to the interferometric measurement.

Additional field and laboratory studies are necessary to clarify DAS parameters, including frequency range, instrument response, minimum sensitivity, self-noise, and dynamic range, as well as separate photonic and cable effects, and characterize other important aspects of this new form of seismometery. The instrument comparison methodologies proposed in this work could be applied to other DAS experiments with other DAS instruments as means of inter-array calibration, specifically to understand the observed differences between the recorded DAS amplitude and true ground motion.

Data Access and Acknowledgements

Chapter 6

Marine Geophysics

This Chapter is presently accepted for publication at *Science* as N J Lindsey, T C Dawe, and J B Ajo-Franklin 2019, "Illuminating seafloor faults and ocean dynamics with dark fiber distributed acoustic sensing".

Summary Distributed fiber-optic sensing technology coupled to existing subsea cables allow observation of ocean and solid earth phenomena. We used an optical fiber from the cable supporting the Monterey Accelerated Research System during a 4-day maintenance period with a Distributed Acoustic Sensing instrument operating on shore, creating a ∼10,000-component, 20-kilometer-long seismic array. Recordings of a minor earthquake wavefield identified multiple submarine fault zones. Ambient noise was dominated by shoaling ocean surface waves, but also contained observations of in situ secondary microseism generation, post-low-tide bores, storm-induced sediment transport, infragravity waves, and breaking internal waves. DAS amplitudes in the microseism band tracked sea state dynamics during a storm cycle in the Northern Pacific. These observations highlight the potential of this method for marine geophysics.

Key Findings

- Optical fibers inside seafloor science and telecommunications cables can be utilized with Distributed Acoustic Sensing instruments operating on shore as seismic arrays.

- Recording of a M3.4 minor earthquake wavefield identified multiple submarine fault zones that potentially link the Aptox Fault Zone to the Monterey Canyon.

- Ambient noise recordings were dominated by primary microseisms related to shoaling ocean surface waves, but also contained observations of in situ secondary microseism generation, post-low-tide bores, storm-induced sediment transport, infragravity waves, and breaking internal waves.

- DAS amplitudes in the microseism band tracked sea state dynamics during a storm cycle in the Northern Pacific.

6.1 Background

The underwater environment which envelopes 70% of Earth's surface poses major logistical challenges to seafloor studies. Marine geophysical research is conducted with large research vessels, temporary ocean-bottom seismometers (Deplus et al. 1998), and a limited number of permanent tethered observatories (Barbara Romanowicz et al. 2009; Trowbridge et al. 2019). Emerging float networks, seafloor GNSS, and high-frequency remote sensing are beginning to infill major data gaps with promising near real-time coverage. The impact has included quantification of offshore seismic hazards (Gracia et al. 2003; Ruiz and Madariaga 2018), submarine volcanism (Mittal and Delbridge 2019), marine ecology, and ocean transport (Levin et al. 2019), yet many oceanographic and solid earth processes remain spatially aliased.

Geophysical observations mostly occur on land because technical, logistical and financial challenges hinder sensor array deployments on the ocean floor. Offshore observation gaps have produced critical knowledge gaps and even bias in research areas like marine ecology (Levin et al. 2019), ocean circulation (Wunsch and Ferrari 2018), coastal erosion(Paull et al. 2018), offshore seismic hazards (Gracia et al. 2003; Ruiz and Madariaga 2018), submarine volcanology (Manga et al. 2018), and deep earth structure (Ranasinghe et al. 2018).

This is most obvious in physical oceanography, where hydrodynamics are constrained by single point observations. These experiments often alias complex short spatial wavelength oceanographic processes. To address this challenge, new distributed autonomous sensor networks have been deployed. The ARGO floats (Roemmich et al. 2009) and Ocean Observing Initiative (Cowles et al. 2010) are presently recording pressure, water velocity, salinity, and/or temperature offshore with subgrid, multi-year resolution. These data have already created new insights into cross-shelf and nearshore transport (Trowbridge et al. 2019), ocean mixing, and even eruption observations of difficult to monitor submarine volcanoes (Mittal and Delbridge 2019).

In the field of marine geophysics, experiments are conducted using one of three methodologies: 1) multi-month ocean bottom seismometer campaigns; 2) a small number of tethered observatories (MARS, T Craig Dawe et al. 2005; ALOHA, Howe, Frederick K Duennebier, and Lukas 2015; NEPTUNE, Barnes et al. 2015, AXIAL Kelley, Delaney, and Juniper 2014, S-net Kanazawa et al. 2016); or 3) large marine research vessel cruises that aim to develop seismic reflection images, map bathymetry, and collect samples from the seafloor. Each tool has its limitations (i.e., power, memory, permitting, telemetry, trawling damage, sub-optimal data retrieval rates, operations and maintenance requirements), which amount to major financial costs and often prohibit discovery. Up-scaling any strategy to observe multi-scale physics, and map or monitor hazardous plate boundaries worldwide is difficult to envision.

New seafloor sensing modalities are critical to seismic and tsunamic hazards. In northern California, for example, large Holocene-active seismogenic faults near the Mendocino triple junction, Hosgri and San Gregorio faults, as well as parts of the San Andreas fault are all primarily offshore (Wesnousky 1986; Barbara Romanowicz et al. 2009). Resolution of earth's interior properties are also dependent on the global seismometer distribution. The

recent call for Scientific Monitoring and Reliable Telecommunications (SMART) cables in which sensors would be attached along the 1.5 x 10^9 m of subsea cables at optical repeater sites every 65 km (Howe, Frederick K Duennebier, and Lukas 2015) is estimated to backfill this observational gap by tripling raypath coverage across the Pacific, Indian and Atlantic oceans (Ranasinghe et al. 2018). Moreover, developing new seafloor seismology and ocean acoustics methodologies is necessary for shoreline-crossing research directions that aim to track typhoons and hurricanes in realtime, understand offshore fault properties in connection with slow-slip and subduction zone processes, capture the origins of Earth's ocean microseism noise, and engineer and monitor seafloor infrastructure, among many other applications.

Seafloor Distributed Acoustic Sensing

Fiber-optic sensing is a novel means of recording dense geophysical information onshore (Jousset et al. 2018; Jonathan B Ajo-Franklin et al. 2019), and should be equally useful offshore with existing seafloor optical fibers. Marra et al. 2018 proposed using transmission time-of-flight of ultra-stable laser pulses inside transoceanic subsea fibers to record cable-averaged seafloor strain. To examine seafloor strain with higher spatial resolution, we used backscattered laser pulses with phase-based coherent optical time-domain reflectometry (ϕ-OTDR), otherwise known as Distributed Acoustic Sensing (DAS), inside the Monterey Accelerated Research System (MARS) science cable that spans the continental shelf offshore California (Figure 6.1; Materials and Methods are available as supplementary materials on Science Online). In contrast to Marra et al. 2018, DAS multiplexes the optical analysis and thus resolves the seafloor strain field every 10 meters, which in our case produced an array dataset totalling 3.2 TB in 4 days.

A different style of photonic measurement, presented in this paper, involves phase-based coherent optical time-domain reflectometry (ϕ-OTDR) measurements, or Distributed Acoustic Sensing (DAS). DAS transforms tens of kilometers of a fiber-optic cable into a dense ($\sim$1 m / sensor), Large-N (10,000's of sensing points), broadband ($\sim$1 mHz - 10 kHz) strainmeter array using a stable laser and an optical interferometer connected to one end of a single-mode fiber-optic. Multiplexed dynamic strain measurements are made by rapidly probing the two-way propagation paths of photons injected into the fiber, which travel at known speed and undergo Rayleigh scattering at density fluctuations embedded by standard fiber-optic manufacturing practices (Posey, G. Johnson, and Vohra 2000; Farhadiroushan, T. R. Parker, and S. Shatalin 2009; AH Hartog 2017; Dean, Cuny, and Hartog 2017). In the present DAS archetype, many tens of thousands of optical phase shift measurements are recorded every millisecond and are directly proportional to the strain-rate field resolved over virtual sensing segments of the fiber approximately 10 m long. Depending on the laser wavelength, power, and optical fiber properties, DAS measurements can reach many tens of linear kilometers before optical phase tracking with the backscattered energy degrades below a usable threshold. Since 2015, DAS has been used across the oil and gas industry as an inexpensive replacement to traditional downhole seismic geophone arrays, often utilized for vertical seismic profiling (VSP). Most recently, DAS has been applied to study earth systems,

including earthquakes (Nathaniel J Lindsey et al. 2017; C. Yu et al. 2019; Jousset et al. 2018; Jonathan B Ajo-Franklin et al. 2019; Lellouch et al. 2019), noise Dou et al. 2017; Xiangfang Zeng et al. 2017; Eileen R Martin et al. 2017, and hydrogeology (Becker, Ciervo, M. Cole, et al. 2017; Jonathan B Ajo-Franklin et al. 2019). In the marine context, to our knowledge, DAS has recently begun to be evaluated as an imaging and continuous monitoring tool in deep water 4-D active source oil field experiments (A Mateeva et al. 2017).

6.2 Data

DAS data were collected using a science cable in Monterey Bay, California. The experiment was conducted during 4 days in March 2018 when Monterey Accelerated Research System (MARS) was taken offline for maintanance. The DAS interrogator (Silixa iDAS, v.2) was positioned on a passive vibration isolation table in the building where the cable emerges onshore. Continuous DAS recordings were acquired from March 10 - 14, 2018 with a limited number of brief interruptions due to power outages associated with cable maintenance. An optical time domain reflectometry measurement of the optical fiber used for DAS showed 0.19 dB/km of loss from shore and the MARS node at 52 km, with minimal losses at the instrument connection point. The DAS interrogator used a 10-m gauge length. Laser pulse timing parameters were set to ensure only one outgoing laser pulse was inside the fiber at a time. Channel spacing was set to 2 m, which resulted in 9,984 channels spanning the first 19.968 km of cable length (pink highlighted portion of cable route in Figure 6.1). Data were digitized at 500 samples per second to preserve seismological and oceanographic signals below ∼250 Hz. A GPS antennae provided accurate timing. DAS data were written continuously via USB 3.0 at 250 MB/s to an external hard disk. In total, 3.2 TB of raw optical phase rate data (proportional to strain-rate) were recorded during the 4 day experiment.

Complimentary datasets were compiled from publically available archives (see Figure 6.1 for station locations). Wind speed and direction, significant wave height, and wave density spectra data products were recorded by an accelerometer package onboard NOAA buoy 46042, the only active buoy in Monterey Bay during this experiment. Buoy 46042 is located 20 km from shore and 15 km south of the MARS cable in transitional water depth (http://www.ndbc.noaa.gov/). Buoy data are used in Figures 6.6 and 6.4. NOAA tide gauge 9413745 in Santa Cruz, CA provided 6-minute water level records (https:// tidesandcurrents.noaa.gov/). Tide gauge data are used in Figure 6.6. Continuous onshore seismometer recordings from the Northern California Seismic Network's three-component broadband station SAO (NC.BK.SAO) located 40 km ESE of Moss Landing were downloaded from the Northern California Earthquake Data Center using the ObsPy FDSN Client module. Seismometer data are used in Figure 6.3. Because the MARS node was de-energized, seafloor instruments were not available. This included seismometer NC.BK.MOBB and the seafloor hydroacoustic sensors connected to the MARS node.
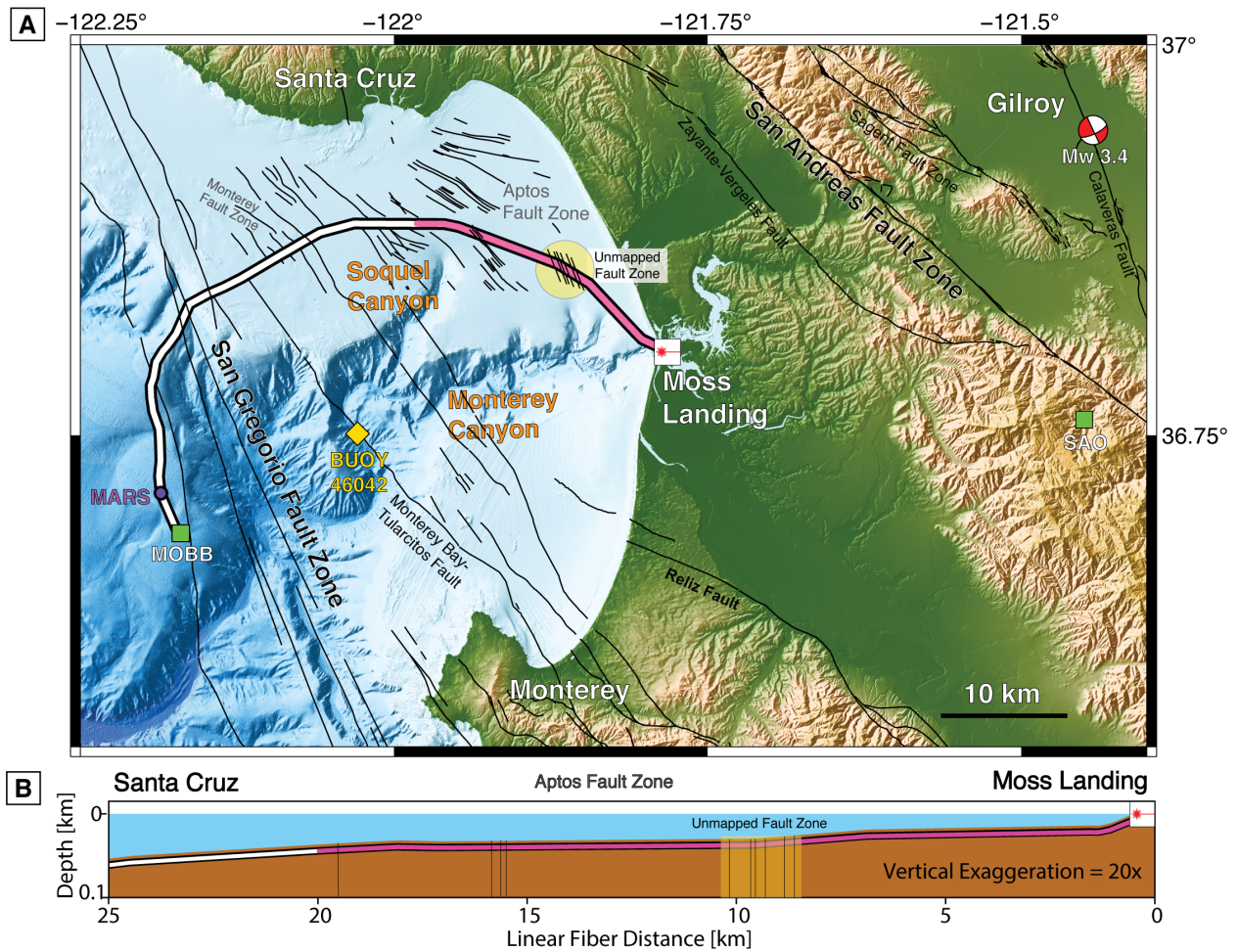
Figure 6.1: Map (A) Map of Monterey Bay, CA shows MARS cable (DAS=pink portion), mapped faults, Gilroy earthquake (star), seismometer (green square), NOAA buoy 46042 (yellow diamond), and major bathymetric features. (B) Cross-section illustration of MARS cable used for DAS [Source: N.L.].

MARS cable design and coupling

The MARS science node is located on the continental slope outside Monterey Bay, California at a depth of 891 m (Figure 6.1). The MARS power and data cable follows a 52-km path across northern slope of Monterey Bay that was chosen to avoid areas of rocky bottom and submarine landslides around Monterey Canyon. Due to the Marine Sanctuary Status of the Monterey Bay the cable path is subject to routine impact assessments; during the most recent the cable was found to be undisturbed Kuhnz et al. 2015. Along most of its route, the MARS cable was buried as much as 1 meter below the seafloor to minimize its effects on marine life and reduce the chance of its being snagged by anchors or fishing gear. This was achieved using a fiber-optic cable laying sled towed by a ship.

The cable used for MARS (Alcatel Submarine Networks OALC4 single armoured cable, documented in 1999; ($http : //www.ic72.com/pdf_file/o/611053.pdf$) was a standard form factor used for repeatered submarine telecommunications. It was 0.028 - 0.031 m in outer diameter, consisting of a core containing 8 single-mode optical fibers and the copper composite electrical conductor, which was surrounded by an insulating sheath, then galvanized steel wires, layers of polypropylene yarn, and all packaged in a synthetic handling compound. No additional details about the outer material's frictional properties are available. The linear mass of this cable in water was 1.4 - 1.8 kg/m. This cable is rated for use at sea depths less than 8 km. This design is meant to resist total stress in order to increase cable lifetime, and so the optical fibers were gel-packed to prevent water penetration and hydrogen. We noted that gel-packed designs are intended to reduce strain transfer.

6.3 Local earthquake wavefield analysis

We recorded the 2018-Mar-11 strike-slip earthquake near Gilroy, CA using the MARS cable. Figure 6.2 shows this earthquake wavefield DAS record after minimal data processing (Materials and Methods). P, pP, PP, S and SS arrivals matched predicted arrival times for the USGS cataloged event solution and cable geometry. The P-wave was barely visible over cable segments, potentially due to particle motion relative to fiber axis ($\theta > 71^o$). Converted pP and PP phases with greater horizontal components were more robustly observed. Time-domain beamforming of the record found that energy arrived with equal components from the epicenteral backazimuth of 81^oN and a direction around 45^oN (Figure 6.2E), interpreted as seismic multipathing through the complex 3-D North American - Pacific plate boundary (Rodgers et al. 2018). A second source of scattering was found to originate from local structure immediately below the seafloor cable.

Following each seismic phase, we observed strong coherent seismic energy propagating outward with apparent velocity of 200 - 600 m/s from discrete points between 15.1 - 16.3 km on the MARS cable, and also between 8.4 - 10.3 km (Figure 6.2B-D). We interpreted this as body wave conversion into Scholte waves at sub-vertical seafloor faults, which act as point scatterers. Scholte waves have Rayleigh-type wave motion and propagate at the ocean-solid
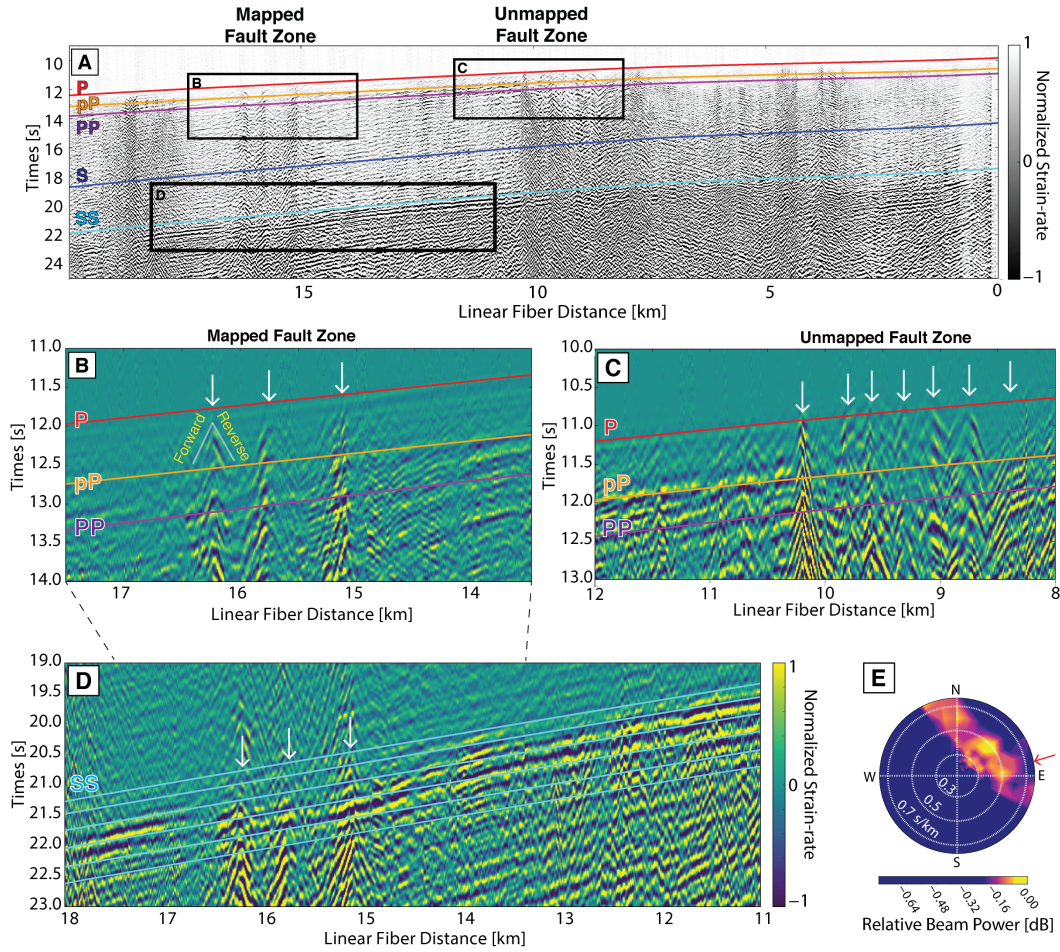
Figure 6.2: M3.4 2018-Mar-11 Gilroy earthquake wavefield (A) Full array observation (0=shore) with predicted seismic phase arrivals (colored lines). (B) Inset shows scattering with recently-mapped submarine fault locations (white arrows). (C) Same as (B) for an unmapped fault zone. (D) Observed 0.25 s wavefront delay in mapped fault zone from (B). Lines show predicted constant phase arrivals immediately following the first SS wavefront. (E) Time-domain beamforming solution shows energy arriving from ENE azimuths, while red arrow shows predicted backazimuth [Source: N.L.].

earth interface. Wavefront tracking of the main SS phase showed slowdown between 14.5 km - 16.5 km, coincident with observed scattering (Figure 6.2D). Assuming wave propagation in the cable axis plane, velocity decreased from 2.1 km/s to 1.2 km/s over less than 1 km. We interpreted this as a waveguide effect where seismic energy interacts with highly-fractured, low-velocity fault zone gouge layers (Y.-G. Li et al. 1990). Similar observations were made for the subsequent M2.7 aftershock.

Recent high-resolution seismic reflection imaging from this section of the continental shelf near Monterey and Soquel canyons identified extensive paleocanyon deposits and the NW-SE striking Aptos Fault Zone, a major step-over relay between the San Andreas Fault Zone onshore and the San Gregorio Fault Zone offshore (S. Y. Johnson et al. 2017; Maier, S. Y. Johnson, and Hart 2018). Four subvertical Aptos faults mapped by (S. Y. Johnson et al. 2017) transect the MARS cable around 15 - 17 km and near 19 km at an oblique angle (Figure 6.1). These fault locations correlate with observed secondary scattering locations from the Gilroy event. We identifed a number of unmapped faults (Figure 6.1 for locations; strike based on regional information) in a segment extending the Aptos Fault Zone 15-20 km SSE parallel to shore, potentially connecting to the Monterey Canyon.

6.3.1 Earthquake data processing

Data processing of the raw DAS data records from the 2018-Mar-11 M3.4 Gilroy earthquake shown in Figure 6.2 involved linear detrending, followed by a standard frequency-wavenumber domain fan filter (f=1-30 Hz; k=0$\pm$0.03 m^{-1} with cosine edge-tapering) to remove dominant ocean and photonic noise (Yilmaz 2001). Then a moving window-median smoothing operator was applied over 3 gauge lengths (30 m) to mitigate photonic fading effects.

6.3.2 Earthquake phase prediction

Synthetic traveltimes for seismic phases from the 2018-Mar-11 M3.4 Gilroy earthquake were computed using a radially-symmetric spectral element forward model provided by the InstaSeis package (Driel et al. 2015). For this numerical calculation we used a modified form of the reference earth model ak135 with a shallow crust model (depth=0-10 km) based on Rodgers et al. 2018. No water boundary condition was employed for the offshore portion. We used the USGS catalog moment tensor solution as the input source. To resolve the distributed sensing channel locations along the cable geometry at a 2-m spacing we interpolated the known cable geometry information delivered by the original cable installation contractor.

6.3.3 Time-domain beamforming with DAS array

According to Rost and C. Thomas 2002, array-based seismic phase observations of differential travel times may be used to solve for the parameters of the propagating plane wave

solution (i.e., backazimuth, horizontal slowness) with a technique known as time-domain beamforming.

Beamforming involves a 2-D grid search over a reasonable range of phase velocities (e.g., $1.5 - 4$ km/s for surface waves) and all possible backazimuths ($\theta = 0 - 360^o$). For any trial solution, station traces (x_i) are numerically shifted in time by the amount proportional to the distance (r_i) between each station and a central reference station/point lying inside the array multiplied by the given plane wave's horizontal slowness (u_{hor}), before summing over all shifted traces ($\tilde{x}_i$) to produce one array "beam trace" (b):

$$b(t) = \frac{1}{M} \sum_{i=1}^{M} \tilde{x}_i(t + r_i * u_{hor}),$$

where M represents the number of stations in the array used to compute b.

One can choose to represent the resulting solution space over all trial beams as any of a number of parameters. We will use the peak power of each beam relative to the maximum peak power found:

$$\bar{B}(\theta, u_{hor}) = log_{10}\left(\frac{B(\theta, u_{hor})}{B_{max}(\theta, u_{hor})}\right)$$

where $B = MaxVal\{||b||^2\}$ and $B_{max} = MaxVal\{B\}$.

Beamforming is easily adapted to DAS arrays (Nathaniel J Lindsey et al. 2017). For the MARS cable DAS array recording of the 2018-Mar-11 M3.4 Gilroy earthquake, we reduced the computational exercise by first trimming the record to include only the first 6 seconds shown in Figure 6.2A ($9 - 15$ seconds after the origin time) and then spatially decimated the array by selecting only the center channel for each 10-m DAS gauge length (20% of the full array). There is no loss in accuracy here based on the wavelength of the highest frequency analyzed ($\lambda = 15$ Hz * 1 km/s = 15 m). We then computed relative time shifts for each gauge length using the center channel from the cabled DAS array as a reference point. We used the catalogued hypocenter as the source position. Normalized DAS records were used to compute all beam traces for 360 bins in backazimuth (1 bin/degree) and 30 bins in horizontal slowness between 0.05 and 0.8 s / km, equivalent to apparent velocities between 1.25 - 20 km/s. Figure 6.2E shows the result of beamforming with the parameter $\bar{B}(\theta, u_{hor})$. Note that on this scale, a value of $\bar{B} = 0$ dB is equivalent to the maximum beam power and $\bar{B} = -0.64$ dB represents a reduction to 86% of peak power.

6.4   Ocean microseism

Ocean-solid earth interactions generate Rayleigh waves between 0.05 Hz and 0.5 Hz which are globally recorded as primary and secondary microseisms (Haubrich and McCamy 1969; Herbers and Guza 1991; Bromirski and Fred K Duennebier 2002; Zhang, Gerstoft, and Bromirski 2010). In principle, horizontal seafloor fibers have zero strain sensitivity to primary microseism (PM) hydrostatic load changes. To test this hypothesis, we fit a PM model based

on buoy wave height records to DAS strain data at 0.05 - 0.15 Hz (Materials and Methods). We found that the DAS records can be explained as PM (Figure S1), likely because the fiber package experiences a Poissonian strain response (Becker, Ciervo, M. Cole, et al. 2017) or an unquantified transverse seafloor current motion in the shallow waters of Monterey Bay.

Tracking microseism energy over 4 days (Figure 6.3), we observed a consistency between buoy wave motion, seafloor DAS strain, and seismometer noise onshore (see Supplementary Materials, Materials and Methods). All three instruments record high amplitudes during the initial period of high storm activity on 2018-Mar-10. Recorded amplitudes decrease as the first storm loses energy, and then increase as the second storm builds. Small absolute frequency shifts and amplitude discrepancies between the three records could be due to a number of variables, including complicated energy partitioning, that is the quality and character of microseism energy conversion at the ocean-continent interface, fiber and seismometer coupling, lateral separation and water depth differences between the buoy and fiber (Bromirski and Fred K Duennebier 2002), and the poor-constraint on ocean site effect (Gualtieri, É. Stutzmann, et al. 2014).

To assess energy partitioning, we decomposed the wavefield in the frequency-wavenumber domain. Shoaling wave loads in shallow water produce PMs (Webb 1998; Bromirski and Fred K Duennebier 2002) that obey the dispersion equation:

$$\omega^2 = gk \tanh(kH)$$

where ω is angular frequency. DAS PM recordings were found to be strongly dispersive (Figure S2). Because PMs are caused by local wave height, outgoing components are due to coast reflection. We thus computed that the reflected PM energy is 1% of the incoming energy.

The leading hypothesis for secondary microseism (SM) generation is that opposing wind-wave trains mix nonlinearly and produce Scholte waves at near-acoustic speeds (Longuet-Higgins 1950b; Hasselmann 1963). Testing this hypothesis requires observation of both opposing ocean waves and the resulting Scholte wave generation, which has only been documented in one deep ocean environment (Muyzert 2007). In Monterey Bay, we observed weak energy at 0.25 - 1.5 Hz and very low wavenumber ($\pm 0.003 m^{-1}$) with symmetric amplitude components traveling at 400-1000 m/s, faster than observed wind-wave speeds. We interpreted this as in situ SM generation ultimately produced by the nonlinear interaction of aforementioned incoming and outgoing wind-waves (see Figure 6.5C). This suggests SMs are generated even when one wind-wave component is vanishingly small. SM amplitudes were 1.5 - 2 dB below PM, likely due to shallow water.

6.4.1 DAS calibration using the primary microseism model

In the shallow water condition of the MARS cable (H = 20 − 50 m), principal oceanographic strain at the seafloor is due to the differential pressure generated by propagating surface gravity wind-waves, otherwise known as the primary ocean microseism (Bromirski
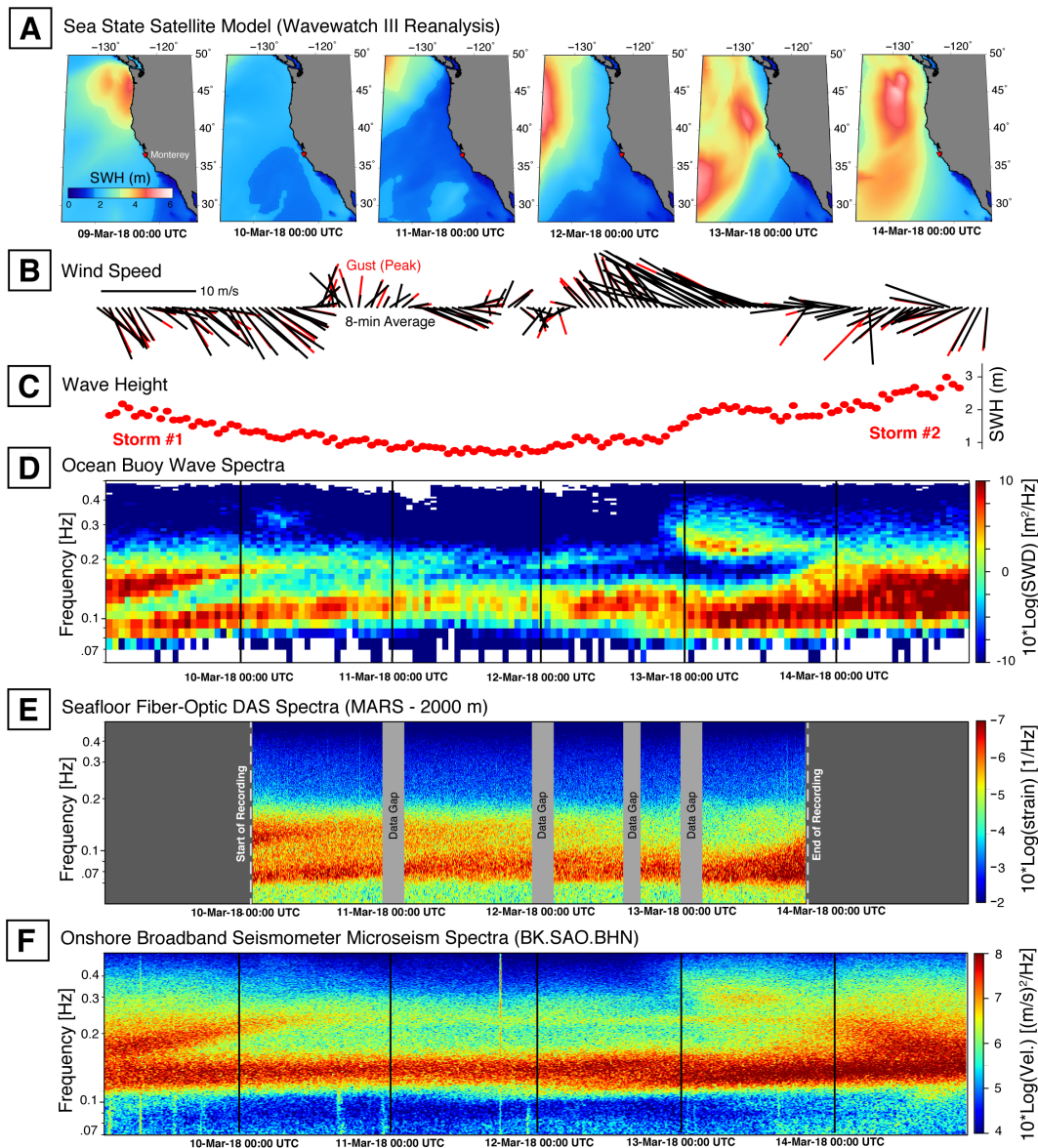
Figure 6.3: Multi-instrument analysis of sea state evolution. (A) Wavewatch III reanalysis of satellite remote sensing data shows ocean wave height outside Monterey Bay (red triangle). (B-D) NOAA buoy 46042 8-min average measurements of wave speed and direction (black) and peak gust (red), and 10-min average wave height and spectral wave density measurements. (E) Seafloor DAS strain from cable location 2 km averaged over a 15-min sliding window. (F) North component of ground velocity from onshore broadband inertial seismometer BK.SAO averaged over a 15-min sliding window. Buoy, DAS and seismometer measurements show time-lapse interactions of primary and secondary ocean microseism between two Pacific storm cycles.
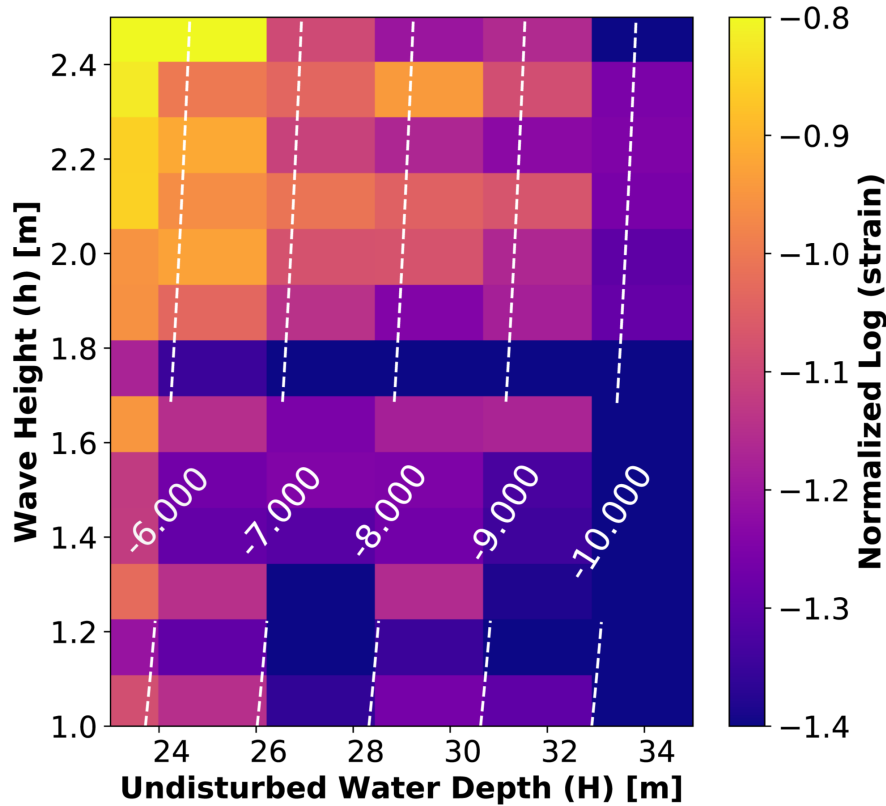
Figure 6.4: Cumulative DAS strain at f=0.056 Hz observed between 1.5 - 20 km during the 4-day experiment. Trends in the recorded strain field are explained by the seafloor pressure predicted using the buoy-observed wave height (white contours) [Source: N.L.].

and Fred K Duennebier 2002). Horizontal seafloor fibers should in principle show zero sensitivity to hydrostatic load changes, yet the strain records show energy in the correct frequency range to be considered primary microseism energy near the coast.

To investigate this further, we analyzed DAS strain records from $1.5 - 20$ km along the MARS cable in the frequency range $0.05 - 0.15$ Hz. From linear wave analysis, the differential pressure related to the primary microseism (P_b) at known water depth (H) is:

$$P_b = \frac{\rho g h}{cosh(kH)}.$$

where the driving force is the sea surface wave amplitude ($\rho g h$, h=wind-wave height), water depth (H) is known from cable installation, and k signifies wavenumber, which was assumed to be 1 m^{-1}. Using buoy wave height time history to estimate h (Figure 6.3C), DAS strain values were summed over 10-minute windows for the experiment (Figure 6.4). The result is overlaid with the primary microseism pressure model (white dashed lines), which we found accurately predicts the first order trends of the DAS data.

6.4.2 Primary microseism wavefield analysis

Leveraging the array-nature of DAS, a 2-D FFT of an evenly-sampled time-distance array of DAS data can be utilized to decompose the wavefield into shoreward-propagating/incoming and seaward-propagating/outgoing components in the frequency-wavenumber domain (Figure 6.5B). We adopt a convention in which the incoming components have negative velocities $(-c = \frac{f}{-k})$ because they propagate from the far end of the cable (channel=9982) to shore (channel=0), while the outgoing waves register as propagating in the positive (cable) direction.

Figure 6.5b shows an example wavefield decomposition for a 5-minute DAS record from 10 - 17 km along the MARS cable shown in Figure 6.5a. Both incoming and outgoing components are dispersive, and match the predicted shallow water wave relationship using an average known water depth of 40 m. One advantage of this wavefield decomposition is that the incoming and reflected energy can now be appraised. We found that the reflected energy constitutes $< 1\%$ of the total, suggesting that the majority of the wave energy is either transferred into the continent or is dissipated.

6.4.3 Secondary microseism wavefield analysis

As explained in the main text, we observed in situ generation of Scholte waves in the form of symmetric incoming and outgoing wave components traveling at near acoustic wave speed. Secondary microseisms are caused by the interaction of oppositely-directed wind-waves with near similar frequency, which lead to nonlinear wave mixing and the emission of an acoustic wave that reaches the seafloor with enough energy to convert into seafloor-bound Scholte waves. This type of wave generation is the dominant microseism generation mode in deep water where the differential wind-wave pressure is insufficient to excite primary microseisms. According to the leading hypothesis for secondary microseism generation, commonly referred to as the Longuet-Higgins-Hasslemann hypothesis after the foundational studies of Longuet-Higgins 1950a and Hasselmann 1963, the generation of secondary microseisms is characterized by Scholte waves which travel outward with equal energy at a speed bound between the acoustic speed of water ($\sim$1500 m/s) and the elastic speed of shallow seafloor sediments (200 - 500 m/s). The frequency of the Scholte waves is predicted to be in the range of the sum of the two wind-wave frequencies. The wavenumber of the Scholte waves is predicted to be in the range of the difference of the two wind-wave wavenumbers.
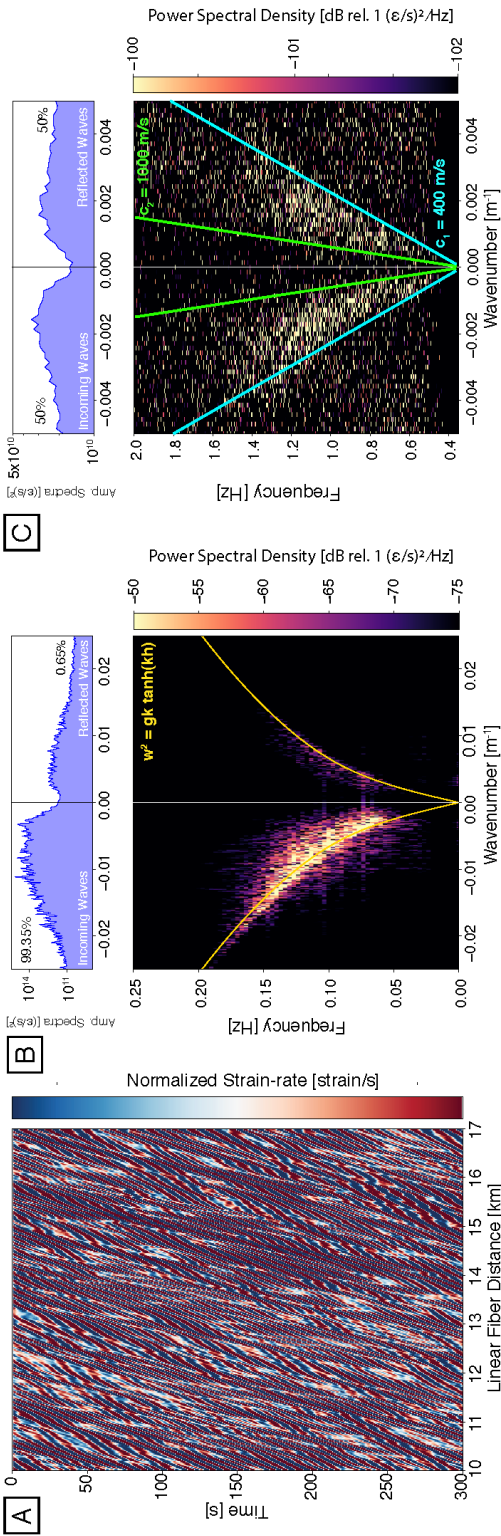
Figure 6.5: Microseism DAS analysis from linear MARS section (10-17 km) on 2018-Mar-10. (A) Raw seafloor strain-rate data reveals a complicated pattern of wave interaction. (B) Primary microseism wavefield separation by frequency-wavenumber projection of (A) shows asymmetric stronger incoming (left) and weaker outgoing/reflected (right) ocean wind-waves. Yellow curves plot the solution for shoaling water waves in shallow water (h=40 m). (C) Secondary microseism separation shows symmetric wave components traveling at near acoustic speed $c_1 < c < c_2$ [Source: N.L.].

Figure 6.5C shows this observation, which is made at a different sector of the frequency and wavenumber space defined previously. The incoming and outgoing components travel outward with equal energy, suggesting in situ generation. The energy was observed to travel between c_1=400 m/s and c_2=1000 m/s in a frequency range around 0.25 - 1.5 Hz and a wavenumber range around ±0.003 m^{-1}.

6.4.4   Satellite remote sensing analysis of storm activity

WaveWatch-III is an operational spectral wave model that incorporates NCEP wind and ice field data resolved every 3-hours on an operational basis (https://polar.ncep.noaa.gov/waves/). Storms manifested in the model as regionally-averaged significant water height maxima around 4-6 m (Figure 6.3A).

On 2018-Mar-09, the first storm (labeled "Storm 1" in Figure 6.3 and Figure 6.6) propagated west-to-east across the North Pacific Ocean where it made landfall on the west coast of North America at the latitude of Oregon, before slowly diminisihing in energy. Beginning on 2018-Mar-11, after approximately 24 hours of quiescence, a second storm ("Storm 2") swept into the area from Alaska. This storm breaks up on 2018-Mar-13, elevating wave height in Monterey Bay. There is an appropriate 3-9 hour phase lag between the satellite observations of the storm and the instrument recordings, which is consistent with the separation between the center of the storm activity and Monterey Bay.

6.5   Broadband hydrodynamic signals

We detected a number of non-microseism hydrodyanmic signals (Figure 6.6). At 0.5 - 5 Hz, we observed decreasing amplitude as the first storm lost energy, consistent with seafloor current-driven sediment transport similar to noise profiles of bedload transport observed onshore near rivers (Hsu, Finnegan, and Brodsky 2011; B Schmandt et al. 2017). At 1 - 2 Hz, we observed transients coincident with rising tide, interpreted as thermal strain related to semi-diurnal internal tidal bores (Carter, Gregg, and Lien 2005; Walter et al. 2012; Cazenave et al. 2011; Colosi et al. 2018). At $0.005 - 0.05$ Hz, we observed tidally-modulated infragravity waves previously observed using the Monterey Bay seismometer supported by MARS Dolenc et al. 2005. At ~ 0.001 Hz, we also observed a strong gliding signal with harmonics declining in energy from 2018-Mar-10. Signal gliding correlated with high and low tide. The signal may be related to the higher harmonics of the Monterey Bay seiche (Breaker, Tseng, and X. Wang 2010), but water level monitoring documented stable seiche amplitudes Park, Sweet, and Heitsenrether 2015. An alternative hypothesis is that this is a solid earth tilt response to slow-moving internal gravity waves, vertical oscillations of the ocean stratification interface, which break near steep bathymetric features such as the Monterey Canyon (Garrett and Munk 1979; Holbrook and Fer 2005; Kunze et al. 2002; Carter, Gregg, and Lien 2005). Internal waves enhance cross-shelf transport of fluid and biology, and are therefore foundational in models of thermohaline ocean circulation and

marine ecology (Alford et al. 2015). Independent of its source, this low frequency DAS signal highlights the potential utility to use this method to study quasi-geodetic strain phenomena.
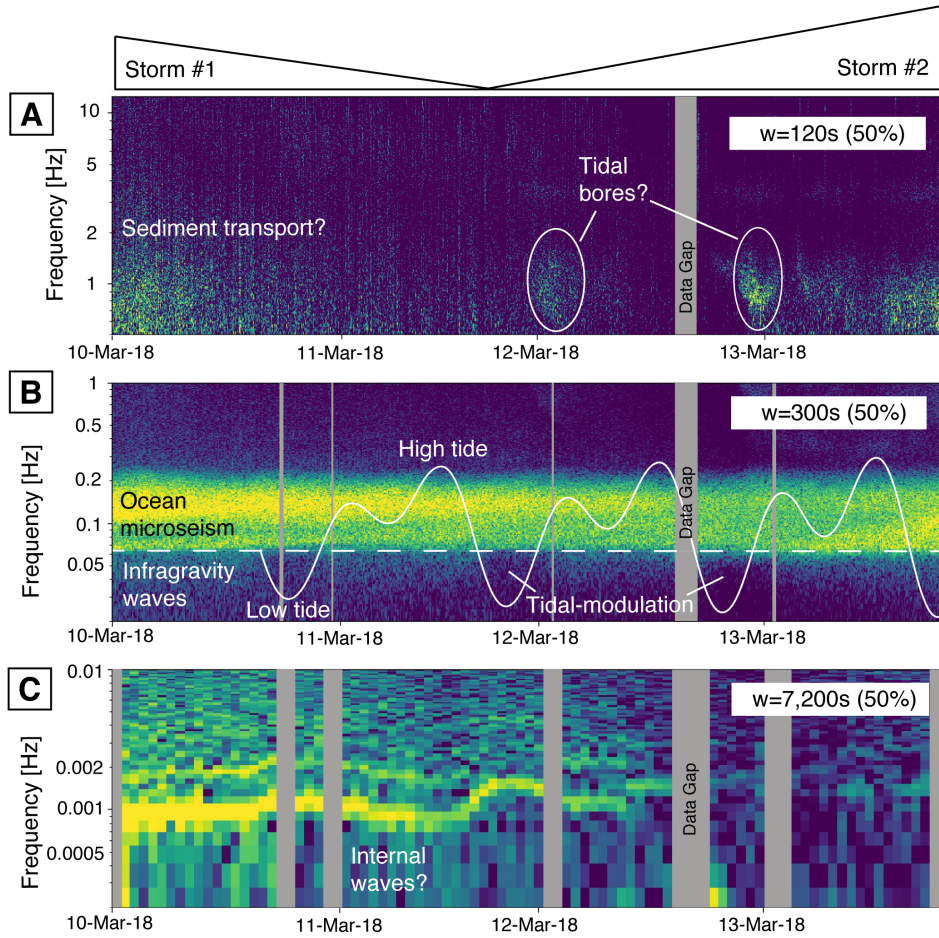
Figure 6.6: Broadband hydrodynamic signals. DAS data for cable location 5.5 km analyzed with a sliding window of 120, 300 or 7200 s duration, 50% overlap. (A) 0.5 - 11 Hz : High-frequency noise consistent with timing of expected storm-induced sediment transport (see Figure 3A for storm activity) and tidal bore activity. (B) 0.02 - 1 Hz : Primary and secondary microseism observations changing energy with storm activity, with tidally-modulated infragravity noise below 0.05 Hz; NOAA tide gauge 9413745 from Santa Cruz, CA plotted for reference (mean lower low waterlevel minimum = -0.03 m, maximum = 1.42). (C) 0.0002 - 0.01 Hz : Tidally-modulated harmonic gliding noise, potentially caused by bay seiche or breaking internal waves at the continental shelf. Data gaps change with window duration [Source: N.L.].

6.6 Concluding remarks

Pairing distributed fiber-optic sensing technologies with subsea fiber-optic telecommunications infrastructure creates the opportunity to validate existing scientific hypotheses. This study, based on a brief experiment during the maintenance period of a scientific cabled observatory, successfully located submarine faults that would be unknown without a marine seismic reflection cruise campaign. It also validated an accepted but unobserved mechanism for how ocean noise is created along coasts. We also documented a number of broadband oceanographic phenomena which have historically only been observable with hydroacoustic, tide gauges, seismometers.

Characterizing offshore fault hazards near densely-populated coastal areas is exceptionally difficult and expensive. The passive offshore imaging techniques demonstrated here with DAS could be utilized to find and orient fault zones, and potentially also characterize fault zone properties. Note that a Large-N seismic experiment with a 100-m station spacing could resolve the bulk seismic wavefront perturbation, but would still alias the secondary scattering off of point scatterers. Adapting seismic imaging techniques to passive earthquake DAS recordings potentially offers additional insight into crustal structure where optical fibers exist (Jousset et al. 2018; C. Yu et al. 2019; Lellouch et al. 2019).

Continuously recording this type of data, effectively expanding our experimental observation window from four days to the average $\sim$ 25-year lifetime of an optical fiber, would enable many different scientific research opportunities. Multi-decadal fiber-optic sensing experiments could also capture the full spectrum of earthquake cycles at active plate boundaries with a longer timeframe that is more representative of the fault recurrence time scale. Broadband DAS observations paired with a distributed static strain sensing (Brillouin DSS, Nikles, Thévenaz, and Robert 1996; Kechavarzi 2016) could effectively measure tectonic creep, interseismic slow-strain, and seismic rupture phases all in one platform, without the need to modify the cable and with only minimal shore instrumentation. Such experiments might also enable recording the oceanographic-seismological sound system as it moves through and responds to tidal, seasonal, annual, and even climatic variability and forcing (Eleonore Stutzmann et al. 2009). Expectations of offshore wind development, deep-sea mining, seafloor data centers, and 5G broadband internet connectivity will continue to drive demand for submarine optical fiber networks, presenting a near-term opportunity for the geoscience community to leverage this expansion as a sensing resource to solve address basic and applied problems.

Data Access and Acknowledgements

Chapter 7

Summary

Distributed fiber-optic acoustic sensing is a newly developed technique that provides access to seismic array datasets in geoscience application areas where logistics historically challenged or prohibited this type of observation. In this dissertation, I applied the DAS technique to study permafrost in Central Alaska, earthquake ground motions on the outskirts of Sacramento, CA, and seafloor faults and near coast hydrodynamics offshore Monterey Bay, CA. This research also featured elements of instrument calibration due to the limited information available about DAS instruments in general and the Silixa iDAS in particular.

In summary, I have shown evidence of the following:

- DAS measures broadband strain (strain-rate) in the frequency range 0.001 - 50 Hz.

- Co-locating a broadband seismometer with a fiber-optic DAS experiment can be used to successfully quantify the experimental instrument response of a DAS fiber system, or in other words calibrate the DAS array to be able to extract absolute ground motion amplitudes in addition to ground motion phase information.

- At periods of 10 - 200 s, there is a 1:1 correspondence between DAS recordings and true ground motion. The phase response is flat over this range, but according to our experimental results DAS amplitude response is reduced below true ground motion by -12.75 dB, potentially due to coupling and/or a photonic effect. At shorter periods of 1 - 10 s, DAS amplitudes increase.

- Continuous DAS records of high frequency (f=1 - 40 Hz) ambient noise can be used to monitor near surface velocity changes due to precipitation and permafrost thaw.

- Vehicle noise recorded with DAS using fiber embedded in horizontal trenches along a road is a reliable source-receiver experimental design for in situ monitoring or seismic imaging; daily averaging of the noise field reduces source field nonstationarity.

- DAS is sensitive enough to record teleseismic, regional, and local earthquake ground motions with either directly-buried experimental fiber laid in a horizontal trench or telecommunication optical fiber inside conduits, onshore or offshore.

- Minor earthquake wavefield observations using DAS provide location of submarine fault zones through wavefield scattering.

- DAS amplitudes in the microseism band track sea state dynamics which can be linked to buoy and onshore seismic datasets.

- Near coast ambient noise DAS recordings are dominated by primary microseisms related to shoaling ocean surface waves recorded in shallow water depth, but also contain observations of in situ secondary microseism generation, post-low-tide bores, storm-induced sediment transport, infragravity waves, and breaking internal waves.

Looking forward, there are many opportunities to grow this research, both in breadth and depth. Below, as a way of concluding this dissertation, I speculatively consider questions linked to several major themes as potential future pathways for continued exploration.

Technical outstanding questions about DAS methodology

Several instrumentation questions related to DAS and fiber-optic sensing stand in the way of the usefulness of the method for many in the earth science community. For example, surface waves generated by passenger trains can be commonly observed with DAS and appear to rapidly change amplitude over the span of a few tens to hundreds of meters. If this effect is a real ground motion effect it could motivate use of DAS for study of near surface ground motion amplification, but due to the uncertainty surrounding the DAS technique and instrument it is necessary to first confirm that the observed amplitude variability is not the result of optical fading or coupling. In fact, at the time of writing, no publication has interpreted absolute amplitudes of DAS data, which is a testament to the utility of seismic phase information.

Along these lines, I am interested in several instrumentation questions regarding fiber sensing:

- What is the possible low frequency range of DAS?

- How does the system-level DAS instrument response (amplitude and phase) depend on particular fiber, cable, installation, and photonic design variables?

- What are the potential sources of DAS measurement noise? What is the self-noise of DAS instruments?

- What is the dynamic range of DAS? Why might DAS data clip? Can this be circumvented?

- How can DAS and DSS methods be optimally integrated given their different strengths in dynamic and static strain sensing to address questions with months to decade timescales (e.g., fault creep)?

At the time of writing, DAS parameter performance testing guidelines are available (SEAFOM MSP-02, `https://seafom.com/?mdocs-file=1270`) but various instrument parameters are not available. Indeed, one recommendation of this thesis is that DAS performance be evaluated in a standard way.

An additional practical question for the seismological community relates to the storage, sharing and management of DAS data. Figure 7.1 shows how the DAS data volume recorded by our research group over the experiments I helped conduct during this thesis (259 TB) compares with the total volume of seismic data archived by the Incorporated Research Institutions for Seismology (510 TB). Many more petabytes of DAS data have been recorded by colleagues at LBNL, and other academic and government agencies. This data volume raises several important questions, including where to archive these data sets, particularly because of the need to colocate storage and compute infrastructure, and how to share these large volumes when upload/download is significant. Future efforts are required to address this practical need in the community with possible strategies to pursue in the near term being data product standardization and cloud storage.
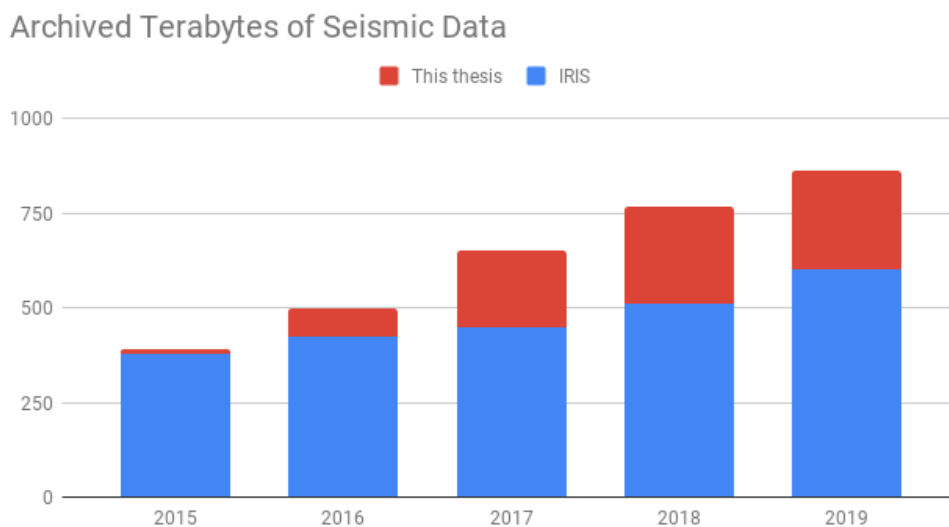
Figure 7.1: Total archived volume of all seismic data at the time of my PhD. From 2014 to 2018, this conservative estimate of the DAS experimental data involving LBNL amounted to half of all new seismic data [Source: N.L.].

Questions about cryosphere processes

Global climate change is modifying the Arctic. Understanding or predicting how landscape and infrastructure will respond to this change requires model calibration with field evidence; however, field datasets have historically been limited (Walvoord and Kurylyk

2016; A. M. Wagner, Nathaniel J Lindsey, et al. 2018; James et al. 2017). As a result, numerical and theoretical process models explaining how permafrost and periglcial terrains degrade outpace real data. What is needed is dense, long-range, long-term data collection methodologies such as distributed fiber-optic geophysics, inexpensive sensor networks, and high-frequency earth observation (Jiang et al. 2019), complemented by on-the-ground campaign geophysical surveys, core analysis, and distributed vertical profiling (Léger et al. 2019). To be effective in climate simulation studies, the results of these decameterscale-to-fieldscale studies must be upscaled to the granularity of watersheds. I am also interested in how these sensor networks could be leveraged for pipeline, road, and rail monitoring as it relates to thaw and subsidence hazards.

Within this area, I am interested in the following questions:

- Why do shallow seismic waves slowdown when it rains in Alaska, but not California?

- Is permafrost thaw gradual or punctuated? What are the critical timescales for early warning based on in situ geophysical sensing?

- How do catastrophic thaw slump features initiate?

- How is lateral heat and fluid transport possible in low-permeability permafrost systems?

- How does fire and precipitation prepare permafrost for thaw?

- How does climate affect the distribution of thermokarst lake geomorphology?

- Do solifluction lobes emit or sequester carbon?

- Does high latitude train derailment correlate with degrading permafrost?

- What is the optimal design for a permafrost thaw early warning system?

Questions about urban utilization and anthropogenic seismic sources

We interact with the outer most layer of Earth's crust in a profound way. Anthropogenic noise is the superposition of thousands of unique seismic wave-generating activities that contribute to the seismic background on continents. At present the seismological community has recently begun to disentangle this noise field into the level of individual cars, trucks and trains as moving noise sources for the purposes of time-lapse seismic imaging (Vs30) of shallow hydrogeology (Dou et al. 2017; J.B. Ajo-Franklin et al. 2019; Brenguier et al. 2019). Understanding individual anthropogenic noise sources enables new subsurface imaging opportunities inside cities (Brandon Schmandt and Clayton 2013; Riahi and Gerstoft 2015; Dıaz et al. 2017), with an eventual aim to develop smart infrastructure and long-term critical infrastructure health-monitoring strategies. Simultaneously, there is a complementary renewed interest in environmental seismology and using natural and anthropogenic noise to

probe aquifers, rivers, landslide processes, and shallow energy reservoirs (Tsai et al. 2012; Clements and Denolle 2018; Gualtieri, Camargo, et al. 2018). This research also crosscuts an important geohealth initiative to build accessible capabilities to monitor unhealthy levels of road traffic and industrial noise in urban areas globally (Apparicio et al. 2018).

Some of the questions I am interested in addressing in this area include:

- What is the source physics description of a car? How does it differ from a truck or train?

- How accurate is source inversion of dense road noise? Can we discriminate vehicle type?

- What does vehicle roadbed deflection tell us about shallow soil properties and vehicle mass?

- How can building mode resonances be measured, monitored, and analyzed (DAS, accelerometers, rotational sensors)?

- How can building mode resonances be used following damaging earthquakes to rapidly quantify structural integrity?

- Can we measure groundwater runoff in cities using vehicles?

- How can we monitor aging levees for seepage and structural integrity?

Questions about seafloor science

The seafloor is a poorly observed critical interface where geology controls interactions of physical, biological, and chemical systems (e.g., Manga et al. 2018; Cowles et al. 2010). Several outstanding questions could be asked about this unexplored research area, but with DAS I am interested in the ways in which dense seismic array datasets that are several tens of kilometers in aperture can be used to study basic questions about seafloor structure, ocean-solid earth interaction, and also be applied to use in early warning, hazard analysis related to storms, earthquakes, tsunami, and submarine landslides, and seafloor infrastructure studies (e.g. deep sea mining, submarine data centers, offshore wind).

The questions I am interested in asking in the future in the area of seafloor science include:

- How is the continental shelf organized?

- What forces govern cross-shelf transport?

- How are ocean microseisms produced? How much microseism energy enters the continent?

- Do offshore faults behave in the same way as onshore faults?

- What is the limit of passive earthquake wavefield imaging?

- How do seafloor fault properties change through the earthquake cycle?

- What is the background ocean soundscape? Where do these signals come from? (e.g., breaking waves in surf zone, cavitation in methane bubble plumes, marine mammals, shipping traffic)

- Can we teach a computer to track whales, ships, and storms using underwater acoustics?

- How does methane migrate, accumulate, and exit the seafloor?

- How do seafloor structures (e.g. canyons, shelf) affect life, chemistry, and soundscape?

- How does seafloor porosity evolve? (long-term, seasonal/storm/tidal cycles, between waves)

- Are submarine canyons episodically triggered? If so, how?

- How does bathymetry and coastline geometry dictate storm evolution, patterns of coastal erosion, spatiotemporal distributions of continental ambient seismic noise?

- What is the optimal network geometry for offshore/onshore earthquake early warning?

Extending the DAS experiment in Montery Bay covered in Chapter 6 to a time series spanning several months to years will fill in the current observational gap and clarify how the processes observed in a short experiment dynamically vary across storm, tide, and seasonal cycles (Dolenc et al. 2005; Gualtieri, É. Stutzmann, et al. 2014). In the future, it may also be possible to couple this type of fiber-optic sensing experiment with submersible pressure vessels to study the deep ocean, and engineered fibers to enhance the sensitivity to strain and record >250 km apertures of seismic, strain and temperature fields off the shelf-break, on the flanks of seafloor volcanoes and vents, and across deep-water faults.

Bibliography

Agnew, Duncan Carr and Frank K Wyatt (2003). "Long-base laser strainmeters: a review". In: *UC San Diego: Scripps Institution of Oceanography.*

Ajo-Franklin, J.B. et al. (2019). "Distributed Acoustic Sensing Using Dark Fiber for Near-Surface Characterization and Broadband Seismic Event Detection". In: *Scientific reports* 9.1, p. 1328.

Ajo-Franklin, Jonathan B et al. (2019). "Distributed Acoustic Sensing Using Dark Fiber for Near-Surface Characterization and Broadband Seismic Event Detection". In: *Scientific reports* 9.1, p. 1328.

Aki, Keiiti and Paul G Richards (2002). *Quantitative seismology.* 2nd ed. University Science Books.

Alford, Matthew H et al. (2015). "The formation and fate of internal waves in the South China Sea". In: *Nature* 521.7550, p. 65.

Apparicio, Philippe et al. (2018). "Exposure to noise and air pollution by mode of transportation during rush hours in Montreal". In: *Journal of Transport Geography* 70, pp. 182–192.

Ardhuin, Fabrice, Lucia Gualtieri, and Eléonore Stutzmann (2015). "How ocean waves rock the Earth: Two mechanisms explain microseisms with periods 3 to 300 s". In: *Geophysical Research Letters* 42.3, pp. 765–772.

Aster, Richard C, Brian Borchers, and Clifford H Thurber (2018). *Parameter estimation and inverse problems.* Elsevier.

Atchley, Adam L et al. (2015). "Using field observations to inform thermal hydrology models of permafrost dynamics with ATS (v0. 83)". In: *Geoscientific Model Development Discussions (Online)* 8.4.

Bakku, Sudhish Kumar (2015). "Fracture characterization from seismic measurements in a borehole". PhD thesis. Massachusetts Institute of Technology.

Barnes, CR et al. (2015). "NEPTUNE Canada: Installation and initial operation of the world's first regional cabled ocean observatory". In: *Seafloor Observatories.* Springer, pp. 415–438.

Barnoski, MK and SM Jensen (1976). "Fiber waveguides: a novel technique for investigating attenuation characteristics". In: *Applied optics* 15.9, pp. 2112–2115.

Becker, C Ciervo, M Cole, et al. (2017). "Fracture hydromechanical response measured by fiber optic distributed acoustic sensing at milliHertz frequencies". In: *Geophysical Research Letters* 44.14, pp. 7295–7302.

Becker, C Ciervo, and T Coleman (2018). "Laboratory testing of low frequency strain measured by distributed acoustic sensing". In: *SEG Technical Program Expanded Abstracts 2018*. Society of Exploration Geophysicists, pp. 4963–4966.

Becker and Thomas Coleman (2019). "Distributed Acoustic Sensing of Strain at Earth Tide Frequencies". In: *Sensors* 19.9, p. 1975.

Benioff, Hugo (1935). "A linear strain seismograph". In: *Bulletin of the Seismological Society of America* 25.4, pp. 283–309.

Bense, VF et al. (2012). "Permafrost degradation as a control on hydrogeological regime shifts in a warming climate". In: *Journal of Geophysical Research: Earth Surface* 117.F3.

Bensen, GD et al. (2007). "Processing seismic ambient noise data to obtain reliable broadband surface wave dispersion measurements". In: *Geophysical Journal International* 169.3, pp. 1239–1260.

Beyens, L et al. (2009). "Are soil biota buffered against climatic extremes? An experimental test on testate amoebae in arctic tundra (Qeqertarsuaq, West Greenland)". In: *Polar biology* 32.3, pp. 453–462.

Beyreuther, Moritz et al. (2010). "ObsPy: A Python toolbox for seismology". In: *Seismological Research Letters* 81.3, pp. 530–533.

Blum, John A, Scott L Nooner, and Mark A Zumberge (2008). "Recording Earth strain with optical fibers". In: *IEEE Sensors Journal* 8.7, pp. 1152–1160.

Bóna, A et al. (2017). "Amplitude and phase response of DAS receivers". In: *79th EAGE Conference and Exhibition 2017*.

Bowden, Daniel C, Victor C Tsai, and Fan-Chi Lin (2017). "Amplification and attenuation across USArray using ambient noise wavefront tracking". In: *Journal of Geophysical Research: Solid Earth* 122.12, pp. 10–086.

Breaker, Laurence C, Yu-heng Tseng, and Xiaochun Wang (2010). "On the natural oscillations of Monterey Bay: Observations, modeling, and origins". In: *Progress in Oceanography* 86.3-4, pp. 380–395.

Brenguier, F et al. (2019). "Train traffic as a powerful noise source for monitoring active faults with seismic interferometry". In: *Geophysical Research Letters*.

Bromirski, Peter D and Fred K Duennebier (2002). "The near-coastal microseism spectrum: Spatial and temporal wave climate relationships". In: *Journal of Geophysical Research: Solid Earth* 107.B8.

Campillo, Michel and Anne Paul (2003). "Long-range correlations in the diffuse seismic coda". In: *Science* 299.5606, pp. 547–549.

Carter, Glenn S, Michael C Gregg, and Ren-Chieh Lien (2005). "Internal waves, solitary-like waves, and mixing on the Monterey Bay shelf". In: *Continental Shelf Research* 25.12-13, pp. 1499–1520.

Cazenave, François et al. (2011). "High-resolution surveys of internal tidal waves in Monterey Bay, California, using an autonomous underwater vehicle". In: *Limnology and Oceanography: Methods* 9.12, pp. 571–581.

Chadburn, Sarah E et al. (2017). "An observation-based constraint on permafrost loss as a function of global warming". In: *Nature Climate Change* 7.5, p. 340.

Clements, Timothy and Marine A Denolle (2018). "Tracking groundwater levels using the ambient seismic field". In: *Geophysical Research Letters* 45.13, pp. 6459–6465.

Cole, Steve et al. (2018). "Source parameter estimation from DAS microseismic data". In: *SEG Technical Program Expanded Abstracts 2018*. Society of Exploration Geophysicists, pp. 4928–4932.

Collette, Christophe et al. (2012). "Inertial sensors for low-frequency seismic vibration measurement". In: *Bulletin of the seismological society of America* 102.4, pp. 1289–1300.

Colosi, John A et al. (2018). "Statistics of internal tide bores and internal solitary waves observed on the inner continental shelf off Point Sal, California". In: *Journal of Physical Oceanography* 48.1, pp. 123–143.

Cowles, Tim et al. (2010). "The ocean observatories initiative: Sustained ocean observing across a range of spatial scales". In: *Marine Technology Society Journal* 44.6, pp. 54–64.

Curtis, Andrew et al. (2006). "Seismic interferometry—Turning noise into signal". In: *The Leading Edge* 25.9, pp. 1082–1092.

Dafflon, Baptiste et al. (2016). "Geophysical estimation of shallow permafrost distribution and properties in an ice-wedge polygon-dominated Arctic tundra region". In: *Geophysics* 81.1, WA247–WA263.

Dakin, J and C Lamb (1991). "A sensing method employing a fibre optic sensor system". In: *WIPO Patent Appl. WO/1991/002946*.

Daley, Thomas M et al. (2013). "Field testing of fiber-optic distributed acoustic sensing (DAS) for subsurface seismic monitoring". In: *The Leading Edge* 32.6, pp. 699–706.

Daley, TM et al. (2016). "Field testing of modular borehole monitoring with simultaneous distributed acoustic sensing and geophone vertical seismic profiles at Citronelle, Alabama". In: *Geophysical Prospecting* 64.5, pp. 1318–1334.

Dawe, T Craig et al. (2005). "Operational Support of regional cabled observatories The MARS Facility". In: *Proceedings of OCEANS 2005 MTS/IEEE*. IEEE, pp. 1–6.

Dean, Cuny, and Hartog (2017). "The effect of gauge length on axially incident P-waves measured using fibre optic distributed vibration sensing". In: *Geophysical Prospecting* 65.1, pp. 184–193.

Deplus, Christine et al. (1998). "Direct evidence of active deformation in the eastern Indian oceanic plate". In: *Geology* 26.2, pp. 131–134.

Dijkstra, Edsger W (1959). "A note on two problems in connexion with graphs". In: *Numerische mathematik* 1.1, pp. 269–271.

Dıaz, Jordi et al. (2017). "Urban seismology: On the origin of earth vibrations within a city". In: *Scientific reports* 7.1, p. 15296.

Dolenc, David et al. (2005). "Observations of infragravity waves at the Monterey ocean bottom broadband station (MOBB)". In: *Geochemistry, Geophysics, Geosystems* 6.9.

Dou, Shan et al. (2017). "Distributed acoustic sensing for seismic monitoring of the near surface: A traffic-noise interferometry case study". In: *Scientific reports* 7.1, p. 11620.

Draganov, Deyan et al. (2009). "Reflection images from ambient seismic noise". In: *Geophysics* 74.5, A63–A67.

— (2013). "Seismic exploration-scale velocities and structure from ambient seismic noise (¿ 1 Hz)". In: *Journal of Geophysical Research: Solid Earth* 118.8, pp. 4345–4360.

Driel, M van et al. (2015). "Instaseis: Instant global seismograms based on a broadband waveform database". In: *Solid Earth* 2, pp. 701–717.

Dziewonski, Adam M and Don L Anderson (1981). "Preliminary reference Earth model". In: *Physics of the earth and planetary interiors* 25.4, pp. 297–356.

Ekström, G (2017). "Short-period surface-wave phase velocities across the conterminous United States". In: *Physics of the Earth and Planetary Interiors* 270, pp. 168–175.

Ekström, Göran (2011). "A global model of Love and Rayleigh surface wave dispersion and anisotropy, 25-250 s". In: *Geophysical Journal International* 187.3, pp. 1668–1686.

Ermert, Laura, Antonio Villasenor, and Andreas Fichtner (2015). "Cross-correlation imaging of ambient noise sources". In: *Geophysical Journal International* 204.1, pp. 347–364.

Farhadiroushan, Mahmoud, T Richard Parker, and Sergey Shatalin (2009). "Method and apparatus for optical sensing". In: *WO2010136810A2*.

Felzer, Karen R (2008). *Calculating California seismicity rates*. Tech. rep. Geological Survey (US).

Fortier, Richard, Anne-Marie LeBlanc, and Wenbing Yu (2011). "Impacts of permafrost degradation on a road embankment at Umiujaq in Nunavik (Quebec), Canada". In: *Canadian Geotechnical Journal* 48.5, pp. 720–740.

French, Scott W and Barbara Romanowicz (2015). "Broad plumes rooted at the base of the Earth's mantle beneath major hotspots". In: *Nature* 525.7567, p. 95.

Frohn, Robert C, Kenneth M Hinkel, and Wendy R Eisner (2005). "Satellite remote sensing classification of thaw lakes and drained thaw lake basins on the North Slope of Alaska". In: *Remote sensing of environment* 97.1, pp. 116–126.

Gabai, Haniel and Avishay Eyal (2016). "On the sensitivity of distributed acoustic sensing". In: *Optics letters* 41.24, pp. 5648–5651.

Garrett, Christopher and Walter Munk (1979). "Internal waves in the ocean". In: *Annual review of fluid mechanics* 11.1, pp. 339–369.

Ge, Shemin et al. (2011). "Exchange of groundwater and surface-water mediated by permafrost response to seasonal and long term air temperature variation". In: *Geophysical Research Letters* 38.14.

Gilbert, F and G Backus (1966). "Propagator matrices in elastic wave and vibration". In:

Goldstein, Peter et al. (2003). "SAC2000: Signal processing and analysis tools for seismologists and engineers". In: *The IASPEI International Handbook of Earthquake and Engineering Seismology* 81, pp. 1613–1620.

Gracia, Eulalia et al. (2003). "Mapping active faults offshore Portugal (36 N–38 N): implications for seismic hazard assessment along the southwest Iberian margin". In: *Geology* 31.1, pp. 83–86.

Grattan, KTV and BT Meggitt (2000). "Optical Fibre Sensor Technology: Advanced Applications-Bragg Gratings and Distributed Sensors". In: *City University, London, UK*.

Grosse, Guido et al. (2016). "Changing permafrost in a warming world and feedbacks to the Earth system". In: *Environmental Research Letters* 11.4, p. 040201.

Gualtieri, Lucia, Suzana J Camargo, et al. (2018). "The persistent signature of tropical cyclones in ambient seismic noise". In: *Earth and Planetary Science Letters* 484, pp. 287–294.

Gualtieri, Lucia, Éléonore Stutzmann, et al. (2014). "Modelling the ocean site effect on seismic noise body waves". In: *Geophysical Journal International* 197.2, pp. 1096–1106.

Gutierrez, Carlos I (2011). "Preliminary geologic map of the Sacramento 30× 60 quadrangle, California". In: *California Geol. Surv. Regional Geologic Map Series* 1.100,000.

Hadziioannou, Céline et al. (2009). "Stability of monitoring weak changes in multiply scattering media with ambient noise correlation: Laboratory experiments". In: *The Journal of the Acoustical Society of America* 125.6, pp. 3688–3695.

Hanson, Paul J, Kenneth W Childs, et al. (2011). "A method for experimental heating of intact soil profiles for application to climate change experiments". In: *Global Change Biology* 17.2, pp. 1083–1096.

Hanson, Paul J, Jeffery S Riggs, et al. (2017). "Attaining whole-ecosystem warming using air and deep-soil heating methods with an elevated CO_2 atmosphere". In: *Biogeosciences (Online)* 14.4.

Harris, Stuart A (2019). *The permafrost environment*. Routledge.

Hartog, AH (2017). *An introduction to distributed optical fibre sensors*. CRC Press.

Hartog, Arthur et al. (2014). "Vertical seismic optical profiling on wireline logging cable". In: *Geophysical Prospecting* 62.4, pp. 693–701.

Haskell, Norman A (1953). "The dispersion of surface waves on multilayered media". In: *Bulletin of the seismological Society of America* 43.1, pp. 17–34.

Hasselmann, K (1963). "A statistical analysis of the generation of microseisms". In: *Reviews of Geophysics* 1.2, pp. 177–210.

Haubrich, Richard A and Keith McCamy (1969). "Microseisms: Coastal and pelagic sources". In: *Reviews of Geophysics* 7.3, pp. 539–571.

Hayashi, Masaki (2013). "The cold vadose zone: Hydrological and ecological significance of frozen-soil processes". In: *Vadose Zone Journal* 12.4.

Hecht, Eugene (1998). *Optics 4th edition. Optics.* Vol. 1, p. 1998.

Herbers, THC and RT Guza (1991). "Wind-wave nonlinearity observed at the sea floor. Part I: Forced-wave energy". In: *Journal of physical oceanography* 21.12, pp. 1740–1761.

Herrmann, Robert B (2013). "Computer programs in seismology: An evolving tool for instruction and research". In: *Seismological Research Letters* 84.6, pp. 1081–1088.

Hinkel, Kenneth M and John K Hurd Jr (2006). "Permafrost destabilization and thermokarst following snow fence installation, Barrow, Alaska, USA". In: *Arctic, Antarctic, and Alpine Research* 38.4, pp. 530–539.

Hohensinn, Roland and Alain Geiger (2018). "Stand-Alone GNSS Sensors as Velocity Seismometers: Real-Time Monitoring and Earthquake Detection". In: *Sensors* 18.11, p. 3712.

Holbrook, W Steven and Ilker Fer (2005). "Ocean internal wave spectra inferred from seismic reflection transects". In: *Geophysical Research Letters* 32.15.

Howe, Bruce M, Frederick K Duennebier, and Roger Lukas (2015). "The ALOHA cabled observatory". In: *SEAFLOOR OBSERVATORIES*. Springer, pp. 439–463.

Hsu, Leslie, Noah J Finnegan, and Emily E Brodsky (2011). "A seismic signature of river bedload transport during storm events". In: *Geophysical Research Letters* 38.13.

Hubbard, Susan S et al. (2013). "Quantifying and relating land-surface and subsurface variability in permafrost environments using LiDAR and surface geophysical datasets". In: *Hydrogeology Journal* 21.1, pp. 149–169.

Hunter, John D (2007). "Matplotlib: A 2D graphics environment". In: *Computing in science & engineering* 9.3, p. 90.

Hutt, Charles R et al. (2009). "Guidelines for standardized testing of broadband seismometers and accelerometers". In: *US Geol. Surv. Open-File Rept* 1295, p. 62.

Hutton, Kate, Jochen Woessner, and Egill Hauksson (2010). "Earthquake monitoring in southern California for seventy-seven years (1932–2008)". In: *Bulletin of the Seismological Society of America* 100.2, pp. 423–446.

Inbal, Asaf, Robert W Clayton, and Jean-Paul Ampuero (2015). "Imaging widespread seismicity at midlower crustal depths beneath Long Beach, CA, with a dense seismic array: Evidence for a depth-dependent earthquake size distribution". In: *Geophysical Research Letters* 42.15, pp. 6314–6323.

Inbal, Asaf, Tudor Cristea-Platon, et al. (2018). "Sources of long-range anthropogenic noise in Southern California and implications for tectonic tremor detection". In: *Bulletin of the Seismological Society of America* 108.6, pp. 3511–3527.

IRIS-PASSCAL (2019). *Sensor Comparison Chart*. URL: https://www.passcal.nmt.edu/content/instrumentation/sensors/sensor-comparison-chart (visited on 01/23/2019).

James, SR et al. (2017). "Improved moving window cross-spectral analysis for resolving large temporal seismic velocity changes in permafrost". In: *Geophysical Research Letters* 44.9, pp. 4018–4026.

Jiang, Ziyu et al. (2019). "ArcticNet: A Deep Learning Solution to Classify Arctic Wetlands". In: *arXiv preprint arXiv:1906.00133*.

Johnson, Lane R and Walt Silva (1981). "The effects of unconsolidated sediments upon the ground motion during local earthquakes". In: *Bulletin of the Seismological Society of America* 71.1, pp. 127–142.

Johnson, Samuel Y et al. (2017). "The California Seafloor and Coastal Mapping Program–Providing science and geospatial data for California's State Waters". In: *Ocean & coastal management* 140, pp. 88–104.

Jorgenson, M Torre, Yuri L Shur, and Erik R Pullman (2006). "Abrupt increase in permafrost degradation in Arctic Alaska". In: *Geophysical Research Letters* 33.2.

Jousset, Philippe et al. (2018). "Dynamic strain determination using fibre-optic cables allows imaging of seismological and structural features". In: *Nature communications* 9.1, p. 2509.

Juškaitis, R et al. (1992). "Distributed interferometric fiber sensor system". In: *Optics letters* 17.22, pp. 1623–1625.

Kanazawa, Toshihiko et al. (2016). "S-net project, cabled observation network for earthquakes and tsunamis". In: *Abstract WE2B–3, Presented at SubOptic 2016*, pp. 18–21.

Karrenbach, Martin et al. (2018). "Fiber-optic distributed acoustic sensing of microseismicity, strain and temperature during hydraulic fracturing". In: *Geophysics* 84.1, pp. D11–D23.

Kechavarzi, Cedric (2016). "Distributed fibre optic strain sensing for monitoring civil infrastructure: a practical guide". In: ICE.

Kelley, Deborah S, John R Delaney, and S Kim Juniper (2014). "Establishing a new era of submarine volcanic observatories: Cabling Axial Seamount and the Endeavour Segment of the Juan de Fuca Ridge". In: *Marine Geology* 352, pp. 426–450.

Kokelj, S V and MT Jorgenson (2013). "Advances in thermokarst research". In: *Permafrost and Periglacial Processes* 24.2, pp. 108–119.

Kokelj, Steven V et al. (2017). "Climate-driven thaw of permafrost preserved glacial landscapes, northwestern Canada". In: *Geology* 45.4, pp. 371–374.

Kong, Qingkai et al. (2016). "MyShake: A smartphone seismic network for earthquake early warning and beyond". In: *Science advances* 2.2, e1501055.

Krassovski, MB et al. (2015). "A comprehensive data acquisition and management system for an ecosystem-scale peatland warming and elevated CO_2 experiment". In: *Geoscientific Instrumentation, Methods and Data Systems (Online)* 4.2.

Kreger, Stephen T et al. (2015). "Distributed Rayleigh scatter dynamic strain sensing above the scan rate with optical frequency domain reflectometry". In: *Proc. of SPIE Vol. 9480 948006-1, Fiber Optic Sensors and Applications XII*. Vol. 13, p. 270.

Krischer, Lion et al. (2015). "ObsPy: A bridge for seismology into the scientific Python ecosystem". In: *Computational Science & Discovery* 8.1, p. 014003.

Kuhnz, LA et al. (2015). "Potential impacts of the Monterey Accelerated Research System (MARS) cable on the seabed and benthic faunal assemblages". In: *MARS Biological Survey Report, Monterey Bay National Marine Sanctuary, NOAA*.

Kunze, Eric et al. (2002). "Internal waves in Monterey submarine canyon". In: *Journal of Physical Oceanography* 32.6, pp. 1890–1913.

Kuvshinov (2016). "Interaction of helically wound fibre-optic cables with plane seismic waves". In: *Geophysical Prospecting* 64.3, pp. 671–688.

Ladanyi, Branko and OB Andersland (2004). *Frozen ground engineering*. Wiley.

Laine, Jérôme and Denis Mougenot (2014). "A high-sensitivity MEMS-based accelerometer". In: *The Leading Edge* 33.11, pp. 1234–1242.

Lawrence, Jesse F and Germán A Prieto (2011). "Attenuation tomography of the western United States from ambient seismic noise". In: *Journal of Geophysical Research: Solid Earth* 116.B6.

Lay, Thorne and Terry C Wallace (1995). *Modern global seismology*. Vol. 58. Elsevier.

Léger, Emmanuel et al. (2019). "A distributed temperature profiling method for assessing spatial variability in ground temperatures in a discontinuous permafrost region of Alaska". In: *The Cryosphere* 13.11, pp. 2853–2867.

Lehmann, I (1936). "Inner earth". In: *Publ Bur Centr Séism Int Sér A* 14, pp. 3–31.

Lellouch, A et al. (2019). "Seismic velocity estimation using passive downhole distributed acoustic sensing records–examples from the San Andreas Fault Observatory at Depth". In: *Journal of Geophysical Research: Solid Earth.*

Levin, Lisa A et al. (2019). "Global Observing Needs in the Deep Ocean". In: *Frontiers in Marine Science* 6, p. 241.

Li, Ling, Sanjay Nimbalkar, and Rui Zhong (2018). "Finite element model of ballasted railway with infinite boundaries considering effects of moving train loads and Rayleigh waves". In: *Soil Dynamics and Earthquake Engineering* 114, pp. 147–153.

Li, Yong-Gang et al. (1990). "Seismic trapped modes in the Oroville and San Andreas fault zones". In: *Science* 249.4970, pp. 763–766.

Lin, Fan-Chi, Dunzhu Li, et al. (2013). "High-resolution 3D shallow crustal structure in Long Beach, California: Application of ambient noise tomography on a dense seismic array". In: *Geophysics* 78.4, Q45–Q56.

Lin, Fan-Chi, Morgan P Moschetti, and Michael H Ritzwoller (2008). "Surface wave tomography of the western United States from ambient seismic noise: Rayleigh and Love wave phase velocity maps". In: *Geophysical Journal International* 173.1, pp. 281–298.

Lindsey, N J, T C Dawe, and J B Ajo-Franklin (2019). "Illuminating seafloor faults and ocean dynamics with dark fiber distributed acoustic sensing". In: *Science* XX.XX, pp. XXX–XXX.

Lindsey, Nathaniel J et al. (2017). "Fiber-optic network observations of earthquake wavefields". In: *Geophysical Research Letters* 44.23, pp. 11–792.

Lindsey, N.J., H. Rademacher, and J.B. Ajo-Franklin (2019). "On the broadband instrument response of fiber-optic DAS arrays". In: *Journal of Geophysical Research: Solid Earth* XX.XX, pp. XXX–XXX.

Liu, L et al. (2015). "Remote sensing measurements of thermokarst subsidence using InSAR". In: *Journal of Geophysical Research: Earth Surface* 120.9, pp. 1935–1948.

Long, Derek A (2002). *The Raman effect: A unified treatment of the theory of Raman scattering by molecules.* Wiley.

Longuet-Higgins, Michael Selwyn (1950a). "A theory of the origin of microseisms". In: *Philosophical Transactions of the Royal Society of London. Series A, Mathematical and Physical Sciences* 243.857, pp. 1–35.

— (1950b). "A theory of the origin of microseisms". In: *Philosophical Transactions of the Royal Society of London. Series A, Mathematical and Physical Sciences* 243.857, pp. 1–35.

Lopez, J et al. (2017). "Valuation of distributed acoustic sensing VSP for frequent monitoring in deepwater". In: *SEG Technical Program Expanded Abstracts 2017.* Society of Exploration Geophysicists, pp. 6044–6048.

Louie, John N (2001). "Faster, better: shear-wave velocity to 100 meters depth from refraction microtremor arrays". In: *Bulletin of the Seismological Society of America* 91.2, pp. 347–364.

Maier, Katherine L, Samuel Y Johnson, and Patrick Hart (2018). "Controls on submarine canyon head evolution: Monterey Canyon, offshore central California". In: *Marine Geology* 404, pp. 24–40.

Manga, Michael et al. (2018). "The pumice raft-forming 2012 Havre submarine eruption was effusive". In: *Earth and Planetary Science Letters* 489, pp. 49–58.

Marra, Giuseppe et al. (2018). "Ultrastable laser interferometry for earthquake detection with terrestrial and submarine cables". In: *Science* 361.6401, pp. 486–490.

Martin, Eileen Rose (2018). "Passive Imaging and Characterization of the Subsurface with Distributed Acoustic Sensing". PhD thesis. Stanford University.

Martin, Eileen R et al. (2017). "Seismic monitoring leveraging existing telecom infrastructure at the SDASA: Active, passive, and ambient-noise analysis". In: *The Leading Edge* 36.12, pp. 1025–1031.

Masoudi, Ali and Trevor P Newson (2016). "Contributed Review: Distributed optical fibre dynamic strain sensing". In: *Review of Scientific Instruments* 87.1, p. 011501.

Mateeva, Albena et al. (2014). "Distributed acoustic sensing for reservoir monitoring with vertical seismic profiling". In: *Geophysical Prospecting* 62.4, pp. 679–692.

Mateeva, A et al. (2017). "4D DAS VSP as a tool for frequent seismic monitoring in deep water". In: *The Leading Edge* 36.12, pp. 995–1000.

McKenzie, Jeffrey M, Clifford I Voss, and Donald I Siegel (2007). "Groundwater flow with energy transport and water–ice phase change: numerical simulations, benchmarks, and application to freezing in peat bogs". In: *Advances in water resources* 30.4, pp. 966–983.

McNamara, Daniel E and Raymond P Buland (2004). "Ambient noise levels in the continental United States". In: *Bulletin of the seismological society of America* 94.4, pp. 1517–1527.

Melvin, April M et al. (2017). "Climate change damages to Alaska public infrastructure and the economics of proactive adaptation". In: *Proceedings of the National Academy of Sciences* 114.2, E122–E131.

Meng, Haoran and Yehuda Ben-Zion (2018). "Characteristics of airplanes and helicopters recorded by a dense seismic array near Anza California". In: *Journal of Geophysical Research: Solid Earth* 123.6, pp. 4783–4797.

Mestayer, J et al. (2011). "Field trials of distributed acoustic sensing for geophysical monitoring". In: *SEG Technical Program Expanded Abstracts 2011*. Society of Exploration Geophysicists, pp. 4253–4257.

Mikesell, T Dylan et al. (2015). "A comparison of methods to estimate seismic phase delays: Numerical examples for coda wave interferometry". In: *Geophysical Journal International* 202.1, pp. 347–360.

Miller, DE et al. (2016). "Simultaneous acquisition of distributed acoustic sensing VSP with multi-mode and single-mode fibre-optic cables and 3C-geophones at the Aquistore CO2 storage site". In: *CSEG Recorder* 41.6.

Mittal, Tushar and Brent Delbridge (2019). "Detection of the 2012 Havre submarine eruption plume using Argo floats and its implications for ocean dynamics". In: *Earth and Planetary Science Letters* 511, pp. 105–116.

Moschetti, MP, MH Ritzwoller, and NM Shapiro (2007). "Surface wave tomography of the western United States from ambient seismic noise: Rayleigh wave group velocity maps". In: *Geochemistry, Geophysics, Geosystems* 8.8.

Munn, Jonathan D et al. (2017). "Novel cable coupling technique for improved shallow distributed acoustic sensor VSPs". In: *Journal of Applied Geophysics* 138, pp. 72–79.

Muyzert, Everhard (2007). "Seabed property estimation from ambient-noise recordings: Part I—Compliance and Scholte wave phase-velocity measurements". In: *Geophysics* 72.2, U21–U26.

Nakata, Norimitsu et al. (2011). "Shear wave imaging from traffic noise using seismic interferometry by cross-coherence". In: *Geophysics* 76.6, SA97–SA106.

Nakata, Nori et al. (2015). "Body wave extraction and tomography at Long Beach, California, with ambient-noise interferometry". In: *Journal of Geophysical Research: Solid Earth* 120.2, pp. 1159–1173.

Nanjo, KZ et al. (2010). "Analysis of the completeness magnitude and seismic network coverage of Japan". In: *Bulletin of the Seismological Society of America* 100.6, pp. 3261–3268.

Natali, Susan M, Edward AG Schuur, and Rachel L Rubin (2012). "Increased plant productivity in Alaskan tundra as a result of experimental warming of soil and permafrost". In: *Journal of Ecology* 100.2, pp. 488–498.

Natali, Susan M, Edward AG Schuur, Christian Trucco, et al. (2011). "Effects of experimental warming of air, soil and permafrost on carbon balance in Alaskan tundra". In: *Global Change Biology* 17.3, pp. 1394–1407.

Natali, Susan M. et al. (2014). "Permafrost degradation stimulates carbon loss from experimentally warmed tundra". In: *Ecology* 95.3, pp. 602–608. DOI: 10.1890/13-0602.1. eprint: https://esajournals.onlinelibrary.wiley.com/doi/pdf/10.1890/13-0602.1. URL: https://esajournals.onlinelibrary.wiley.com/doi/abs/10.1890/13-0602.1.

Nelson, Frederick E, Oleg A Anisimov, and Nikolay I Shiklomanov (2001). "Subsidence risk from thawing permafrost". In: *Nature* 410.6831, p. 889.

Nikles, Marc, Luc Thévenaz, and Philippe A Robert (1996). "Simple distributed fiber sensor based on Brillouin gain spectrum analysis". In: *Optics letters* 21.10, pp. 758–760.

Olmsted, Franklin Howard and George Hamilton Davis (1961). *Geologic features and groundwater storage capacity of the Sacramento Valley, California*. US Government Printing Office.

Paitz, Patrick, Korbinian Sager, and Andreas Fichtner (2018). "Rotation and strain ambient noise interferometry". In: *Geophysical Journal International* 216.3, pp. 1938–1952.

Papp, Bence et al. (2017). "A study of the geophysical response of distributed fibre optic acoustic sensors through laboratory-scale experiments". In: *Geophysical Prospecting* 65.5, pp. 1186–1204.

Park, J, WV Sweet, and R Heitsenrether (2015). "Water level oscillations in Monterey Bay and Harbor". In: *Ocean Science* 11.3, pp. 439–453.

Parker, LM et al. (2018). "Active-source seismic tomography at the Brady Geothermal Field, Nevada, with dense nodal and fiber-optic seismic arrays". In: *Seismological Research Letters* 89.5, pp. 1629–1640.

Parker, Tom, Sergey Shatalin, and Mahmoud Farhadiroushan (2014). "Distributed Acoustic Sensing–a new tool for seismic applications". In: *first break* 32.2, pp. 61–69.

Pasyanos, Michael E, Douglas S Dreger, and Barbara Romanowicz (1996). "Toward real-time estimation of regional moment tensors". In: *Bulletin of the Seismological Society of America* 86.5, pp. 1255–1269.

Paull, Charles K et al. (2018). "Powerful turbidity currents driven by dense basal layers". In: *Nature communications* 9.1, p. 4114.

Personick, SD (1977). "Photon probe—An optical-fiber time-domain reflectometer". In: *The bell system technical journal* 56.3, pp. 355–366.

Poli, P et al. (2012). "Body-wave imaging of Earth's mantle discontinuities from ambient seismic noise". In: *Science* 338.6110, pp. 1063–1065.

Posey, R, GA Johnson, and ST Vohra (2000). "Strain sensing based on coherent Rayleigh scattering in an optical fibre". In: *Electronics Letters* 36.20, pp. 1688–1689.

Prieto, German A et al. (2010). "Impulse response of civil structures from ambient noise analysis". In: *Bulletin of the Seismological Society of America* 100.5A, pp. 2322–2328.

Prieto, Germán A et al. (2011). "On amplitude information carried by the ambient seismic field". In: *Comptes Rendus Geoscience* 343.8-9, pp. 600–614.

Quiros, Diego A, Larry D Brown, and Doyeon Kim (2016). "Seismic interferometry of railroad induced ground motions: Body and surface wave imaging". In: *Geophysical Supplements to the Monthly Notices of the Royal Astronomical Society* 205.1, pp. 301–313.

Ranasinghe, N et al. (2018). "Enhanced Global Seismic Resolution Using Transoceanic SMART Cables". In: *Seismological Research Letters* 89.1, pp. 77–85.

Reinsch, Thomas, Tom Thurley, and Philippe Jousset (2017). "On the mechanical coupling of a fiber optic cable used for distributed acoustic/vibration sensing applications—a theoretical consideration". In: *Measurement Science and Technology* 28.12, p. 127003.

Rempel, Alan W (2012). "Hydromechanical processes in freezing soils". In: *Vadose Zone Journal* 11.4.

Retailleau, Lise and Lucia Gualtieri (2019). "Toward High-Resolution Period-Dependent Seismic Monitoring of Tropical Cyclones". In: *Geophysical Research Letters* 46.3, pp. 1329–1337.

Riahi, Nima and Peter Gerstoft (2015). "The seismic traffic footprint: Tracking trains, aircraft, and cars seismically". In: *Geophysical Research Letters* 42.8, pp. 2674–2681.

Richter, Peter et al. (2019). "High-resolution distributed acoustic sensor using engineered fiber for hydraulic fracture monitoring and optimization in unconventional completions". In: *SEG Technical Program Expanded Abstracts 2019*. Society of Exploration Geophysicists, pp. 4874–4878.

Rodgers, Arthur J et al. (2018). "Broadband (0–4 Hz) ground motions for a magnitude 7.0 Hayward fault earthquake with three-dimensional structure and topography". In: *Geophysical Research Letters* 45.2, pp. 739–747.

Roemmich, Dean et al. (2009). "The Argo Program: Observing the global ocean with profiling floats". In: *Oceanography* 22.2, pp. 34–43.

Romanovsky, Vladimir E, Sharon L Smith, and Hanne H Christiansen (2010). "Permafrost thermal state in the polar Northern Hemisphere during the international polar year 2007–2009: a synthesis". In: *Permafrost and Periglacial processes* 21.2, pp. 106–116.

Romanowic, Barbara and Domenico Giardini (2001). *The future of permanent seismic networks.*

Romanowicz, B, L Gee, and RA Uhrhammer (1992). "Berkeley Digital Seismic Network: a broadband network for northern and central California". In: *IRIS Newsletter* 11, pp. 1–5.

Romanowicz, Barbara et al. (2009). "Acquiring real time data from the broadband ocean bottom seismic observatory at Monterey Bay (MOBB)". In: *Seismological Research Letters* 80.2, pp. 197–202.

Rost, Sebastian and Christine Thomas (2002). "Array seismology: Methods and applications". In: *Reviews of geophysics* 40.3, pp. 2–1.

Roux, Philippe et al. (2005). "P-waves from cross-correlation of seismic noise". In: *Geophysical Research Letters* 32.19.

Rowland, J C, B J Travis, and CJ Wilson (2011). "The role of advective heat transport in talik development beneath lakes and ponds in discontinuous permafrost". In: *Geophysical Research Letters* 38.17.

Rücker, Carsten, Thomas Günther, and Florian M Wagner (2017). "pyGIMLi: An open-source library for modelling and inversion in geophysics". In: *Computers & Geosciences* 109, pp. 106–123.

Ruiz, S and R Madariaga (2018). "Historical and recent large megathrust earthquakes in Chile". In: *Tectonophysics* 733, pp. 37–56.

Sabra, Karim G et al. (2005). "Extracting time-domain Green's function estimates from ambient seismic noise". In: *Geophysical Research Letters* 32.3.

Schaefer, Kevin et al. (2014). "The impact of the permafrost carbon feedback on global climate". In: *Environmental Research Letters* 9.8, p. 085003.

Schimmel, Martin et al. (2011). "Polarized Earth's ambient microseismic noise". In: *Geochemistry, Geophysics, Geosystems* 12.7.

Schmandt, Brandon and Robert W Clayton (2013). "Analysis of teleseismic P waves with a 5200-station array in Long Beach, California: Evidence for an abrupt boundary to Inner Borderland rifting". In: *Journal of Geophysical Research: Solid Earth* 118.10, pp. 5320–5338.

Schmandt, B et al. (2017). "Seismic array constraints on reach-scale bedload transport". In: *Geology* 45.4, pp. 299–302.

Schuur, Edward AG et al. (2015). "Climate change and the permafrost carbon feedback". In: *Nature* 520.7546, pp. 171–179.

Seats, Kevin J, Jesse F Lawrence, and German A Prieto (2012). "Improved ambient noise correlation functions using Welch s method". In: *Geophysical Journal International* 188.2, pp. 513–523.

Sens-Schönfelder, Christoph and Ulrich Wegler (2006). "Passive image interferometry and seasonal variations of seismic velocities at Merapi Volcano, Indonesia". In: *Geophysical research letters* 33.21.

Shapiro, Nikolai M et al. (2005). "High-resolution surface-wave tomography from ambient seismic noise". In: *Science* 307.5715, pp. 1615–1618.

Shatalin, Sergey V, Vladimir N Treschikov, and Alan J Rogers (1998). "Interferometric optical time-domain reflectometry for distributed optical-fiber sensing". In: *Applied optics* 37.24, pp. 5600–5604.

Snieder, Roel (2004). "Extracting the Green's function from the correlation of coda waves: A derivation based on stationary phase". In: *Physical Review E* 69.4, p. 046610.

Snieder, Roel and Eric Larose (2013). "Extracting Earth's elastic wave response from noise measurements". In: *Annual Review of Earth and Planetary Sciences* 41.

Spikes, Kyle T et al. (2019). "Comparison of geophone and surface-deployed distributed acoustic sensing seismic data". In: *Geophysics* 84.2, A25–A29.

Stutzmann, Eleonore et al. (2009). "Global climate imprint on seismic noise". In: *Geochemistry, Geophysics, Geosystems* 10.11.

Taira, Taka'aki et al. (2018). "Monitoring reservoir response to earthquakes and fluid extraction, Salton Sea geothermal field, California". In: *Science Advances* 4.1, e1701536.

Tape, Carl et al. (2015). "Transtensional tectonics of the Minto Flats fault zone and Nenana basin, central Alaska". In: *Bulletin of the Seismological Society of America* 105.4, pp. 2081–2100.

Thomson, William T (1950). "Transmission of elastic waves through a stratified solid medium". In: *Journal of applied Physics* 21.2, pp. 89–93.

Tribaldos, Verónica Rodrıguez et al. "Surface Wave Imaging using Distributed Acoustic Sensing Deployed on Dark Fiber: Moving Beyond High Frequency Noise". In:

Trowbridge, John H et al. (2019). "The Ocean Observatories Initiative". In:

Tsai, Victor C et al. (2012). "A physical model for seismic noise generation from sediment transport in rivers". In: *Geophysical Research Letters* 39.2.

Uchida, Shun, Kenichi Soga, and Koji Yamamoto (2012). "Critical state soil constitutive model for methane hydrate soil". In: *Journal of Geophysical Research: Solid Earth* 117.B3.

Verliac*, Michel, Vladislav Lesnikov, and Coline Euriat (2015). "The Rousse-1 DAS VSP experiment—Observations and comparisons from various optical acquisition systems". In: *SEG Technical Program Expanded Abstracts 2015*. Society of Exploration Geophysicists, pp. 5534–5538.

Viens, Loıc et al. (2017). "Retrieving impulse response function amplitudes from the ambient seismic field". In: *Geophysical Journal International* 210.1, pp. 210–222.

Vincent, Warwick F, Mickaël Lemay, and Michel Allard (2017). "Arctic permafrost landscapes in transition: towards an integrated Earth system approach". In: *Arctic Science* 3.2, pp. 39–64.

Wagner, Anna M, Marc C Beede, and Jon E Zufelt (2013). *Permafrost Ecosystem Warming Prototype: Installation, Operation, and Initial Site Characterization*. Tech. rep. ENGI-

NEER RESEARCH and DEVELOPMENT CENTER HANOVER NH COLD REGIONS RESEARCH . . .

Wagner, Anna M, Nathaniel J Lindsey, et al. (2018). "Permafrost Degradation and Subsidence Observations during a Controlled Warming Experiment". In: *Scientific reports* 8.1, p. 10908.

Wainwright, Haruko M et al. (2015). "Identifying multiscale zonation and assessing the relative importance of polygon geomorphology on carbon fluxes in an Arctic tundra ecosystem". In: *Journal of Geophysical Research: Biogeosciences* 120.4, pp. 788–808.

Walter, Ryan K et al. (2012). "Nearshore internal bores and turbulent mixing in southern Monterey Bay". In: *Journal of Geophysical Research: Oceans* 117.C7.

Walvoord, Michelle A, Frederick D Day-Lewis, et al. (2015). *Improved Understanding of Permafrost Controls on Hydrology in Interior Alaska by Integration of Ground-Based Geophysical Permafrost Characterization and Numerical Modeling.* Tech. rep. ENGINEER RESEARCH and DEVELOPMENT CENTER FORT RICHARDSON AK COLD REGIONS . . .

Walvoord, Michelle A and Barret L Kurylyk (2016). "Hydrologic impacts of thawing permafrost—A review". In: *Vadose Zone Journal* 15.6.

Wang, Herbert F et al. (2018). "Ground motion response to an Ml 4.3 earthquake using co-located distributed acoustic sensing and seismometer arrays". In: *Geophysical Journal International* 213.3, pp. 2020–2036.

Wapenaar, Kees (2006). "Green's function retrieval by cross-correlation in case of one-sided illumination". In: *Geophysical Research Letters* 33.19.

Wapenaar, Kees and Jacob Fokkema (2006). "Green's function representations for seismic interferometry". In: *Geophysics* 71.4, SI33–SI46.

Weaver, Richard L and Oleg I Lobkis (2005). "Fluctuations in diffuse field–field correlations and the emergence of the Green's function in open systems". In: *The Journal of the Acoustical Society of America* 117.6, pp. 3432–3439.

Webb, Spahr C (1998). "Broadband seismology and noise under the ocean". In: *Reviews of Geophysics* 36.1, pp. 105–142.

Webster, P et al. (2013). "Micro-seismic detection using distributed acoustic sensing". In: *SEG Technical Program Expanded Abstracts 2013.* Society of Exploration Geophysicists, pp. 2459–2463.

Wesnousky, Steven G (1986). "Earthquakes, Quaternary faults, and seismic hazard in California". In: *Journal of Geophysical Research: Solid Earth* 91.B12, pp. 12587–12631.

Wielandt, E and G Streckeisen (1982). "The leaf-spring seismometer: Design and performance". In: *Bulletin of the Seismological Society of America* 72.6A, pp. 2349–2367.

Wiemer, Stefan and Max Wyss (2000). "Minimum magnitude of completeness in earthquake catalogs: Examples from Alaska, the western United States, and Japan". In: *Bulletin of the Seismological Society of America* 90.4, pp. 859–869.

Williams, Ethan et al. (2019). "Teleseisms and Microseisms on an Ocean-Bottom Distributed Acoustic Sensing Array". In:

Willis, Mark, Jonathan Ajo-Franklin, and Baishali Roy (2017). "Introduction to this special section: Geophysical applications of fiber-optic distributed sensing". In: *The Leading Edge* 36.12, pp. 973–974.

Wu, Xiang et al. (2017). "Compressional-and shear-wave studies of distributed acoustic sensing acquired vertical seismic profile data". In: *The Leading Edge* 36.12, pp. 987–993.

Wunsch, Carl and Raffaele Ferrari (2018). "100 Years of the Ocean General Circulation". In: *Meteorological Monographs* 59, pp. 7–1.

Yang, Yingjie et al. (2007). "Ambient noise Rayleigh wave tomography across Europe". In: *Geophysical Journal International* 168.1, pp. 259–274.

Yilmaz, Özdoğan (2001). *Seismic data analysis*. Vol. 1. Society of exploration geophysicists Tulsa, OK.

Yu, Chunquan et al. (2019). "The Potential of DAS in Teleseismic Studies: Insights From the Goldstone Experiment". In: *Geophysical Research Letters* 46.3, pp. 1320–1328.

Zeng, Xiangfang et al. (2017). "Properties of noise cross-correlation functions obtained from a distributed acoustic sensing array at Garner Valley, California". In: *Bulletin of the Seismological Society of America* 107.2, pp. 603–610.

Žgalj, Amela, Edvin Skaljo, and Esad Kadušić (2011). "Pulse width as an influencing factor in Optical Time Domain Reflectometry measurements". In: *2011 19thTelecommunications Forum (TELFOR) Proceedings of Papers*. IEEE, pp. 832–835.

Zhan, Ge, Jan Kommedal, and Jay Nahm (2015). "VSP field trials of distributed acoustic sensing in Trinidad and Gulf of Mexico". In: *SEG Technical Program Expanded Abstracts 2015*. Society of Exploration Geophysicists, pp. 5539–5543.

Zhan, Zhongwen et al. (2010). "Retrieval of Moho-reflected shear wave arrivals from ambient seismic noise". In: *Geophysical Journal International* 182.1, pp. 408–420.

Zhang, Jian, Peter Gerstoft, and Peter D Bromirski (2010). "Pelagic and coastal sources of P-wave microseisms: Generation under tropical cyclones". In: *Geophysical Research Letters* 37.15.

Zhirnov, Andrey et al. (2016). "Effects of laser frequency drift in phase-sensitive optical time-domain reflectometry fiber sensors". In: *arXiv preprint arXiv:1604.08854*.

Zhou, Jun et al. (2013). "Characteristics and Explanations of Interference Fading of a ϕ-OTDR With a Multi-Frequency Source". In: *Journal of lightwave technology* 31.17, pp. 2947–2954.